Summer 8-15-2017

Synthesis, characterization, and biological activity of spherical nucleic acid (SNA) constructs for cancer therapy and imaging

Colin Calabrese
Washington University in St. Louis

WASHINGTON UNIVERSITY IN ST. LOUIS

Department of Chemistry

Dissertation Examination Committee:
Prof. John-Stephen Taylor, Chair
Prof. Jonathan Barnes
Prof. Yongjian Liu
Prof. Liviu Mirica
Prof. Chad A. Mirkin

Synthesis, Characterization, and Biological Activity of Spherical Nucleic Acid (SNA) Constructs for Cancer Therapy and Imaging

by

Colin Calabrese

A dissertation presented to
The Graduate School
of Washington University in
partial fulfillment of the
requirements for the degree
of Doctor of Philosophy

August 2017
St. Louis, Missouri

Table of Contents

List of Figures

Chapter 1

Chapter 2

Chapter 3

Chapter 4

Chapter 5

Chapter 6

List of Schemes

List of Tables

Acknowledgments

First, I would like to thank my advisor and mentor, Prof. Chad Mirkin, for his invaluable support and guidance during my graduate school career. I feel I have grown immensely as a chemist and critical thinker under his tutelage, and I consider myself extremely privileged to have worked with such an outstanding scientist. I also owe a deep debt of gratitude to Chancellor Mark Wrighton, Prof. William Buhro, and Prof. Richard Loomis for giving me the opportunity to continue my graduate work at Washington University in St. Louis. I am honored that you believed in me to take such a great leap into a new environment and explore new research challenges. I deeply appreciate the assistance from Rachel Dunn in helping me navigate the requirements of the Chemistry Department and Barbara Tessmer for assisting me in the dissertation defense process. I thank Prof. John-Stephen Taylor and Prof. Yongjian Liu for advising me during my tenure at Washington University in St. Louis. Both of you have proven extremely accessible and helpful any time I needed guidance or a critical set of eyes and ears on my work. I also thank Prof. Liviu Mirica and Prof. Jonathan Barnes for serving on my defense committee and taking the time to learn about my research and offer their insights and critical suggestions.

I also want to acknowledge all the incredible colleagues and friends I have worked with throughout my graduate school career who helped me with various collaborations and contributed to the skill set I am so grateful to be equipped with today. I particularly acknowledge Dr. Alexander Scott and Dr. Todd Hovey for not only their material support but also their emotional support and friendship which I believe will be lifelong. I also acknowledge my friends, collaborators and co-authors Dr. Jonathan Choi, Dr. Resham Singh Banga, Nikunjkumar Savalia, Dr. William Briley, Dr. Timothy Merkel, Dr. Pratik Randeria, Dr. Suguna Narayan, Dr.

Jessica Rouge, Dr. Chuan Zhang, and Dr. Liangliang Hao. I thank my current collaborators at Northwestern University, Dr. Lisa Cole, Tanushri Sengupta, Robert Stawicki, and Sasha Ebrahimi, for assisting in ongoing studies. I thank my great colleagues in the Liu lab for their eagerness to share their knowledge as I delved into radiochemistry and *in vivo* studies: Debbie Sultan, Lisa Detering, Dr. Gyu Seong Heo, and Hannah Luehmann.

Lastly, I would like to sincerely thank my parents, my grandparents, and my extended family for believing in me and supporting me through my long and difficult path towards earning my doctoral degree. Dad, you are a role model to me as both a chemist and a father and I wish I had the raw motivation and talent to finish a PhD in chemistry in 3.5 years. Mom, without your love and support during the times I felt down on myself I don't know if I would have had the motivation to keep going. Earning my PhD has taught me a lot about the importance of family support as I have grown into adulthood and has served as a learning process not only intellectually, but emotionally and spiritually.

-Colin Calabrese

Dedicated to my parents.

ABSTRACT OF THE DISSERTATION

Synthesis, Characterization, and Biological Activity of

Spherical Nucleic Acid (SNA) Constructs

for Cancer Therapy and Imaging

by

Colin Calabrese

Doctor of Philosophy in Chemistry

Washington University in St. Louis, 2017

Professor John-Stephen Taylor, Chair

This dissertation focuses on the development of biocompatible oligonucleotide-based nanomaterials, known as spherical nucleic acids (SNAs), as therapeutic and diagnostic agents for intracellular gene regulation and *in vivo* cancer imaging by positron emission tomography (PET). SNAs consist of a nanoparticle core functionalized with a dense shell of oligonucleotides such as deoxyribonucleic acid (DNA). Detailed synthetic procedures and characterization of novel SNAs with purpose-built biocompatible core materials are described. The SNAs exhibit comparable chemical, physical and biological properties regardless of core composition. The functionalities of the SNAs were further tailored by deliberate design and chemical modification of their oligonucleotide sequences.

The SNA nanostructures studied in this dissertation include those with cores made from infinite coordination polymers (ICPs), self-assembled block copolymer micelles, ^{64}Cu-alloyed gold nanoclusters, and commercially-available monodisperse gold nanoparticles. *In vitro* and *in vivo* investigations of each SNA type are described. The first two examples, functionalized on their surface with DNA, entered a variety of cell lines without the need for transfection agents,

and inhibited the translation of disease-related messenger RNA (mRNA). The ^{64}Cu-alloyed gold nanoclusters, functionalized on their surface with either DNA or phosphorodiamidate morpholino (PMO) oligonucleotides, were evaluated *in vivo* to determine their pharmacokinetics and biodistribution in mice. The blood circulation time of PMO-modified nanoclusters was far superior to DNA-modified nanoclusters, enabling their use in tumor pre-targeting studies wherein a non-radioactive nanocluster was first injected, allowed to accumulate at the tumor site, and then probed by injection of a complementary oligonucleotide labeled with ^{64}Cu. Studies in mouse tumor models demonstrated the feasibility of *in vivo* hybridization-based pre-targeting using SNA nanomaterials. Furthermore, the basic chemical and biophysical properties of PMO-modified commercial gold nanoparticles were studied. It was determined that PMO-based SNAs display very similar cellular interactions as compared to their DNA analogues, including the capability of entering cells in a transfection-free manner and effecting gene knockdown. The neutral charge of the SNAs based upon PMO oligonucleotides exhibit more rapid capture kinetics of complementary oligonucleotides compared to DNA SNAs, as well as higher melting temperatures of hybridized duplexes. Taken together, the chemical versatility of SNAs has led to significant advances in understanding their basic properties and improving their viability for *in vivo* translation for biomedical applications.

Specifically, we uncovered further evidence for the central hypothesis that the unique properties of SNAs, specifically active cellular uptake and their sharp thermal denaturation curves, are core-independent and rely on the spherical orientation of DNA around a nanoparticle core. We also discovered that the cellular interactions of SNAs, mainly active uptake, are likewise independent of the charge of the nucleic acid shell. However, the chemical composition of the SNA-bound oligonucleotides strongly influences their *in vivo* pharmacokinetics, with

neutral oligonucleotides conferring much longer blood circulation times compared to negatively-charged SNAs. We also found that the kinetics and thermodynamics of hybridization of neutral SNAs to complementary oligonucleotides are superior to those of negatively-charged SNAs, expanding their potential uses not only as biomedical agents but also as *in vivo* "click chemistry" tools capable of the bioorthogonal connection of multiple components under *in vivo* physiological conditions. Collectively, the studies presented herein demonstrate that the rational design of the core material and oligonucleotide shell impart novel properties to SNAs that expand their capabilities as therapeutic, diagnostic, and bioorthogonal assembly agents.

Chapter 1

Introduction

Nucleic acids are best known as nature's universal storage medium for genetic information. The ability of nucleic acids to encode and transmit data arises from Watson-Crick base pairing among the five canonical nucleobases found in ribonucleic acid (RNA) and deoxyribonucleic acid (DNA) oligonucleotides: the purines adenine (A) and guanine (G), and the pyridmidines cytosine (C), thymine (T), and uracil (U) which pair in the fashion A:T, G:C, and A:U. (Figure 1.1). Uracil is found exclusively in RNA whereas thymine is found in DNA.

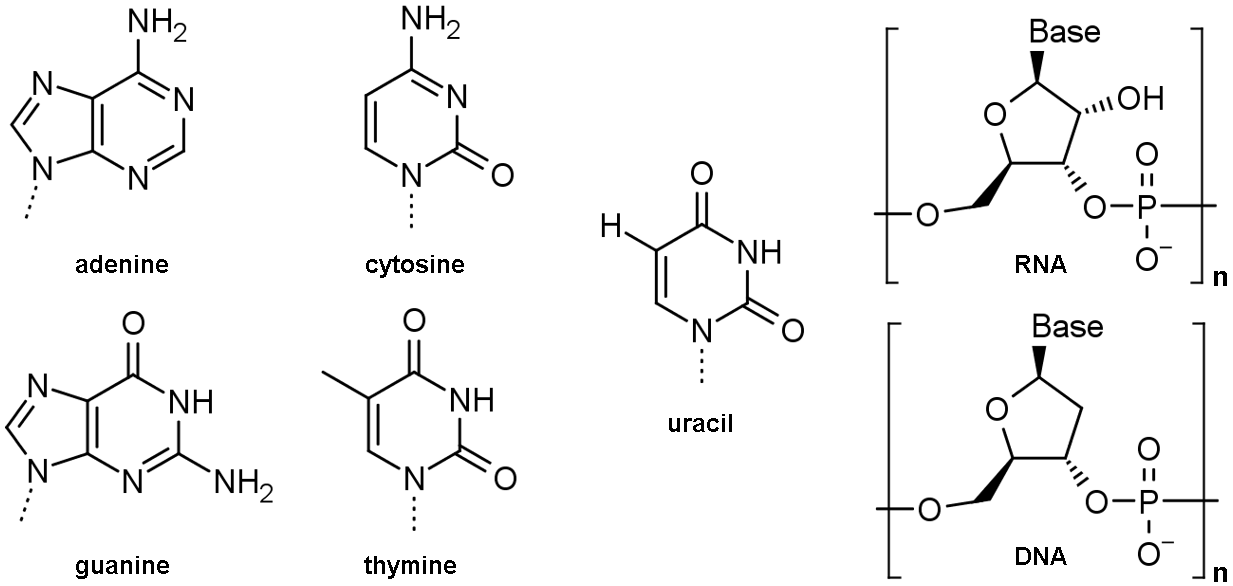

Figure 1.1. Chemical structures of nucleic acids. Left: The five naturally-occurring nucleobases (dotted lines represent point of attachment to sugar backbone). Right: Structure of RNA and DNA repeating units (5´→3´).

An additional feature of the specific hydrogen bond-mediated hybridization between nucleic acid strands is their capacity to spontaneously form more complex secondary, tertiary and quaternary three-dimensional structures.[1] Perhaps one of the most important biological examples is transfer RNA (tRNA), whose three-dimensional folded structure serves as a macromolecular adapter to

translate the data in messenger RNA (mRNA) into the corresponding amino acids during protein synthesis in the ribosome.[2] Similarly, ribozymes are RNA molecules whose supramolecular, highly organized structures enable them to catalyze biochemical reactions inside cells just like traditional protein enzymes.[3] Thus, in living organisms, nucleic acids not only store information but also behave as nanoscale building blocks for precise assembly of functional endogenous nanomaterials that are crucial to cellular functioning.

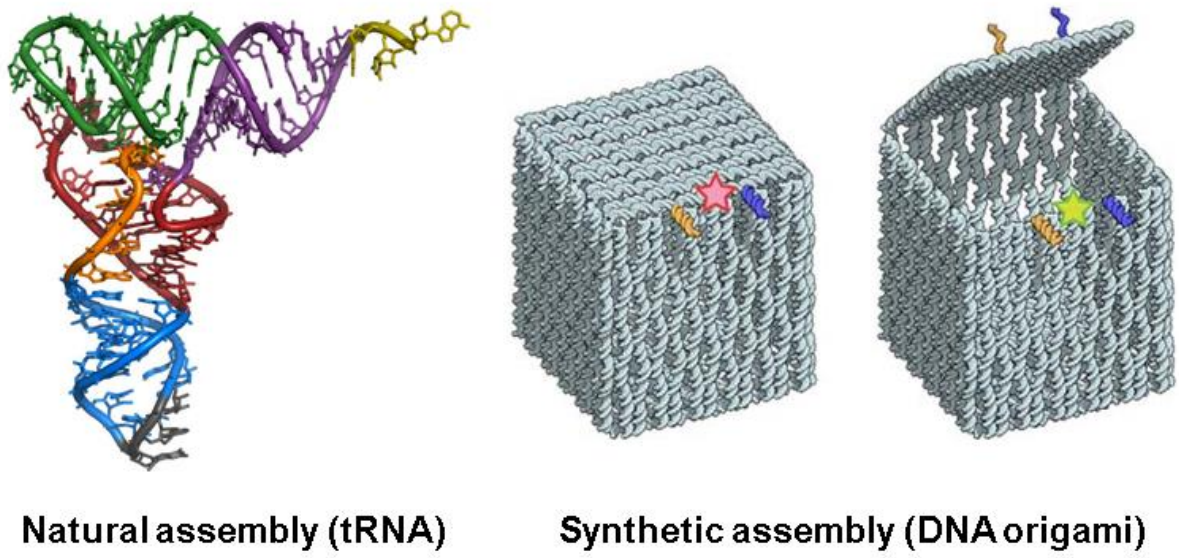

Figure 1.2. Comparison of natural and synthetic assembly of functional 3D nucleic acid nanostructures.

Researchers have harnessed the programmable nature of nucleic acid hybridization to build synthetic nucleic acid nanomaterials with a wide variety of applications ranging from electronic materials to biomedicine.[4-10] With the advent of automated solid-phase nucleic acid synthesis enabled by advances in phosphoramidite chemistry, chemists can easily generate large libraries of custom oligonucleotides with high chemical purity on large scales.[11-12] One type of artificial nucleic acid nanomaterial, termed "DNA origami," relies on computer-aided design to fold a multicomponent mixture of oligonucleotides into atomically precise and molecularly identical three-dimensional structures.[13] Such structures can be stimuli-responsive, such as a

DNA origami “box” which can carry cargo and open in response to a “key” oligonucleotide (Figure 1.2).[14] The naturally-occurring nucleic acids, however, possesses limited chemical functionality. To design more advanced functional nanomaterials, oligonucleotides can be conjugated to small organic molecules,[15-23] other biomacromolecules,[24-27] polymers,[28-32] and nanoparticles.[33-38] Such hybrid building blocks can then be assembled into higher-order structures based on the programmed hybridization of the attached DNA base sequences.[39-45]

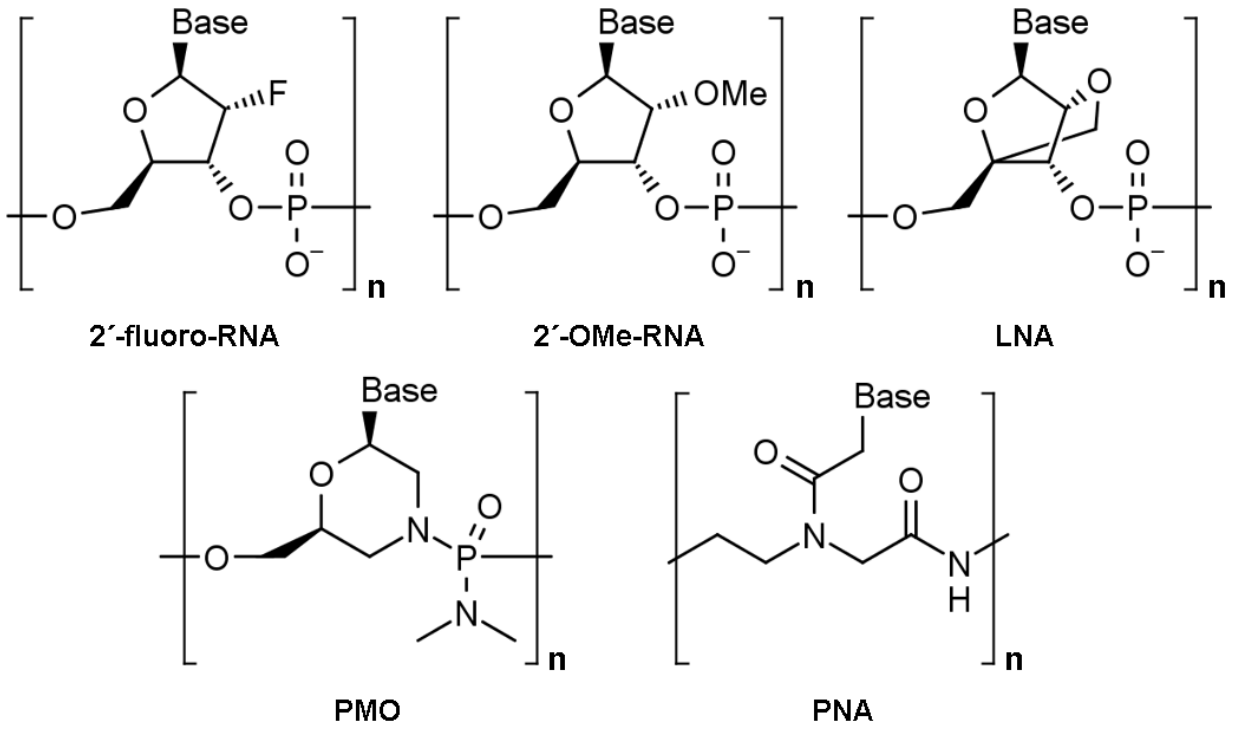

Figure 1.3. Structures of selected synthetic nucleic acid analogues.

In addition, synthetic nucleic acids have been developed that possess artificial backbones imparting novel chemical attributes. RNA derivatives such as 2´-fluoro-RNA and 2´-OMe-RNA exhibit enhanced resistance to base-catalyzed decomposition and nuclease degradation.[46-47] Locked nucleic acids (LNAs) possess a modified bicyclic sugar backbone that restricts their conformational flexibility, imparting higher stability to their duplexes with DNA and RNA.[48] Fully neutral nucleic acid analogues have also been synthesized, namely peptide nucleic acids

(PNA) and phosphorodiamidate morpholino oligonucleotides (PMO) which possess no net charge, and as a consequence form extremely stable duplexes with complementary nucleic acids due to the absence of electrostatic repulsion.[49-50] Chemists thus have a useful toolbox of chemically varied nucleic acids to select from when designing nanomaterials (Figure 1.3).

One of the emerging classes of hybrid nucleic acid nanomaterials are spherical nucleic acids (SNAs), which are comprised of a nanoparticle core decorated with a dense shell of oligonucleotides (Scheme 1.1).[51] The first examples utilized thiolated oligonucleotides which readily adsorb onto the surface of gold nanoparticles (AuNPs) with a bond dissociation energy of 40-50 kcal/mol, approaching the strength of a covalent bond (80-90 kcal/mol).[52] Gradually increasing the NaCl concentration during the adsorption process, called "salt aging," screens the negative charge of the phosphodiester backbone of the DNA molecules as they associate with Na+ cations, thereby increasing the density of DNA packing on the surface.[53]

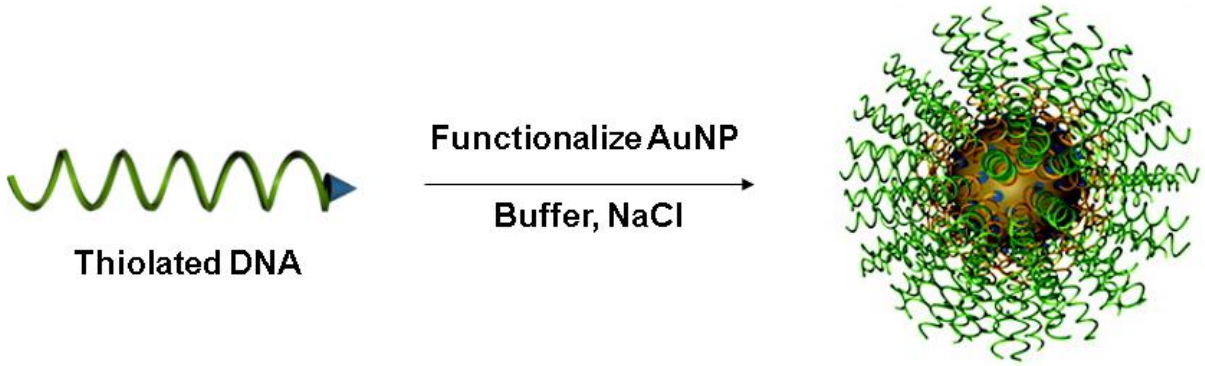

Scheme 1.1. Functionalization of gold nanoparticles to afford spherical nucleic acids (SNAs).

Consequently, the behavior of nucleic acid oligonucleotides changes dramatically when they are arranged around a spherical core. The binding affinity of SNAs for complementary oligonucleotides is higher than linear DNA, resulting in higher melting transition temperatures (T_m) and sharper thermal denaturation curves.[54] Initially, AuNP-based SNAs saw great promise in biodetection schemes due to their ability to detect target oligonucleotides with high specificity,

such as in colorimetric sandwich-type assays that rely on the aggregation-dependent color change of gold nanoparticles in the presence of a complementary strand.[55-56] Chemically-amplified biodetection schemes using SNAs have also been described, where target proteins can be detected down to attomolar concentrations.[57] SNAs have also been employed in the detection of toxic heavy metal ions.[58-59] More broadly, SNAs can be thought of as "programmable atom equivalents" which self-assemble into extended superlattices of a desired symmetry and morphology based on the oligonucleotide sequences attached to the nanoparticle core(s).[60-62] This approach enables the synthesis of macroscopic nanoparticle "alloys," for example by alternating gold and platinum nanoparticles in a well-defined repeating binary lattice structure.[63] SNA superlattices have found applications primarily in catalysis, for example in the gold-mediated oxidation of alcohols to aldehydes,[64] as well as the assembly of bioactive enzyme-cored SNAs into catalytic superlattices.[65]

A major discovery was realized when the interaction of SNAs with cell membranes was first probed. In cell culture, linear oligonucleotides exhibit poor cellular uptake due to their negative charge, and typically must be transfected with polycations or cationic lipids to deliver them across the cell membrane via passive diffusion.[66-67] Counterintuitively, SNAs were found to undergo active cell uptake and rapidly cross cell membranes without the need for transfection agents, despite their higher negative charge density and larger size.[68] In fact, higher density of the oligonucleotide loading on the surface was found to correlate directly with improved cellular uptake.[69] These striking findings prompted efforts to discover the mechanism by which SNAs are taken up and internalized by cells. The evidence points to an active uptake mechanism triggered by recognition of SNAs by class A scavenger receptors (SR-As), which were first discovered in macrophages but are now known to be widely expressed on the surface of mammalian cells.[70-71]

SR-As bind naturally-occurring endogenous and exogenous polyanions, triggering their endocytosis for eventual destruction in lysosomes.[72] SNAs were found to enter cells via SR-A-mediated endocytosis, with sufficient escape of nucleic acids from the endosome to engage in knockdown of target messenger RNA.[73]

Recognition of SNAs by SR-As is believed to be due to the natural affinity of the receptor for poly(guanosine) (poly-G) DNA.[74] Poly-G spontaneously assembles into three-dimensional four-stranded helical structures known as G-quadruplexes, which are stabilized by Hoogsteen hydrogen bonding and monovalent cations, particularly potassium. It is believed that the dense, highly oriented packing geometry of oligonucleotides on the SNA surface mimics the 3D structure of the G-quadruplex, leading to recognition by SR-As and subsequent endocytosis. Supporting this hypothesis, SNAs bearing G-rich oligonucleotides are found to possess superior uptake to SNAs functionalized with poly-T, poly-A, or poly-C DNA, though SNAs of virtually any sequence exhibit superior uptake to single-stranded oligonucleotides.[71]

The cellular uptake of spherical nucleic acids makes them very attractive agents in the rapidly-evolving toolkit of nanomedicine. Studies have demonstrated excellent biocompatibility of SNAs, such as minimal immune response as well as enhanced resistance to nucleases which degrade nucleic acids by cleaving the phosphate backbone.[75-76] Once inside cells, SNAs are capable of behaving as gene regulation agents by binding to and preventing the translation of messenger RNA into disease-related proteins, independent of SNA core composition.[77-78] Other types of nucleic acids have been employed as well, such as locked nucleic acids (LNA), small interfering RNAs (siRNA), peptide nucleic acids (PNA) and catalytically active ribozymes.[79-82] SNAs can also act as immunomodulatory agents by binding toll-like receptors (TLRs) expressed on the inner surfaces of endosomal compartments.[83]

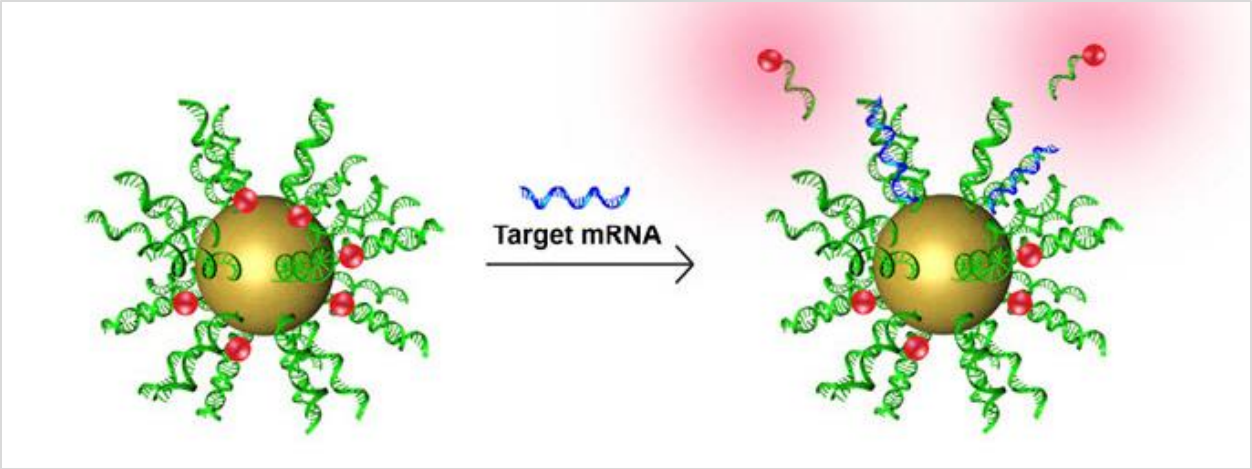

Scheme 1.2. Displacement of nanoflares by target messenger RNA restores fluorescence of attached fluorophores.[84]

Perhaps the most successful commercial application of SNA technology is the multi-component nanosystem referred to as the "nano-flare," which takes advantage of the polyvalent binding of dye-labelled "reporter" oligonucleotides to SNAs.[85-86] The reporter oligonucleotides, when bound to a AuNP SNA, exhibit low fluorescence due to quenching by the gold core. Once the SNA binds to target mRNA, the reporter flares are displaced and the fluorescence of the dye is restored, allowing quantitative detection of virtually any mRNA sequence in live cells by confocal microcopy and flow cytometry (Scheme 1.2). This elegant technology harnesses both the active uptake of SNAs along with their high DNA loading and programmable multivalent interactions with complementary oligonucleotides.

This dissertation is focused on the design, synthesis, and characterization of novel, rationally-designed SNAs with expanded capabilities arising from either modified core composition or modified oligonucleotide chemistry compared to the classical DNA-modified AuNP SNAs. For *in vivo* translation, SNAs with biocompatible cores are highly desired due to concerns about the possible long-term chronic toxicity of gold nanoparticles and their tendency to accumulate in the body.[87] Our initial efforts focused on the design of SNAs assembled via

metal-ligand coordination bonds, an approach not previously explored for constructing SNA nanomaterials. The tailorable and reversible nature of metal coordination bonds provides an opportunity to create programmable DNA nanomaterials that respond to variable physiological conditions such as pH, ionic strength, and/or presence of endogenous competitive ligands. In **Chapter 2** we report the synthesis and characterization of Fe^{3+}-crosslinked DNA nanoparticles assembled from 3,4-hydroxypyridinone (HOPO)-modified DNA duplexes. We demonstrate that Fe^{3+}-HOPO coordination bonds are strong enough to serve as chemically orthogonal cross-links between DNA strands, and the iron atoms are site-selectively incorporated at the HOPO ligands rather than chelated by the phosphate backbone or nucleobases of DNA. However, the DNA-Fe^{3+} nanoparticles synthesized by this approach did not exhibit appreciable cellular uptake, likely due to the random orientation of nucleic acids comprising the nanoparticle. Thus, this study highlighted the importance of the DNA packing geometry in determining cellular uptake and the same coordination chemistry approach was further adapted to generate bioactive SNAs.

In **Chapter 3** the synthesis of Fe^{3+}-HOPO infinite coordination polymer (ICP) nanoparticles and their subsequent functionalization with DNA is described. Drawing from previous lessons, the core material was generated first and then modified with a dense shell of oligonucleotides. A rigid, ditopic HOPO ligand with an azide functional handle was synthesized and mixed with Fe^{3+} under dilute aqueous conditions, affording amorphous ICP nanoparticles. The azide-bearing ICP particles were subsequently mixed with DNA oligonucleotides containing a strained cyclooctyne, enabling DNA functionalization via copper-free click chemistry under ambient conditions with no special additives. A particular advantage of the Fe^{3+}-HOPO coordination bond is its pH sensitivity. At physiological pH, the *tris*-$Fe(HOPO)_3$ complex is the predominant species, but at lower pH values, particularly endosomal pH (6.0-6.5), the *tris*

complex dissociates to the *bis* complex, providing a mechanism for disassembly of the core material and release of oligonucleotides. The cellular uptake of the DNA-ICP nanoparticles was probed in several cell lines and found to be comparable to their AuNP-based counterparts. In addition, the DNA-ICP particles were capable of knocking down a disease-related protein in ovarian cancer cells in a dose-dependent fashion without the need for transfection agents.

Chapter 4 describes an alternate approach to pH-sensitive SNA core construction by employing self-assembled DNA-polyester block copolymer micelles. Using poly(caprolactone) (PCL) as the hydrophobic block and DNA as the hydrophilic block, self-assembled micelles presenting an outer layer of DNA were obtained. Furthermore, appending several DNA strands to the terminus of the polycaprolactone block in a brush-like fashion increased the DNA surface density on the self-assembled micelles. The PCL core material, being a polyester, also exhibits slow pH-dependent hydrolysis in acidic conditions, providing a release mechanism for the oligonucleotides. These self-assembled micelle SNAs were capable of cell entry and intracellular gene knockdown of green fluorescent protein (GFP). Most importantly, comparison of the biophysical properties of the linear and DNA-brush type micelles showed that the higher DNA loading on the surface of the micelle led to higher cellular uptake as well as sharper melting transitions between cross-linked micelles, lending further credence to the hypothesis that DNA density on the surface of SNAs is inextricably linked to their biological properties.

Transitioning from cell culture to *in vivo* studies, **Chapter 5** describes the development and evaluation of SNA nanoclusters (NCs) as potential agents for imaging of breast cancer in a mouse model by positron emission tomography (PET) *via* a tumor pre-targeting strategy. We designed the SNA to function as a reverse "nano-flare" which localizes at the tumor site, and subsequently captures and releases circulating ^{64}Cu-labeled oligonucleotides for sensitive and

specific imaging of the tumor tissue with minimal uptake in off-target organs. In vitro, we found that the nanosystem was extremely efficient at capturing and releasing a target oligonucleotide under physiologically relevant conditions, with kinetics several orders of magnitude faster than state-of-the-art covalent pre-targeting nanosystems based on irreversible click chemistry reactions such as the tetrazine-cyclooctene Diels-Alder cycloaddition. A major advantage of our design is its programmability based on the particle-bound and tracer oligonucleotide sequence(s) as well as its reversibility.

Importantly, the core composition of the SNAs was chosen in a way to enable alloying with ^{64}Cu for studying their biodistribution, as well as rapid fabrication of libraries of SNAs with varying surface compositions due to the ready availability of thiolated ligands and their simple surface functionalization chemistry with gold. As opposed to functionalizing pre-fabricated nanoparticle cores with oligonucleotides, the pre-targeting SNA nanoclusters were synthesized *via* a one-pot reaction by mixing thiolated oligonucleotides with Au^{3+} followed by reduction with sodium borohydride to afford ultrasmall AuNC SNAs (~2.5 nm diameter). Inclusion of $^{64}CuCl_2$ in the reaction mixture afforded ^{64}CuAuNCs which could be tracked *in vivo* to determine their biodistribution. We discovered that the blood circulation time of DNA-functionalized ^{64}CuAuNCs was extremely short (<1% remaining in blood after 1 hour) due to their high negative charge density, leading to protein corona formation and sequestration in the spleen and liver, rendering them unsuitable for pre-targeting studies.[88]

Replacement of the DNA oligonucleotide shell with a mixture of PEG and phosphorodiamidate morpholino (PMO) oligonucleotides afforded colloidally stable SNA NCs which exhibited greatly improved circulation time (20-30x), enabling *in vivo* pre-targeting studies. Our results indicated that the SNA AuNCs accumulate in tumor tissue after injection and

are able to capture circulating ^{64}Cu-labeled oligonucleotides, enabling visualization of tumor tissue by PET via a novel SNA-based pre-targeting strategy. Ongoing studies are focused on improving the tumor-to-muscle ratio of the PET images, comparing the effectiveness of the pre-targeting strategy compared to a single radionuclide injection, and optimizing the overall binding kinetics of the nanosystem.

The studies outlined in **Chapter 6** were prompted by the discovery that neutral PMO-modified SNAs exhibit vastly different pharmacokinetics compared to their charged analogs. The final chapter focuses on the basic chemical and biophysical properties of PEG/PMO-modified gold nanoparticles. Monodisperse, commercially-available citrate-capped 10 nm gold nanoparticles were used as the starting material to generate PMO SNAs, primarily to ensure batch-to-batch reproducibility and simplify their purification and characterization due to the well-studied chemical and optical properties of AuNPs. The binding kinetics of PMO SNAs with complementary oligonucleotides were studied and found to vastly exceed the rates observed with DNA SNAs. Similarly, the hybridization thermodynamics of PMO SNAs with DNA SNAs showed much stronger association compared to DNA SNA pairs as measured by thermal denaturation experiments. The effect of the co-adsorbed PEG length on the colloidal stability and cellular interactions of the PMO SNAs was also studied. Shorter PEG lengths imparted poorer colloidal stability but facilitated superior cellular uptake, presumably due to exposure of the nucleobases to the cell surface and subsequent recognition by scavenger receptors. Longer PEG lengths did not affect the ability of PMO SNAs to capture complementary oligonucleotides but negatively affected their cell uptake. Having established the optimal blending ratio of PEG and PMOs for both colloidal stability and cellular uptake, the ability of PMO SNAs to engage in intracellular gene regulation was evaluated. Our preliminary results indicated that PMO SNAs

knocked down disease-related mRNA in ovarian cancer cells without the need for transfection agents or ancillary targeting moieties, a property not associated with any PMO-modified nanocarrier to date. Ongoing studies are underway to compare the knockdown effect of PMO SNAs with previously-validated positive controls such as lipid-transfected DNA.

Taken together, the studies presented in this dissertation contribute both to the fundamental understanding of SNA behavior *in vitro* and *in vivo* as well as the practical synthetic considerations for their translation into viable therapeutic and diagnostic agents for nanomedicine. The following chapter will begin the discussion of SNAs for gene regulation by rational bottom-up design of the SNA core material.

Chapter 2

Development of a biocompatible Fe^{3+} coordination strategy for the synthesis of nucleic acid complexes, nanoparticles, and metallogels

[Portions of this work have been published previously as Chad A. Mirkin, Colin M. Calabrese, William Morris. Metal-Ligand Coordination Polymer Nanoparticles and Methods for Making. US Patent No. 9,677,075. 2017.]

Abstract

The synthesis of chemically modified nucleic acids capable of forming 3D networks *via* metal coordination bonds is reported. A novel Fe^{3+}-chelating 3-hydroxy-4-pyridinone phosphoramidite was obtained in 3 steps and incorporated onto oligonucleotides using an automated DNA synthesizer. The resulting modified oligonucleotides were capable of selectively and quantitatively binding Fe^{3+} in aqueous media. $Fe(DNA)_3$ complexes were formed from single-stranded DNA, whereas nanoparticles and coordination polymer metallogels were formed from double-stranded DNA in aqueous buffer, depending on reaction conditions. This work represents a general and practical synthetic strategy for the assembly of biocompatible DNA-metal structures for medicine and materials, and demonstrates that biocompatible metal-ligand coordination bonds are a selective and stable means for joining nucleic acids together to form higher-order structures.

Introduction

Living organisms employ DNA for the storage of genetic information, but its use as a synthetic building block in the construction of nanomaterials has expanded rapidly in the last thirty years. Advances in automated oligonucleotide synthesis have afforded researchers a simple and reliable way to form chemically programmable linkages at the nanoscale *via* Watson-Crick base pairing of complementary DNA strands.[89] The predictable, reversible, and hence controllable nature of DNA hybridization makes it an extremely valuable structural design element in the nanotechnologist's toolbox.

DNA can spontaneously fold into nanostructures by the rational design of nucleobase sequences that hybridize into prearranged 2D and 3D shapes.[90-91] Native DNA, however, possesses few modifiable chemical handles for further synthetic elaboration. To design functional materials, oligonucleotides can be covalently bound to a vast library of organic small molecules,[92-99] polymers,[100-105] and nanoparticles.[106-107] These nucleic acid conjugates can subsequently assemble into rationally-designed supramolecular structures based on the sequence-specific hybridization of the attached DNA oligonucleotides.[108-111] Due to the biological origin of DNA, many of these hybrid materials find applications in therapeutics and biosensing. DNA nanostructures have shown promise as novel drug carriers,[112-117] gene regulation agents,[68, 118-120] and disease biomarker detectors.[85, 121-123] Furthermore, engineered macroscopic DNA hydrogels have attracted interest for use in tissue engineering,[124-125] 3D cell culture,[126] biomolecule detection,[127] and controlled drug release.[128]

Consequently, researchers have increasingly sought additional methods for the generation of DNA nanostructures in a biocompatible and bioorthogonal fashion. Common bioconjugate

chemistries include thiol-maleimide, alkyne-azide, and tetrazine-alkene "click" reactions, which are popular because the functional groups on DNA and other biomolecules do not interfere with the progress of the reaction. However, these approaches involve irreversible covalent modifications to DNA, creating unnatural linkages with potentially unknown biological activity. An alternative approach is to employ metal coordination bonds to assemble oligonucleotides, which offers the advantage of tunable, reversible, and dynamic linkages that can be formed *in situ* from individual DNA components.

The engineering of metal-DNA assemblies is an emerging field of research. Significant efforts have been dedicated to the synthesis of nucleic acids containing artificial metallo-base pairs.[129-133] Coordination-driven assembly of DNA into larger structures has also been investigated by several research groups. Discrete structures, such as DNA-Fe^{2+} triangles,[134] DNA-decorated coordination cages,[135] and cyclic dimers[136] have been described. Extended coordination polymers of DNA are also known,[137-142] though some examples involve DNA tethered to a pre-fabricated metal complex.[143-146] This topic has also been covered in several reviews.[147-150] However, most literature examples of metal-binding oligonucleotides involve lengthy ligand syntheses on small scales and rely on potentially toxic metal/ligand combinations. We sought to prepare macroscopic quantities of modified oligonucleotides so their metal-complexing behavior could be investigated at high concentrations. Furthermore, no DNA-metal coordination polymer structures have been investigated for biological applications. Since these materials can be comprised almost entirely of DNA, they are inherently biocompatible if paired with a nontoxic metal-ligand combination. Employing DNA as a ligand adds a degree of complexity due to its hydrophilicity, high molecular weight, and intrinsic affinity for transition metal cations. The system described herein overcomes these challenges, opening the door for a

new class of metal coordination-based DNA materials and proving that metal coordination bonds comprise a novel and viable self-assembly technique for biocompatible nucleic acid nanomaterials.

Experimental Procuedures

Materials and methods. Diphenylcarbamoyl chloride was purchased from TCI America (Portland, OR). All reagents for oligonucleotide synthesis were purchased from Glen Research (Sterling, VA) and used according to manufacturer instructions. 10X phosphate-buffered saline was purchased from Invitrogen (Carlsbad, CA). Deuterated solvents were purchased from Cambridge Isotope Laboratories Inc. (Andover, MA). All other reagents were purchased from Sigma-Aldrich (St. Louis, MO) and used without further purification. NMR spectra were recorded on a Bruker Avance 400 MHz NMR spectrometer. ^{1}H NMR spectra were referenced internally to residual proton signals in the deuterated solvents. $^{31}P\{^{1}H\}$ NMR spectra were referenced to an external 85% H_3PO_4 standard. Electrospray ionization (ESI) mass spectra were recorded on an Agilent 6120 LC-TOF instrument in positive ionization mode. UV-Vis spectra were collected on an Agilent Cary 5000 UV-Vis spectrometer in quartz cuvettes having a path length of 1 cm. Matrix-assisted laser desorption/ionization time-of-flight (MALDI-TOF) data was collected on a Bruker AutoFlex III MALDI-ToF mass spectrometer (Bruker Daltonics, Billerica, MA).

Crystallography. Single crystals of ligand **(1)** and two stereoisomers of its iron complex **Fe(L)$_3$** were mounted in inert oil (Infineum V8512). All measurements were made on a CCD area detector with graphite monochromated Cu Kα radiation. Data were collected using a Bruker APEXII detector and processed using APEX2 from Bruker. Structures were solved using direct

methods. The non-hydrogen atoms were refined anisotropically. Hydrogen atoms were included in idealized positions, but not refined. Their positions and isotropic displacement parameters were restrained relative to their parent atoms using the HFIX command in SHELXL-97.

Oligonucleotide synthesis. Oligonucleotide synthesis was carried out on a BioAutomation MM48 DNA synthesizer according to the manufacturer standard trityl-on protocol. The ligand phosphoramidite (3) was coupled for an extended period of time (5 minutes). All oligonucleotides were synthesized in 1 μmol columns and deprotected by treatment with 30% aqueous ammonium hydroxide (55ºC, 17h). Ligand-capped oligonucleotides (AL) and (BL) were then directly purified by reverse-phase HPLC. Dimethoxtyrityl-capped oligonucleotide (A) was purified by reverse-phase HPLC, then detritylated by treatment with 20% AcOH for 1 hr, followed by extraction with ethyl acetate (3x) and lyophilization of the aqueous layer.

HPLC purification. Oligonucleotides were purified on a Varian ProStar HPLC system fitted with a DynaMax Microsorb 300-10 C18 column. The mobile phase consisted of triethylammonium acetate buffer (pH 7.0) and acetonitrile. Oligonucleotide (A) was purified employing a gradient of 0-75% acetontrile over 45 minutes, with the desired product eluting after ~25 minutes. Fractions were collected, lyophilized, and detritylation was carried out as described above. All other oligonucleotides were eluted employing a gradient of 0-35% acetonitrile over 45 minutes, with the desired products eluting after ~20 minutes. Fractions were collected, pooled, and lyophilized to afford the pure, fully-deprotected oligonucleotides.

Synthesis of 1-(4'-(2-hydroxyethyl)phenyl)-2-methyl-3-hydroxy-4-pyridinone (1). To a 100 mL round-bottomed flask with a magnetic stirrer was added maltol (3.00 g, 23.8 mmol), 4-aminophenethyl alcohol (6.53 g, 47.6 mmol), and 25 mL dilute HCl (0.25N). The mixture was

heated and refluxed for 24 hr with stirring, resulting in the precipitation of the desired product. Upon cooling to room temperature, the reaction mixture was diluted with H_2O and vacuum-filtered to recover the precipitate. The filter cake was washed with H_2O followed by methanol and allowed to dry on the filter, yielding 5.19 g (21.2 mmol, 90%) of (1) as a tan, microcrystalline powder. Crystals suitable for X-ray diffraction analysis were obtained by recrystallization from hot DMF. ^{1}H NMR (400 MHz, DMSO-d_6) δ 7.48 (d, J = 7.3 Hz, 1H), 7.37 (d, J = 8.5 Hz, 2H), 7.30 (d, J = 8.4 Hz, 2H), 6.16 (d, J = 7.3 Hz, 1H), 3.63 (t, J = 6.8 Hz, 2H), 2.78 (t, J = 6.8 Hz, 2H), 1.93 (s, 3H). ^{13}C NMR (101 MHz, DMSO-d_6) δ 169.98, 145.45, 141.28, 140.03, 138.38, 130.46, 129.13, 127.03, 111.24, 62.13, 38.80, 13.81. HRMS-EI (*m/z*): $[M+H]^+$ calculated for $C_{14}H_{16}NO_3$ 246.1125, found 246.1130.

Synthesis of FeL_3 complex from ligand (1). To a 50 mL round-bottomed flask with a magnetic stirrer was added (1) (0.500 g, 2.04 mmol) and 10 mL absolute EtOH. To the resulting suspension was added 0.275 g (0.680 mmol) of ferric nitrate nonahydrate, causing the color to change to dark purple. Concentrated aqueous ammonium hydroxide was added dropwise, with stirring, until the color of the solution turned red. The mixture was heated overnight at 40° C with stirring, then poured into ethyl acetate (100 mL), causing precipitation of the complex. The solids were filtered, washed with additional ethyl acetate, and dried in vacuo to afford 0.480 g (0.61 mmol, 90%) of complex (1a) as a red powder. Crystals suitable for X-ray diffraction analysis were grown by slow diffusion of acetonitrile into a methanol solution of the complex. HRMS-EI (m/z): $[M+H]^+$ calculated for $C_{42}H_{43}FeN_3O_9$ 787.2390, found 787.2392.

Synthesis of diphenylcarbamoyl-protected pyridinone (2). To a 100 mL round-bottomed flask with a magnetic stirrer was added (1) (2.00 g, 8.15 mmol) followed by diphenylcarbamoyl chloride (2.08 g, 8.97 mmol) and dry pyridine (25 mL). The resulting suspension was stirred

under N_2 and *N,N*-diisopropylethylamine (1.56 mL, 8.97 mmol) was added dropwise via syringe. After stirring overnight, the reaction mixture was poured into 200 mL dilute HCl (1M) and the resulting suspension vacuum-filtered and dried *in vacuo* to afford a brown solid. The crude product thus obtained was suspended in methylene chloride (10 mL) and shaken vigorously. The suspension was suction-filtered and washed with additional methylene chloride to afford 2.59 g of (2) as an off-white powder (5.88 mmol, 72%). ^{1}H NMR (400 MHz, DMSO-d_6) δ 7.63 (d, J = 7.6 Hz, 1H), 7.50 – 7.15 (m, 14H), 6.22 (d, J = 7.6 Hz, 1H), 4.67 (s, 1H), 3.62 (t, J = 6.6 Hz, 2H), 2.76 (t, J = 6.8 Hz, 2H), 1.90 (s, 3H). ^{13}C NMR (101 MHz, DMSO-d_6) δ 170.48, 151.82, 150.04, 142.94, 141.65, 141.38, 141.12, 140.04, 139.47, 136.54, 130.63, 129.46, 127.47, 127.11, 126.82, 124.33, 115.82, 62.09, 38.80, 14.68. HRMS-EI (*m/z*): $[M+H]^+$ calculated for $C_{27}H_{25}N_2O_4$ 441.1809, found 441.1811.

Diphenylcarbamoyl-protected pyridinone phosphoramidite (3). In an oven-dried 50 mL Schlenk flask with a magnetic stirrer was suspended (2) (0.500 g, 1.14 mmol) in 5 mL dry, degassed methylene chloride. The mixture was stirred under N_2 and *N,N*-diisopropylethylamine (0.59 mL, 3.41 mmol) was added via syringe, followed by O-cyanoethyl-*N,N*-diisopropylchlorophosphoramidite (0.51 mL, 2.27 mmol). After 1 hr, methanol (0.1 mL) was added and the mixture stirred for an additional 30 min. Solvent was removed by rotary evaporation and the crude product purified by column chromatography on silica gel, eluting with 3:1 acetone/$CHCl_3$ containing 1% triethylamine (v/v). Fractions containing the desired product (Rf ~ 0.75) were pooled and evaporated to afford 0.53 g phosphoramidite (3) (0.82 mmol, 73%) as a colorless foam. Prior to DNA synthesis, (3) was dissolved in anhydrous acetonitrile at a concentration of 0.1M and stored overnight at -20ºC over 3Å molecular sieves. ^{1}H NMR (400 MHz, CD_2Cl_2) δ 7.61 – 7.03 (m, 14H), 6.38 (d, J = 7.6 Hz, 1H), 3.99 – 3.83 (m, 2H), 3.83 – 3.70

(m, 2H), 3.57 (dtd, *J* = 13.6, 6.8, 3.3 Hz, 2H), 2.99 (t, *J* = 6.5 Hz, 2H), 2.60 (t, *J* = 6.3 Hz, 2H), 2.00 (s, 3H), 1.14 (dd, *J* = 16.8, 6.8 Hz, 12H). $^{31}P\{^{1}H\}$ NMR (162 MHz, CD_2Cl_2) δ 147.71. HRMS-EI (*m/z*): $[M+H]^+$ calculated for $C_{36}H_{42}N_4O_5P$ 614.2901, found 641.2897.

AFM imaging. AFM imaging was carried out according to established protocols for DNA origami structures. Particles were drop-cast onto freshly-cleaved mica sheets pre-treated with 10 mM $MgCl_2$ to promote DNA adhesion to the surface. The droplet was allowed to stand for 10 minutes, then the surface was washed repeatedly with distilled H_2O and dried under a stream of N_2. Images were collected by tapping mode in air on a Bruker Dimension Icon atomic force microscope equipped with a POINTPROBE-PLUS® Silicon-SPM-Sensor.

MTT assay procedure. SKOV-3 cells were seeded in a 96-well plate at a population of $5x10^3$ cells per well. After 24 h, the cells were treated with 0.1 mL of a solution of compound **1** (diluted from DMSO stock solution into Opti-MEM) and incubated at 37°C for 24 h. After incubation, the compound was removed from the cells and replaced with 0.1 mL of complete McCoy's 5A medium (supplemented with 10% fetal bovine serum and 1% penicillin/streptomycin). Cell viability was measured by MTT assay at 48 h and 72 h following the addition of compound **1** to the cells. Briefly, cells were incubated with 0.1 mL of complete McCoy's 5A medium. 10 µL of MTT solution (5 mg/mL MTT in 1x PBS; Molecular Probes) was added into each well of cells and cells were incubated at 37°C for 2 h. After incubation, 0.1 mL of SDS-HCl solution (0.1 g/mL SDS in 0.01 M HCl) was added to each well to solubilize the formazan product, and cells were further incubated at 37°C overnight. After overnight incubation, the absorbance of the cell lysate was measured at 570 nm using a Synergy H4 Multimode Microplate Reader (Biotek). The relative cell viability was calculated compared to vehicle-treated cells. Reported values represent the mean ± SD of three replicates.

Cellular uptake experiments. All microscopy was performed using an SP5 laser scanning confocal microscope exciting at 494 nm. C166 mouse endothelial cells were incubated with 1 mL of cell culture medium containing the particle mixture at a total DNA concentration of 100 nM or 1 μM. After 24 hr, the cells were treated with Hoechst 33258 nuclear stain (Life Technologies), fixed, washed, and then examined by confocal fluorescence microscopy. Cell uptake of fluorescein-labeled DNA was observed, and images collected in Z-stack mode verified that the dye was present in the cytosol rather than the exterior of the cell membrane. The modified DNA was found to be nontoxic to cells under the conditions tested with no visible loss of cell viability after 24 hr. Equivalent methods were used for flow cytometry, however cells were not treated with Hoechst and instead were trypsinized for 3 minutes in 0.5% trypsin-EDTA (GIBCO), resuspended in Opti-MEM, and analyzed using a Guava Easycyte 8HT (Millipore) equipped with a 532nm laser.

Gene regulation experiments. The gene knockdown capability of the supramolecular DNA-Fe^{3+} nanoparticles was evaluated with skmel-28 human melanoma cells. Cells were cultured in OptiMEM serum-free buffer, in 48-well plates with a density of 15,000 cells/well. Cells were then treated with nanoparticles alone or nanoparticles mixed with Lipofectamine® RNAiMAX (Invitrogen) according to manufacturer instructions to give a total DNA concentration of 30 nM. The cells were incubated for a total of 48 hours, replacing the media after 16 hours. Cells were then harvested and the total survivin mRNA expression was quantitated by RT-qPCR.

Results and Discussion

Synthesis of hydroxypyridinone-modified oligonucleotides. We first set out to synthesize a Fe^{3+}-specific ligand which could be attached to the 5´ hydroxyl group of an oligonucleotide *via*

automated DNA synthesis. The ligand chosen for this purpose is structurally related to deferiprone (Ferriprox®), an FDA-approved iron chelator classified as a 3-hydroxy-4-pyridinone (3,4-HOPO).[151] The coordination chemistry and pharmacological properties of these compounds have been thoroughly investigated.[152] 3,4-HOPOs exhibit pH-dependent iron-chelating behavior in aqueous solution (Figure 2.1), forming the FeL^{2+} complex at low pH (<4), the FeL_2^{+} complex at intermediate pH (3-7), and the FeL_3 complex at physiological pH (≥7.4). The pH dependence is due to competition between Fe^{3+} and H^{+} at the enolic 3-hydroxy position. The stability

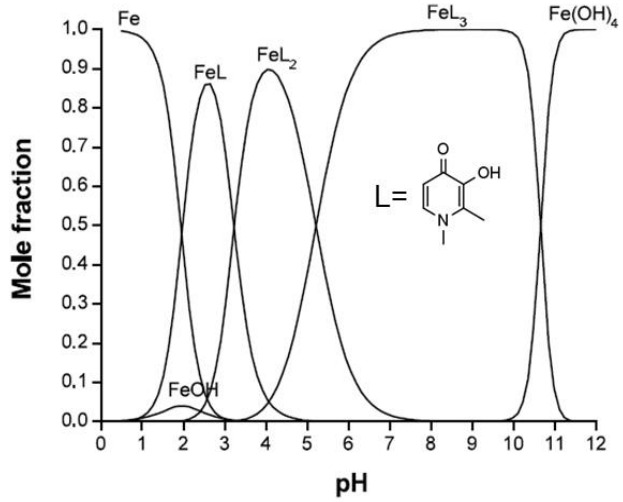

Figure 2.1. Speciation of deferiprone-Fe^{3+} complexes.[152]

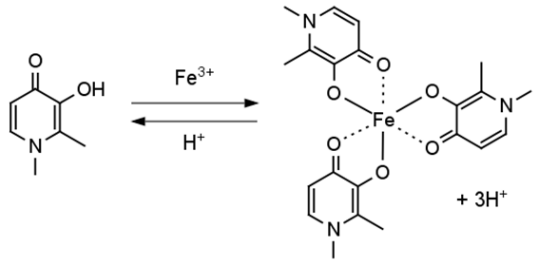

Stability constants (deferiprone)		
log K_1	15.10	FeL^{2+}
log K_2	11.51	FeL_2^{+}
log K_3	9.27	FeL_3

Table 2.1 Stability constants for Fe^{3+}/deferiprone.[155]

constant of the deferiprone *tris*-iron complex is large (log $\beta_3 \approx 10^{36}$), making it an attractive choice for coordination-driven self-assembly (Table 2.1). Recently, 3,4-HOPO ligands have been utilized for the formation of PEG metallogels[153] as well as crosslinking whole cells *in vitro*.[154]

An *N*-aryl-3-hydroxy-4-pyridinone phosphoramidite was synthesized in 3 steps from inexpensive, commercially available starting materials (Scheme 2.1). Overnight reflux of maltol and 4-aminophenethyl alcohol in dilute hydrochloric acid afforded the free ligand **(1)**, which was

recrystallized from DMF. Selective carbamoylation of the enolic hydroxyl group followed by phosphitylation of the primary alcohol furnished the phosphoramidite **(3)**, which was coupled to DNA after purification by column chromatography**.** To confirm the structure of the iron chelate, the red *tris*-Fe^{3+} complex of the unprotected ligand was obtained by treatment of **(1)** with 0.33 equiv. ferric nitrate and ammonium hydroxide in ethanol followed by precipitation from ethyl acetate. Crystals suitable for X-ray diffraction analysis were grown by slow diffusion of acetonitrile into a methanol solution of the complex. Both Δ-*fac* and Λ-*mer* stereoisomers were obtained as separate single crystals (Figure 2.2 and A2.3). Additionally, the cytotoxicity of **(1)** was investigated in C166 mouse endothelial cells using the MTT assay. Over 72 hours, negligible loss in cell viability was observed at the highest concentration tested (Figure A2.1).

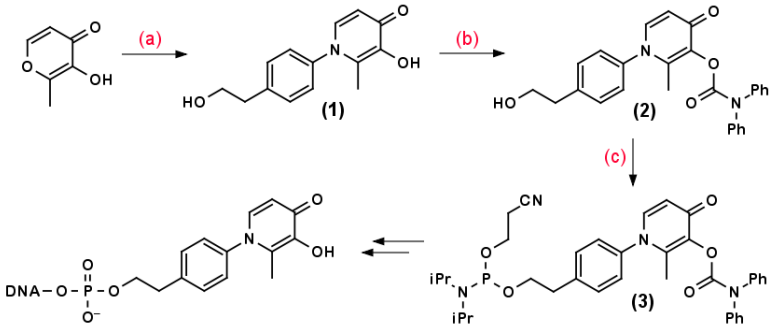

Scheme 2.1. Synthesis of ligand phosphoramidite. Reagents and conditions: a) 4-aminophenethyl alcohol, dilute HCl, reflux 24h; b) diphenylcarbamoyl chloride, pyridine, Hünig's base, RT, 16h; c) 2-cyanoethyl-*N*,*N*-diisopropylchlorophosphite, Hünig's base, RT, 1h

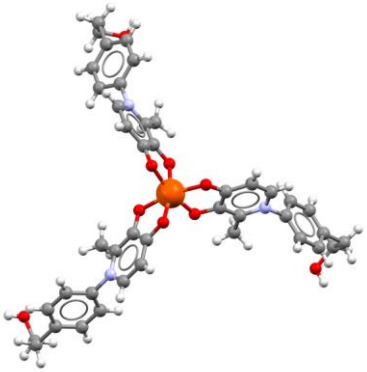

Figure 2.2 Crystal structure of a Δ-*fac*-FeL_3 complex (*mer* isomer not shown)

The ligand phosphoramidite was coupled to the 5´ terminus of a 20-mer oligonucleotide **(AL)** and its complement **(BL)** sharing a 15-base overlap. Oligonucleotides having a 20-base overlap, **(SV1L)** and **(SV2L)**, were also synthesized. **SV1L** is an antisense oligonucleotide sequence which targets the mRNA encoding the apoptosis inhibitor protein survivin, which is upregulated in many cancer cell lines and promotes resistance to chemotherapeutics and more aggressive disease progression.[156] DNA synthesis was carried out in 1 μmol columns according to the

manufacturer standard trityl-on protocol, followed by cleavage and deprotection in concentrated NH_4OH. The crude oligonucleotides were purified by reverse-phase HPLC and characterized by MALDI-TOF. The desired ligand-capped oligonucleotides eluted after the truncated failure sequences due to the slight hydrophobicity of the terminal modification. The control oligonucleotide **(A)** lacking any chemical modifications was likewise synthesized and purified by trityl-on protocol.

Oligo	**Sequence (5´→3´)**	**FW (calc'd)**	**$[M-H]^-$ (found)**
A	A_5-ATC-CTT-ATC-AAT-ATT	6067	6071
AL	Ligand-AAAAA-ATC-CTT-ATC-AAT-ATT	6374	6374
BL	Ligand-AAAAA-AAT-ATT-GAT-AAG-GAT	6511	6512
SV1L	Ligand-CCC-AGC-CTT-CCA-GCT-CCT-TG	6272	6276
SV2L	Ligand-CAA-GGA-GCT-GGA-AGG-CTG-GG	6579	6572
SV1FL	Ligand-CCCAGCCT**T***CCAGCTCCTTG	6783	6785

Table 2.2 Oligonucleotides synthesized for this study with the calculated and found masses (MALDI-TOF). T* = fluorescein-deoxythymidine (Glen Research)

Synthesis and characterization of $Fe(DNA)_3$ complexes. To ensure that iron binds to the modified DNA in the expected fashion, we first carried out experiments to synthesize the $Fe(DNA)_3$ complex as a proof-of-concept. The *tris*-Fe^{3+} complex of **(1)** exhibits a ligand-to-metal charge transfer (LMCT) band in the visible spectrum, with an associated λ_{max} of 460 nm and ε_{460} = 5700 L·mol/cm^{-1}. The *bis* and *mono* complexes absorb at longer wavelengths. Thus, UV-Vis may be used to monitor the reaction of the ligand-modified DNA with iron, since DNA does not absorb in this region.[i] As expected, a 100 μM solution of **(AL)** in phosphate-buffered saline (pH 7.4) quantitatively formed the $Fe\mathbf{(AL)}_3$ complex after standing overnight in the presence of stoichiometric $Fe(NO_3)_3{\cdot}9H_2O$, as measured by UV-Vis (Figure 2.3). No LMCT was observed when the unmodified oligonucleotide **A** was treated with Fe^{3+} under the same conditions (Figure 2.4).

[i] Extinction coefficients of the ligand (ε_{260} = 3900 L·mol/cm^{-1}) and the FeL_3 complex (ε_{460} = 5700 L·mol/cm^{-1}) were determined by the Beer-Lambert relationship from serial dilution the compounds in PBS buffer.

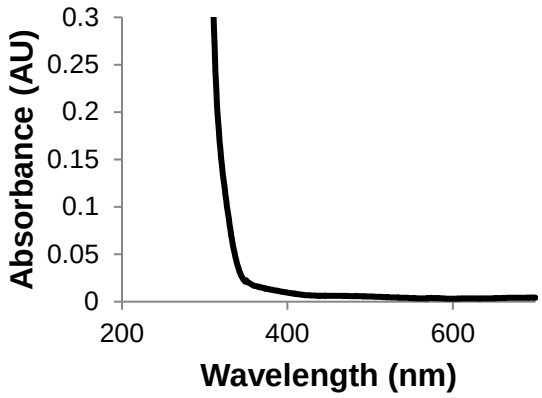

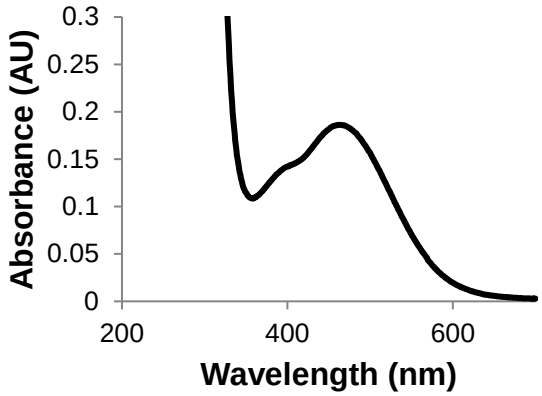

Figure 2.3 Top: 100 µM **(AL)** in 1X PBS. Bottom: 100 µM **(AL)** in 1X PBS treated with 33 µM Fe^{3+}.

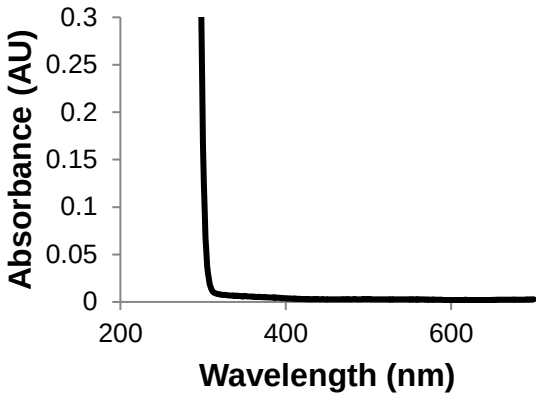

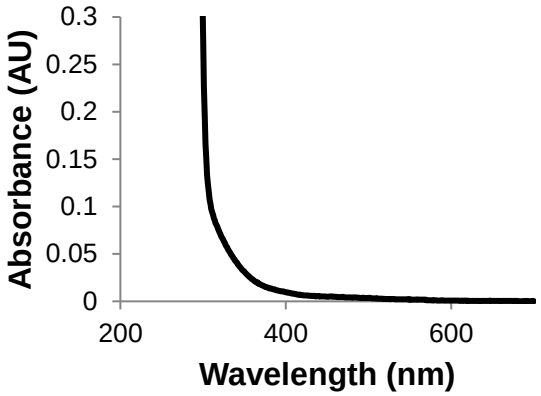

Figure 2.4 Top: 100 µM **(A)** in 1X PBS. Bottom: 100 µM **(A)** in 1X PBS treated with 33 µM Fe^{3+}.

Titration of 100 µM **(AL)** with increasing concentrations of $Fe(NO_3)_3 \cdot 9H_2O$ showed a clear 3:1 binding ratio of DNA:Fe^{3+} (Figure 2.5-6). These results confirm the site-specific complexation of iron by the DNA macroligand. Furthermore, kinetics experiments indicated that complexation of iron by the free ligand occurred roughly 10 times faster as compared to the DNA macroligand, suggesting a diffusion-limited complexation process due to the much larger molecular weight of the macroligand (Figure A2.4).

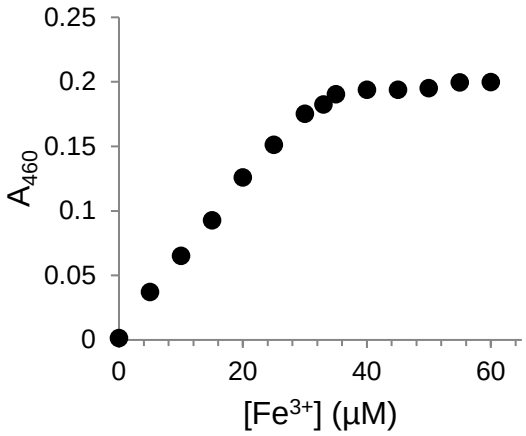

Figure 2.5. Titration of a 100 µM solution of **(AL)** with ferric nitrate in 1X PBS buffer.

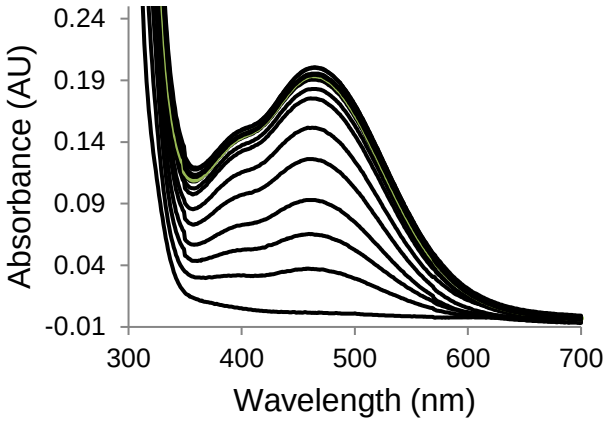

Figure 2.6. UV-Vis spectra corresponding to the titration curve shown to the left.

Formation of DNA-Fe^{3+} metallogel at high concentrations. With the iron-binding DNA in hand, we set out to determine its ability to self-assemble into higher order structures when hybridized into a duplex. (Scheme 2.2)

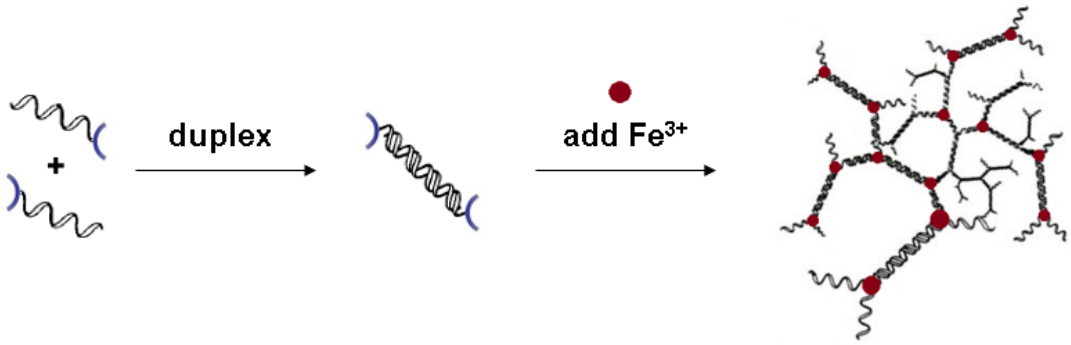

Scheme 2.2. Synthesis of extened DNA-Fe^{3+} coordination networks by a two-step assembly process.

This could be verified macroscopically by forming duplex DNA **(AL·BL)** in buffer at concentrations sufficient for gel formation, followed by addition of Fe^{3+}. A 0.25 mL solution of **(AL·BL)** was prepared in 1X PBS containing 2 mM of the duplex and 1.33 mM Fe^{3+}. Control samples contained either no iron, 2 mM of **(AL)** alone, or 2 mM of **(AL·BL)** in the presence of 1.6 mM deferoxamine B (DFO), a hexadentate iron chelator capable of competitively removing

iron from the HOPO-Fe^{3+} complex (Table 2.3). Only in the first case was gelation observed, with the control samples remaining as free-flowing liquids (Figure 2.7). These results indicated that higher-order DNA coordination polymer structures are indeed formed from the **(AL·BL)** duplex. At least 1 mM of duplex was required for gelation to occur. In addition, we found the gelation of the DNA solution could be reversed by heating above the melting temperature ($T_m \approx 40°$ C) of the duplex,[ii] affording a liquid which solidified upon cooling to room temperature. This opens up the possibility of novel thermo-responsive DNA metallogels with tunable melting temperatures depending on the DNA base sequence.

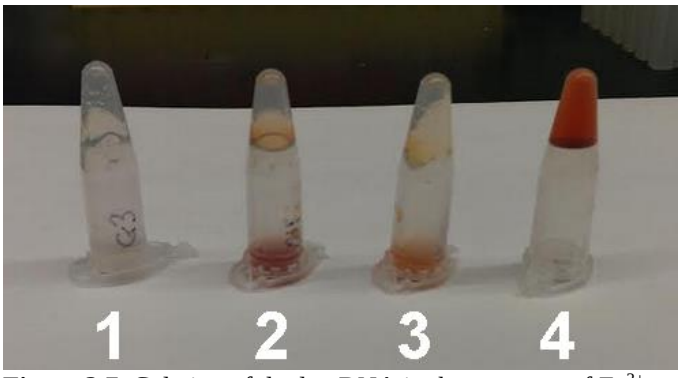

Figure 2.7. Gelation of duplex DNA in the presence of Fe^{3+} at room temperature (25° C)

Sample	Reagent	Metal	Gel
1	**(AL·BL)**	None	No
2	**(AL)**	Fe^{3+}	No
3	**(AL·BL) + DFO**	Fe^{3+}	No
4	**(AL·BL)**	Fe^{3+}	Yes

Table 2.3. Screening of conditions required for gelation of DNA/ Fe^{3+} solutions

A metallogel was also synthesized from the **(SV1·SV2)** duplex, which possesses a higher melting temperature ($T_m \approx 70°$ C) due to its greater number of base pairs and higher GC content.

T (ºC)	(AL·BL)	(SV1L·SV2L)
25	gel	gel
55	liquid	gel
75	liquid	liquid

Table 2.4. Temperature-dependent gelation of DNA/Fe^{3+} solutions

A 2 mM solution of **(SV1·SV2)** in 1X PBS, containing 1.33 mM Fe^{3+}, was prepared. At 55° C, the **(AL·BL)**/Fe^{3+} solution flowed freely as a liquid whereas the **(SV1·SV2)**/Fe^{3+} solution remained as a gel. At 75° C, both solutions melted completely.

[ii] Oligonucleotide melting temperatures were calculated using OligoAnalyzer software from Integrated DNA Technologies (Skokie, IL)

(Figure 2.8) Furthermore, decreasing the pH of the medium is also expected to decrease the viscosity of the gel as the metal complexes dissociate to *bis* and *mono* species due to competition with H^+. This effect has been demonstrated with similar catechol-based metallogels formed by complexation of ferric iron.[157]

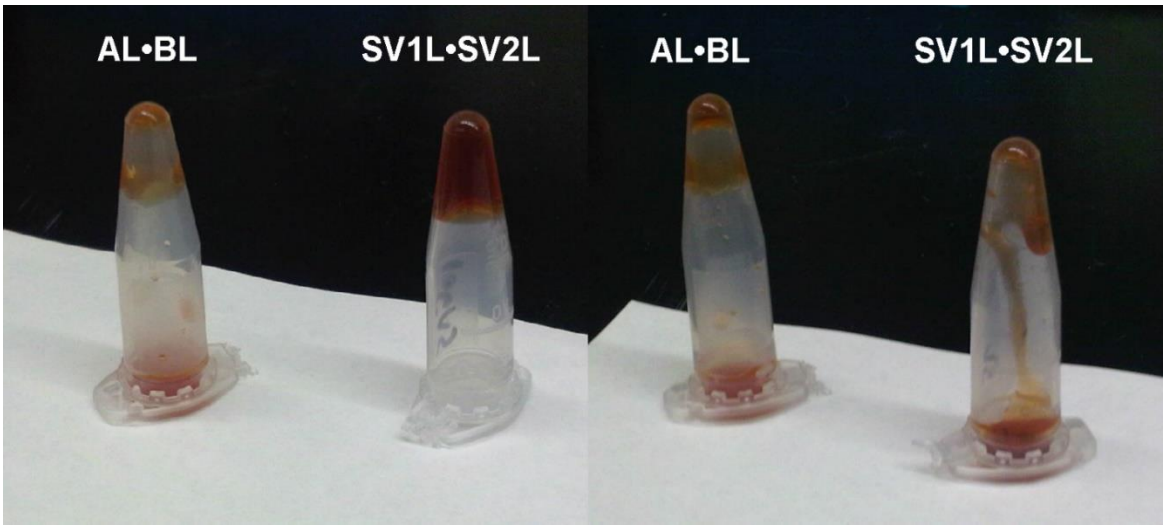

Figure 2.8. Temperature-dependent gelation of DNA metallogels heated to 55° C (left) and 75° C (right)

Formation of DNA-Fe^{3+} nanoparticles at lower concentrations. At concentrations lower than those required for gelation, the **(SV1L·SV2L)** duplex forms DNA nanoparticles in the presence of Fe^{3+}. The following procedure was developed for their synthesis. First, a 1 mL stock solution was prepared containing 50 μM **(SV1L)** and 50 μM (**SV2L)** in PBS, affording the **(SV1L·SV2L)** duplex at a total DNA concentration of 100 μM. Stoichiometric $Fe(NO_3)_3 \cdot 9H_2O$ (33 μM) was then added and the mixture allowed to stand overnight at room temperature. The progress of the reaction was monitored by UV-Vis, in combination with dynamic laser light scattering (DLS) to verify the formation of higher-order structures. Prior to iron addition, DLS shows a single monodisperse peak ($d_H \approx 6$ nm) corresponding to the **(SV1L·SV2L)** duplex. After iron addition, self-aggregation occurs, giving rise to a broad size distribution typically ranging

from 10-200 nm or higher. Large structures (>10 nm) are not seen when **(SV1L)** alone is treated with Fe^{3+} (Figure A2.2).

Precise control of particle size was an initial roadblock. Precipitation of the DNA-iron mixture into water-miscible organic solvents (ethanol, THF) yielded very large aggregates (250-1000 nm) which were unstable upon re-immersion in buffer, potentially due to the denaturing effect of the organic solvent. We also investigated altering the ratio of complementary strands, with the excess single-stranded DNA acting as a chain stopper, but this approach gave inadequate size control. In the end, gel-filtration chromatography (GFC) provided the best results. In a typical synthesis, the crude reaction mixture was passed through a short column (3-5 mL) of Sepharose CL-4B, a crosslinked agarose matrix. In addition, this technique removes unmetallated DNA and residual synthesis impurities.

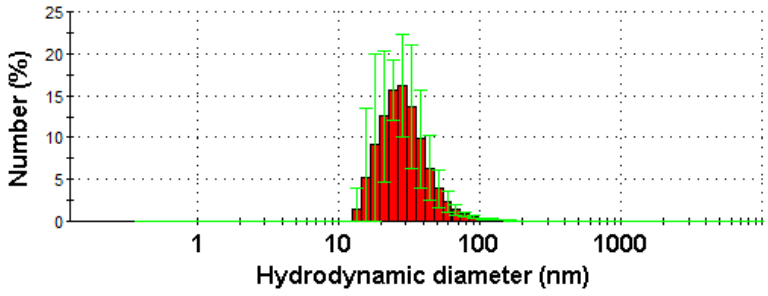

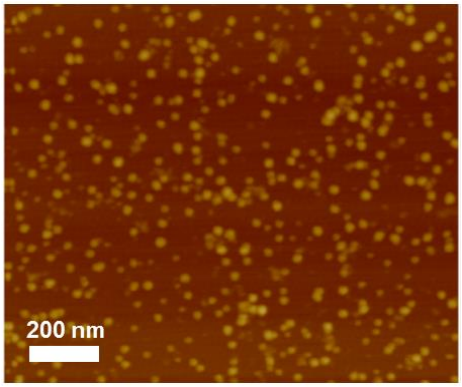

Figure 2.9. (Left) DLS size distribution of particles purified by GFC. **Figure 2.10**. (Right) AFM image of particles deposited on mica.

Fractions were collected and analyzed by DLS, showing separation of particles by size. With this technique, fractions containing particles with a mean diameter of 20-40 nm were obtained, comparable in size to existing DNA-nanoparticle conjugates. To corroborate the DLS data, fractions were also imaged by atomic force microscopy (AFM), revealing spherical nanostructures with a size distribution analogous to that found with DLS (Figure 2.9-10).

Synthesis of fluorescent DNA-Fe^{3+} nanoparticles and cellular uptake. DNA and RNA nanoparticles have attracted interest due to their potential uses as gene regulatory agents. Having obtained particles of the ideal size for cell entry,[158-159] we then examined the level of cell uptake compared to single-stranded DNA. To visualize internalization, it was necessary to incorporate a fluorescent dye into the DNA. The sequence of **SV1** was modified with a commercially-available fluorescein-bearing thymidine base (T*), affording **SV1FL** (Table 2.1). **SV1FL** was then duplexed with **SV2** and particles were synthesized according to the protocol outlined previously. Particle size distributions were determined by AFM, due to interference of the fluorescent dye with DLS size measurements. Sedimentation of heavier fractions occurred upon prolonged standing, likely due to the hydrophobic nature of the fluorescein modification (Figure 2.11). This observation suggests that the colloidal stability of the particles is altered by the conjugation of hydrophobic compounds. C166 mouse endothelial cells were then incubated with three different size fractions of fluorescein-labeled particles at a total DNA concentration of either 1 µM or 100 nM in Opti-MEM medium, with iron-free **SV1FL** serving as the control. The treatment period was 16 hours.

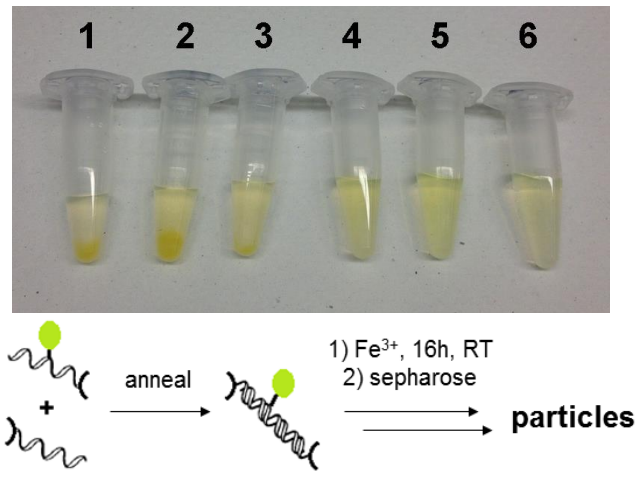

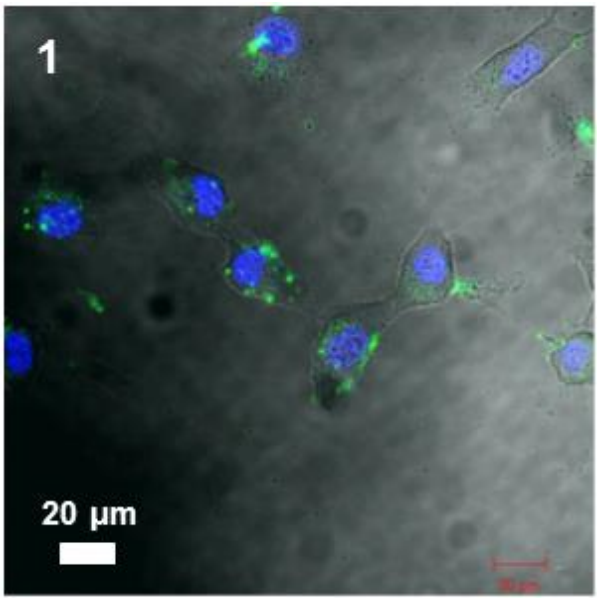

Figure 2.11. (Left) Synthesis of dye-labelled particles and fractions obtained from GFC showing settling of heavy particles. **Figure 2.12.** (Right) Uptake in C166 cells

Confocal microscopy and flow cytometry indicated that the DNA-iron particles entered cells at roughly the same rate compared to the iron-free control DNA (Figure A2.5). This result demonstrates that, with the current design, the DNA-iron coordination polymer particles do not behave analogously to classical SNAs and are not actively transported into the cell. However, preliminary RT-qPCR experiments indicated that the particles are indeed capable of survivin mRNA knockdown if transfected into the cell using a Lipofectamine®, a commercially-available transfection agent (Figure 2.13). This result suggests that, at the very minimum, the individual components comprising the DNA-Fe^{3+} particles are capable of gene regulation once inside the cell, with the barrier to transfection-free gene regulation being the lack of active transport.

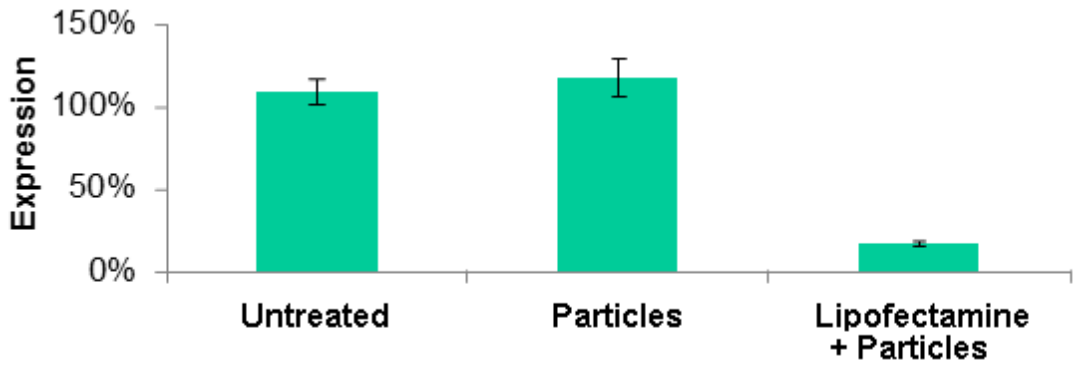

Figure 2.13. Survivin expression in skmel-28 melanoma cells, 30 nM total DNA, quantitated by RT-qPCR.

Conclusions

We have synthesized and characterized complexes and coordination polymers of ligand-modified DNA with iron. The 3-hydroxy-4-pyridinone ligand has proven effective for assembling iron(III) complexes of single-stranded DNA and coordination polymers of duplex DNA under physiological pH and salt concentration. Importantly, we carried out the synthesis of the modified DNA on large scales (>20 µmol) following simple, user-friendly synthetic methods. At

high concentrations, metallogels are obtained whose properties can be tuned based on the DNA base sequence. At lower concentrations, we obtained coordination polymer nanoparticles possessing a spherical morphology, consistent with literature reports of metal-free DNA assemblies constructed from similar building blocks.[160-163] The cellular uptake of DNA-Fe^{3+} nanoparticles was examined but their behavior was not analogous to other spherical nucleic acids (SNAs) previously described, most likely to due to random orientation of the DNA strands comprising the particle as well as the low density of surface-exposed single-stranded DNA. Entry of DNA nanostructures into cells is highly dependent on the geometric conformation of the oligonucleotides.[164-165] Furthermore, as evidenced by the concentration-dependent degree of polymerization of the DNA-Fe^{3+} polymer, dilution of the nanoparticles for cell culture experiments can potentially cause the particles to fragment into smaller oligomers. Nevertheless, we believe this work opens the door to novel DNA-based materials for biological applications. The DNA metallogels described herein are easy to synthesize, and may be a promising biocompatible medium for cell transplant therapy and tissue engineering. The DNA nanoparticles described herein also serve as a proof-of-concept study demonstrating that iron coordination bonds are an effective means to assemble DNA nanostructures. In **Chapter 3** the same chemistry is applied to generate SNAs capable of spontaneous cellular uptake, applying the lessons learned from the studies in this chapter.

Chapter 3

Biocompatible infinite-coordination-polymer nanoparticle-nucleic-acid conjugates for antisense gene regulation

[Portions of this work have been published previously as Chad A. Mirkin, Colin M. Calabrese, William E. Briley, Timothy J. Merkel. Biocompatible infinite coordination polymer nanoparticle-nucleic acid conjugates for antisense gene regulation. US Patent No. 9,617,451. 2017; and Calabrese, C. M.; Merkel, T. J.; Briley, W. E.; Randeria, P. S.; Narayan, S. P.; Rouge, J. L.; Walker, D. A.; Scott, A. W.; Mirkin, C. A. Biocompatible Infinite Coordination Polymer Nanoparticle-Nucleic Acid Conjugates For Antisense Gene Regulation. *Angew. Chem. Int. Ed*. **2015**, *54*, 476-480.]

Abstract

Herein, we report the synthesis of DNA-functionalized infinite-coordination-polymer (ICP) nanoparticles as biocompatible gene-regulation agents. ICP nanoparticles were synthesized from ferric nitrate and a ditopic 3-hydroxy-4-pyridinone (HOPO) ligand bearing a pendant azide. Addition of Fe(III) to a solution of the ligand produced nanoparticles, which were colloidally unstable in the presence of salts. Conjugation of DNA to the Fe(III)-HOPO ICP particles by copper-free click chemistry afforded colloidally stable nucleic-acid nanoconstructs. The DNA-ICP particles, when cross-linked through sequence-specific hybridization, exhibited narrow, highly cooperative melting transitions consistent with dense DNA surface loading. The ability of the DNA-ICP particles to enter cells and alter protein expression was also evaluated. Our results indicate that these novel particles carry nucleic acids into mammalian cells without the need for transfection agents and are capable of efficient gene knockdown.

Introduction

Spherical nucleic acids (SNAs) have emerged as an interesting new class of materials that have shown promise in programmable materials synthesis,[41, 166] bio-detection,[121, 167-168] and intracellular gene regulation.[68, 169] Such structures are often comprised of a nanoparticle core functionalized with a dense layer of oligonucleotides, although hollow, core-free versions have been developed.[78, 170] The earliest example of SNAs involved gold nanoparticles modified with a dense layer of alkylthiol-functionalized DNA,[33] but iron oxide,[171-172] silver,[173-175] semiconductor quantum dot,[176-177] and organic cores have been explored as well.[29, 178-179] Notably, the chemical and biological properties of SNAs are markedly different from their linear counterparts. SNAs exhibit cooperative binding and sharp thermal denaturation profiles, enter cells without the need for cationic transfection agents, and have the ability to bind to receptors in a polyvalent fashion.[51] Consequently, they are powerful new entities for manipulating cellular processes through gene regulation,[80, 180] drug delivery,[113, 181] and immunomodulatory pathways.[182] The active uptake of SNAs occurs *via* caveolin-mediated endocytosis, triggered by their binding to class A scavenger receptors (SR-As).[70, 183] Although SNAs made from gold have shown commercial promise as medical diagnostic and research tools and have shown no acute toxicity *in vivo*,[79] there are concerns about the potential long term toxicity of gold nanoparticles and their metabolic fate.[184] Consequently, new forms of SNAs with cores made of biocompatible materials are highly sought after. Herein, we report a strategy that employs the use of infinite coordination polymer (ICP) nanoparticles made from ferric ions and a rigid ditopic chelating ligand to synthesize novel SNA nanoparticle conjugates. These DNA-ICPs are designed from chemical building blocks approved by the FDA for other pharmaceutical uses, exhibit cooperative binding,

and can readily cross mammalian cell membranes and inhibit protein expression in a targeted fashion.

ICP nanoparticles consist of amorphous networks of organic ligands bridged by metal nodes.[185-186] They are promising materials for SNA construction as the ligand/metal combination that defines the ICP structure can be rationally designed to optimize the toxicological and pharmacokinetic profiles of the DNA-ICP conjugate. One major limitation of many ICPs designed for medicinal applications is their instability in aqueous buffers. Some researchers have circumvented this limitation by encapsulating the particle core in silica[187-188] or a shell of lipids.[189] In contrast, we have sought to design ICP particles that could be synthesized, purified, and stored indefinitely under aqueous conditions and without specialized equipment or reagents. Furthermore, the use of relatively nontoxic metal ions is a crucial requirement for biological applications. These goals were accomplished by synthesizing ICP nanoparticles from strongly chelating 3-hydroxy-4-pyridinone (3,4-HOPO) ligands in combination with Fe^{3+}, the most abundant transition metal in the body. The coordination chemistry and pharmacology of the 3,4-HOPOs have been thoroughly investigated,[152] and the 1,2-dimethyl derivative (deferiprone) is FDA-approved for the treatment of iron overload in humans.[151] Furthermore, the $Fe(HOPO)_3$ complex is known to dissociate below physiological pH.[190] This provides a potential release mechanism for delivering DNA into the cytosol following cell entry, a novel property not typically associated with SNAs prepared to date.

It is known that ditopic HOPO and catechol ligands, being isoelectronic, can form insoluble coordination polymers with oxophilic metal cations such as Fe^{3+}, Cr^{3+}, Ga^{3+} and others, however, such polymers are poorly understood and have not been well-studied in the literature.[191-193] These ligands have mainly been studied for metal sequestration and chelation as

opposed to materials synthesis. Therefore, we saw an opportunity to construct a novel biocompatible nanoparticle scaffold for modification with DNA.

Experimental Procuedures

Materials and methods. 3,5-Diaminobenzoic acid was purchased from TCI America (Portland, OR). 4-Azido-butan-1-amine was purchased from Synthonix, Inc. (Wake Forest, NC). All reagents for oligonucleotide synthesis were purchased from Glen Research (Sterling, VA) and used according to manufacturer instructions. Buffer solutions were purchased from Invitrogen (Carlsbad, CA). Deuterated solvents were purchased from Cambridge Isotope Laboratories Inc. (Andover, MA). Gold nanoparticles were purchased from Ted Pella (Redding, CA). Amicon® Ultra centrifugal filter units were purchased from EMD Millipore (Billerica, MA). All other reagents were purchased from Sigma-Aldrich (St. Louis, MO) and used without further purification. ^{1}H NMR spectra were recorded on a Bruker Avance 400 MHz NMR spectrometer. ^{1}H NMR spectra were referenced internally to residual proton signals in the deuterated solvents. ^{13}C NMR spectra for compounds **3** and **4** were collected on an Agilent DD2 500 MHz NMR spectrometer operating at an internal temperature of 100° C. Electrospray ionization (ESI) mass spectra were recorded on an Agilent 6120 LC-TOF instrument in positive ionization mode. UV-Vis spectra and thermal denaturation curves were collected on an Agilent Cary 5000 UV-Vis spectrometer in quartz cuvettes having a path length of 1 cm. Matrix-assisted laser desorption/ionization time-of-flight (MALDI-ToF) data was collected on a Bruker AutoFlex III MALDI-ToF mass spectrometer employing 2,5-dihydroxyacetophenone (DHAP) as the matrix material. FTIR spectra were collected on a Perkin-Elmer Spectrum 100 FTIR spectrometer. AFM images were collected on a Bruker Dimension Icon atomic force microscope in non-contact

mode equipped with a POINTPROBE-PLUS® Silicon-SPM-Sensor. TEM images were collected on a Hitachi H8100 transmission electron microscope operating at an accelerating voltage of 200kV. TEM and EDX data were collected on a Hitachi HD2300 STEM equipped with two Thermo Scientific X-ray EDX detectors. Dynamic light scattering (DLS) and zeta potential measurements were collected on a Zetasizer Nano ZS (Malvern Instruments Ltd). ICP-MS data were collected on a Thermo X-series II ICP-MS. Elemental analysis was conducted off-site by Intertek Pharmaceutical Services (Whitehouse, NJ).

Synthesis of diaminobenzoic acid *mono*-hydroxypyridinone (2) To a 100 mL round-bottomed flask with a magnetic stirrer was added 3,5-diaminobenzoic acid (5.00 g, 32.86 mmol), maltol (8.70 g, 69.00 mmol) and 30 mL of acidic n-propanol (49:1 propanol/12M HCl). The reaction vessel was fitted with a water-cooled condenser and the mixture heated to reflux for 16 h. The resulting suspension was vacuum-filtered while hot and the solids washed with acetone (200 mL) to yield 4.84 g of **(1)** as a tan powder (18.60 mmol, 57%). Propanol may be substituted with 5:1 EtOH/H_2O affording similar yields. ^{1}H NMR (400 MHz, DMSO-d_6) δ 7.52 (d, J = 7.4 Hz, 1H), 7.28 – 7.26 (m, 1H), 6.92 (t, J = 1.7 Hz, 1H), 6.67 (t, J = 2.1 Hz, 1H), 6.16 (d, J = 7.3 Hz, 1H), 5.77 (s, 2H), 1.96 (s, 3H). ^{13}C NMR (101 MHz, DMSO-d_6) δ 169.96, 167.24, 150.62, 145.45, 142.79, 138.07, 133.21, 129.02, 115.64, 115.35, 114.34, 111.30, 13.61. HRMS-ESI (*m/z*): $[M+H]^+$ calculated for $C_{13}H_{13}N_2O_4$ 261.0870, found 261.0875.

Synthesis of diaminobenzoic acid *bis*-hydroxypyridinone (3) To a 100 mL round-bottomed flask with a magnetic stirrer was added **(2)** (5.90 g, 22.67 mmol), maltol (3.57 g, 28.34 mmol), and 30 mL of acidic 2-ethoxyethanol (49:1 ethoxyethanol/12M HCl). The reaction vessel was fitted with a water-cooled condenser and the mixture heated to reflux for 64 h. The resulting suspension was vacuum-filtered while hot and the solids washed with water (50 mL), followed

by acetone (50 mL), to afford the crude product as a fine brown solid. The *bis* product was selectively isolated by precipitation from boiling pyridine (100 mL), filtration, and further precipitation from hot dimethylformamide (100 mL) and drying *in vacuo* to afford 0.98 g of **(3)** (2.66 mmol, 12%) as a grey powder sparingly soluble in methanol, soluble in hot DMSO and DMF. ^{1}H NMR (400 MHz, DMSO-d_6) δ 8.03 (d, J = 2.0 Hz, 2H), 8.00 (t, J = 2.0 Hz, 1H), 7.64 (d, J = 7.4 Hz, 2H), 6.22 (d, J = 7.4 Hz, 2H), 2.02 (s, 6H). ^{13}C NMR (126 MHz, DMSO-d_6) δ 170.43, 165.59, 145.52, 142.92, 138.79, 138.26, 134.82, 130.74, 130.47, 128.55, 111.45, 111.28, 13.79, 13.60. HRMS-ESI (*m/z*): $[M+H]^+$ calculated for $C_{19}H_{17}N_2O_6$ 369.1081, found 369.1084.

Synthesis of diiaminobenzoic acid *bis*-HP azide (4) To a 50 mL round-bottomed flask with a magnetic stirrer was added **(3)** (0.400 g, 1.09 mmol) fully dissolved in anhydrous DMSO (30 mL). HATU (0.414 g, 1.09 mmol) and diisopropylethylamine (0.48 mL, 2.73 mmol) were subsequently added and the reaction vessel was capped with a rubber septum. After 5 minutes, 4-azidobutan-1-amine (0.187 g, 1.64 mmol) was injected via syringe and the mixture allowed to stir for 4 h under N_2. The organic phase was diluted with 1 volume of water and allowed to stand for 1 h. The resulting grey precipitate was collected by vacuum filtration and washed extensively with water (150 mL), followed by acetonitrile (100 mL), and allowed to dry on the filter. The obtained azide monomer **(4)** was used without further purification. (0.283 g, 0.61 mmol, 56%). ^{1}H NMR (400 MHz, DMSO-d_6) δ 8.72 (t, J = 5.7 Hz, 1H), 8.00 (d, J = 2.0 Hz, 2H), 7.91 (t, J = 1.9 Hz, 1H), 7.63 (d, J = 7.3 Hz, 2H), 6.23 (d, J = 7.4 Hz, 2H), 3.41 – 3.19 (m, 4H), 2.03 (s, 6H), 1.60 – 1.53 (m, 4H). ^{13}C NMR (126 MHz, DMSO-d_6) δ 170.41, 164.21, 145.55, 142.74, 138.81, 138.27, 137.87, 128.68, 128.54, 126.92, 126.78, 111.39, 111.23, 51.14, 39.56, 26.72, 26.37, 13.81, 13.62. HRMS-ESI (*m/z*): $[M+H]^+$ calculated for $C_{23}H_{25}N_6O_5$ 465.1881, found 465.1881. FTIR (KBr): ν_{max} 2093 cm^{-1} (N=N=N stretch)

Synthesis of DABA-bis-HP-N_3 ICP particles (ICP-N_3 NPs) In a typical experiment, an aqueous stock solution of DABA-bis-HP-N_3 was prepared consisting of 2.28 mM ligand and 24.5 mM NaOH. The ligand is freely soluble in water as its disodium salt. A stock solution of $Fe(NO_3)_3 \cdot 9H_2O$ was prepared consisting of 10.80 mM Fe^{3+} and 4 mM HCl (as stabilizer). To a glass vial was added 877 µL ligand stock solution, followed by 1 mL Milli-Q H_2O, followed by 123 µL Fe(III) stock and the resulting orange-red mixture (2 mL) shaken for 10 minutes. The as-synthesized particles have a mean diameter ranging from 10-20 nm (DLS). Particles were purified by filtration through an Amicon Ultra 15 mL centrifugal filter with a nominal molecular weight cutoff (MWCO) of 100 kDa, washing with 3 x 3 mL portions of Milli-Q H_2O, spinning at 5000 rcf for 10 minutes each. The particles were resuspended in 2 mL of H_2O to give an approximate azide concentration of 1 mM. The particle solution was lyophilized and the resulting dark red powder characterized by FTIR (KBr), showing the characteristic azide stretch at 2093 cm^{-1} is retained after the nanoparticle synthesis.

Characterization of ICP-N_3 nanoparticles. To determine the stoichiometry of metal-ligand binding, we conducted a titration wherein samples each containing a fixed concentration of 200 µM DABA-bis-HP-N_3 (4) in 1 mL H_2O were prepared with increasing amounts of $Fe(NO_3)_3 \cdot 9H_2O$ ranging from 0 to 220 µM. The absorbance at 460 nm was measured for each sample. The LMCT band at 460 nm is characteristic of the *tris*-HOPO-Fe^{3+} coordination complex._ENREF_117 The equivalence point was reached at 133 µM (0.66 equiv.), consistent with Fe_2L_3 stoichiometry (Figure A3.2). Further increase in absorbance is due to the presence of uncoordinated iron precursor salt. Additionally, we conducted elemental analysis on a lyophilized sample of the particles to assess their composition. Calc'd for $C_{69}H_{66}Fe_2N_{18}O_{15}$: C 55.28%, H 4.44%, N 16.82%. Found C 49.10%, H 4.18%; N 14.18%. The lower observed

organic content may be explained by the porous nature of the ICP particles and their ability to entrap polar solvent molecules, e.g. H_2O. Lastly, we studied the bare ICPs by energy dispersive X-ray spectroscopy (Hitachi H2300-A STEM) (Figure A3.3).

ICP-MS and UV-Vis were used in tandem to determine the extinction coefficient ε_{460} of the particles in Milli-Q H_2O. Briefly, five samples of ICP-N_3 particles in H_2O were prepared at varying dilutions and the absorbance at 460 nm was measured by UV-Vis. Subsequently, the iron concentration of each sample was determined by ICP-MS. Each sample was prepared in a matrix consisting of 3% HNO_3, 5 ppb indium (internal standard), and deionized water. The iron concentration was plotted vs. A_{460}, and the data was fit by a simple linear regression model. The slope of the line corresponds to $\varepsilon_{460} \approx 2870$ L·mol^{-1} cm^{-1} arising from the LMCT of the ICP-N_3 particles, allowing for spectroscopic determination of iron concentration.

The weight of the particles produced by the above procedure is expected to be in the range of 10-1000 kDa, since a small portion of the as-synthesized particles pass through a 100 kDa cutoff filter. Supporting this observation, the predicted degree of polymerization for ditopic 3,4-HOPOs is approximately 1000 repeat units under the reaction conditions given above, when estimated from literature stability constants of the 3,4-HOPO-Fe(III) complex.[155]

Oligonucleotide synthesis. All DNA synthesis was carried out on a BioAutomation MM48 DNA synthesizer, according to the standard manufacturer trityl-on protocol with an additional 5 minute coupling time for non-nucleosidic phosphoramidites. Ac-dC and dmf-dG phosphoramidites were used to enable room-temperature deprotection of the nucleobases. Oligonucleotides were synthesized on 1 μmol scale and deprotected in concentrated NH_4OH (30%) for 17 hours at room temperature, except for poly(CCT)-Cy5-containing oligonucleotides,

which were deprotected for 2 hours at room temperature. The resulting crude oligonucleotides were purified on a Varian Prostar HPLC fitted with a DynaMax Microsorb C18 Column, employing a gradient of 0-75% acetonitrile in triethylammonium acetate buffer (pH 7.0) over 45 minutes. The optical absorbance of the eluent was monitored at 254/310 nm for DBCO-containing oligonucleotides, 254/649 nm for Cy5-containing oligonucleotides, and 254/280 nm for all other oligonucleotides. DBCO-terminated oligonucleotides were lyophilized, resuspended in H_2O, and conjugated immediately to ICP-N_3 nanoparticles. Disulfide-terminated oligonucleotides were lyophilized, reduced to the free thiol and conjugated to AuNPs as described in previous reports.[53]

Synthesis of AuNP-DNA conjugates. AuNP-SNAs synthesized in this study were prepared according to established protocols.[3] For AuNP-SNAs employed in cell uptake experiments, the number of oligonucleotides/AuNP were determined by fluorescence measurements. Oligonucleotide loading on AuNP-SNAs was quantified using a 5nM solution of Cy5 labeled AuNP-SNAs. The Au core was dissolved using 100mM KCN diluted in deionized water. The mixture was then incubated at room temperature for 20 minutes, and the resultant fluorescence measured against a standard curve. The standard curve consisted of the equivalent oligonucleotide sequence at a range of concentrations, dissolved in water, treated with KCN and incubated in the same manner as the SNAs. All fluorescence measurements were made using a Synergy H4 fluorescent plate reader (BioTek). Loading on the CCT-Cy5-AuNPs used as a positive control for cell uptake experiments was 113 strands/particle (**CCT-Cy5-AuNP**). Loading on the Cy5-T_{20}-AuNPs was 157 strands/particle (**Cy5-T_{20}-AuNP**). Similar values were assumed for the non-fluorescent AuNP-SNA (**A-AuNP**).

Synthesis of DNA-ICP conjugates. In a typical procedure, a solution was prepared containing 100 μM of the desired cyclooctyne-DNA, 0.5M NaCl, and ICP-N_3 particles (500 μM in azide) in 2 mL Milli-Q H_2O. The resulting clear, orange solution was shaken for 16 h at 25°C. The reaction mixture was purified by ultrafiltration through an Amicon® Ultra 15 mL centrifugal filter (100 kDa MWCO), washing with 4 x 3 mL portions of 0.1M Tris buffer (pH 8.0), spinning at 5000 rcf for 10 minutes. The particles were resuspended in 1 mL of 0.1M Tris (pH 8.0). DNA-ICP particles remain colloidally stable at high salt concentrations (up to 1M NaCl), in contrast to the bare ICP-N_3 particles, which sediment within minutes in 1M NaCl. This observation indicates a stabilizing DNA surface layer has been successfully conjugated to the particle.

Characterization of DNA-ICP conjugates. The size, charge, and DNA-loading of DNA-ICP particles were analyzed by DLS, zeta potential, and UV-Vis. The DNA concentration of a particle solution was determined by UV-Vis using the ratio (A_{260}/A_{460}). Bare particles in Milli-Q H_2O possess $A_{260}/A_{460} \approx 5.4$. DNA-decorated particles were synthesized having a ratio A_{260}/A_{460} varying from 10.9 to 15.5, indicating the presence of DNA attached to the particles. Extensive washing was conducted to ensure no free DNA remained in solution. Loading of Cy5-containing DNA was significantly lower, potentially due to the steric bulk of the dye label. Finally, the zeta potential of the bare and DNA-loaded ICPs was compared, with all samples prepared at identical dilution in 10 mM Tris buffer (pH 8.0) and 0.1M NaCl. (Table A3.1).

Thermal denaturation studies. DNA-ICP particles bearing complementary sequences with a 17 base-pair overlap (**A-ICP** and **B-ICP**) were mixed at varying salt concentrations in 0.1M Tris buffer (pH 8.0) and heated from 20°C to 80°C at a rate of 0.25°C per minute. At room temperature, insoluble aggregates formed within 30-60 minutes of mixing the complementary DNA-ICPs. Upon heating, a sharp melting transition was observed, consistent with high DNA

surface loading of the ICP particles. The same behavior was not observed for a pair of DNA-ICPs with mismatched sequences (**B-ICP** and **NonTarget-ICP**). The free DNA duplex has a melting temperature of 54°C in 0.3M NaCl, compared to >60°C for the DNA-ICPs, depending on the NaCl concentration. The same experiment was repeated using a gold nanoparticle/DNA-ICP pair (**A-AuNP** and **B-ICP**).

MTT toxicity assay of ICP ligands. To ensure the parent ligand comprising the particle core did not exhibit cellular toxicity, an MTT assay was performed. SKOV-3 cells were seeded in a 96-well plate at a population of $5x10^3$ cells per well. After 24 h, the cells were treated with 0.1 mL of a solution of compound **3** or **4** (diluted from DMSO stock solution into Opti-MEM) and incubated at 37ºC for 24 h. After incubation, the compound was removed from the cells and replaced with 0.1 mL of complete McCoy's 5A medium (supplemented with 10% fetal bovine serum and 1% penicillin/streptomycin). Cell viability was measured by MTT assay at 48 h and 72 h following the addition of compound **3** or **4** to the cells.

Briefly, cells were incubated with 0.1 mL of complete McCoy's 5A medium. 10 µL of MTT solution (5 mg/mL MTT in 1x PBS; Molecular Probes) was added into each well of cells and cells were incubated at 37ºC for 2 h. After incubation, 0.1 mL of SDS-HCl solution (0.1 g/mL SDS in 0.01 M HCl) was added to each well to solubilize the formazan product, and cells were further incubated at 37ºC overnight. After overnight incubation, the absorbance of the cell lysate was measured at 570 nm using a Synergy H4 Multimode Microplate Reader (Biotek). The relative cell viability was calculated compared to vehicle-treated cells. Reported values represent the mean ± SD of three replicates.

Cell culture and uptake studies. For visualizing cell uptake by confocal microscopy, ovarian cancer (SKOV-3), cervical cancer (HeLa) and C166 mouse endothelial cells were cultured in DMEM supplemented with 10% Fetal Bovine Serum (Atlanta Biologicals) and 1% Penicillin/streptomycin (Life Technologies).

All microscopy was performed using an SP5 laser scanning confocal microscope. Cellular images were obtained by culturing HeLa cells in supplemented Dulbecco's Modified Eagle Medium (DMEM, Life Technologies) at approximately 30% confluency in Nunc Lab-Tek II borosilicate-bottom chamber slides (Thermo Scientific). Cells were allowed to attach for 24 hours, after which they were washed once with PBS and resuspended in OptiMEM. Cells were then treated with either linear DNA, AuNP-SNAs, or DNA-ICPs at a concentration of 100 nM (DNA basis). After 24 hours the cells were washed once with OptiMEM, and resuspended in DMEM containing Hoechst 33258 (Life Technologies). All images are of live cells. Equivalent methods were used for flow cytometry, however cells were not treated with Hoechst and instead were trypsinized for 3 minutes in 05% trypsin-EDTA (GIBCO), resuspended in Opti-MEM, and analyzed using a Guava Easycyte 8HT (Millipore) equipped with a 633nm laser.

For naked-eye visualization of cell uptake, MCF-7 and SKOV-3 cells were plated in 6 well plates (~100,000 cells/well). After incubating the cells for 24 hours in DMEM + 10% FBS containing medium, the cell media was changed to Opti-MEM and the following concentrations of DNA-ICPs were added to individual wells (DNA basis): 0.0, 0.1, 0.5, 1.0, 2, and 5 μM. The particles were incubated in cells for 24 hours, after which the cells were washed thrice in PBS, cells were replenished with fresh media, and the cells were incubated for an additional 48 hours. Thereafter, cells were rigorously washed to remove any extracellular ICP particles, trypsinized, and immediately transferred to 1.5 ml Eppendorf tubes containing PBS. The cells were then

centrifuged at 1100 RPM for 5 minutes to form cellular pellets. Pictures of the cell pellet were taken against a white background to show a concentration dependent increase in ICP uptake.

Western blot and gene knockdown analysis. SKOV3 cells were obtained from American Tissue Culture Collection (ATCC). The cells were incubated in 5% CO_2 at 37˚C in McCoy's 5A medium supplemented with 10% heat-inactivated FBS. Cells were cultured in 6 well cell culture plates (BD Biosciences) with 100,000 cells per well seeded 24 hours before treatment with ICPs. Medium was replaced with Opti-MEM (Life technologies) immediately prior to treatment with ICPs or Lipofectamine RNAimax (Life technologies) DNA. Lipofectamine transfection was performed according to manufacturer's instructions to deliver 25 pmole of DNA. After 12 hours, the medium was replaced with fresh media (McCoy's 5A with 10% FBS) and the cells incubated for another 48 hours. The cells were then washed three times with PBS, trypsinized and the pellet was resuspended in 100 μL of mammalian cell lysis buffer (Cell Signalling) containing protease and phosphatase inhibitor (Thermo Scientific). The whole cell lysates were then purified and collected by centrifugation and frozen at -80 ˚C. Protein concentrations were determined using the BCA Protein Assay Kit (Pierce). Equal amounts of protein samples (25 μg) were fractionated by 4-20% precast gradient gel (Bio-Rad) and transferred to nitrocellulose membranes (Thermo Scientific). Membranes were dried overnight, rehydrated in PBS, then blocked for 1 hour at room temperature in blocking buffer (LI-COR Biosciences). Proteins were detected with rabbit primary antibodies against HER2 (1000:1) (Cell Signaling), mouse antibody against beta-tubulin (1000:1) (Thermo Scientific) and anti-rabbit or anti-mouse IgG-dye conjugated secondary antibodies (10,000:1) (LI-COR Biosciences). The fluorescence signal was recorded and quantified using the Odyssey Infrared Imaging System (LI-COR Biosciences) and quantified using Image Studio software (LI-COR Biosciences).

Agarose gel analysis of DNA-ICP degradation. To visualize the amount of nucleic acids released from DNA-ICP particles under acidic conditions, an agarose gel experiment was carried out. Briefly, five aliquots of DNA-ICPs (**B-ICP**) containing 12.2 μM total DNA were diluted 1:1 with the following buffer solutions (100 mM each): KHP buffer, pH 4.0; HEPES buffer, pH 5.5; MES buffer, pH 6.0, PBS buffer, pH 7.4, or Tris buffer, pH 8.0. As a control, a sample was prepared with the single-stranded oligonucleotide (**B-DBCO**) containing the same total amount of DNA in deionized H_2O. The solutions were allowed to stand at RT for 48 h, then were subsequently diluted again 1:1 with 0.5x TAE buffer. The samples were then analyzed in 1% agarose gel run at 90V for 1 hour in 0.5x TAE buffer. Agarose gels were imaged on a Fujifilm FLA-5100 gel imager and 1X SYBR® Gold stain was used to visualize oligonucleotides.

Results and Discussion

Synthesis of infinite coordination polymer particles. For the purpose of polymerizing Fe^{3+} into coordination polymer nanoparticles, we synthesized a new ditopic ligand DABA-bis-HP-N_3 (**4**), which deliberately employs the inexpensive building blocks maltol and 3,5-diaminobenzoic acid (DABA, **1**) (Scheme 3.1a). Two sequential acid-catalyzed condensations of maltol with DABA (**1** to **2**; **2** to **3**) followed by HATU-mediated amidation of the carboxylic acid afforded the azide-bearing ditopic ligand **4**. Importantly, the carboxylic acid in **3** may be amidated with a wide variety of amine building blocks, affording ICP particles with tailorable post-synthetic chemistry dictated by the pendant functional groups.

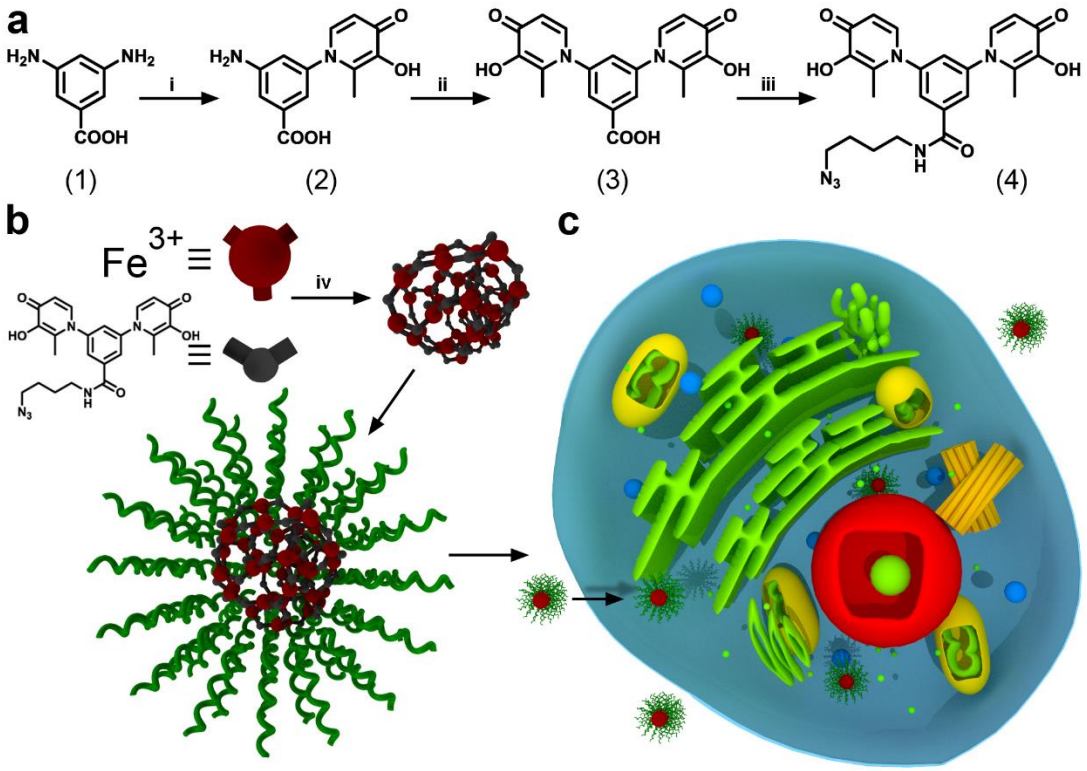

Scheme 3.1. Synthesis and assembly of ICP particles and their cellular uptake. a) Synthetic scheme for bis-3,4-HOPO azide (**4**). b) Assembly of ICP particles from $Fe(NO_3)_3$ and compound **4**, followed by conjugation with DNA via a Cu free 'Click' reaction. c) Scheme depicting the cellular uptake of ICP-DNA conjugates. Reaction conditions: i) maltol, n-propanol, reflux, 16 h. ii) maltol, ethoxyethanol, 64 h, reflux. iii) 4-azido-butan-1-amine, HATU, diisopropylethylamine, DMSO, RT, 4 h. iv) $Fe(NO_3)_3 \cdot 9H_2O$, NaOH (aq.), RT, 10 min. v) Dibenzocyclooctyne-DNA, 0.5M NaCl, RT, 16 h

To synthesize ICP nanoparticles from ligand **4**, we prepared a dilute NaOH solution of ligand **4** (1.07 mM ligand, 1877 µL) and injected a solution of ferric nitrate (10.8 mM, 123 µL) into it (Scheme 3.1b). Particle formation occurs instantaneously and the color of the solution turns from clear to red due to the ligand-metal charge transfer band (LMCT) of the *tris*-HOPO-Fe^{3+} complex ($\lambda_{max} \approx 460$ nm).[194] The resulting ICP-N_3 nanoparticles were colloidally unstable in the presence of low concentrations of salts (NaCl, Tris·HCl), leading to gradual precipitation of a red, insoluble material. (Figure 3.1).

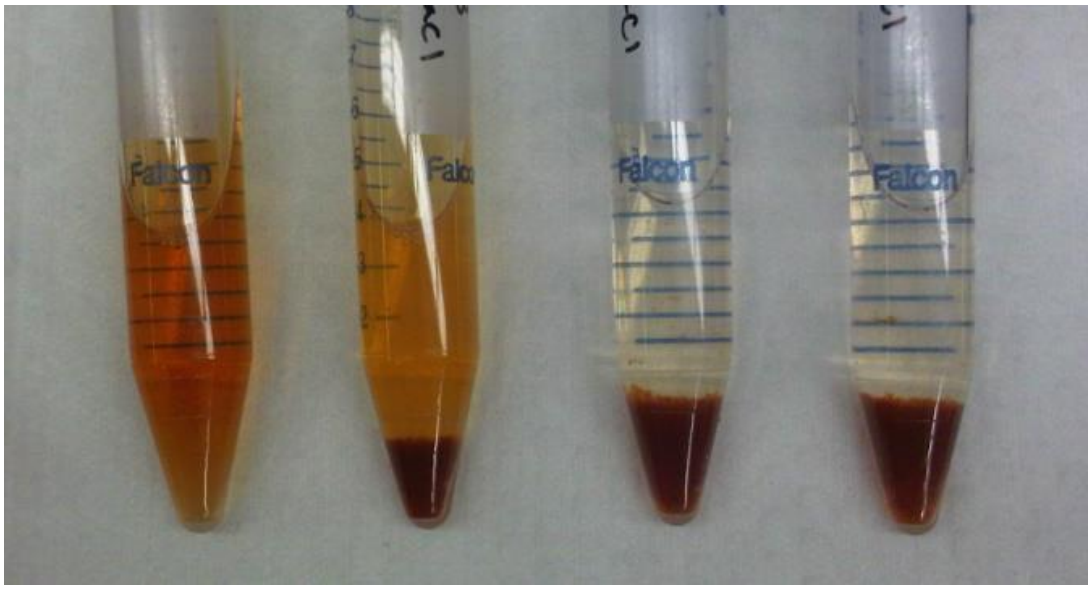

Figure 3.1. Bare colloidal ICP-N_3 nanoparticles stored overnight at varying concentrations of NaCl. From left to right: 0 M, 0.1 M, 0.5 M, 1.0 M

The crude ICP-N_3 particles were purified by centrifugal filtration (100 kDa molecular weight cut-off) and re-suspended in H_2O. The particles were retained on the filter, as they were too large to pass through. Minimal loss of material through the filter indicated a colloidal dispersion of high molecular weight species was obtained. In deionized H_2O, the as-synthesized particles were stable, with a mean hydrodynamic diameter of 10-20 nm, determined by dynamic light scattering (DLS) (Figure 3.2). TEM and AFM imaging revealed aggregates of small nanoparticles, with some degree of fusion occurring upon drying (Figure A3.4). Furthermore, the composition of the ICP-N_3 particles was probed spectroscopically. Aliquots containing a fixed concentration of DABA-bis-HP-N_3 ligand in H_2O were prepared and treated with increasing amounts of iron ranging from 0 to 1.1 equivalents. The absorbance at 460 nm increased until 0.66 equivalents of Fe^{III} were added, consistent with a metal-ligand stoichiometry of Fe_2L_3 (Figure A3.2).

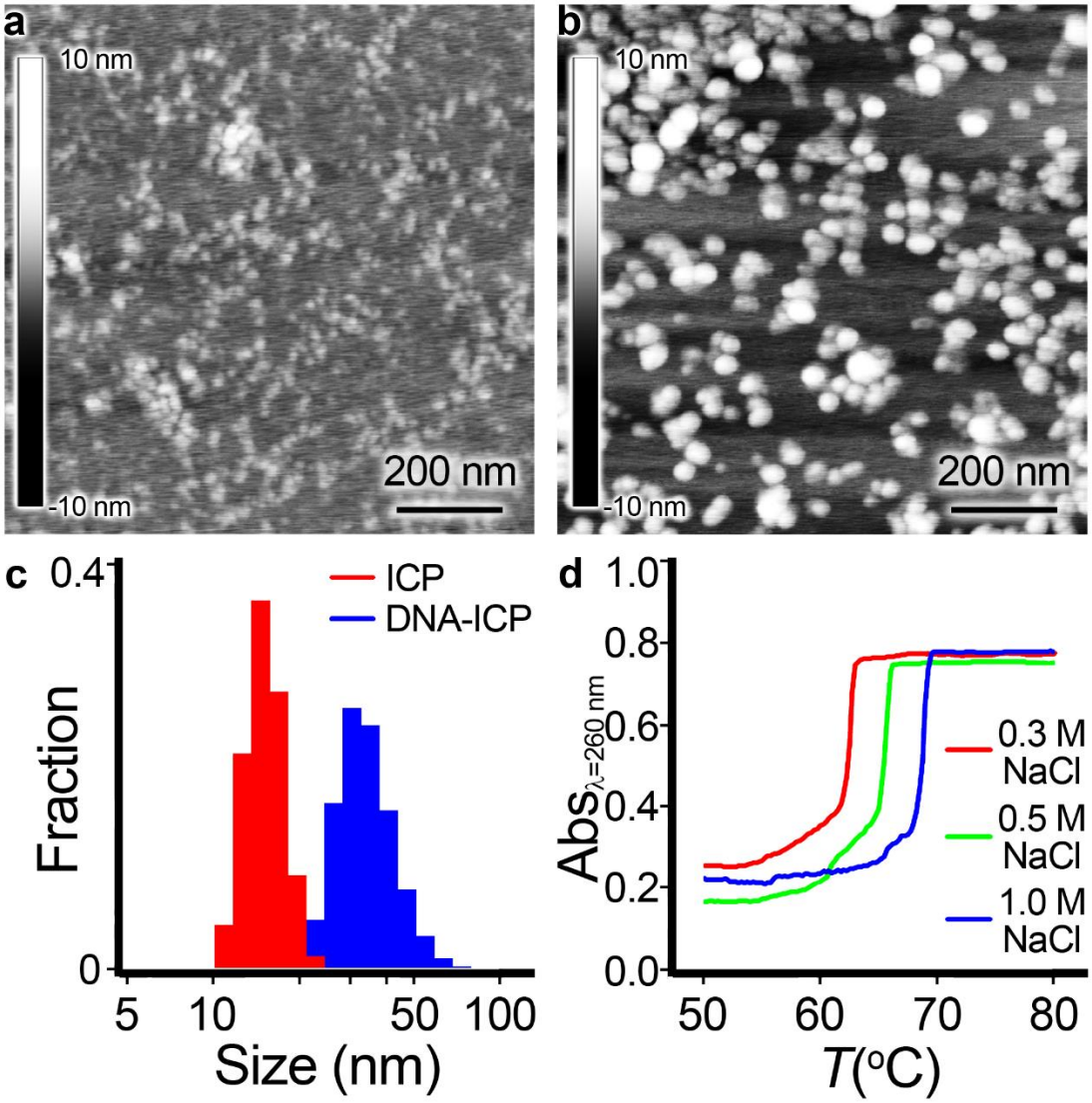

Figure 3.2. Characterization of DNA-ICP particles. AFM image of (a) Bare ICP particles drop-cast and dried on mica. b) DNA-functionalized ICP particles drop-cast and dried on mica. c) DLS histograms comparing size distributions of bare and DNA-functionalized ICPs. d) Cooperative melting of ICP-DNA aggregates.

Conjugation of oligonucleotides to ICP particles. For conjugation to bare ICP-N_3 particles, all oligonucleotides were made on an automated DNA synthesizer, purified by reverse-phase HPLC, and characterized by MALDI-ToF. Dibenzocyclooctyne (DBCO) phosphoramidites are commercially available and easily incorporated onto the 5′ termini of the oligonucleotides. DNA strands modified with a Cyanine 5 (Cy5) dye were used for intracellular imaging studies. DNA strands modified with a 5′ alkylthiol were used to construct AuNP-SNAs for comparison with

DNA-ICP particles (Table 3.1). DBCO-bearing oligonucleotides were conjugated to ICP-N_3 particles by simply mixing the two reactants in aqueous NaCl (0.5M) followed by repeated filtration to remove unreacted DNA. Importantly, gradual addition of salt was not necessary to prevent aggregation of the nanoparticles, unlike their gold counterparts. The resulting DNA-ICP particles were suspended in Tris·HCl buffer (100 mM, pH 8.0) and remained colloidally stable when stored at 5°C or when heated up to 80 °C over the course of a melting analysis.

Oligo Name	**Sequence (5´→3´)**	FW (Calc'd)	$[M-H]^-$ (Found)
A-DBCO	DBCO-TEG-A_4-AATCCTTATCAATATTT	6942	6951
B-DBCO	DBCO-TEG-A_4-AAATATTGATAAGGATT	7080	7082
A-SH	HS-$(CH_2)_6$-A_4-AATCCTTATCAATATTT	6699	6689
HER2-DBCO	DBCO-TEG-CTC-CAT-GGT-GCT-CAC	5075	5070
NONT-DBCO	DBCO-TEG-GAG-CTG-CAC-GCT-GCC-GTC-A	6360	6369
Cy5-DBCO	DBCO-TEG-CCTCCTCCT-Cy5-CCTCCTCCT	6337	6341
CCT-Cy5-SH	HS-$(CH_2)_6$-CCTCCTCCT-Cy5-CCTCCTCCT	6094	6098
Cy5-T_{20}-SH*	Cy5-TTTTTTTTTTTTTTTTTTTT-$(CH_2)_3$-SH	7084	7084

Table 3.1. All oligonucleotides synthesized for conjugation to ICP-NPs and AuNPs with mass determined by MALDI-ToF. *Purchased from TriLink BioTechnologies (San Diego, CA)

Characterization of DNA-ICP SNAs. In addition to increasing colloidal stability, the conjugation of DNA to the surface of ICP-N_3 particles resulted in changes to particle size, surface charge, and morphology (Figure 3.2). DLS and zeta potential measurements showed a consistent increase in hydrodynamic diameter and surface charge, respectively. Particles were imaged by AFM to visualize changes in size and morphology. UV-Vis spectroscopy was used to calculate the relative contribution of DNA to the absorbance at 260 nm, and hence the DNA concentration was determined. Inductively-coupled plasma mass spectrometry (ICP-MS) was used to calculate directly the extinction coefficient ε_{460} of the ICP particles (Figure 3.4a). Lastly, incubation of DNA-ICP particles in aqueous buffers ranging from physiological pH (7.4) to low lysosomal pH (4.0) showed a clear red-shift in the LMCT λ_{max}, indicating partial dissociation of the *tris*-coordinated Fe^{3+} nodes comprising the particle (Figure 3.4b). Likewise, agarose gel

analysis of DNA-ICP particles incubated in buffers of various pH showed significant shedding of DNA from the particle core at pH values below physiological pH. (Figure 3.3) Other coordination polymers based on HOPOs and catechols exhibit similar pH dependence.[153, 195-196]

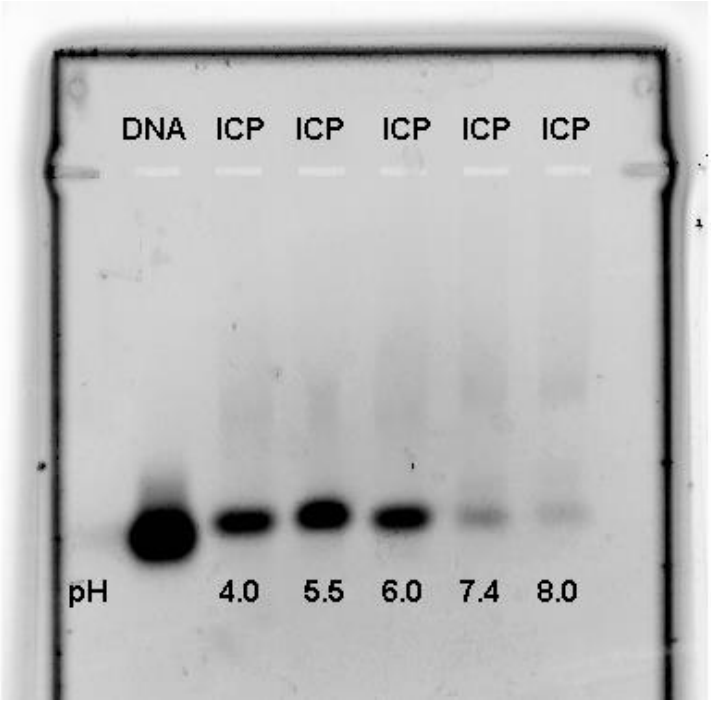

Figure 3.3. Agarose gel analysis of ICP degradation after 48 hours. Note that the DNA released from the ICP is slightly retarded in the gel due to its higher molecular weight after reaction with the ligand (**4**).

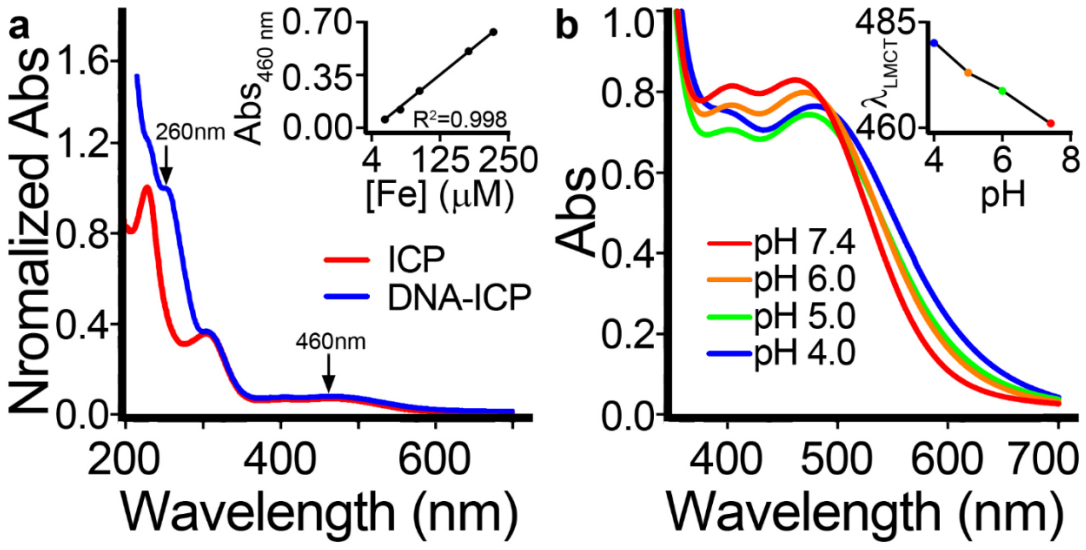

Figure 3.4. UV-Vis analysis of DNA-ICP particles. a) Comparison of bare ICP particles with DNA-ICP particles showing the DNA absorbance at 260 nm. Inset: determination of LMCT ε_{460}. b) pH dependence of LMCT absorbance. The red-shift of λ_{max} with decreasing pH is indicative of complex dissociation (see inset).

Thermal denaturation studies. In order to probe the surface density of oligonucleotides on the DNA-ICP particles, thermal denaturation experiments were carried out wherein ICPs with complementary sequences (**A-ICP** and **B-ICP**) were mixed, allowed to hybridize, and then heated above the melting transition of the duplex. The free double-stranded DNA duplex possesses a 17 base-pair overlap with T_m = 54.0°C in 0.3M NaCl. In contrast, the same complementary strands form duplexes with a T_m = 66.9°C when conjugated to ICP-N_3 particles, an increase of nearly 13°C. The melting transition of the DNA-ICP particle aggregates is extremely narrow, an indication of cooperativity; the full width at half-maximum of the melting curve is typically <2°C, compared to 10-20°C for free double-stranded DNA (Figure 3.2d). **A-ICP** particles alone exhibited no aggregation or melting under the experimental conditions, nor did **A-ICP** particles mixed with non-complementary particles (**NonTarget-ICP**). We also studied the interaction of DNA-ICP particles with conventional AuNP-SNAs (**A-AuNP)** that were prepared and purified according to established protocols. Similar aggregation and melting behavior was observed between **A-AuNP** and **B-ICP** particles mixed in a 1:1 ratio (Figure A3.5). Overall, these studies suggest high DNA surface loading on the ICP-N_3 particles.

Cellular uptake studies. Due to the high apparent oligonucleotide density on the DNA-ICP surface, we hypothesized that they would function as efficient gene delivery agents, much like their gold predecessors. To test this assumption, ICP-N_3 particles were functionalized with the poly(CCT) oligonucleotide **Cy5-DBCO** bearing an internal fluorophore-label to afford **Cy5-ICP** particles. Likewise, gold nanoparticles (15 nm) were functionalized with the analogous **Cy5-SH** oligonucleotide to afford **Cy5-AuNP** particles having a loading of approximately 113 strands/AuNP, as determined by fluorescence. To test our hypothesis, uptake was examined in HeLa cervical cancer cells (Figure 3.5). The DNA-ICP particles were found to cross cell

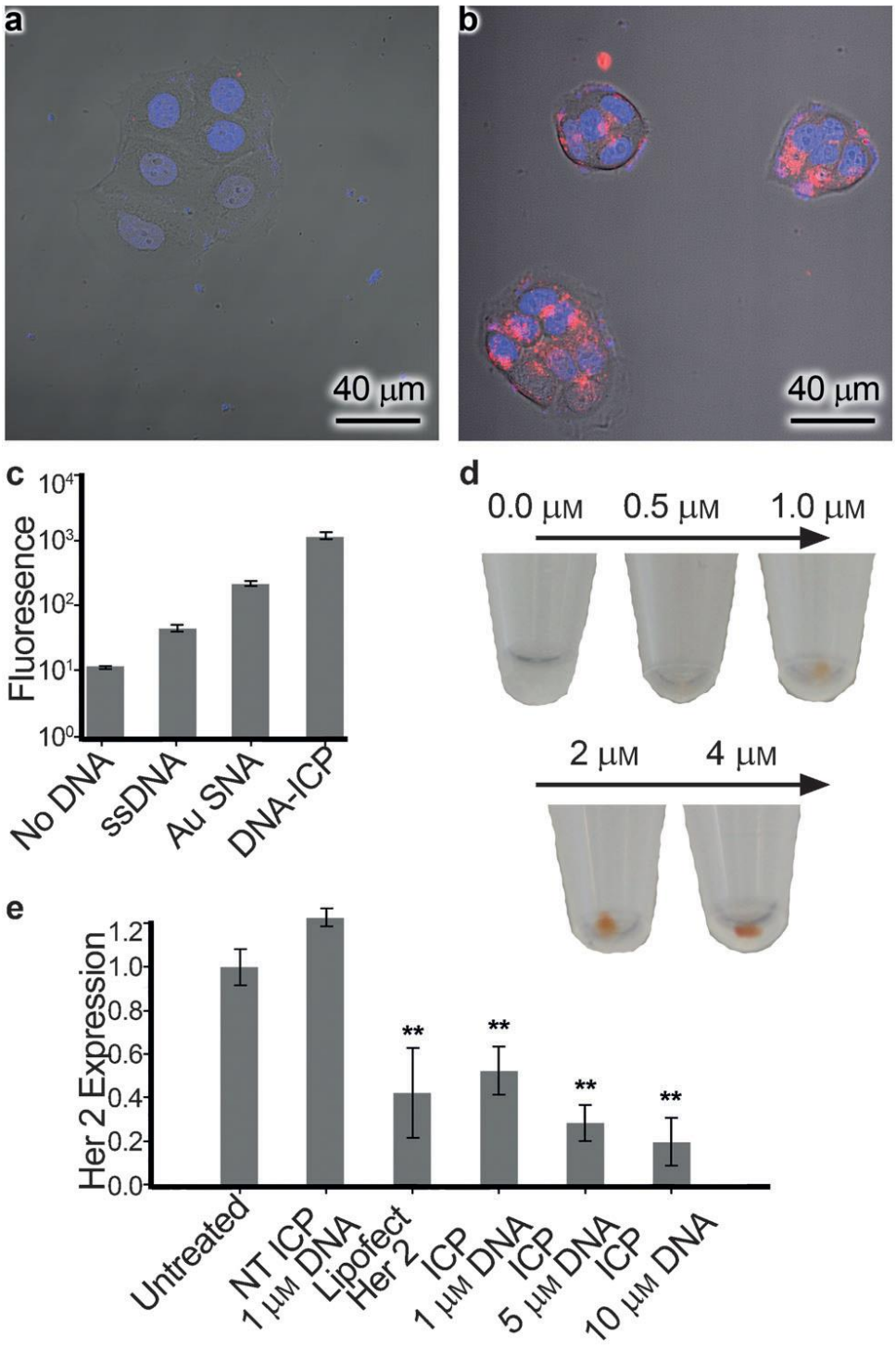

Figure 3.5. Cellular uptake and gene knockdown. Confocal microscopy image of HeLa cells treated with (a) Cy5-ssDNA and (b) DNA-ICP particles (100 nM DNA in each case). Hoechst stain denotes the nucleus in blue while the Cy5 dye attached to the DNA is red. c) Fluorescence intensity of Cy5 dye quantified by flow cytometry. d) Naked-eye visualization of DNA-ICPs taken up in pelleted SKOV-3 ovarian cancer cells e) Expression of HER2 protein in SKOV-3 cells treated with non-targeting DNA-ICPs, HER2 targeting ssDNA + Lipofectamine (25 nM DNA basis), and HER2 targeting DNA-ICPS. Starred bars (**) indicate knockdown was significant ($p<0.05$) as determined by unpaired student's T test.

membranes more efficiently than the free DNA strands, and exhibited comparable uptake to AuNP-SNA nanoparticles bearing the same sequence.

These results suggest that DNA-ICP nanoparticles have the potential to transport large amounts of DNA to the cytosol. A dose-dependent increase in iron concentration was found after incubation of DNA-ICPs in SKOV-3 ovarian cancer and MCF-7 breast cancer cells for 24 hours. The color of the iron complex could be seen by the naked eye in pelleted cells treated with DNA-ICPs. Confocal microscopy experiments with SKOV-3 and C166 cells confirmed that DNA-ICPs enter such cell lines, demonstrating that these structures exhibit comparable uptake characteristics to AuNP-SNAs (Figures A3.6-A3.8).

Gene knockdown studies. Having demonstrated the ability of DNA-ICP conjugates to enter cells in a manner analogous to AuNP-SNAs, we probed their ability to alter protein expression by targeting a known cancer-related mRNA transcript. SKOV-3 ovarian cancer cells were chosen as they over-express human epithelial growth factor receptor 2 (HER2), which is involved in signal transduction pathways leading to malignant cell growth and differentiation.[197] We performed a series of gene knockdown experiments utilizing anti-HER2 DNA-ICPS. SKOV-3 cells were incubated with different concentrations of antisense DNA-ICPS (**HER2-ICP**) or non-targeting DNA-ICPS (**NonTarget-ICP**), with free anti-HER2 DNA complexed with Lipofectamine® (Life Technologies) as a positive control. After 3 days, cells were harvested and HER2 expression was determined by Western blot analysis (Figure 3.5e). Treatment with anti-HER2 DNA-ICPs reduced HER2 expression by up to 81%, in a dose dependent fashion. This is comparable to results achieved with commercial transfection kits, and with no change in HER2

expression observed with non-targeting DNA-ICPs. Lastly, no toxic effects or cell death resulted from treatment with DNA-ICPs, as predicted by MTT assays (Figure A2.1 and A3.1).

Conclusions. We have reported a facile method to synthesize biocompatible, DNA-decorated infinite coordination polymer nanoparticles that are capable of cell entry and gene regulation without transfection agents. Iron(III)-based ICP nanoparticles, synthesized in water, can be conjugated directly to oligonucleotides and carry them across cell membranes. By confocal microscopy, we observed punctate fluorescence when cells were treated with dye-labelled ICP particles, which is also seen with classical AuNP SNAs, suggesting they share a similar endocytotic uptake pathway. Furthermore, the core is comprised of benign building blocks that are not expected to pose significant health hazards. This work represents a major step towards the construction of clinically viable gene regulation constructs for *in vivo* applications in the treatment of cancer and other genetic diseases.

Chapter 4

Biodegradable DNA-brush block copolymer spherical nucleic acids enable transfection agent-free intracellular gene regulation

[Portions of this work have been published previously as Zhang, C.*; Hao, L. L.*; Calabrese, C. M.*; Zhou, Y.; Choi, C. H. J.; Xing, H.; Mirkin, C. A., Biodegradable DNA-Brush Block Copolymer Spherical Nucleic Acids Enable Transfection Agent-Free Intracellular Gene Regulation. *Small* **2015,** *11*, 5360-5368.]

*These authors contributed equally to this work. C. M. Calabrese carried out the chemical synthesis and characterization of DNA-block copolymers described herein and was responsible for conducting the additional experiments requested by peer reviewers prior to publication.

Abstract

A new strategy for synthesizing spherical nucleic acid (SNA) nanostructures from biodegradable DNA block copolymers is reported. Multiple DNA strands are grafted to one end of a polyester chain (poly-caprolactone) to generate an amphiphilic DNA brush block copolymer (DBBC) structure capable of assembling into spherical micelles in aqueous solution. These novel DBBC-based micelle-SNAs exhibit a higher surface density of nucleic acids compared to micelle structures assembled from an analogous linear DNA block copolymer (DBC), which endows them with the ability to more efficiently enter cells without the need for transfection agents. Importantly, the new SNAs show effective gene regulation without observable cellular toxicity in mammalian cell culture.

Introduction

Spherical nucleic acids (SNAs) are an emerging class of nanostructure, typically consisting of a nanoparticle core densely functionalized with a nucleic acid shell.[33, 51] These structures exhibit a wide variety of novel properties that are substantively different from their linear nucleic acid counterparts, making them especially attractive for intracellular applications.[68, 79, 169] Specifically, they are recognized by Class A scavenger receptors and naturally internalized by many cell types *via* caveolin-mediated endocytosis.[70] They have been used as novel probes for measuring intracellular genetic content and as potent gene regulation agents.[198-199] They are especially attractive as gene regulation materials since they do not need ancillary transfection agents such as viruses, peptides, lipids or cationic polymers to cross the cell membrane.[73] Thus far, SNAs have been made with a variety of core materials, including many inorganic compositions[63, 171] and several polymer compositions,[29, 80, 100, 178, 200-208] and there are now a few examples of hollow SNA structures that are held together by cross-linked DNA or silica shells.[78, 170] Although the nanoparticle core typically plays little role in determining the general chemical and biological properties of the corresponding SNAs, it can be a major concern when such structures are being considered as therapeutic candidates.[209-210] Indeed, a significant synthetic challenge for the chemistry community is to design totally biocompatible and biodegradable SNAs that exhibit the hallmark properties of conventional SNAs with inorganic cores. One approach has been to use liposomal architectures as cores,[77] but an alternative approach that may provide even greater tailorability is the use of polymer micelle architectures. Although a variety of nucleic acid polymer micelle architectures have been reported, [124-133] none have been developed and optimized with regard to general SNA features and intracellular biological activity. Indeed, a few studies involving polymer micelle structures for intracellular

gene regulation have been undertaken, but they either required a cationic transfection agent (*e.g.* polyethyleneimine) for transfection or were constructed using non-degradable polymers.[80, 211] To date, there are no biodegradable DNA block copolymer (DBC) based micelle structures that have been shown to exhibit the natural cellular uptake properties of SNAs, and therefore the use of such structures with respect to intracellular and therapeutic applications has been limited. Importantly, SNA-like properties are directly related to the orientation and high density of nucleic acids on the nanoparticle surface.[69]

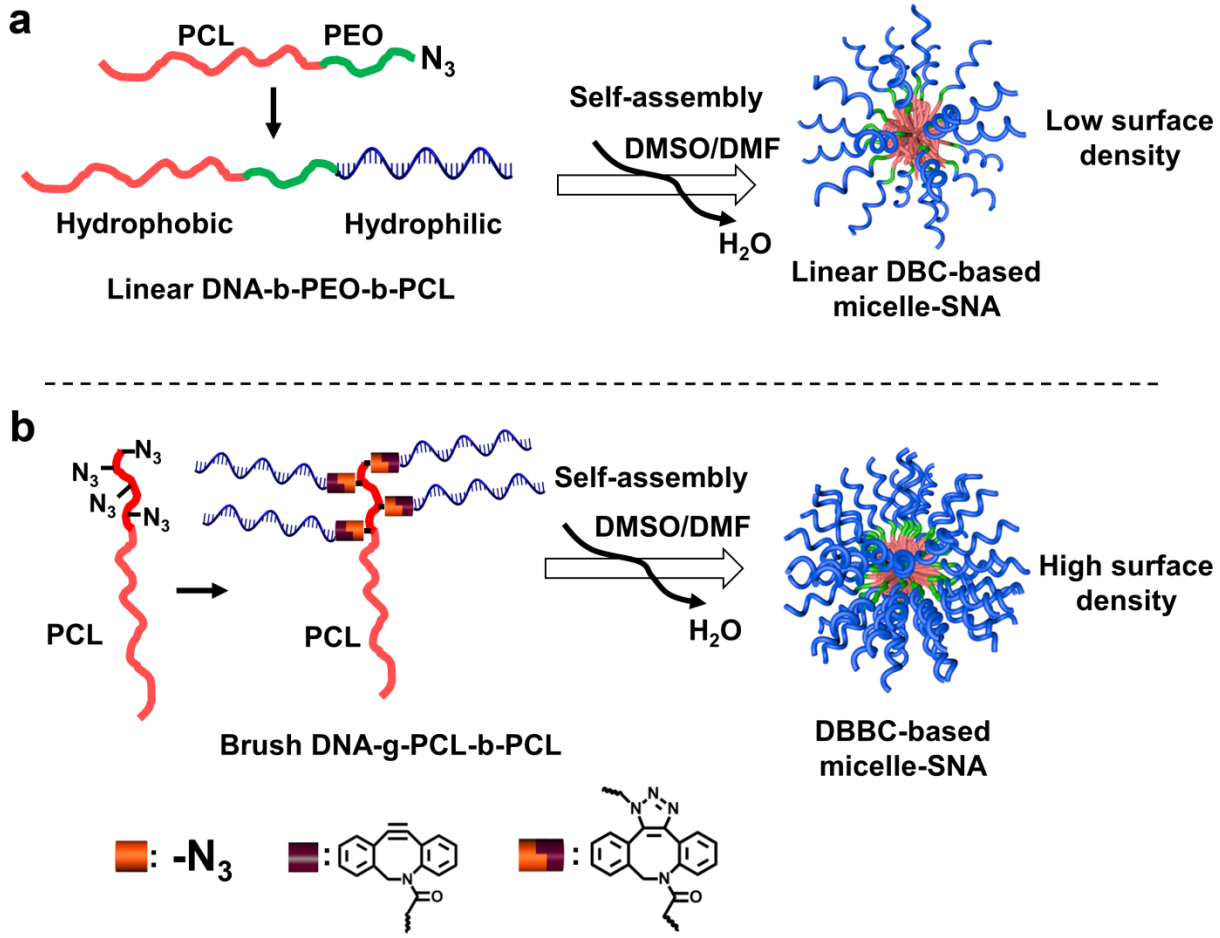

Scheme 4.1. Schematic showing the synthesis of DNA grafted block copolymer-based micelle SNAs. (a) The synthesis of the linear DNA-b-PEO-b-PCL block copolymer and the corresponding formation of micelle-SNAs (LDBC-SNAs). (b) The synthesis of the brush DNA-g-PCL-b-PCL block copolymer and the formation of micelle SNAs (DBBC-SNAs) with a higher surface density of nucleic acids.

To overcome the problem of low cell internalization associated with DNA block copolymer micelle structures, we identified the need to synthesize micelle SNAs with a dense layer of nucleic acids on the polymer core surface. Herein, we describe a strategy for preparing DBC micelle-SNAs with a biodegradable core and a dense layer of highly oriented oligonucleotides projecting from the surface of the aforementioned core. Traditionally, approaches to synthesizing DBC micelle architectures have involved the linear coupling of nucleic acids to hydrophobic polymer blocks (Scheme 4.1a).[100] We have found this approach does not reliably yield structures with a nucleic acid density high enough and suitable for optimal SNA cellular transfection capabilities (*vide infra*). Therefore, our synthetic approach relies on the generation of a DNA-brush block copolymer (DBBC) based micelle structure (Scheme 4.1b), which was pioneered by Gianneschi *et al.* in the context of non-degradable constructs for materials assembly purposes.[212] In our synthetic approach, the key components of the DBBC micelle structures are prepared by grafting multiple DNA strands onto the terminal segment of a diblock copolymer consisting of polycaprolactone (PCL; a component in FDA-approved therapeutics[213]) and azide-modified PCL *via* copper-free click chemistry to form a DBBC macromolecule. Then, when transferred from an organic solvent mixture consisting of 1:1 DMSO/DMF into an aqueous solution, the as-synthesized amphiphilic DNA-brush block copolymers assemble into ~ 40 nm diameter spherical micelles (Scheme 4.1b). For comparative purposes, we also prepared a similarly sized micelle structure from a linear DBC component (Scheme 4.1a).

Experimental Procuedures

Materials and Methods. All DNA synthesis was carried out on a BioAutomation MM48 DNA synthesizer according to the standard manufacturer trityl-on protocol. All reagents for

oligonucleotide synthesis were purchased from Glen Research (Sterling, VA) and used following the manufacturer's instructions. Ac-dC and dmf-dG phosphoramidites were used to enable room-temperature deprotection of the nucleobases. α-Chlorocyclohexanone, sodium azide, *N*,*N*-dimethylformamide (DMF), tin(II) octanoate, caprolactone (CL), and all other solvents were purchased from Sigma-Aldrich (St. Louis, MO) and used without further purification. *M*-chloroperoxybenzoic acid (mCPBA) was purchased from Fluka (Buchs, Switzerland).

Oligonucleotide synthesis. Oligonucleotides were synthesized on 1 μmol scale and deprotected in concentrated NH_4OH (30%) for 17 hours at room temperature. The resulting crude oligonucleotides were purified on a Varian Prostar HPLC fitted with a DynaMax Microsorb C18 Column, employing a gradient of 0-75% acetonitrile in triethylammonium acetate buffer (pH 7.0) over 45 minutes. The optical absorbance of the eluent was monitored at 254/310 nm for DBCO-containing oligonucleotides, 254/494 nm for fluorescein-containing oligonucleotides, and 254/280 nm for all other oligonucleotides. Fractions were collected, lyophilized, and the DNA concentration quantified by UV-Vis.

Synthesis of α-chloro-ε-caprolactone. To a solution of 10 g (75 mmol) of 2-chlorocyclohexanone in 100 mL dichloromethane was added 20 g (81 mmol) of mCPBA (70%). The reaction mixture was stirred for 3 days at room temperature, then the reaction vessel was cooled to -20 °C to precipitate mCPBA. After vacuum filtration, the filtrate was washed with saturated aqueous $NaHSO_3$ (3x), followed by saturated aqueous $NaHCO_3$ (3x), and finally with H_2O. After drying over $MgSO_4$, the organic phase was vacuum-filtered, and the solvent was removed under reduced pressure to yield the crude product (yield not quantitated) which was used immediately in the next step.

Synthesis of Diblock Copolymer Poly(α-N_3-εCL-*b*-εCL). The monomer α-chloro-ε-caprolactone was prepared by the Baeyer-Villager oxidation of α-chlorocyclohexanone using excess mCPBA. After isolation, 0.5 g monomer (3.36 mmol) was mixed with 3.0 g commercially available polycaprolactone (M_W = ~ 14 kDa, as macro-initiator) in dry toluene (10 mL). The mixture was dried by repeated (3×) azeotropic distillation with toluene. Then, the solution was heated to 130 °C in a preheated oil bath and stirred under N_2. The reaction mixture was stirred for 5 min at 130 °C and then one drop of tin(II) octanoate was added *via* syringe. The temperature was maintained at 130 °C for another 3 hours. The resulting viscous mixture was rapidly cooled, upon which it solidified. The crude polymer was purified by repeated dissolution in dichloromethane and heptane precipitation (3×), resulting in a white solid after drying. Then the pendant chlorides of the as-synthesized poly(α-Cl-εCL-*b*-εCL) were converted into azides by treatment with sodium azide in DMF overnight at room temperature. After removal of DMF *in vacuo*, 15 mL of toluene was added, and the remaining NaN_3 was removed by centrifugation (4000 rpm at 25 °C for 20 min). The diblock copolymer was recovered by precipitation in heptane. After washing with heptane multiple times, the solid precipitate was collected by vacuum filtration and dried under reduced pressure to afford 2.2 g (73% yield, PCL basis) of azide-modified copolymer.

Synthesis of Azide-terminated PEO-PCL Diblock Copolymer. Azide-terminated oligo(ethylene oxide) with 4 PEG units ($C_8H_{16}O_4N_3$, 109 mg, 0.5 mmol) was weighed into a dry flask and ε-caprolactone (8.5 g with M/I ratio of ~ 150:1) was subsequently added. The synthesis and purification of single azide-terminated PEO-PCL diblock copolymer follow the same procedures for poly(α-Cl-εCL-*b*-εCL) as mentioned above with similar isolated yield of the desired product after precipitation into heptane.

DNA Conjugation. For each azide-containing polymer, the same procedure was followed. First, the polymer was dissolved in a 1:1 DMSO/DMF solution, and then a large excess of DBCO-DNA dissolved in DMSO was added to the polymer solution and incubated at 40 °C overnight. After conjugation, the resulting linear and brush DBC samples were used immediately for micelle formation.

Formation and Purification of Micelle-SNAs. Briefly, DBCs dissolved in an organic solvent (DMSO/DMF, 1:1) were loaded in a dialysis bag with a 50 kDa MW cutoff membrane and the solution was dialyzed against deionized water for 12 hours. After removal of large aggregates by filtration through a 0.2 μm syringe filter, the micelle-SNA conjugates were purified using an Amicon Ultra-15 ultrafiltration device (Millipore, MWCO 50 kDa) to remove excess free DNA.

Characterization. ^{1}H NMR spectra were recorded on a Bruker Avance 400 MHz NMR spectrometer and referenced internally to residual proton signals in the denatured solvents. FTIR spectra were collected on a Perkin-Elmer Spectrum 100 FTIR spectrometer using disposable KBr plates. Gel permeation chromatography (GPC) was carried out in THF at 32 °C at 1 mL/min with a Viscotek TDAmax liquid chromatograph (Malvern Instruments, UK) equipped with a programmable autosampler and refractive index detector. AFM images were obtained with a Bruker Dimension Icon atomic force microscope in a tapping mode under ambient conditions. DLS hydrodynamic size and zeta potential measurements were collected on a Malvern Zetasizer Nano-ZS (Malvern Instruments, UK) with a laser wavelength of 633 nm. Cryogenic TEM images were collected on a JEM 1230 microscope (JEOL) at an accelerating voltage of 80 kV. NTA measurements were performed with a NanoSight LM10 (NanoSight, Amesbury, UK) equipped with a sample chamber with a 638 nm laser and a Viton fluoroelastomer O-ring.

Confocal fluorescence images of the cells treated with micelle-SNAs were collected with a Zeiss LSM 510 inverted confocal scanning microscope.

Cell Culture, Flow Cytometry, and Western Blotting. Cells were cultured at 37 °C and 5% CO_2 in DMEM supplemented with 10% FBS and 1% streptomycin/penicillin. For cellular uptake study, HeLa cells were seeded in a 6-well plate 24 h prior to treatment and incubated with micelle-SNAs derived from linear or brush block copolymer structures, respectively. Right before flow cytometry analysis, cells were trypsinized, washed, suspended in 0.5 ml 1× phosphate-buffered saline (PBS) and fixed by addition of 0.5 ml of 3.7% formaldehyde in PBS. The fluorescence intensity from fluorescein (excitation wavelength at 488 nm, emission wavelength at 520 nm) of 10,000 cells was collected using a BD LSR II flow cytometer. For western blotting, C166 cells over-expressing EGFP were transfected with micelle-SNAs (with 0.5, 1, and 2 μM of total DNA in OptiMEM) overnight and further incubate for another 2 days after medium change. Protein lysate with equal amount of total protein were fractionated by 4-20% Precast gradient gel (Bio-Rad). The intact gel was then transferred to a nitrocellulose membrane (Thermo Scientific) and blocked in odyssey blocking buffer (LI-COR Biosciences). Proteins were detected with primary antibodies against actin (1:500) (Santa Cruz Biotechnology), EGFP (1:1000) (Clontech Laboratories Inc) followed by IRDye 680 secondary antibodies (1: 10,000) (LI-COR Biosciences) diluted in PBST containing 5% non-fat milk. The desired bands were visualized using the Odyssey® CLx Infrared Imaging System (LI-COR Biosciences).

Thermal denaturation studies. In binary (2-component) nanoparticle systems, two different sets of SNAs were prepared with different linkers (Type A and Type B) presenting

complementary sticky ends (5´-TTCCTT-3´ and 5´-AAGGAA-3´). In a typical experiment, the DNA linkers were first hybridized to the appropriate particles by combining the linkers and either micelle-SNAs or 15 nm AuNP-SNAs in 0.5 M phosphate buffered saline (PBS) solution, heating the solution to 40 °C for approximately 30 minutes, then slowly cooling to room temperature. This was done to ensure that the maximum number of DNA linkers were hybridized to each particle. The micelle-SNA and AuNP-SNA solutions containing complementary linkers were then combined in the appropriate ratio, resulting in the formation of visible aggregates within minutes. To determine the melting temperature of each aggregate, approximately 1 mL of the suspension was placed into a quartz absorbance cuvette (Hellma) equipped with a magnetic stirrer and loaded into a Cary 5000 UV/Vis spectrophotometer (Agilent). The melting transitions were determined by monitoring the absorbance increase at 260 nm, which occurs upon DNA sticky end dehybridization resulting in aggregate dissociation.

Confocal Microscopy and Immunofluorescence. Cells were seeded in a 35 mm FluoroDish and incubated with fluorescein-labelled DBBC-SNAs (with total DNA 1 μmol) in complete DMEM for different time points. Cells were rinsed with PBS, fixed in 3.7% PFA in PBS for 15 min, and imaged under a Zeiss LSM 510 inverted confocal scanning microscope. The excitation wavelength of fluorescein-labelled DBBC-SNAs was 488 nm, and the corresponding emission filter was 500-550 nm. To track the colocalization of SNAs with intracellular proteins, after incubation with fluorescein-labelled DBBC-SNAs (with total [DNA] = 1 μM) for different time points, cells were rinsed with PBS, fixed with 3.7% PFA in PBS, and permeated with 0.1% Triton X-100 for 3min. After blocking with 5% BSA in PBS for 1 h, cells were stained with a primary antibody against the protein marker of interest at 5 μg/mL (1% BSA in PBS) overnight at 4 °C. After rinses with 0.05% Tween-20 in PBS, cells were stained with an Alexa Fluor 633-

labeled secondary antibody (Invitrogen Alexa Fluor 633 Goat Anti-Rabbit or mouse IgG (H+L) at 1 μg/mL (1% BSA in PBS) for 1 hour at RT. The excitation wavelength of the secondary antibody was 633 nm, and the corresponding emission filter was 660 - 710 nm. The primary antibodies include rabbit against Rab9 (Abcam ab179815), and mouse against LAMP1 (Santa Cruz sc-20011).

Cytotoxicity analysis. The cytotoxicity of the micelle-SNAs was evaluated with a Vybrant® MTT Cell Proliferation Kit (Molecular Probes) following the protocol provided by the manufacturer. Briefly, HeLa cells were seeded in a 96-well plate in 100 μL of media and incubated for 24 h. The cells were then treated with micelle-SNAs (2 μM, total DNA concentration) and the same concentration of single-stranded DNA. Cells without any treatment were used as a control group. At varying lengths of time (1, 2, 3 and 4 days), the media was removed, the cells were washed with PBS buffer (3×) and then incubated with 100 μL fresh culture medium and 10 μL of freshly-made 12 mM MTT solution at 37°C in 5% CO_2 for 4 h. After this step, 100 μL lysis buffer (1 g of SDS in 10 mL of 0.01 M HCl) per well was added. Cells were further incubated overnight and the absorbance was measured at 570 nm using a Multiskan® Spectrum (Thermo Scientific). Each set of conditions was repeated in three independent experiments and the results averaged.

Gel electrophoresis. Agarose gel electrophoresis was used to check the formation of micelle-SNAs either by linear DBC or DNA grafted DBBC. Gels containing 1% agarose (w/w) were run on an FB-SB-710 electrophoresis unit (FisherBiotech) at room temperature in 1×Tris-Borate EDTA (TBE) buffer (50 V, constant voltage). The gels were directly imaged if the DNA was labeled with fluorescein; otherwise, imaging was carried out by ethidium bromide staining and

UV illumination (302 nm). Denaturing PAGE analysis for DBBC conjugates was performed in a gel containing 15% acrylamide (19:1, acrylamide/bisacrylamide), 8 M urea, and 1×TBE buffer. The sample solutions were heated up to 95 °C for 10 minutes for denaturing. Then, the samples were loaded into the gel and run on a SE600 cooled vertical electrophoresis unit (Hoefer, 300 V, constant voltage) with 1×TBE buffer. After electrophoresis, the gels were stained with ethidium bromide and imaged in a gel reader (Alpha Innotech). Under denaturing conditions, the DBBC based micelle-SNAs could not run into the gel and remained in the loading well after electrophoresis (Figure A4.5), indicating that the as-synthesized micelle-SNAs were quite stable in aqueous solution. To demonstrate the DBBC macromolecules contain multiple DNA strands on each polycaprolactone chain, we synthesized DBBC macromolecules with only a few DNA brushes loaded on the polymer chain. By reducing the ratio of DNA/PCL to ~ 3 during the click conjugation reaction, the as-prepared DNA-brush block copolymer was analyzed by denaturing PAGE again. In Figure A4.5, a series of bands can be seen on the gel, which can be attributed to DNA-PCL conjugates with a different number of DNA strands on each polycaprolactone chain. Again, the major product consisted of large micelle structures that accumulated at the bottom of the loading well.

Degradation of DBBC-SNAs. To visualize the amount of nucleic acids released from DBBC-SNAs under different pH conditions an agarose gel experiment was carried out. Briefly, fluorescein-labeled DBBC-SNAs containing 10 μM total DNA were diluted 1:1 with the following buffer solutions (100 mM each): HEPES buffer, pH 5.5; MES buffer, pH 6.0, PBS buffer, pH 7.4. As a control, a sample was prepared with the AuNP functionalized with the same oligonucleotides (anti-EGFP antisense DNA) diluted 1:1 with the buffers described above, respectively. The solutions were allowed to stand at RT for 18, 24, 48, and 72 hours, then

analyzed by agarose gel electrophoresis (1% agarose). The agarose gels were imaged on a Fujifilm FLA-5100 gel imager with a 473 nm laser to visualize the fluorescein-labeled DNA.

Results and Discussion

In a typical DBBC micelle-SNA synthesis (Figure A4.1), α-chloro-ε-caprolactone (α-Cl-εCL) prepared by the Baeyer-Villager oxidation of α-chlorocyclohexanone[214] was employed as a monomer for polymerization. The diblock copolymer poly(α-Cl-εCL-*b*-εCL) was synthesized from the monomer, α-Cl-εCL, and commercially available polycaprolactone (M_W = ~ 14 kDa) as the macro-initiator. The pendant chlorides of the as-synthesized poly(α-Cl-εCL-*b*-εCL) were converted into azides by treatment with sodium azide in DMF overnight at room temperature.[215] ^{1}H NMR spectroscopy was used to characterize the product, and the spectrum suggested the as-synthesized diblock copolymer contained on average 15 N_3 groups, as determined by integration (peak A and G in Figure A4.2). In addition, FT-IR spectroscopy of the azide-containing PCL diblock copolymer showed the characteristic azide band at 2106 cm^{-1} (N=N=N stretch, Figure A4.3).[216] Gel permeation chromatography (GPC) analysis was also consistent with block copolymer formation as evidenced by an increase in molecular weight from ~ 14 to ~ 16 kDa (Figure A4.4). When substituted with azide groups, the poly(α-N_3-εCL-*b*-εCL) exhibited a slightly shorter retention time than that of poly(α-Cl-εCL-*b*-εCL) in the GPC column. Finally, poly(α-N_3-εCL-*b*-εCL) and an excess of cyclooctyne-terminated DNA strands were added to an organic solvent mixture (1:1 DMSO:DMF) to initiate the copper-free click reaction of DNA strands with the azide-modified block, resulting in the formation of the DNA-*g*-PCL-*b*-PCL macromolecule. For comparative purposes, a linear DBC was also

synthesized. Instead of using 14 kDa PCL as the macro-initiator, an azide-terminated poly(ethylene oxide) with 4 ethylene glycol units was employed to initiate the caprolactone polymerization to synthesize a PEO-*b*-PCL block copolymer with a comparable molecular weight (~18 kDa based on ^{1}H NMR integration). Again, click chemistry was used to conjugate DNA to the as-synthesized PEO-*b*-PCL block copolymer and generate the linear DNA-*b*-PEO-*b*-PCL block copolymer. After the DNA conjugation reaction, both the DNA brush block copolymer micelle-SNAs (DBBC-SNAs) and the linear DNA block copolymer micelle-SNAs (LDBC-SNAs) were prepared and purified according to literature protocols used for analogous linear non-biodegradable structures.[29] In this process, excess DNA was removed by an ultrafiltration device with a MWCO of 50 kDa membrane. The amount of DNA conjugated to the polymer was determined by measuring the absorbance of the micelle-SNA solutions at 260 nm. Based on the total amount of polymer used for conjugation, it was determined that an average of 10 DNA strands were successfully conjugated onto each polymer chain. Moreover, polyacrylamide gel electrophoresis, under denaturing conditions, was used to analyze the resulting DNA-*g*-PCL-*b*-PCL macromolecules. The bands representing DBBC conjugates containing multiple DNA strands can be clearly identified on the gel when excess DNA was used for the conjugation (Figure A4.5).

SNA	**Sequence (5' → 3')**
Micelle-SNA:EGFP	DBCO-$(EG)_4$-(spacer 18)$_x$- CGGACACGCTGAACTTGTGG
Scrambled antisense DNA	DBCO-$(EG)_4$-(spacer 18)$_x$- CGGATACGCTGATCTTGTGG
Fluorescein-SNA	DBCO-$(EG)_4$-(spacer 18)$_x$- CGGACACGCTGAACTTGTGG-Fl
AuNP-SNA	Propylthiol-(spacer 18)$_5$- ACA TCC ACG TAG TCT TAG
Linker Strand-1 (hybridized with AuNP-SNA)	AAGGAA T CTA AGA CTA CGT GGA TGT

Linker Strand-2 (hybridized with micelle-SNA)	TTCCTT T CCA CAA GTT CAG CGT GTC CG

Table 4.1. Oligonucleotide sequences used in this study. Fl = fluorescein; DBCO = dibenzocyclooctyne; EG = ethylene glycol. "Spacer 18" denotes a phospodiester followed by 6 ethlyene glycol units in the DNA backbone. x=0 when the DNA was used in the formation of linear DNA-*b*-PEO-*b*-PCL, x=1 when the DNA was used in the formation of DNA-*g*-PCL-*b*-PCL.

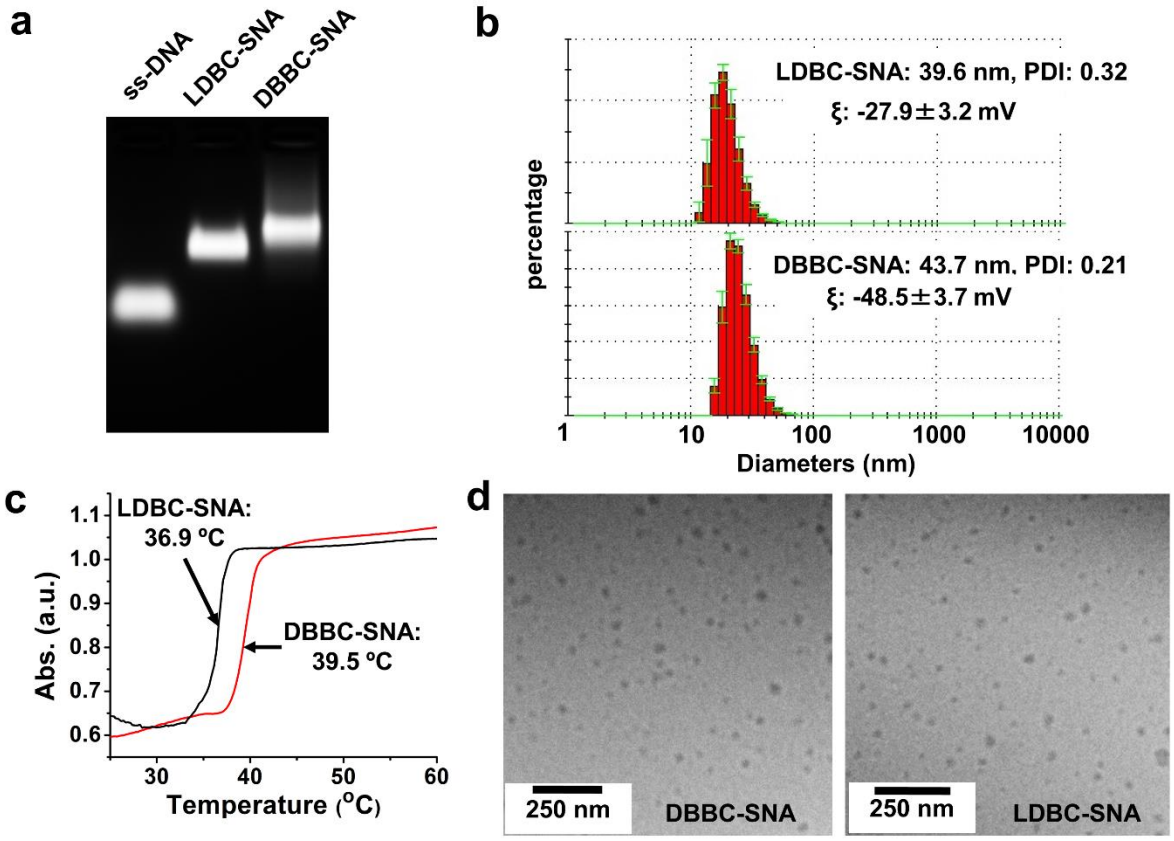

Figure 4.1. Characterization of as-synthesized polycaprolactone-based micelle-SNAs. (a) 1% agarose gel electrophoresis; nucleic acids were stained with ethidium bromide; (b) A typical DLS measurement of micelle-SNAs derived from (top) linear and (bottom) brush block copolymer structures; (c) Melting transition behaviour for micelle-SNAs hybridized to complementary 15 nm AuNP-SNAs; (black trace) micelle-SNAs made from linear structures and (red trace) micelles made from the brush architecture; (d) Cryogenic TEM images of micelle-SNAs derived from brush block copolymer. Both DBBC-SNA and LDBC-SNA nanoparticles remain intact under cryogenic conditions and are relatively uniform in size with diameters ~ 30-50 nm.

With purified samples, multiple techniques were employed to characterize these two polycaprolactone-based SNAs (Figure 4.1). Gel electrophoresis (1% agarose gel, Figure 1a) showed a single major band for each sample on the gel image, indicating the micelle-SNAs have

a narrow size distribution. Compared to unmodified DNA of the same sequence, the electrophoretic mobilities of the micelle-SNAs are greatly decreased, consistent with the significant difference in size and overall charge. Notably, the electrophoretic mobility of SNA made from the brush architecture is slightly lower than that of one made from the linear structure, indicating that the former SNA is slightly larger. The size distributions of the micelle-SNAs were also probed by dynamic light scattering (DLS), which indicated an average hydrodynamic diameter of 44 nm for the SNAs derived from the brush architecture and 40 nm for ones derived from the linear architecture (Figure 4.1b), consistent with the gel analysis. Meanwhile, zeta potential analysis gave values of -48.5 ± 3.7 mV and -27.9 ± 3.2 mV, respectively (Figure A4.6), consistent with the micelle derived from the brush architecture having a higher density of DNA. Furthermore, the micelle-SNAs were cast on mica and imaged by atomic force microscopy in dry form (Figures A4.7); in both cases, spherical structures were readily apparent. To visualize the morphology of the micelle-SNAs in an environment closer to the one in which they are prepared, cryogenic transmission electron microscopy (Cryo-TEM) was used (Figure 4.1d). In this method, a very thin layer of micelle-SNA-containing solution was quickly frozen and directly imaged. Cryo-TEM imaging avoids dehydration-induced artifacts, allowing the fully intact nanoparticles to be visualized. Indeed, round 30-50 nm diameter particles of both DBBC-SNAs and LDBC-SNAs were observed, which are consistent with the DLS size data.

Since the density of DNA on the particle surface is a key factor that leads to its SNA-like properties, it is important to determine nucleic acid surface coverage. In contrast with conventional AuNP-SNAs, where particle concentration can be easily determined by measuring the plasmon resonance peak associated with AuNPs, it is difficult to directly determine the

micelle particle concentration using spectrophotometric methods. Alternatively, we used nanoparticle tracking analysis (NTA)[217-218] to determine the particle concentrations for micelle-SNAs (see details in *Appendix*, Figure A4.8 and Table A4.1). Importantly, the DNA loading for the brush block copolymer based micelle-SNAs (302 strands/particle; 22.2 pmol/cm^2) was significantly higher than the linear block copolymer based micelle-SNA (190 strands/particle; 15.6 pmol/cm^2), which is comparable to AuNP-based SNAs of similar sizes (300 strands/particle for 30 nm AuNP cores; corresponding to a DNA density of 17.6 pmol/cm^2).[53] Another important feature of SNA structures is their cooperative hybridization properties, arising from the association of multiple DNA strands between each particle. This results in a sharp melting transition during the thermal denaturation of hybridized complementary particles.[29, 51] Generally, higher DNA loading results in higher melting temperatures and sharper transitions under comparable conditions. The thermal denaturation of micelle-SNAs was carried out by hybridizing both brush and linear block copolymer based micelle-SNAs with AuNP-SNAs containing complementary sticky ends, respectively, and then monitoring the absorbance change at 260 nm with gradual heating (Figure 4.1c and Figure A4.9). Around the melting temperature, extinction dramatically increased due to the hyperchromic effect of cooperative DNA dehybridization. As shown in Figure 1c, the melting curves for both types of micelle-SNAs when hybridized with AuNP-SNAs were sharp and elevated, with the T_m of the DBBC-based micelle-SNA (39.5 ˚C) being almost 3 degrees higher than the linear DBC-based micelle-SNA (36.9 ˚C). The higher melting temperature for the DBBC-based micelle-SNA is consistent with a structure with a higher surface density of nucleic acids.[219]

With well-characterized micelle-SNAs in hand, we evaluated their biological function with *in vitro* cell uptake studies. Both micelle-SNAs exhibit the ability to enter cells without the

assistance of cationic transfection reagents, but with different efficiencies. Confocal microscopy revealed that fluorescein-labelled micelle-SNAs (1 μM total DNA) enter HeLa cells after 16 h of incubation. Notably, the green fluorescence from micelle-SNAs consisting of brush block copolymers was significantly more intense than that of the linear block copolymer based micelle-SNAs (Figure 4.2d,e), indicating more efficient uptake of the former as opposed to the latter. This result was also confirmed by quantifying the fluorescence intensity of the cell population using flow cytometry.

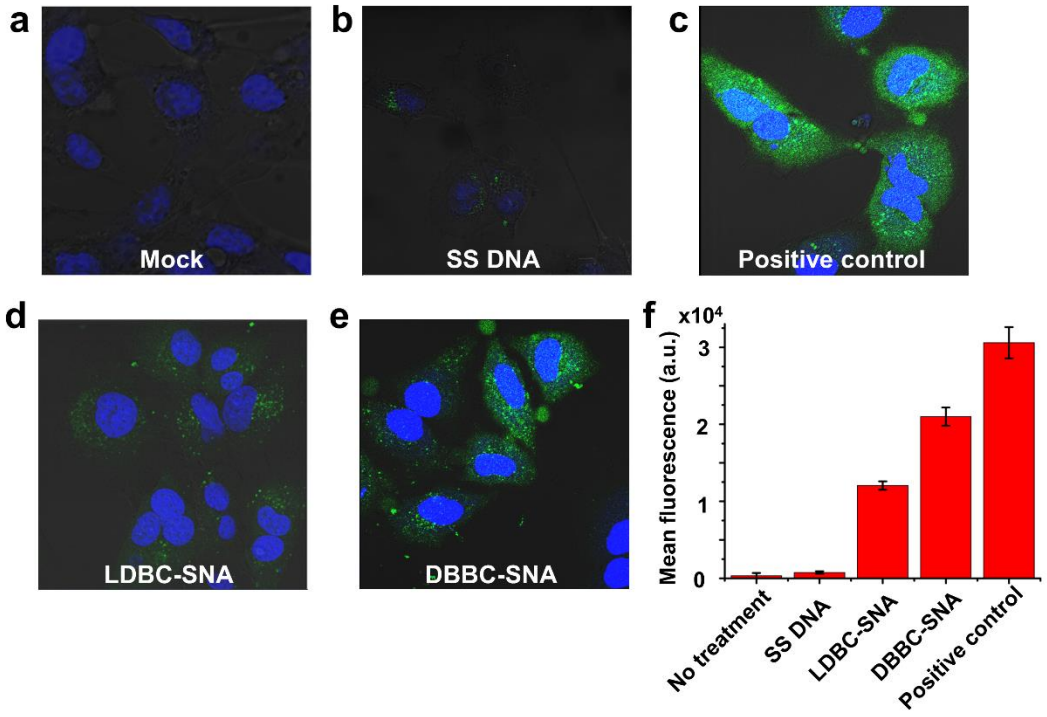

Figure 4.2. Cellular uptake of micelle-SNAs. (a-e) Fluorescence micrograph of HeLa cells incubated with different forms of nucleic acids at a total DNA concentration of 1 μM for 16 h. DNA strands were labelled at the 5'-end with fluorescein and the dye molecules are located at the outside terminus of the micelle-SNA structure. a) negative control, cells without DNA incubation; b) single stranded fluorescein-labelled DNA (Fluo-DNA); c) positive control, single stranded Fluo-DNA transfected with Lipofectamine® 2000; d) micelle-SNAs derived from linear block copolymer structures; e) micelle-SNAs derived from brush block copolymer structures. In the fluorescence images, micelle-SNAs assembled from the brush block copolymer show significantly higher uptake compared to those derived from the linear analog or component single stranded DNA; (f) Fluorescence-activated cell sorting (FACS) analysis of the cells when incubated with different forms of nucleic acids. FACS data also confirm the brush block copolymer based micelle-SNA has higher cell uptake efficiency than that of the linear block copolymer based micelle-SNA. Single stranded DNA and DNA transfected by conventional Lipofectamine® 2000 were used as controls.

Although incubated with equal amounts of total DNA, the mean fluorescence intensity of cells treated with brush block copolymer based micelle-SNAs was almost twice that of linear block copolymer based micelle-SNAs (Figure 2f), presumably due to their higher surface density of nucleic acids. Compared to the positive control which utilized Lipofectamine® 2000 as the transfection agent, DBBC-SNAs show slightly lower but comparable transfection efficiency without any co-carrier. We further studied the intracellular location of DBBC-SNAs as a function of incubation time under conditions where HeLa cells were continuously incubated with fluorescein-labelled micelle-SNAs (1 μM total DNA). AuNP SNAs traffic through the endocytic pathway into late endosomes and reside there without accumulating in lysosomes.[210] We hypothesized that the DBBC-SNAs follow the same route upon cellular entry due to their similar architecture. In these experiments, the DBBC-SNAs carry a green fluorophore (fluorescein), and the cells are stained with a complementary Alexa dye-labeled marker of interest (red). As shown in Figure 4.3, strong colocalization of SNAs with Rab9 (a protein which preferentially localizes in late endosomes) was observed after 6 h of incubation, and colocalization persisted 24 h post-incubation. Importantly, we did not observe appreciable colocalization between the fluorescent signals of DBBC-SNAs and markers for lysosomes (LAMP-1) over a 24 h period of time. From these data, we conclude that SNAs primarily remain inside late endosomes and do not migrate beyond this point to the lysosome. These observations confirm that within a typical cell doubling time (23-24 h for HeLa cells), the micelle-SNAs likely employ the same intracellular trafficking pathway as AuNP-based SNAs.

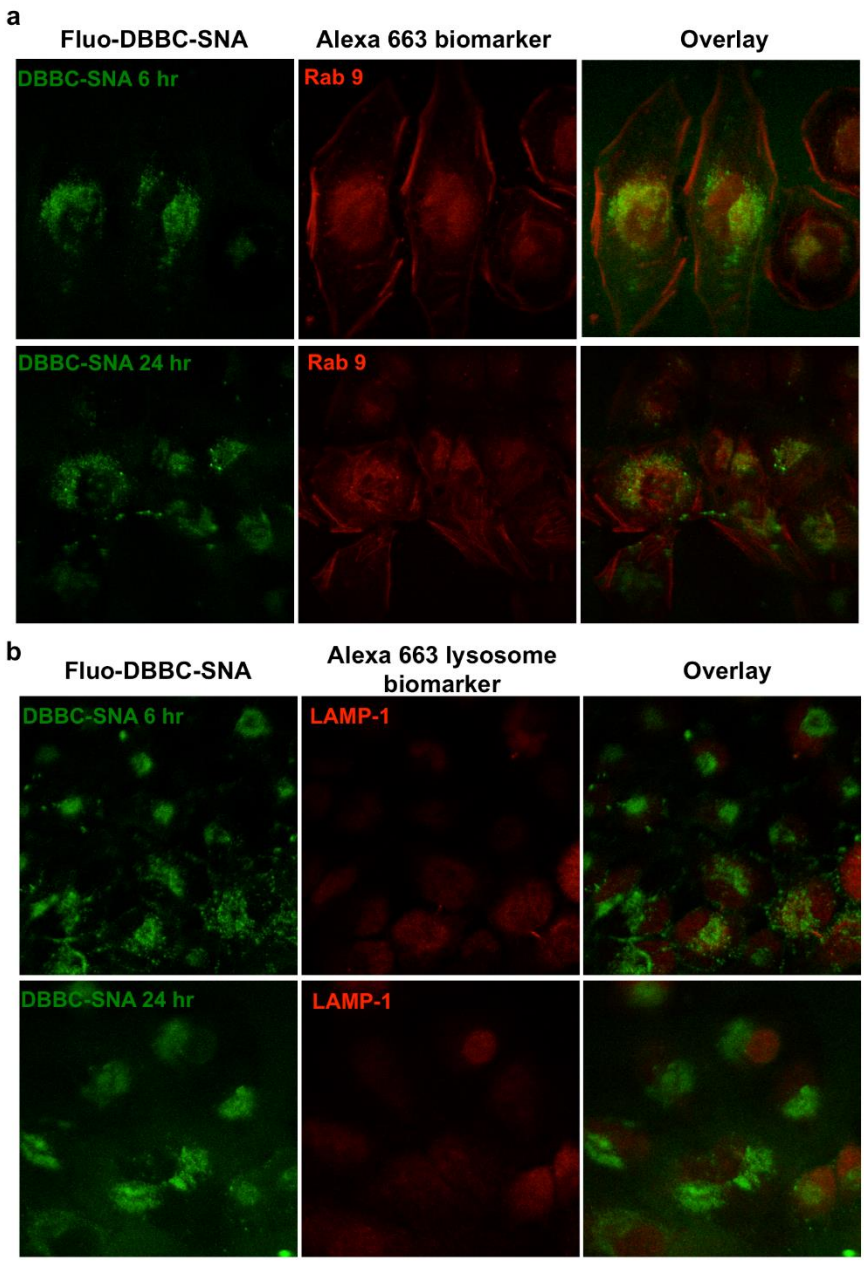

Figure 4.3. Confocal microscopy of fluorescein-labelled DBBC-SNA and immunofluorescence staining of organelle markers (red, labelled by Alexa Fluor 663). Biomarkers are Rab9 (for late endosomes) and LAMP-1 (for lysosomes). Note that most DBBC-SNAs colocalize with late endosomes during the incubation in HeLa cells. There is no significant colocalization of DBBC-SNAs with lysosomes, which is consistent with the behaviour of AuNP-SNAs.

We further tested the intracellular gene regulation capacity of the DBBC-based micelle-SNAs in specialty C166 mouse endothelial cells over-expressing enhanced Green Fluorescent Protein (eGFP). The DNA strands on the micelle-SNAs were synthesized with an antisense

sequence against the eGFP mRNA. After transfection and further incubation for 48 h, eGFP knockdown was readily apparent by fluorescence microscopy (Figure 4.4a,b). Importantly, the quantification of eGFP protein expression *via* western blot shows a concomitant ~ 52% reduction in eGFP expression (Figure 4.4c), demonstrating that the micelle-SNA can effectively bind the cytosolic mRNA target and alter the expression of its associated protein. Compared to LDBC-SNAs under the same conditions, DBBC-SNAs are more effective at regulating gene expression *via* the antisense mechanism (Figure 4.4d).

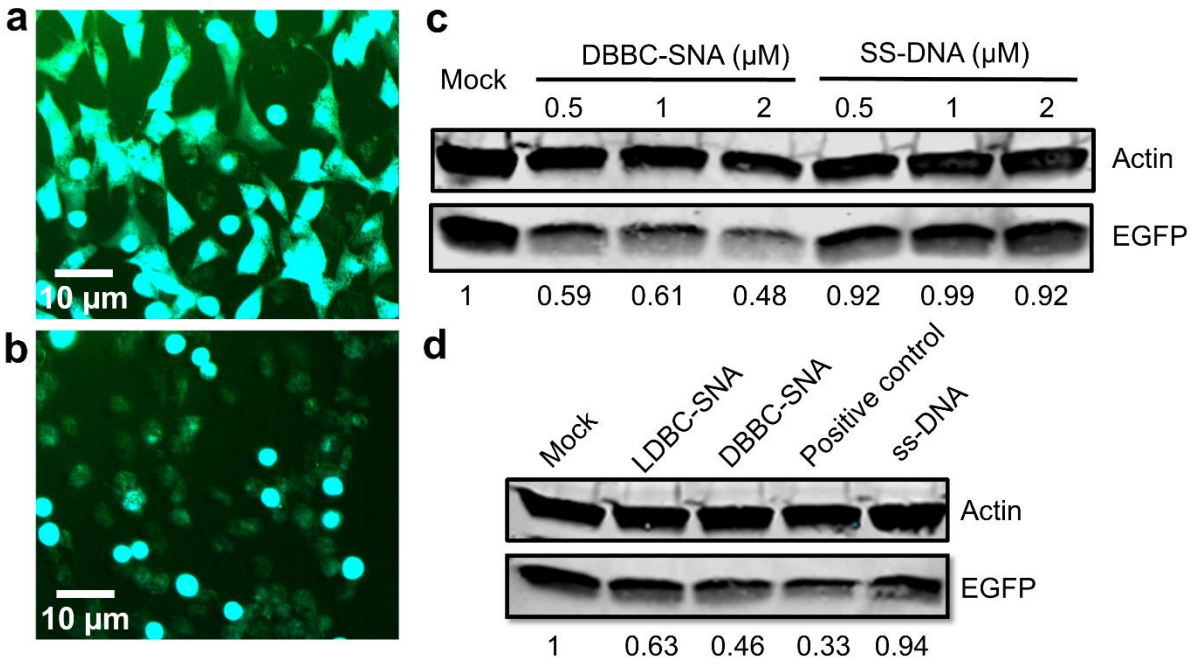

Figure 4.4. Gene regulation by DBBC-based micelle-SNAs. (a) Fluorescence micrograph of C166 mouse endothelial cells that highly express the EGFP protein before DBBC-based micelle-SNA treatment. (b) Fluorescence micrograph of C166 mouse endothelial cells after DBBC-SNA treatment. The green fluorescence was significantly suppressed due to the EGFP gene knockdown. The micelle-SNAs were equipped with anti-EGFP sequence and the cells were cultured for another 2 days after SNA transfection. (c) Western blotting of EGFP expression in C166 cells after treatment with anti-EGFP DBBC-based micelle-SNAs and single stranded DNA samples under various total DNA concentrations. (d) Western blotting of EGFP expression in C166 cells after treatment with anti-EGFP DBBC-SNAs and control samples under total DNA concentrations of 2 μM. The positive control sample was antisense DNA transfected by conventional Lipofectamine® 2000. Actin was used as an internal reference.

When the DBBC-based micelle-SNAs are modified with a scrambled DNA sequence, EGFP expression does not change at all concentrations tested (0.5-2 μM of total DNA), indicating the gene knockdown effect is sequence-specific (Figure A4.10). To further validate that our new constructs may have significant potential for biomedical applications, we tested the biodegradation and cellular toxicity of DBBC-SNAs. During the transfection and intracellular trafficking process, SNAs will encounter quite different chemical environments, such as varied pH values and ionic strength in serum, endosomes, and lysosomes. This may cause the PCL core of the micelle particles to degrade at a different rate depending on their location.

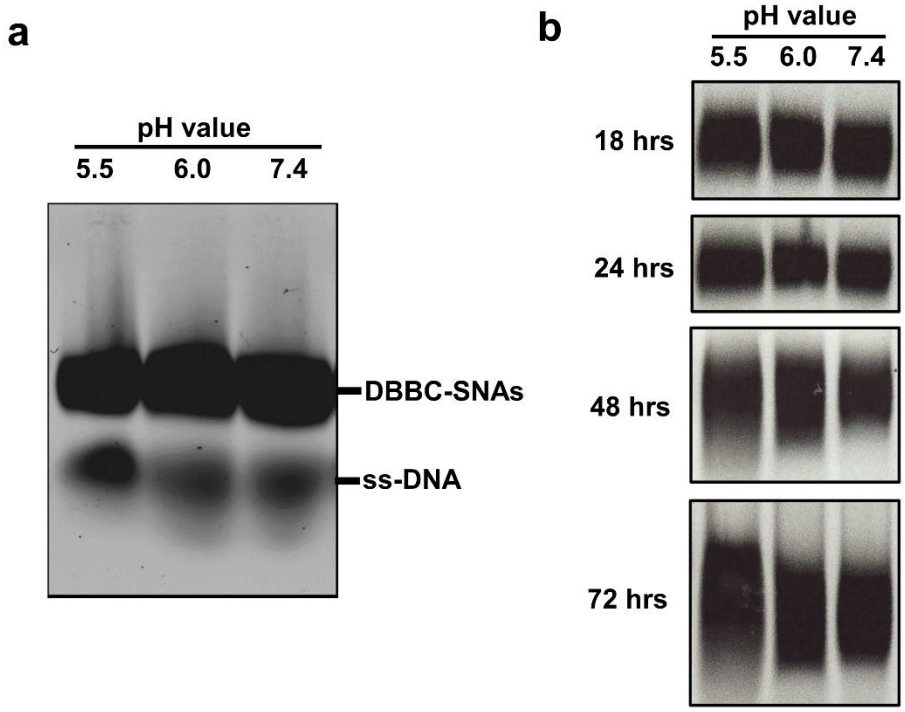

Figure 4.5. The pH-dependent degradation of DBBC-based micelle-SNAs. Samples were incubated in 50 mM MES buffer (pH 5.5), 50 mM HEPES buffer (pH 6.0), or 1X PBS (pH 7.4). Agarose gel electrophoresis was used to monitor the degradation process. a) Degradation of DBBC-based micelle-SNAs after 24 hour incubation under different pH buffer conditions. Note that a significant amount of single stranded DNA can be observed in the gel image; b) the mobility and shape of the DBBC-based SNA bands over incubation time under different buffer conditions. In the first 24 hours, the SNA bands look relatively sharp. However, as the incubation time increases, the bands become smeared and diffuse, indicating the gradual degradation of the entire micellar structures. Note that the micelles held at lower pH (5.5) suffer considerably more degradation after 72 hours.

To evaluate their biodegradability, we incubated the DBBC-SNAs in buffers of varied pH values to mimic different intracellular environments. As shown by agarose gel electrophoresis, component single-stranded DNA appeared after 24 h incubation, indicating the degradation of micelle-SNAs and shedding of DNA oligonucleotides (Figure 4.5a). Meanwhile, gel bands representing the DBBC-SNAs became smeared and diffused with increased incubation time (Figure 4.5b). Notably, micelle-SNAs degraded faster in lower pH buffer conditions, pointing to the possibility of their faster degradation when trafficking through intracellular vesicles with low pH, such as the endosomes.[210] The cellular toxicity of DBBC-based micelle-SNAs was analyzed using the standard MTT assay (Figure 4.6).[220]

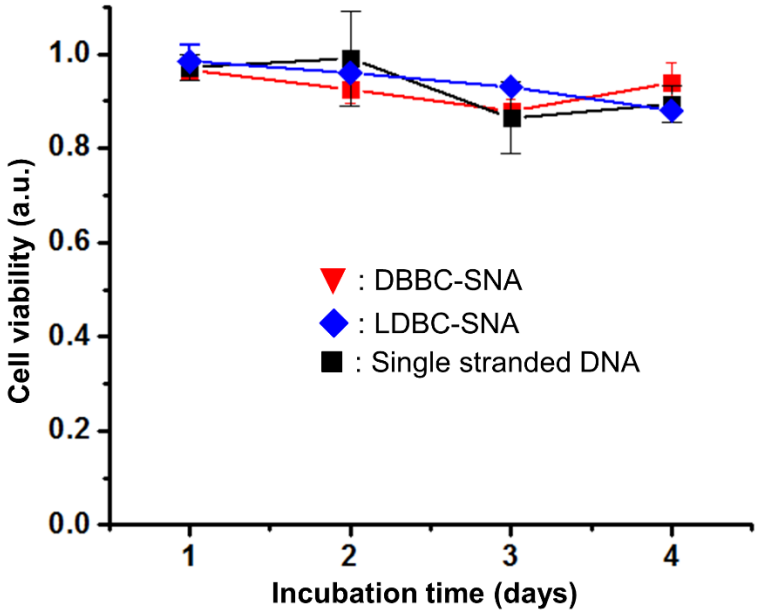

Figure 4.6. Cellular toxicity of DBBC-based micelle-SNAs analyzed by a standard MTT assay. Cells treated with DBBC-SNAs (red), LDBC-SNAs (blue), and single stranded DNA (black) at the same total DNA concentration (2 μM). Viable cells with active metabolism convert MTT into a purple colored formazan product with an absorbance maximum near 570 nm, and cell viability was quantified by normalization of the absorbance at 570 nm to non-treated cells. Error bars represent the standard deviation of absorbance at 570 nm from 3 independent wells of cells in a 96-well plate.

Even with an incubation time of up to 4 days, we found that cell viability remained essentially unchanged. This confirms that the as-synthesized micelle-SNAs with biocompatible and biodegradable polycaprolactone cores do not have measurable cellular toxicity under these conditions.

Conclusions. We have developed a novel strategy to construct a DNA-brush block copolymer based micelle-SNA with increased DNA surface density, which endows the new construct with properties similar to existing AuNP SNAs. Compared to the micelle-SNAs constructed from linear block copolymers, the DBBC-based micelle-SNAs exhibit a higher surface density of nucleic acids, a more negatively charged surface, a higher melting temperature, a more cooperative thermal denaturation profile, and more effective transfection agent-free cellular uptake. Importantly, the micelle-SNAs derived from the DNA-brush block copolymer show effective target gene knockdown *in vitro*.

It is worthwhile to note that since the polymer core can gradually degrade under physiological conditions due to acid-catalyzed or esterase-catalyzed cleavage of the ester backbone bonds,[221] these constructs open new avenues towards the controllable, continuous release of nucleic acids as regulatory agents for intracellular biological processes. Generally, in addition to PCL, a wide variety of polyesters, such as PLA[222] and PLGA[223] can be employed to initiate polymerization and then form DBBC-based SNAs consisting of different types of polyester cores. As such, the rate of particle degradation and nucleic acid release may be tuned by judicious monomer selection. We anticipate that this synthetic approach can be extended to a wide variety of polyesters to generate a new class of nanostructured materials with highly tailorable properties for various nucleic-acid based therapeutic approaches. In addition, this study further demonstrates that high surface density of nucleic acids on SNAs is directly correlated

with their cooperative binding behavior and cellular uptake, and that the self-assembled micelle SNAs undergo the same endocytotic intracellular trafficking pathway as classical AuNP SNAs. These results point to a shared recognition and uptake mechanism among all SNAs regardless of core composition.

Chapter 5

CCR5 pre-targeted nanosystem for breast cancer imaging and therapy based on *in vivo* nucleic acid hybridization of spherical nucleic acid nanoclusters

Abstract

Positron emission tomography (PET) probes for the sensitive and specific imaging of tumor tissue, relying on nucleic acid hybridization-based pre-targeting, were synthesized and evaluated in a mouse breast cancer model. Ultrasmall gold nanoclusters (< 3 nm) functionalized with a dense shell of phosphorodiamidate morpholino (PMO) oligonucleotides and targeting peptides were fabricated and their biodistribution was studied by alloying the gold core with ^{64}Cu. We hypothesized that the polyvalent nature of the spherical nucleic acid nanoclusters (AuNC SNAs) would enable faster and more specific pre-targeting than linear nucleic acid hybridization. The ability of these nanoclusters to capture and release a target oligonucleotide was evaluated *in vitro* and the kinetics of the target capture were determined. Injection of rodents with the AuNC SNAs followed by a complementary ^{64}Cu-radiolabeled target oligonucleotide demonstrated specific localization of the probe at the tumor site after accumulation of the nanoclusters. The sequence-specificity of the capture process was also investigated. Studies are ongoing to assess the relative tumor accumulation of hybridized ^{64}Cu-oligo compared to direct-targeted ^{64}CuAuNC SNAs and their targeting efficiency.

Introduction

Imaging probes for sensitive and specific detection of biomarkers specifically expressed during breast cancer (BC) progression to determine the tumor burden, rate of progression, and metastatic sites are extremely important in clinical oncology.[224-226] More importantly, the accurate determination of these biomarkers may help to design targeted therapeutic intervention to improve the treatment outcome of patients. Of the probes developed for BC imaging, positron emission tomography (PET) probes, especially PET radionuclide-labeled nanoparticles have been widely used for both pre-clinical and clinical investigations due to their enhanced targeting specificity, imaging sensitivity, and optimal target-to-background (T/B) contrast ratio.[227-231] However, non-specific tumor retention of nanoprobes may interfere with accurate quantitative measurements of the targets for precise diagnosis and specific treatment, especially for early stage tumors and metastases.

Recently, the Liu laboratory developed an ultra-small gold nanocluster alloyed with ^{64}Cu (^{64}CuAuNC) for PET imaging of BC that shows low non-specific tumor retention and significant clearance from non-target tissues *in vivo*.[232] This is a critical advance given the capability of these ^{64}CuAuNCs to afford extended blood retention, radiolabel stability, and multivalency for improved targeting efficiency. Of the targets assessed as prognostic markers for BC, the chemokine receptor CCR5, is of interest due to the important role of CCL5/CCR5 axis in promoting tumor progression and metastases and the overexpression of CCR5 in tumors compared to normal breast tissue.[233-241] For accurate detection of biomarkers expressed in tumors, the pre-targeting strategy is a promising method to improve detection efficiency and T/B contrast ratio compared to the direct targeting strategy. Pre-targeting involves the delivery of two

components: a non-radioactive tumor-seeking antibody, peptide, or particle, and subsequent late binding radiolabeled molecules that specifically interact with the pre-targeting moiety associated with the tumor.[242-244] Of the pre-targeted systems, the nucleic acid hybridization strategy is attractive due to the fast hybridization kinetics, duplex stability, programmability, and reversibility.[245] Gold was chosen as the core material for the initial development of this system due to the ease of rapidly prototyping different nanocluster designs using commercially-available thiolated oligonucleotides, polymers, and heterobifunctional linkers.

Numerous pre-targeting systems for *in vivo* PET imaging have been described based on both irreversible bioorthogonal "click" reactions as well as hybridization of nucleic acids. Irreversible pre-targeting reactions demonstrated to work *in vivo* include strained cyclooctyne-azide cycloaddition and inverse electron-demand Diels-Alder cycloaddition.[246-247] Nucleic acid hybridization strategies have been investigated employing linear DNA, locked nucleic acid (LNA), peptide nucleic acid (PNA), PMOs, and PMO dendrimers.[248-252] We hypothesized the efficiency and specificity of the pre-targeting approach could be increased by introducing the pre-targeted oligonucleotides in the form of polyvalent spherical nucleic acid (SNA) nanoclusters. SNAs hybridize with target oligonucleotides much more rapidly than their linear counterparts and form more thermodynamically stable duplexes.[253-254] In addition, presentation of a tumor-targeting ligand on the SNA surface allows for multivalent interaction with the disease-related receptor.[255]

Herein, we report a CCR5 pre-targeted nanosystem using nonradioactive spherical nucleic acid nanoclusters (AuNC SNAs) with multiple copies of PEG-DAPTA and phosphorodiamidate morpholino (PMO) oligonucleotides conjugated to the surface (DAPTA-PMO SNAs). PMO oligonucleotides were found to be far superior to conventional DNA

oligonucleotides for surface functionalization of the SNAs due to their enhanced blood circulation time. After the clearance of non-specifically retained AuNC SNAs, the SNAs bound on the surface of tumor cells can be illuminated following the administration of a complementary oligo radiolabeled with ^{64}Cu through *in vivo* nucleic acid hybridization. We investigate the *in vitro* capture and release kinetics of this nanosystem and demonstrate the feasibility of this approach under physiological conditions. Further, we report the imaging of tumor tissue in a mouse breast cancer model with this pre-targeted nanosystem. While the focus of this research is on BC, this strategy potentially has wide applicability across a variety of diseases and will enable not only imaging, but tumor treatment with either cytotoxic drugs or therapeutic radionuclides. We further demonstrate the sequence-specificity of *in vivo* nucleic acid hybridization.

Experimental Procuedures

Materials and methods. DBCO-Cy5 was purchased from AAT Bioquest (Sunnyvale, CA). All reagents for oligonucleotide synthesis were purchased from Glen Research (Sterling, VA) or ChemGenes (Wilmington, MA) and used according to manufacturer instructions. Custom phosphorodiamidate morpholino oligonucleotides were synthesized by Gene Tools (Philomath, OR). 1,4,7,10-tetraazacyclododecane-1,4,7,10-tetraacetic acid (DOTA)-NHS ester was purchased from Macrocyclics (Plano, TX). $^{64}CuCl_2$ was produced on-site at the the Mallinckrodt Institute of Radiology (MIR) cyclotron facility and received as a stock solution in 0.1N HCl. Thiolated poly(ethylene glycol) derivatives were purchased from Creative PEGWorks (Chapel Hill, NC). Thiol-PEG5K-NHS ester was purchased from Nanocs (Boston, MA). Buffer solutions and cell culture media were purchased from Gibco (Gaithersburg, MD). D-Ala-Peptide-T-amide was custom-synthesized by CPC Scientific (Sunnyvale, CA). All other reagents were purchased

from Sigma-Aldrich (St. Louis, MO) and used as received. UV-Vis spectra were collected on a Cary 60 spectrometer in quartz cuvettes with a path length of 1 cm. TEM images were collected on a JEOL JEM-1400Plus transmission electron microscope. Dynamic light scattering (DLS) and zeta potential measurements were collected on a Zetasizer Nano ZS (Malvern Instruments Ltd). MALDI spectra were collected on an Applied Biosystems Voyager-DE STR MALDI-TOF spectrometer.

Synthesis of DNA and RNA conjugates. DNA and 2´-OMe-RNA oligonucleotides were synthesized on a MerMade MM12 automated oligonucleotide synthesizer according to standard manufacturer protocols. OMe-RNA oligonucleotides were modified at the 5´ terminus with commercial monomethoxytrityl (MMT)-protected alkylamino, cyanine dye (Cy5), and PEG modifiers from Glen Research following manufacturer instructions. The OMe-RNA oligonucleotides were purified by reverse-phase HPLC on C18-coated silica with triethylammonium acetate buffer (0.03M, pH 7.0) and acetonitrile as the mobile phase ramping from 0-75% acetonitrile over 45 minutes. Fractions were pooled, lyophilized, and deprotected by treatment with 20% acetic acid for 1 hour at room temperature. The aqueous layer was washed 3x with ethyl acetate, lyophilized again, and the resulting dried RNA characterized by UV-Vis and MALDI-TOF. Amino-modified OMe-RNA was reacted with an excess of DOTA-NHS ester in a mixture of 9:1 DMSO/4-methylmorpholine for 16 hours at room temperature. The reaction mixture was diluted with water and the crude product purified by ultrafiltration (3 kDa MWCO Amicon Ultra-4, Millipore) spinning at 7500 x g for 30 minutes. The retained OMe-RNA was suspended in 0.5 mL PBS buffer and purified once more by eluting through a NAP-5 desalting column (GE Life Sciences). Fractions were collected and pooled and the resulting DOTA-modified OMe-RNA characterized by MALDI-TOF spectroscopy.

Synthesis of Cy5-PMO-OPSS. 5´-azide and 3´-ortho-pyridyl disulfide (OPSS) modified PMO oligonucleotide was purchased from Gene Tools. A stock solution of 1 mg DBCO-Cy5 in 1 mL anhydrous DMSO was prepared (~825 nmole/mL), and 80 µL of DBCO-Cy5 stock solution was mixed with 50 µL of PMO stock solution (1 mM in H_2O). The mixture was shaken at 37° C overnight and diluted to 0.5 mL with 1X PBS. The crude reaction mixture was purified by size exclusion chromatography (NAP-5 column equilibrated in 1X PBS) to remove excess Cy5 and fractions collected and analyzed for purity by UV-Vis and MALDI-TOF.

Radiolabeling of OMe-RNA-DOTA conjugates. In a typical experiment, 1 nanomole of OMe-RNA-DOTA conjugate was mixed with 0.5-1 mCi of $^{64}CuCl_2$ buffered with 0.1M NH_4OAc (pH 5.5) for 45 minutes at 45° C. The mixture was purified by repeated ultrafiltration (3 kDa MWCO) to remove unbound $^{64}CuCl_2$ and a small portion of the retentate (3 µL) analyzed by radio-iTLC on silica gel with 1:1 10% NH_4OAc buffer (pH 5.5) and methanol as the mobile phase. Radiochemical purity was assessed by integration of the TLC trace and the radiochemical yield and specific activity determined by the relative activity in the retentate vs the filtrate post-purification.

Synthesis of Thiol-PEG5K-DAPTA. To a 1.5 mL centrifuge tube was added 0.1 mL anhydrous DMSO, 19.3 mg of thiol-PEG5K-NHS (.004 mmol, 1 equiv.) and 10 mg of D-Ala-Peptide-T-amide (DAPTA) (0.006 mmol, 1.5 equiv.) and the mixture shaken overnight at 37° C. Afterwards, the reaction mixture was diluted to 0.5 mL in 1X PBS and purified by gel filtration through a NAP-5 column (GE Healthcare Life Sciences) equilibrated with 1X PBS to remove excess DAPTA. Fractions were collected and pooled and the presence of conjugated DAPTA was established by UV-Vis ($\lambda_{max} \approx 280$ nm). The starting material and product were both analyzed by MALDI-TOF to confirm conjugation of DAPTA. The molecular weight distribution

of the starting material showed a maximum at 4830 Da, whereas the MW distribution of the product showed a maximum at 5776 Da, an overall shift consistent with the molecular weight of DAPTA appended to the polymer (MW = 856.9 g/mol).

Synthesis of ^{64}CuAuNC PMO SNAs. To a 20 mL glass vial with a magnetic stirrer was added 2 mL of Milli-Q H_2O, 8.6 µL of $HAuCl_4$ stock solution (58 mM), 20 µL of IGEPAL CA-630 solution (1% w/v in H_2O), 50 µL PMO- OPSS stock solution (1 mM in H_2O) and an equal amount of PEG5K-thiol stock solution (1 mM in H_2O). Finally, 1 mCi of ^{64}CuCl buffered in 0.1M NH_4OAc (pH 5.5, 10 µCi/µL) was added and the reactants equilibrated with stirring for 30 min at room temperature. For the synthesis of non-radioactive SNAs, the ^{64}CuCl addition step was omitted. Next, 0.4 mL of sodium borohydride solution (40 mM in H_2O) was added, causing the reaction mixture to turn a deep maroon color. The reaction mixture was stirred overnight followed by the addition of a second portion of sodium borohydride after 16 hours to ensure complete incorporation of ^{64}Cu. The particles were purified by ultrafiltration (Amicon Ultra-15 30 kDa MWCO) with 3 x 4 mL washes of Milli-Q H_2O spinning at 5000 x g. The retained particles were suspended in 1 mL H_2O and radiochemical purity was assessed by radio-iTLC on silica gel with 1:1 10% NH_4OAc (pH 5.5) and methanol as eluent and subsequent integration of the region(s) of interest. (Figure A5.2) For synthesis of ^{64}CuAuNC DNA SNAs, the same procedure was followed as described for PMO SNAs, but instead, 3´-thiolated DNA was employed and the reaction mixture treated with 10 × 20 µL portions of 5M NaCl over ~ 12 h.

Oligonucleotide capture studies. Non-radioactive PMO AuNC SNAs were synthesized as described above with a 1:1 ratio of PMO/PEG5K. For each batch of SNA, the extinction coefficient of the clusters at 520 nm was determined by UV-Vis and ICP-MS (Figure A5.3). Estimation of cluster core size by TEM was used to calculate the average number of Au atoms

per cluster according to the equation: atoms/cluster = $(r_{cluster}/r_{atom})^3$. The calculated gold concentration in a sample of AuNCs was divided by the calculated number of gold atoms per cluster to give the concentration of clusters. In a typical synthesis, the number of gold atoms per cluster was approximately 700-800. Binding rates were determined using fluorescence measurements collected on an ISS K2 spectrometer with an excitation wavelength of 633 nm and an emission wavelength of 670 nm. For each binding curve, a solution of 500 pM Cy5-labeled antisense 2´-OMe-RNA in 1 mL 1X PBS was prepared in a polymethacrylate cuvette and allowed to warm to 37° C using the internal temperature controller. Then, the OMe-RNA solution was mixed with AuNCs and the change in fluorescence over time was measured in 2 second increments. Bimolecular rate constants were derived by curve-fitting the acquired data for each nanocluster concentration tested (1, 2.5, 5, 10 and 25 nM) in triplicate.

Cellular uptake and surface association studies. 4T1-Luc breast cancer cells (ATCC, Manassas, VA) were suspended in 1.5 mL microcentrifuge tubes containing Gibco DMEM phenol red-free media supplemented with 10% fetal bovine serum at a density of $5.0 \cdot 10^5$ cells/tube. Cells were treated in triplicate with Cy5-labeled AuNC s at a total AuNC concentration of 4 nM per group and incubated for 24 hours. The media was removed and the cell pellets were washed with 3 × 1 mL portions of 1X PBS, resuspended in PBS by vigorous pipetting, then transferred to polystyrene tubes cooled in an ice bath for flow cytometry analysis. The relative fluorescence intensity of each group of cells was measured exciting at a wavelength of 633 nm on a BD FACSCalibur flow cytometer and the mean fluorescence intensity was calculated in triplicate. For cellular surface association studies, the same treatment protocol was followed, but the washed cell pellets were instead incubated with NaCN (10 mM in 1 mL PBS) for 30 minutes to allow dissolution of surface-associated AuNCs and subsequent release of

fluorophore labels. The fluorescence of the supernatants was measured on an ISS K2 spectrometer with an excitation wavelength of 633 nm and an emission wavelength of670 nm. The relative fluorescence intensity was calculated in triplicate for each group of cells.

Animal biodistribution studies. All animal studies were performed in compliance with guidelines set forth by the NIH Office of Laboratory Animal Welfare and approved by the Washington University Animal Studies Committee. Normal female C57BL/6 mice (Charles River Laboratory, Wilmington, MA) were used for the biodistribution studies. About 10 μCi of ^{64}Cu radiotracer in 100 μL saline (APP Pharmaceuticals, Schaumburg, IL) was injected via the tail vein. The mice were anesthetized with inhaled isoflurane and re-anesthetized before euthanizing them by cervical dislocation at each time point (1 h, 4 h, and 24 h post injection, n = 3 per group). Organs of interest were collected, weighed, and counted in a well Beckman 8000 gamma counter (Beckman, Fullerton, CA). Standards were prepared and measured along with the samples to calculate the percentage of the injected dose per gram of tissue (%ID/gram) and the and the percentage of injected dose per organ (%ID/organ).

Micro-PET/CT imaging. The human breast cancer 4T1 cell line (ATCC, Manassas, VA) was cultured in RPMI 1640 medium supplemented with 10% FCS, 50 units mL^{-1} sodium penicillin, 50 units mL^{-1} streptomycin sulfate, and 2 mM L-glutamine at 37 °C with 5% CO2. Female Balb/c mice at 6 weeks age (Charles River Laboratory, Wilmington, MA) were subcutaneously implanted with 3 × 106 4T1 cells into the right flank. The tumors were allowed to grow for 1 week to reach a size of approximately 0.5–0.8 g before the mice were used for the PET/CT imaging studies. Mice were anesthetized with isoflurane and injected with 60-70 μCi of ^{64}Cu radiotracer in 100 μL of saline via the tail vein. MicroPET scans were performed on either microPET Focus 220 (Siemens, Malvern, PA) or the Inveon PET/CT system (Siemens, Malvern,

PA) at 1 hour (20 min frame), 4 hours (30 min frame), and 24 hours post-injection (60 min frame). The microPET images were corrected for attenuation, scatter, normalization, and camera dead time and co-registered with microCT images. All of the PET scanners were cross-calibrated periodically. The microPET images were reconstructed with the maximum a posteriori (MAP) algorithm and analyzed using Inveon Research Workplace. The tumor uptake of ^{64}Cu radiotracer was calculated in terms of the percent injected dose per gram (%ID g^{-1}) of tumor tissue in three-dimensional regions of interest (ROI) without the correction for partial volume effect.

Results and Discussion

Design of pre-targeting system. Our initial design for the catch-and-release pre-targeting nanosystem relied on SNA nanoclusters functionalized on their surface with a "sense" DNA sequence, and complementary 2´-OMe-RNA "antisense" and "comptetitor" strands to deliver the radionuclide cargo and subsequently release it, respectively. (Table 5.1).

Oligo	**Sequence (5´→3´)**	**FW (calc'd)**	**[M-H]$^-$ (found)**
Sense*	CCC AGC CTT CCA GCT CCT TGA-**OPSS**	7328	7329
DOTA Antisense‡	**DOTA**-C_{12}-UCA AGG AGC UGG AAG	5738	5764
Cy5 Antisense‡	**Cy5**-UCA AGG AGC UGG AAG	5622	5607
DOTA Scr Antisense‡	**DOTA**-C_6-GGC GAA UAU GAC GGA	5654	5661
Competitor‡	UCA AGG AGC UGG AAG GCU GGG	7165	7143
Competitor*	TCA AGG AGC TGG AAG GCT GGG	7274	7277
Sense-Cy5*	**Cy5**-CCC AGC CTT CCA GCT CCT TGA-**OPSS**	8641	8642
Sense-PEG6†	**PEG$_6$**-CCC AGC CTT CCA GCT CCT TGA-**PEG$_6$-SH**	7211	7201
Sense-PEG2000†	**PEG2K**-CCC AGC CTT CCA GCT CCT TGA-**PEG$_6$-SH**	8867	8831
Sense-DAPTA†	**DAPTA**-C_{12}-CCC AGC CTT CCA GCT CCT TGA-**PEG$_6$-SH**	7956	8012

Table 5.1. Oligonucleotide sequences employed in this study with molecular weights determined by MALDI-TOF in negative ionization mode. Oligos denoted with a (*) = PMO, (†) = DNA, (‡) = 2´-OMe-RNA

The sequence design was based on previously-reported studies with SNAs probing the kinetics of complementary strand displacement from duplexes bound to the SNA surface.[256] We anticipated this approach would offer kinetics suitable for *in vivo* for pre-targeting experiments, as well as synthetic modularity, allowing the attachment of targeting moieties to the 5´ terminus

of the sense strand as well as varied cargoes to the 5´ terminus of the antisense strand. (Scheme 5.1). 2´OMe-RNA was chosen for antisense and competitor oligonucleotides due to its enhanced nuclease resistance and the higher thermodynamic stability of DNA-RNA duplexes relative to DNA-DNA duplexes.[257] 1,4,7,10-tetraazacyclododecane-1,4,7,10-tetraacetic acid (DOTA) was selected as the chelating moiety for ^{64}Cu due to its high association constant with Cu^{2+} ions,[258] commercial availability of functionalized derivatives (e.g. DOTA-NHS ester), and FDA approval for *in vivo* use in human clinical trials of radiopharmaceuticals.[259]

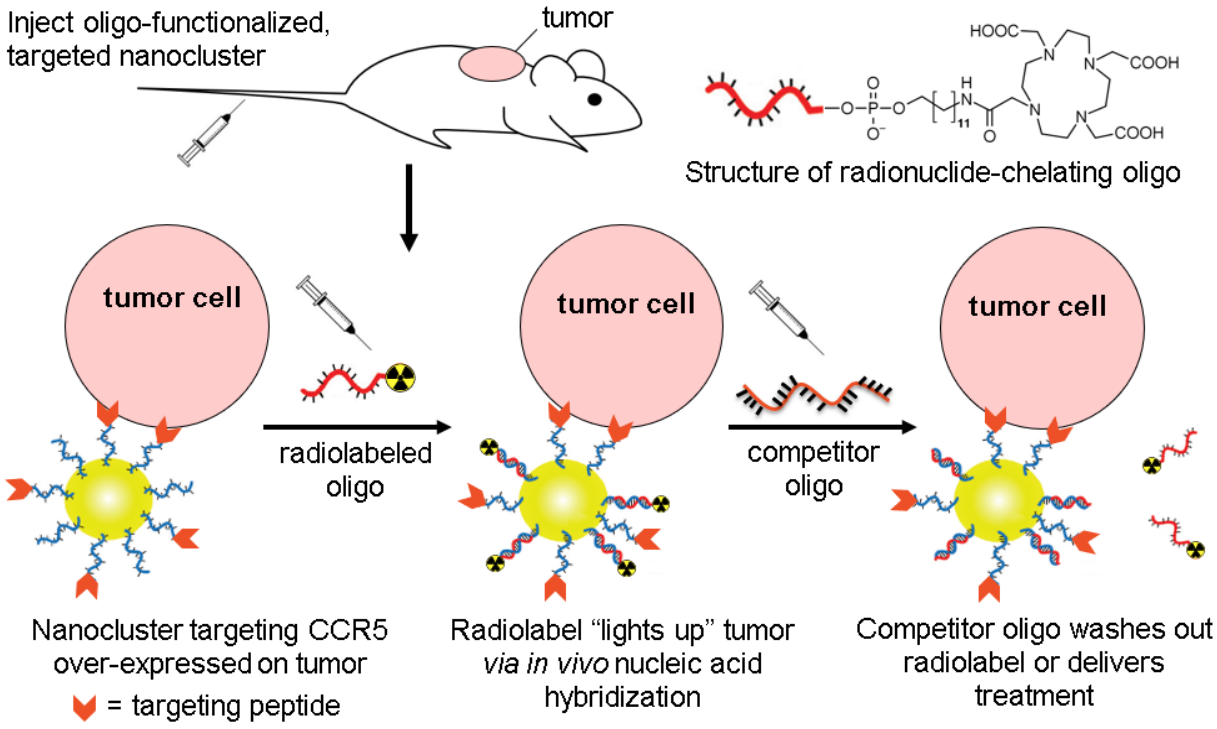

Scheme 5.1. Proposed pre-targeting nanosystem based on *in vivo* SNA hybridization.

Synthesis, characterization and biodistribution of SNAs. Radiosynthesis of ^{64}Cu-alloyed AuNC SNAs was carried out via a one-pot sodium borohydride reduction of $HAuCl_4$ in the presence of thiolated oligonucleotides adapted from previously reported methods (see *Experimental Procedures*).[232] *In vivo* biodistribution experiments revealed that ^{64}Cu-labeled

DNA-SNA nanoclusters exhibited very short circulation time in mice, with less than 1% of the injected dose remaining in the blood after one hour. Various lengths of PEG modification as well as the hydrophobic CCR5-targeting peptide (D-Ala-peptide T-amide) were presented on the surface of the SNA nanoclusters but none achieved blood circulation greater than 1% ID/gram after one hour. Our findings were consistent with the previously-reported *in vivo* biodistribution of 13 nm AuNP siRNA SNAs as determined by ICP-MS in non-tumor-bearing mice.[79]

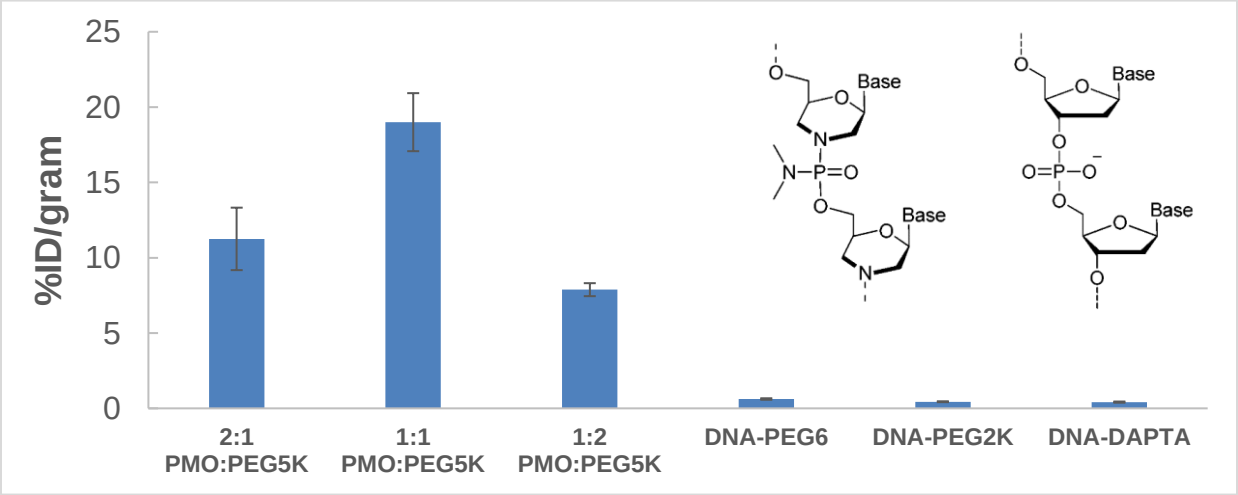

Figure 5.1. Blood circulation of AuNC SNAs 1 hour post-injection in female C57 mice. Inset: structural comparison of PMO (left) and DNA oligos is shown (right)

None of the terminal DNA modifications tested ameliorated the rapid sequestration of the SNAs in the liver and spleen, suggesting that the negative charge of DNA is not effectively screened by conjugation of neutral molecules (PEG, peptides) to the 5´ DNA terminus. These results demonstrated that a DNA SNA-based pre-targeting strategy is hampered by the pharmacokinetics of the DNA-SNA nanoconstruct, including virtually any other *in vivo* application requiring delivery to specific tissues. We saw this as an opportunity to expand the versatility of the SNA platform for *in vivo* biomedical use, and our findings prompted us to alter the chemical composition of the oligonucleotides on the surface of the SNA nanoclusters.

Switching the particle-bound nucleic acids from DNA to PMO oligonucleotides

dramatically improved the blood circulation time, but also required the inclusion of thiol-PEG in the reaction mixture to coadsorb on the surface of the nanoclusters, rendering them colloidally stable. PMO-only nanoclusters irreversibly aggregated upon attempted purification. A ratio of 1:1 PEG (average M_n = 5000) to PMO oligonucleotide was found to provide the longest blood circulation time, sufficient for *in vivo* pre-targeting studies (Figure 5.1 and Figure A5.1).

Blood circulation of the 1:1 PEG5K/PMO SNAs was 19.0 ± 1.9 %ID/gram at 1 hour post-injection, compared to 0.62 ± 0.05% ID/gram for PEG6-capped DNA SNAs. The blood circulation of the PMO SNA remained high at 4 hours (12.0 ± 0.22% ID/gram) and 24 hours (5.5 ± 1.2% ID/gram). After one hour, the majority of the DNA SNA ended up in the liver (38.3 ± 1.2% ID/gram) and spleen (29.5 ± 4.1% ID/gram), compared to the PMO SNA which exhibited much lower liver and spleen accumulation (17.0 ± 1.8 and 4.7 ± 0.3% ID/gram, respectively).

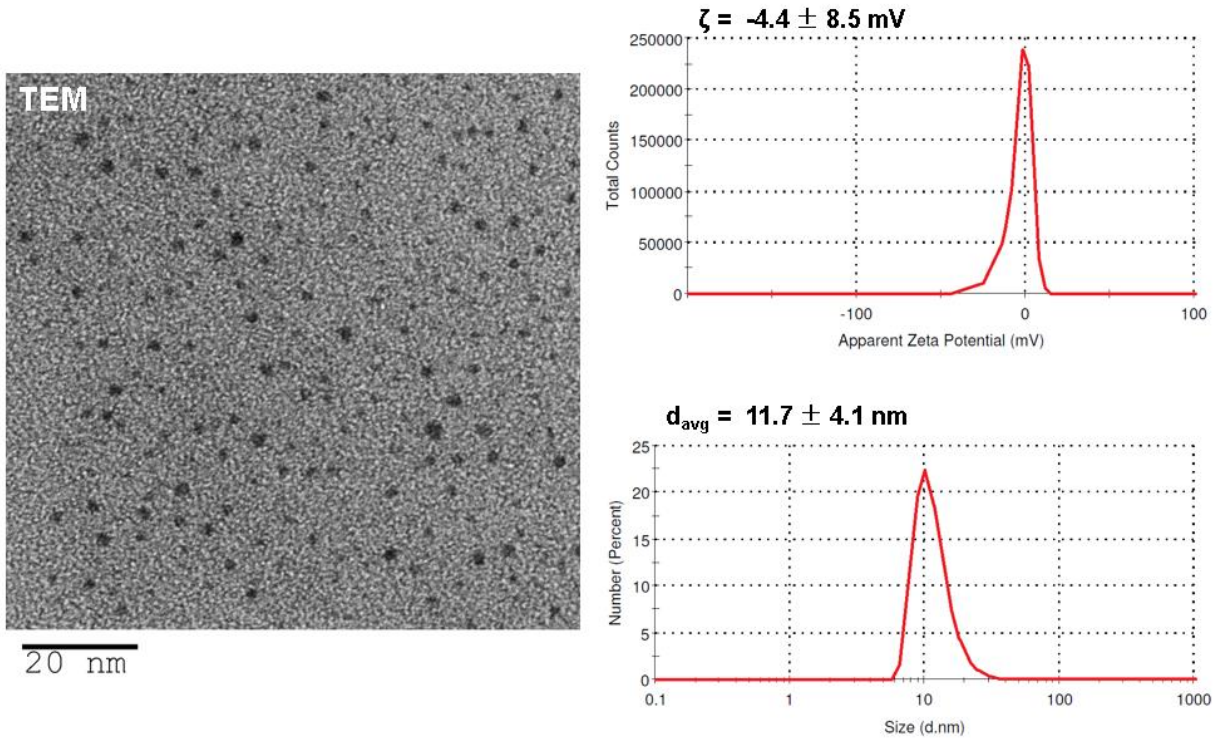

Figure 5.2. Core size, hydrodynamic diameter, and zeta potential characterization of AuNC PMO SNAs.

The PEG/PMO-decorated AuNC SNAs were characterized by DLS, TEM, and zeta potential measurements (Figure 5.2). The loading of PMO oligonucleotides and PEG on the surface of the clusters was determined to be 22 ± 2 PMOs/cluster and 19 ± 1 PEG/cluster. The gold core was dissolved with sodium cyanide, and the released ligands were isolated by size-exclusion chromatography and quantified by UV-Vis spectroscopy. The loading is higher than the reported values for DNA SNAs of similar size (~5 oligonucleotides per 2 nm cluster), presumably due to the absence of electrostatic repulsion between the surface ligands.[260]

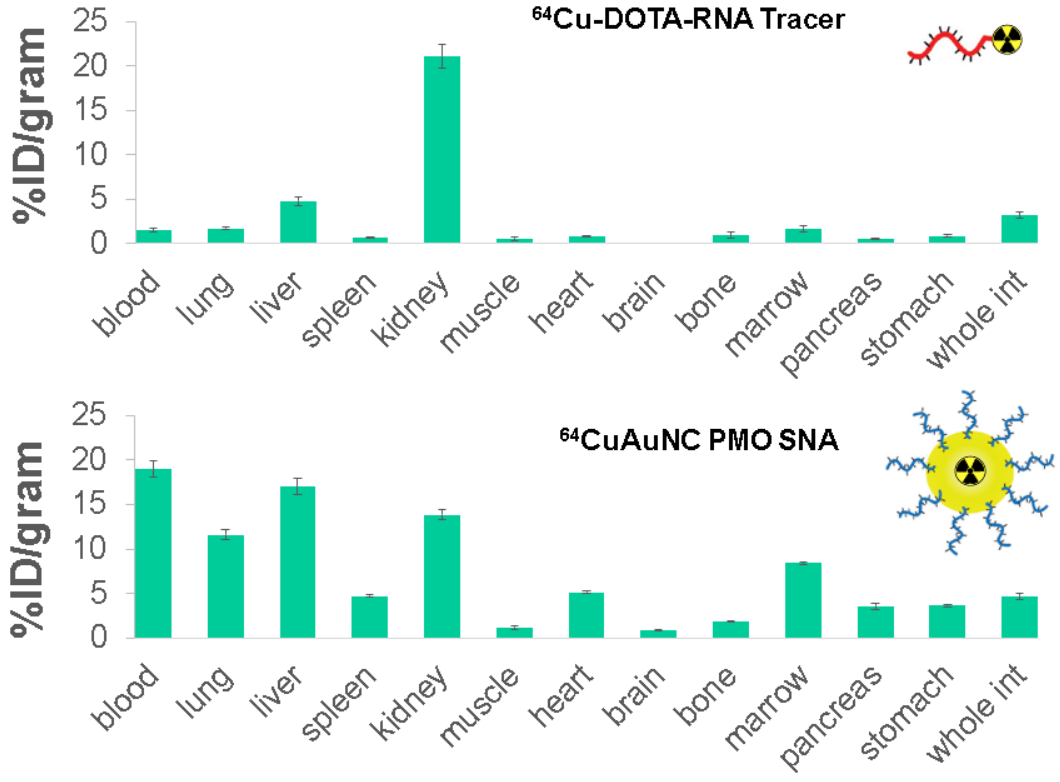

Figure 5.3. Biodistribution of ^{64}Cu-OMe-RNA radiotracer (top) and PMO SNA nanocluster (bottom) in female C57 mice 1 hour post-injection. Biodistribution of nanoclusters at longer time points is shown in Figure A5.1.

The biodistribution of the antisense ^{64}Cu-DOTA-2´-OMe-RNA strand was also studied. In a typical experiment, the free DOTA-RNA was incubated with $^{64}CuCl_2$ for 45 minutes at 45° C and purified by ultrafiltration, with a radiochemical yield of 87-88% and radiochemical purity >99%. On average, the measured specific activity of ^{64}Cu-DOTA-RNA was between 0.5-1

mCi/nmol depending on the amount of ^{64}Cu added to the reaction mixture, consistent with literature reports.[261] The pharmacokinetics of the ^{64}Cu-DOTA-2´-OMe-RNA were consistent with the behavior of similar short 2´-modified oligonucleotides, exhibiting rapid excretion with most of the tracer residing in the kidneys (21.1 ± 2.6 %ID/gram) after one hour (Figure 5.3).[262]

Binding kinetics measurements. With both the pre-targeting SNAs and the cargo in hand, we then set out to determine the kinetics of the antisense strand capture *in vitro* at physiologically relevant concentrations via fluorescence quenching experiments. AuNC SNA concentrations ranging from 1 to 25 nM were examined for their ability to capture 500 pM of antisense Cy5-2´OMe-RNA in 1X PBS at 37° C, relying on the quenching of the dye label upon hybridization to the nanocluster to monitor the rate of the reaction. The change in fluorescence over time was measured and k_{obs} for each binding curve was determined by fitting the data to the simple association kinetics equation:

$$([\mathbf{Target\ Bound}] = [\mathbf{Target\ Bound}]\mathbf{max} \cdot e^{k_{obs}} \cdot \mathbf{time})$$

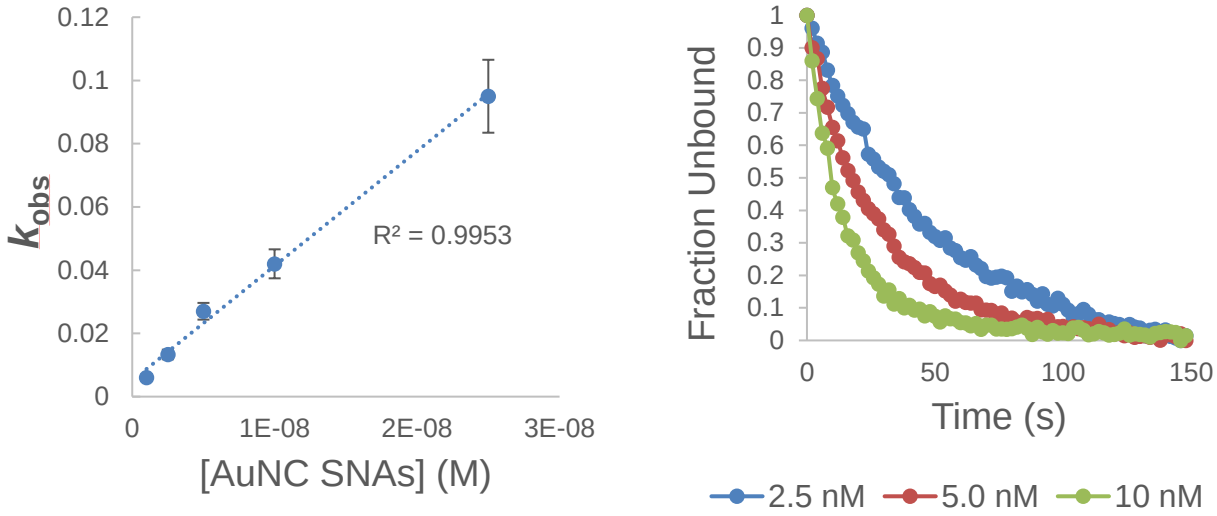

Figure 5.4. Binding kinetics measurements. Left: Representative linear fit to determine k_{on} (slope) and k_{off} (intercept). Right: Binding curves of antisense Cy5-OMe-RNA to AuNCs at different AuNC concentrations.

Both k_{on} and k_{off} were determined using a linear fit ($k_{on} = (k_{obs} - k_{off}) / [SNAs]$). From our measurements, the bimolecular rate constant for capture of the antisense strand k_{on} by the PMO SNA nanoclusters was 3,360,000 ± 234,000 M^{-1} s^{-1}, several orders of magnitude faster than previously described DNA-SNA systems as well as commercially-available bioorthogonal click reaction pairs such as the tetrazine-cyclooctene Diels-Alder cycloaddition (Figure 5.4).[263] The dissociation constant K_d of the hybridized OMe-RNA was 1.70 ± 0.12 nM, indicating that hybridization would indeed be achievable under physiological conditions.

Further, the ability of the competitor to release the hybridized antisense strand was studied. While introduction of an excess (10 µM) of 2´-OMe-RNA competitor strand resulted in the displacement of ~50% of the bound antisense strand from the SNA surface, addition of the same amount of PMO competitor strand possessing an identical sequence released 100% of the bound antisense strand, likely due to the lack of charge repulsion experienced by the incoming competitor strands. (Figure 5.5).

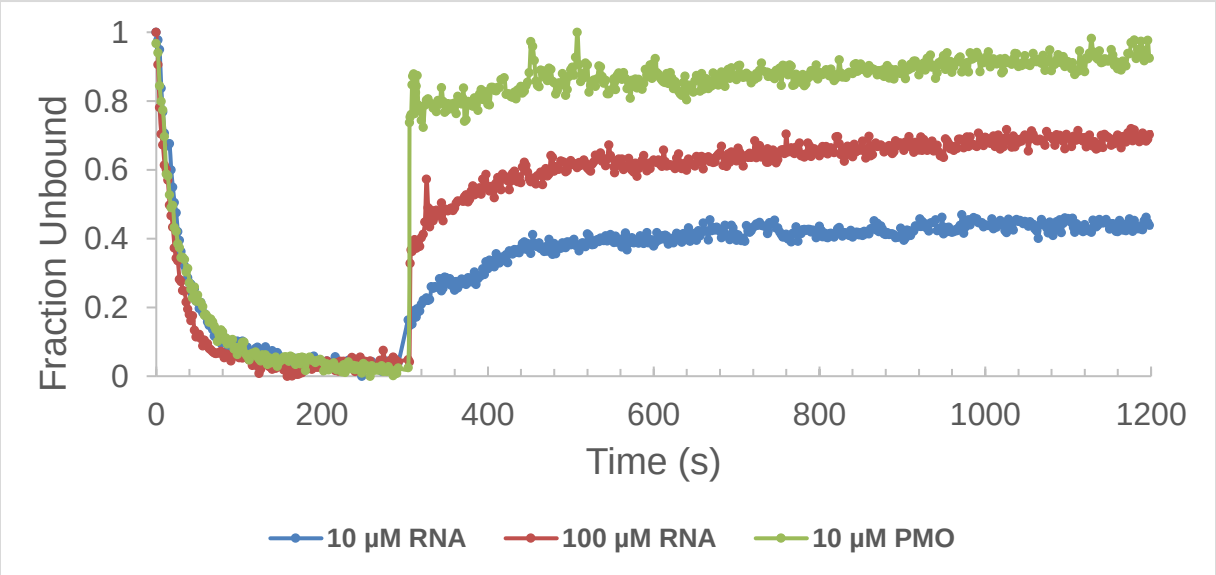

Figure 5.5. Representative capture-and-release curves of PMO AuNC SNAs. At t=0 s, 10 nM of nanocluster is added to a solution of 500 pM antisense Cy5-OMe-RNA. At t=300 s, various concentrations of competitor oligonucleotide are added and the fluorescence is restored as the OMe-RNA is displaced from the nanocluster.

Taken together, our results indicated that the pre-targeting nanosystem would be effective under *in vivo* conditions due to both the favorable biodistribution of the key components (SNA and tracer) as well as their rapid binding kinetics under dilute conditions.

Cellular uptake experiments. Internalization of the SNAs into the tumor cells poses a potential issue as they would be rendered unavailable to bind the circulating antisense strand *in vivo*. DNA SNAs are well-known for their ability to rapidly cross cell membranes without transfection agents, thus, this phenomenon would have to be avoided in the case of PMO SNAs, since linear oligonucleotides do not cross cell membranes readily.[68]

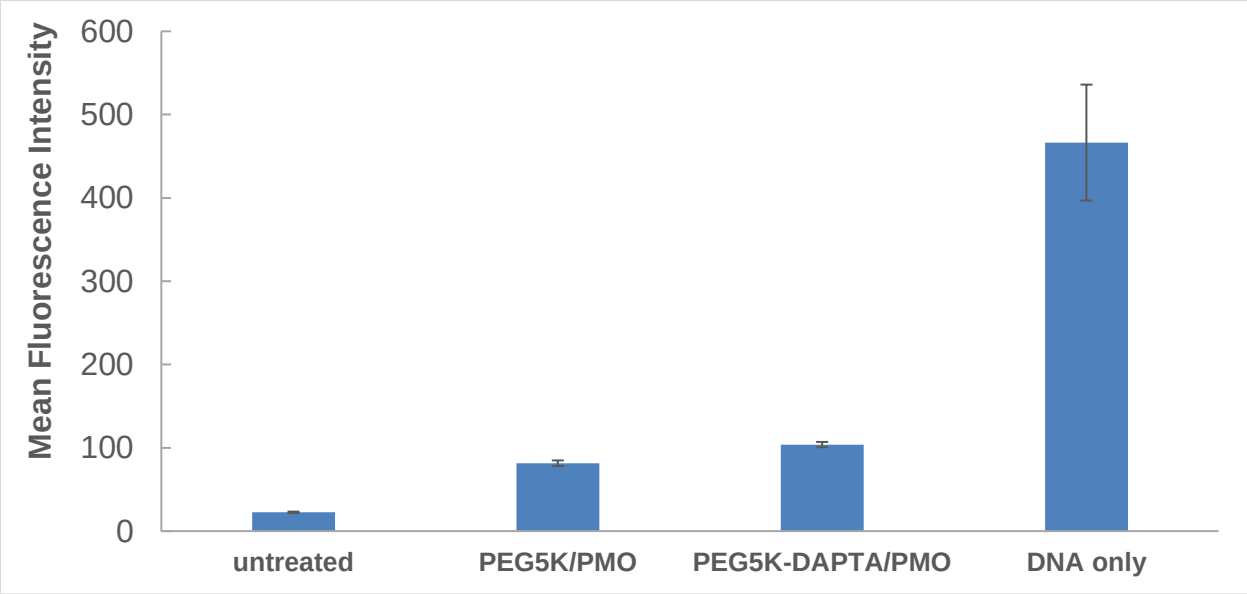

Figure 5.6. Uptake of PMO and DNA AuNCs with varying surface ligand coating in 4T1 breast cancer cells.

To test whether internalization would prohibit effective *in vivo* hybridization, 4T1 breast cancer cells were treated in suspension with several variants of fluorescent cyanine dye-labeled nanoclusters to deconvolute the relative contribution of the oligonucleotides as well as the targeting ligand DAPTA to their degree of internalization. Nanoclusters were prepared with surfaces bearing the sense sequence DNA-Cy5, PMO-Cy5/PEG5K (1:1), or PMO-Cy5/PEG5K-

DAPTA (1:1) and incubated for 24 hours with 4T1 cells at a nanocluster concentration of 4 nM. The cells were subsequently washed and then analyzed by flow cytometry. The DNA SNAs, as expected, exhibited the highest degree of internalization followed by PMO SNAs (Figure 5.6). In addition, to probe the surface association of the various nanocluster types with 4T1 cells, the same experiment was repeated, but after 24 hours, the cells were gently washed with PBS and the suspended cell pellet treated with 10 mM NaCN for 30 minutes to dissolve any surface-associated gold nanoclusters, releasing the Cy5 label into solution. The results of this experiment indicated that the DAPTA-functionalized nanoclusters had the highest surface association with the cells (Figure 5.7), as expected due to the role of DAPTA as an antagonist of the CCR5 receptor.[264] These results suggested that the majority of PMO SNAs would not be trapped inside cellular compartments and would be available for hybridization at the tumor site.

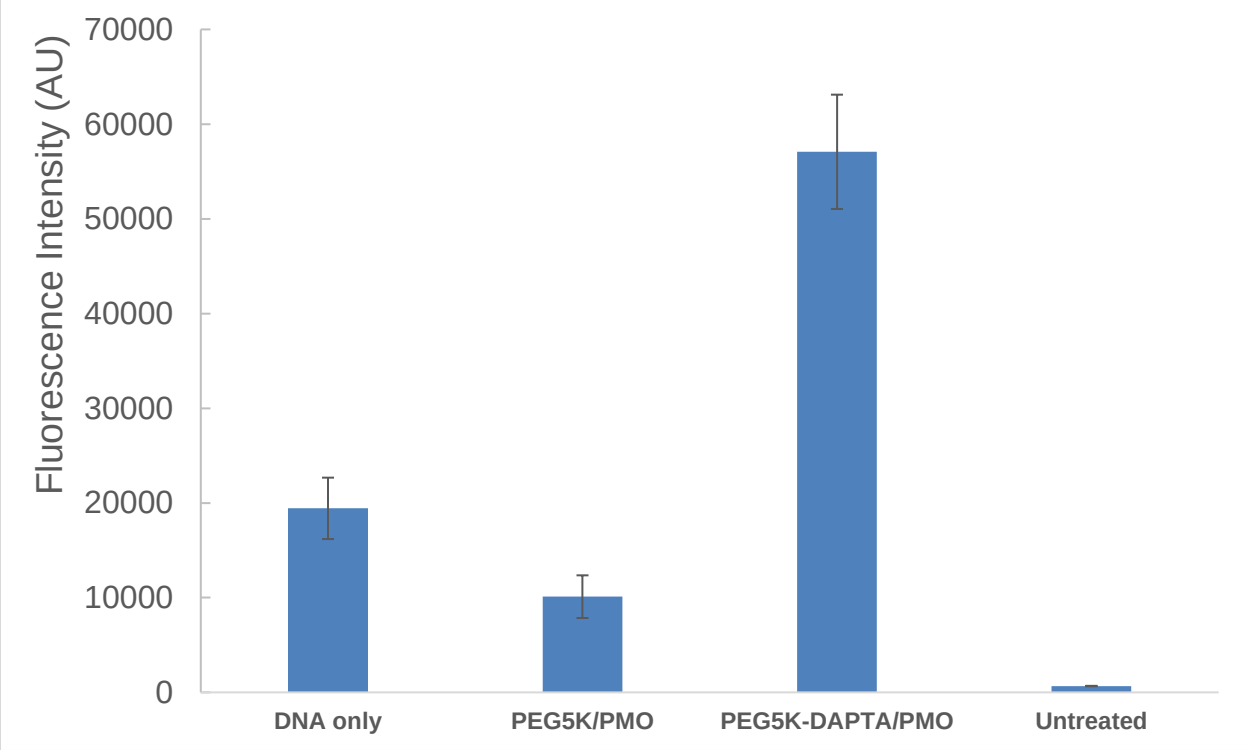

Figure 5.7. 4T1 cell surface association of DNA and PMO AuNCs with varying surface ligand coating after NaCN treatment of cell pellet.

Optimization of pre-targeting schedule. Successful PET imaging of tumor tissue by *in vivo* pre-targeting is highly dependent on the wait time (pretargeting interval) between the injection of the non-radioactive targeting capture moiety and the radioactive cargo. Our initial *in vivo* pre-targeting experiment was designed to determine the optimal time between introduction of the SNA and the radioactive cargo to allow hybridization of ^{64}Cu-OMe-RNA at the tumor site. 4T1 tumors were implanted in the mammary fat pads of female BALB/c mice and SNA nanoclusters functionalized with 1:1 PMO/PEG5K-DAPTA were injected one week post-implant. The total dosage of SNA delivered per animal was 11.4 µg (Au basis) or roughly 72.5 pmol (SNA basis). Then, mice were injected with 60-70 µCi of ^{64}Cu-OMe-RNA tracer (specific activity = 577 µCi/nmol) either 4 hours, 24 hours, or 48 hours post-injection of SNA (n=3 mice in each group). Mice were imaged by PET/CT 4 hours post-injection of the ^{64}Cu-OMe-RNA tracer and the tumor uptake quantitated for each injection delay timepoint. Activity of the ^{64}Cu-OMe-RNA tracer in the tumor increased from 0.39 ± .05% ID/gram at 4 hours to 1.85 ± 0.32% ID/gram at 24 hours and remained constant at 1.98 ± 0.45% ID/gram after 48 hours (Figure 5.7). This initial result was promising as it suggested that tumor accumulation of the ^{64}Cu-OMe-RNA tracer was indeed dependent on presence of SNA at the tumor site. The rapid elimination of ^{64}Cu-OMe-RNA would preclude its nonspecific tumor accumulation in the absence of SNA pre-treatment.

Likewise, the tumor-to-muscle ratio more than doubled from approximately 2.5 in the 4 hour group to ~6.6 in the 48 hour group, demonstrating increased tumor imaging sensitivity with an increased pre-targeting interval. Consistent with previous studies with ^{64}CuAuNCs in a different tumor model, we observed low non-specific tumor retention of the tracer by the enhanced permeability and retention (EPR) effect (<3% ID/gram).[232]

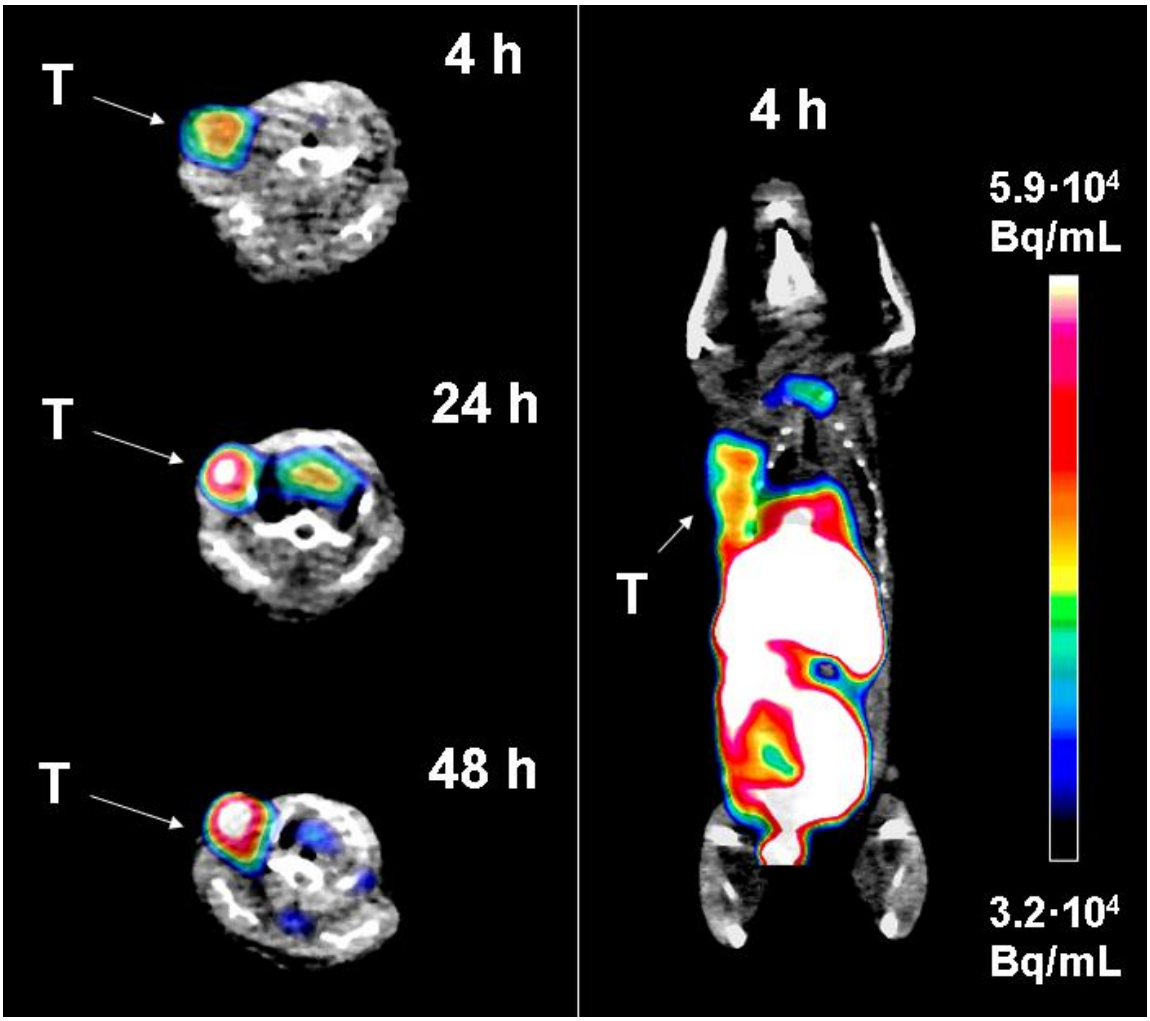

Figure 5.8. Left: Representative axial PET images of tumor-bearing mice at different pretargeting intervals. Right: coronal image of mouse in 4-hour group showing tumor localization.

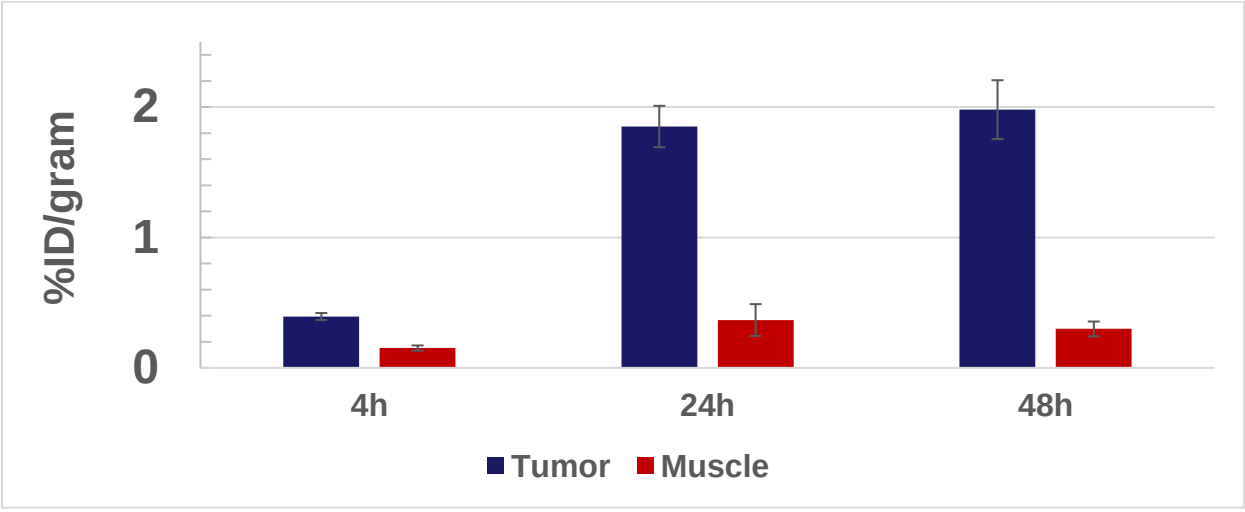

Figure 5.9. Accumulation of ^{64}Cu-OMe-RNA tracer in tumor tissue at different pretargeting intervals.

To expand on this preliminary study, we conducted a repeat experiment to confirm the sequence-specificity of the tumor accumulation of the tracer. Two groups of 4T1 tumor-bearing mice (n=3 each) were pre-treated with injections of SNA nanoclusters functionalized with 1:1 PMO/PEG5K-DAPTA (52.6 μg injected per animal, Au basis).

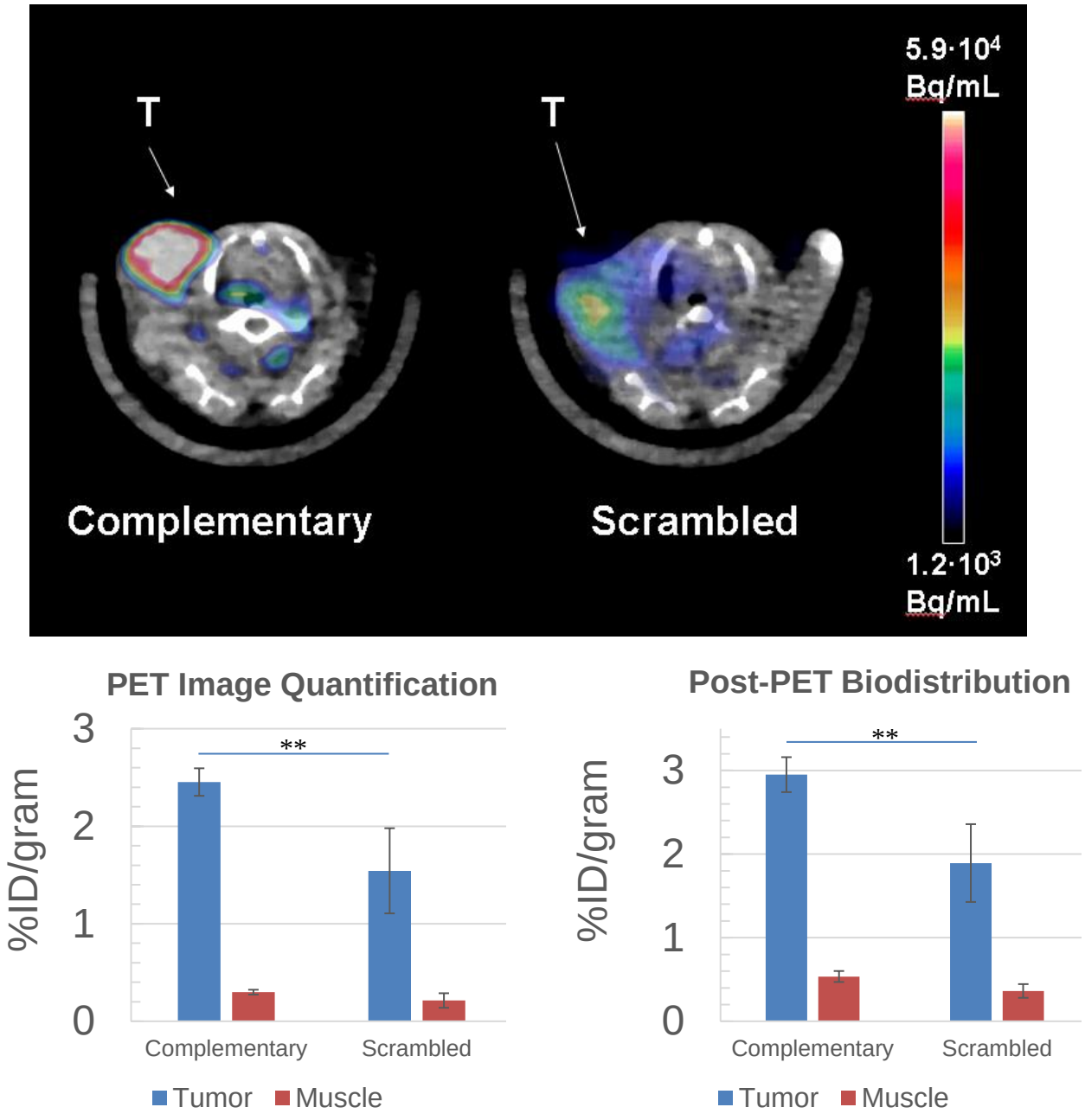

Figure 5.10. Tumor uptake of active vs. scrambled ^{64}Cu-OMe-RNA tracer in 4T1 tumor mice. Top: Representative PET images of mice receiving either scrambled or active tracer. Left: Quantification via PET/CT imaging. Right: Quantification via post-PET biodistribution. Starred bars (**) indicate statistical significance ($p < 0.05$).

24 hours later, the mice were injected with 60-70 µCi of ^{64}Cu-OMe-RNA tracer, with 3 mice receiving the complementary antisense OMe-RNA sequence and 3 mice receiving the scrambled sequence. Mice were imaged by PET/CT 4 hours post-injection of the ^{64}Cu-OMe-RNA tracer and the tumor uptake quantitated for each animal. Subsequently, the animals were sacrificed, tumors were excised, and the activity of ^{64}Cu-OMe-RNA in the tumors and other organs of interest was determined by gamma counting (Figure 5.10-5.11). Finally, the tumors were sectioned and imaged by autoradiography to visualize the relative tumor uptake of the antisense and scrambled tracers (Figure 5.12).

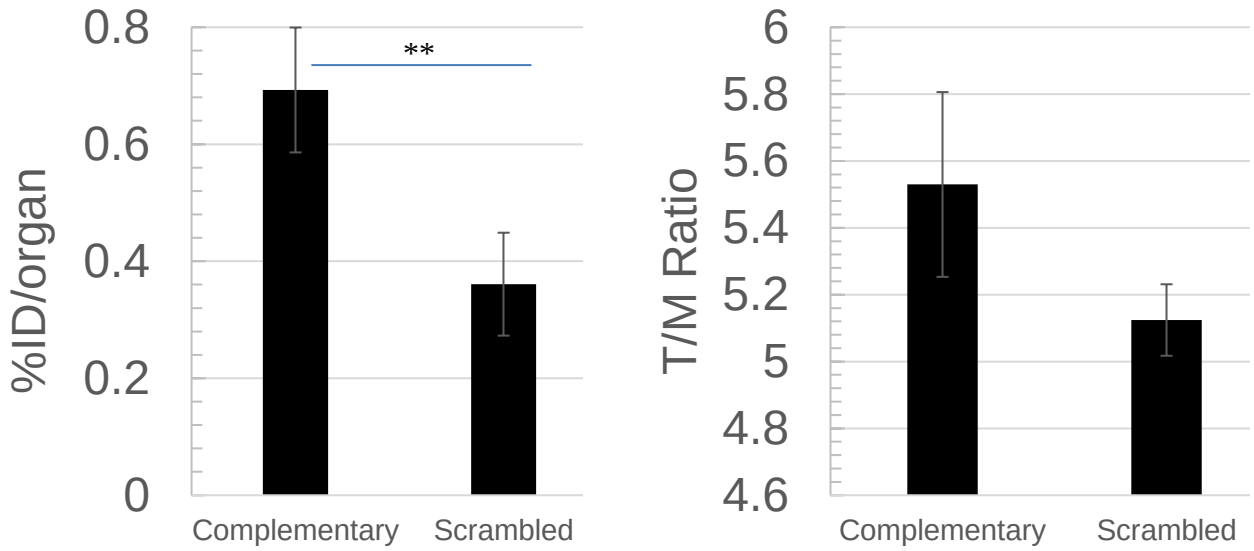

Figure 5.11. Post-PET biodistribution quantification of ^{64}Cu-OMe-RNA tumor uptake. Left: Percent injected dose per organ (tumor). Right: Tumor-to-muscle ratio calculated by post-PET biodistribution. Starred bars (**) indicate statistical significance ($p < 0.05$).

The results of this study indicated that the complementary ^{64}Cu-OMe-RNA tracer exhibits increased tumor uptake relative to the scrambled tracer, confirming that the pre-targeting effect is sequence-specific. The PET image quantification, post-PET biodistribution, and autoradiography results suggest a 1.5 to 2-fold increase in tumor accumulation of the complementary tracer compared to the scrambled tracer. Post-PET biodistribution indicated that the complementary

tracer exhibited %ID/tumor nearly double than that of the scrambled tracer. The tumor-to-muscle ratio was slightly higher for the complementary tracer, but not significant. (Figure 5.11).

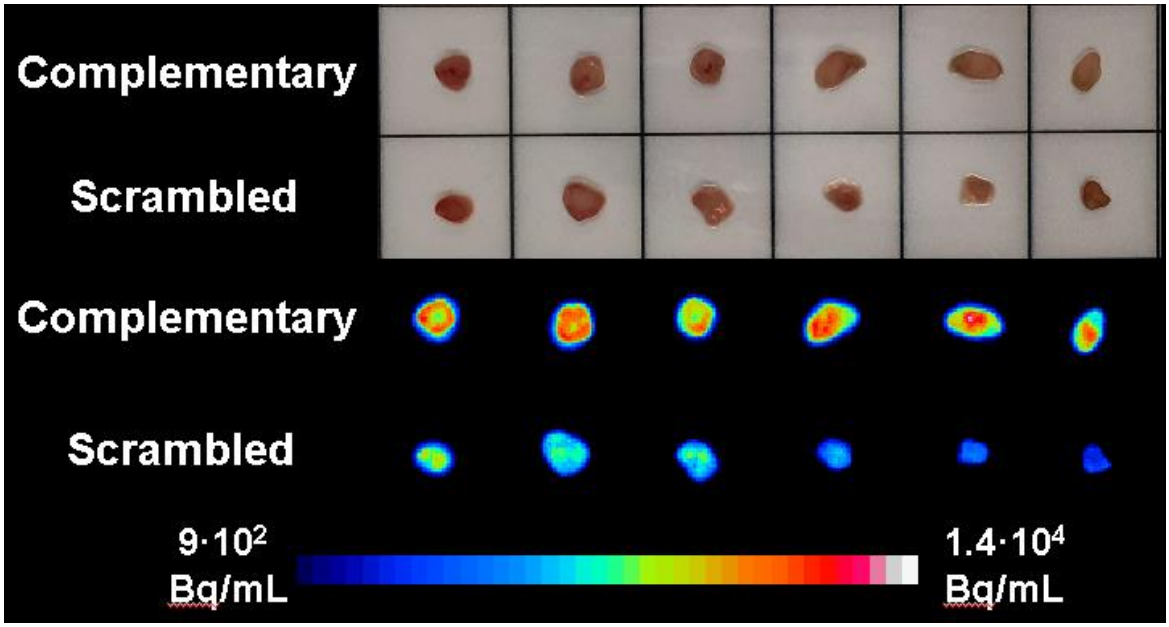

Figure 5.12. Representative images of tumor sections and their activity visualized by autoradiography.

Due to the stability of the PMO/OMe-RNA duplex, we believe the tumor-to-muscle ratio can increased by extending the imaging time post-injection of the ^{64}Cu-OMe-RNA, permitting further clearance of non-specifically bound oligonucleotides.

Studies are ongoing to evaluate direct-targeted PMO SNAs alloyed with ^{64}Cu (and no subsequent oligonucleotide tracer) co-functionalized with PEG5K or PEG5K-DAPTA in comparison to the pre-targeting system. An additional control group consists of ^{64}Cu-OMe-RNA tracer with no prior SNA injection. We hypothesized that the PET signal arising from direct-targeted ^{64}CuAuNC SNAs would be less intense than that of pre-targeted SNAs hybridized with the radiotracer OMe-RNA, since the alloying of ^{64}Cu in the core of the nanocluster typically only results in trace ^{64}Cu incorporation (roughly one ^{64}Cu atom per 10^5 atoms of gold, with a typical cluster comprising fewer than 1000 atoms).[232] In contrast, each PMO-functionalized SNA has

over 20 potential binding sites for a complementary radiolabeled oligonucleotide. Therefore, the pre-targeting strategy has the potential to deliver significantly more ^{64}Cu atoms per nanoparticle to the tumor site. At the time of writing. these experiments are ongoing in tumor-bearing mice using the 4T1 BC model.

Conclusions. We have developed a novel nanocluster SNA-based pre-targeting nanosystem aimed at sensitive and specific imaging of tumor tissue via *in vivo* nucleic acid hybridization in a mouse breast cancer model. Ultrasmall nanoclusters bearing neutral PMO oligonucleotides were synthesized and characterized, and their pharmacokinetics far outperformed analogous nanoclusters with conventional charged DNA oligonucleotides. To our knowledge, this is the first example of SNAs exhibiting extended blood retention time *in vivo*, enabling a variety of new applications not limited to PET imaging. The *in vitro* kinetics of the capture process between the pre-targeted AuNC SNAs and the complementary 2´-OMe-RNA oligonucleotide were investigated. The rate constant for the hybridization between the SNA and the target RNA was superior to existing covalent pretargeting reactions, with single-digit nanomolar binding affinity between the SNA and its complementary oligonucleotide. Effective release of the cargo was also demonstrated by introduction of a longer competitor oligonucleotide. Cell culture studies indicated that the AuNC PMO SNAs did not exhibit significant internalization in the targeted cancer cell line and the presence of the targeting peptide DAPTA on the nanocluster increased cell surface association, suggesting the nanoclusters would be available to capture complementary oligonucleotides circulating in the blood. Lastly, preliminary *in vivo* PET imaging studies indicated that injection of AuNC SNAs followed by complementary ^{64}Cu-labeled OMe-RNA resulted in increased PET signal in the tumor tissue as the time interval between SNA injection and radiolabel injection was increased, and this effect was sequence-

specific, though the tumor-to-muscle ratios were not statistically different. Studies are ongoing to confirm that the pre-targeting system results in a stronger PET signal and higher tumor-to-background ratio relative to direct-targeted ^{64}CuAuNC SNAs, and that DAPTA-functionalized SNAs exhibit superior tumor localization compared to non-targeting SNAs. Future directions will focus on further improving the kinetics of hybridization by employing an all-PMO nanosystem (nanocluster, tracer, and competitor) as well as studying PEGylation of the tracer to improve circulation time and subsequent tumor accumulation. In addition, the tracer cargo may be altered to instead deliver treatment in the form of a cytotoxic drug or a therapeutic radionuclide.

Chapter 6

Synthesis, characterization, and biological properties of neutral phosphorodiamidate morpholino (PMO) spherical nucleic acids

Abstract

Herein, we describe the synthesis, characterization, and biological properties of spherical nucleic acids (SNAs) constructed from neutral phosphorodiamidate morpholino (PMO) oligonucleotides and Au nanoparticles (AuNPs). Commercially available, monodisperse AuNPs were chosen as the core material to ensure reproducibility and uniformity of the synthesized nanoconstructs. The surfaces of AuNPs (10 nm diameter) were densely modified with a mixture of thiolated PMOs and poly(ethylene glycol), resulting in colloidally stable SNAs resistant to aggregation at high salt concentrations (up to 0.5M NaCl). The PMO SNAs, as compared with conventional SNAs, exhibit the ability to more rapidly capture complementary RNA oligonucleotides, a consequence of their neutral charge. PMO SNAs, when hybridized with complementary SNAs, exhibit cooperative thermal denaturation transitions, consistent with dense PMO loading. Finally, PMO SNAs were found to undergo cell uptake without transfection agents in a manner analogous to their DNA counterparts, affording a novel nanosystem for PMO delivery without the use of potentially toxic cationic polymers or cell penetrating peptides. Their ability to engage in intracellular gene regulation is also examined.

Introduction

Spherical nucleic acids (SNAs) have emerged as a powerful new class of functional nanomaterials that have shown promise in supramolecular assembly,[265-267] disease biomarker detection, [268-269] and antisense gene regulation.[270] The classical SNA structure is comprised of a gold nanoparticle core functionalized with a dense layer of deoxyribonucleic acid (DNA) oligonucleotides.[51] A wide range of core materials have been explored including transition metals,[174-175, 271] metal oxides,[272-275] organic materials,[276-277] metal-organic frameworks,[278] and self-assembling micellar structures.[279] The high negative surface charge arising from the phosphate backbone of the nucleic acid shell imparts colloidal stability due to electrostatic repulsion between particles. In solution, SNAs behave much differently from linear nucleic acids. SNAs exhibit cooperative binding and narrow thermal melting transitions when hybridized with complementary particles or oligonucleotides. They are also able to cross cell membranes without the need for ancillary transfection agents despite their high negative charge density. Consequently, they are valuable tools for manipulating cellular processes through gene regulation,[280] drug delivery,[281] and immunomodulation.[282] For the cell types studied thus far, the active uptake of SNAs occurs *via* endocytosis, triggered by their binding to class A scavenger receptors (SR-As) expressed on the surface of mammalian cells.[183, 283] Although SNAs made from naturally-occurring oligonucleotides (DNA, RNA) have shown commercial promise as diagnostic, therapeutic, and research tools, their biodistribution *in vivo* suffers from low blood circulation due to their high surface charge, resultant protein corona accumulation, and susceptibility to nuclease degradation.[284-285] Therefore, for therapeutic purposes, SNA research has focused heavily on topical or local uses (e.g. the skin, immunomodulation)[286-287] and on the development of new strategies for improving blood circulation and nuclease resistance.[288-289]

Consequently, we decided to explore and develop a new form of SNA, based upon neutral PMO oligonucleotides. PMOs have shown promise as intracellular gene regulation agents due to their extremely high binding affinity for target mRNA.[290] They can be synthesized using straightforward phosphoramidite chemistry.[291] The higher binding affinity of morpholino oligonucleotides for complementary oligonucleotides, which is reflected in a higher duplex melting temperature, is due to the lower charge repulsion between the hybridized strands.[292] However, linear PMOs, like linear DNA and RNA oligonucleotides, do not readily enter cells without the aid of cationic transfection agents,[293-294] electroporation,[295] or cell-penetrating peptides[296-297] and therefore alone are not suitable for regulating intracellular processes, including gene knockdown. Gold nanoparticle-PMO conjugates have been described, with one example requiring both a targeting protein for cellular uptake and subsequent localized photocleavage to release PMOs into the cytosol.[298] Other examples of AuNP-PMO conjugates have been described for the purpose of detecting target oligonucleotides in colorimetric assays, but such particles are not stable in solutions of high ionic strength and require a potentially toxic fluorosurfactant during the synthesis procedure.[299-300] Herein we describe methods for the one-step synthesis of the first PMO SNAs stable under physiological conditions, their hybridization behavior with complementary oligonucleotides and SNAs, their unusual ability to cross cell membranes without the need for ancillary transfection agents, and their intracellular gene regulation behavior.

Experimental Procedures

Materials and methods. Citrate-capped gold nanoparticles were purchased from Ted Pella (Redding, CA). PMO oligonucleotides were purchased from Gene Tools (Philomath, OR).

Uranyl acetate solution was purchased from Electron Microscopy Sciences (Hatfield, PA). DNA and RNA synthesis reagents were purchased from ChemGenes (Wilmington, MA) and Glen Research (Sterling, VA). Buffer solutions and cell culture media were purchased from Gibco (Gaithersburg, MD). Thiolated poly(ethylene glycol) derivatives were purchased from Creative PEGWorks (Chapel Hill, NC) and Nanocs (Boston, MA). DBCO-Cy5 was purchased from AAT Bioquest (Sunnyvale, CA). All other reagents were purchased from Sigma-Aldrich (St. Louis, MO) and used as received. UV-Vis spectra and thermal denaturation curves were collected on an Agilent Cary 5000 UV-Vis spectrometer in quartz cuvettes having a path length of 1 cm. Dynamic light scattering (DLS) and zeta potential measurements were collected on a Zetasizer Nano ZS (Malvern Instruments Ltd). TEM images were collected on a JEOL JEM-1400Plus transmission electron microscope and samples were negative-stained with 2% uranyl acetate solution for 30 seconds prior to imaging.

Synthesis of PMO SNAs. To a 15 mL centrifuge tube was added 20 µL 1 mM PMO-ortho-pyridyl disulfide (OPSS) solution, 2.0 mL Ted Pella 10 nm gold colloid (~9 nM stock solution), 20 µL IGEPAL CA-630 1% solution,100 µL 0.1M phosphate buffer (pH 7.4), and the mixture shaken for 30 minutes at room temperature to allow adsorption of the PMO oligonucleotides by spontaneous dissociation of the ortho-pyridyl disulfide bond to release 2-thiopyridone. Then, 20 µL of 1 mM thiolated PEG solution (M_n = 1000, 3000 or 5000 Da) was added and shaking continued overnight at room temperature. The particles were purified by ultrafiltration using an Amicon Ultra-15 100kDa MWCO filter with 3 x 4 mL washes of Milli-Q H_2O spinning at 5000 x g. The particles were resuspended in 1.0 mL Milli-Q H_2O and the concentration was calculated by UV-Vis by measuring the absorbance at 520 nm and dividing by the known extinction coefficient for 10 nm AuNPs ($9.6 \cdot 10^7$ $L \cdot mol^{-1} \cdot cm^{-1}$). DNA-functionalized SNAs were

synthesized according to established protocols employing gradual NaCl addition to increase the loading density of oligonucleotides.[53]

Synthesis of Cy5-PMO-OPSS. 5´-azide and 3´-ortho-pyridyl disulfide (OPSS) modified PMO oligonucleotide was purchased from Gene Tools. A stock solution of 1 mg DBCO-Cy5 in 1 mL anhydrous DMSO was prepared (~825 nmole/mL), and 80 µL of DBCO-Cy5 stock solution was mixed with 50 µL of PMO stock solution (1 mM in H_2O). The mixture was shaken at 37° C overnight and diluted to 0.5 mL with 1X PBS. The crude reaction mixture was purified by size exclusion chromatography (NAP-5 column equilibrated in 1X PBS) and fractions collected and analyzed for purity by UV-Vis and MALDI-TOF.

Synthesis of DNA and 2´-OMe-RNA oligonucleotides. DNA and 2´-OMe-RNA oligonucleotides were synthesized on a MerMade MM12 automated oligonucleotide synthesizer according to standard manufacturer protocols. OMe-RNA oligonucleotides were modified at the 5´ terminus with a commercial cyanine dye (Cy5) modifier from Glen Research following manufacturer instructions. DNA oligonucleotides were prepared using a 3´ disulfide-bearing linker attached to the solid support and modified at the 5´ terminus with a single hexaethylene glycol (Spacer 18) linker from Glen Research. The oligonucleotides were purified by reverse-phase HPLC on C18-coated silica with triethylammonium acetate buffer (0.03M, pH 7.0) and acetonitrile as the mobile phase ramping from 0-75% acetonitrile over 45 minutes. Fractions were pooled, lyophilized, and deprotected by treatment with 20% acetic acid for 1 hour at room temperature. The aqueous layer was washed 3x with ethyl acetate, lyophilized again, and the resulting dried nucleic acids resuspended in Milli-Q H_2O and the oligonucleotide concentration quantified by UV-Vis.

Oligonucleotide capture studies. Binding rates were determined using fluorescence measurements collected on an ISS K2 spectrometer with an excitation wavelength of 633 nm and an emission wavelength of670 nm. For each binding curve, a solution of 100 pM Cy5-labeled antisense 2´OMe-RNA in 1 mL 1X PBS was prepared in a polymethacrylate cuvette and allowed to warm to 37° C using the internal temperature controller. Then, the RNA solution was mixed with PMO SNAs and the change in fluorescence over time was measured in 1 second increments. Bimolecular rate constants were derived by curve-fitting the acquired data for each SNA concentration tested (50, 100, 200, 400 and 800 pM) in triplicate. For comparison purposes, DNA SNAs were likewise tested at concentrations of 100, 200, 400, and 800 pM.

Cellular uptake studies. All microscopy was performed using an Nikon A1Rsi laser scanning confocal microscope exciting at 640 nm. KB human carcinoma cells were plated on glass bottom dishes coated with polylysine (MatTek Corporation, glass no. 1.5), and allowed to grow overnight. Attached cells were treated with 300 µL of cell culture medium containing either Cy5-PMO labeled SNAs at a total concentration of 2.5 nM or single-stranded PMO oligonucleotides at 250 nM. After 2 and 24 hr intervals, Hoechst 33258 nuclear stain (10 µM, Life Technologies) was added and further incubated for 15 min, washed, and then imaged by confocal fluorescence microscopy (exciting at 405 and 640 nm). Images were collected in both normal and Z-stack mode to verify that particles were present in the cytosol rather than the exterior of the cell membrane. Images were analyzed using Nikon NIS-Elements software. For flow cytometry, SKOV3 ovarian cancer cells (ATCC) were plated in a 24-well plate at 20,000 cells per well in DMEM media (Gibco) containing 10% fetal bovine serum (Hyclone) and 1% penicillin-steptomycin (ThermoFisher). Twelve-hours later, cells were treated in triplicate with either Cy5-labeled SNAs at a total SNA concentration of 2.5 nM or Cy5-labeled single-stranded PMO

oligonucleotide at a concentration of 250 nM and incubated for 24 hours. The media was then removed, the cells were washed with 3 × 1 mL portions of 1X PBS, trypsinized to remove from the plate, and pelleted by centrifugation at 350 x g for 5 minutes. The cells were then fixed in 4% paraformaldehyde for 30 minutes at 4 degrees Celsius, washed with 1X PBS, then transferred to polypropylene tubes for flow cytometry analysis. The relative fluorescence intensity of each group of cells was measured exciting at a wavelength of 633 nm on a BD LSR II flow cytometer and the mean fluorescence intensity was calculated in triplicate.

Gene knockdown studies. SKOV3 ovarian cancer cells (ATCC) were plated in a 24-well plate at 100,000 cells per well in DMEM media (Gibco) containing 10% fetal bovine serum (Hyclone) and 1% penicillin-steptomycin (ThermoFisher). Twelve-hours later, cells were washed and treated in triplicate with SNAs (SNA1, SNA2, or non-targeting SNA) at a total SNA concentration of 2.5 nM in Optimem. A positive control of an antisense DNA targeting HER2 was used by treating cells with 250 nM DNA in lipofectamine 2000. Twenty-four hours later, Optimem was removed and fresh growth media (DMEM, 10% FBS, 1% PenStrep) was added for another 48 hours. The total treatment time was 72 hours from the initial transfection. The media was then removed, the cells were washed with 3 × 1 mL portions of ice cold 1X PBS, then the cells were lysed with 100 uL of RIPA lysing buffer. Lysates were collected and total protein concentration was measured with the BCA Protein Assay Kit. Equal amounts of protein (10 ug) were fractionated by a 4-20% precast SDS-polyacrylamide gel (Bio Rad) and transferred to a nitrocellulose membrane (Thermo Fisher). The membranes were then immediately blocked with 1%BSA in PBST for 1 hour at room temperature. Primary rabbit antibodies against HER2 and GAPDH (1000:1, Cell Signaling) and flourescently tagged anti-rabbit IgG secondary antibodies (20000:1, LI-CORE) were used to detect proteins. The

membranes were imaged using a 800 nm laser on the Odyssey Infrared Imaging System (LI-Core) and quantified using ImageJ.

Results and Discussion

DNA SNAs remain colloidally stable without the need for co-adsorption of poly(ethylene glycol) (PEG) or other stabilizing polymers on the gold surface. The charge density of the DNA alone is sufficient to render the DNA SNAs colloidally stable due to their strong interparticle repulsion in solution.[53] In contrast, we found that SNAs synthesized with a surface layer consisting of 100% PMO oligonucleotides led to irreversible aggregation upon purification, irrespective of the oligonucleotide sequence or length. Thus, we experimented with co-adsorption of thiolated PEGs along with ortho-pyridyl disulfide (OPSS)-modified PMOs. We discovered that PEG-thiol (M_n = 5000), mixed 1:1 with 21-mer PMO oligonucleotides in the presence of citrate-capped gold nanoparticles, afforded colloidally-stable PEG/PMO SNAs capable of hybridizing with complementary oligonucleotides and SNAs. (Table 6.1)

Oligo	**Sequence (5´→3´)**
Sense (PMO)	CCC AGC CTT CCA GCT CCT TGA-**OPSS**
Sense (DNA)	PEG_6-CCC AGC CTT CCA GCT CCT TGA-PEG_6-**Thiol**
Sense-Cy5 (PMO, DNA)	**Cy5**-CCC AGC CTT CCA GCT CCT TGA-**Thiol**
Antisense (2´-OMe-RNA)	**Cy5**-UCA AGG AGC UGG AAG
MeltA (PMO, DNA)	TTA TAA CTA TTC CTA AAAAA-**Thiol**
MeltB (PMO, DNA)	TAG GAA TAG TTA TAA AAAAA-**Thiol**
HER2-Target1 (PMO)	CAT GGT GCT CAC TGC GGC TCC GGC-**OPSS**
HER2-Target2 (PMO)	AGG GAG CCG CAG CTT CAT GTC TGT G-**OPSS**
NonTarget (PMO)	CCT CTT ACC TCA GTT ACA ATT TAT A-**OPSS**
HER2-Target (DNA)	CTC CAT GGT GCT CAC

Table 6.1. Oligonucleotide sequences employed in this study. PEG_6 = 6 ethylene glycol unit spacer

The as-synthesized PEG/PMO SNAs had a mean hydrodynamic radius of 25.0 ± 6.0 nm (compared to 8.6 ± 2.3 nm for citrate-capped AuNPs) and a surface zeta potential of -6.9 ± 4.9 mV (compared to -22 ± 5.6 mV for citrate-capped AuNPs), consistent with their neutral overall

charge. To test their colloidal stability, the PEG/PMO SNAs were stored at increasing salt concentrations (up to 0.5M NaCl) and examined for signs of aggregation by dynamic light scattering (DLS). After three months, no aggregation or sedimentation was observed (Figure 6.1, A6.1). The observed hydrodynamic radii of the SNAs was consistent with TEM images produced by negative staining with 2% uranyl acetate (Figure 6.2).

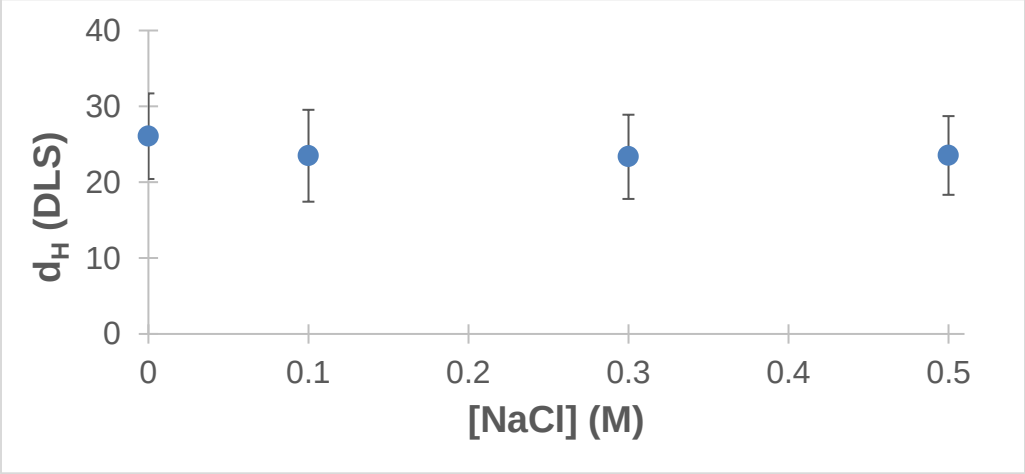

Figure 6.1. Hydrodynamic radius of PMO SNAs vs NaCl concentration. No statistically significant change in d_H was observed, indicating a lack of salt-induced aggregation.

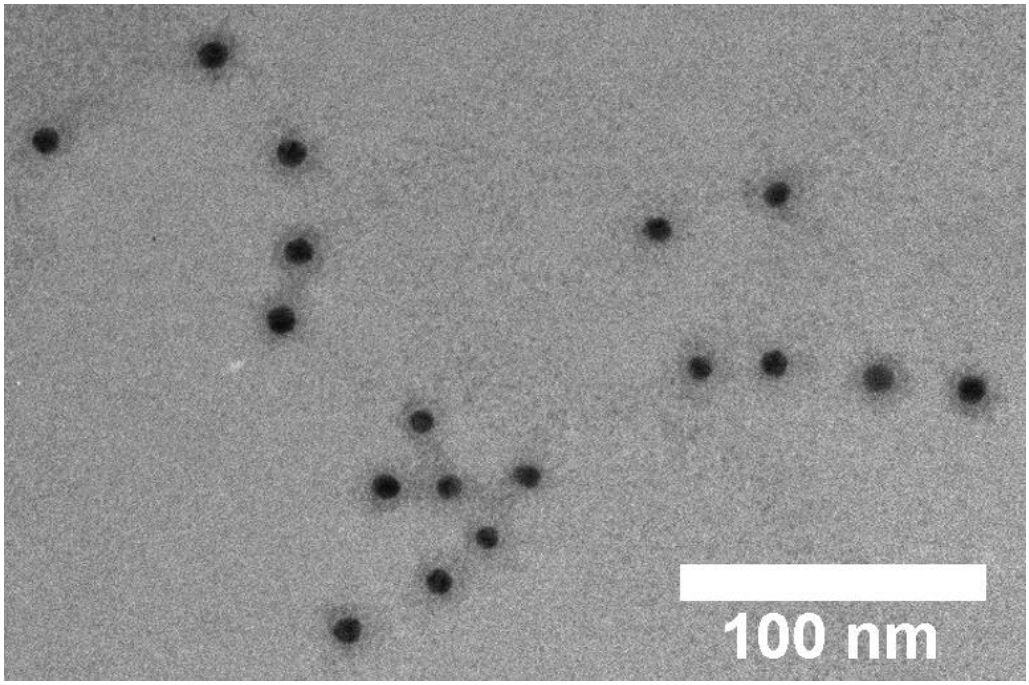

Figure 6.2. TEM image of PEG5K/PMO SNAs stained with uranyl acetate.

PEGs of lower molecular weights (3000 and 1000 Da) were also examined for their ability to stabilize PMO SNAs. The PEG/PMO SNAs exhibited similar stability with 3 kDa PEG-thiol mixed in a 1:1 ratio, but a 1:1 ratio of 1 kDa PEG-thiol was insufficient to stabilize PMO SNAs against aggregation when centrifuged at 20,000 x g for 90 minutes (Figure 6.3). This issue was remedied by increasing the molar ratio of PEG to PMO to 2:1. Most importantly, we found that 1 kDa-PEG modified PMO SNAs were capable of spontaneous cell uptake, whereas 5 kDa-PEG modified PMO SNAs showed no apparent uptake by confocal microscopy (*vide supra*). Therefore, both the colloidal stability and cellular interaction of PMO SNAs is dependent on the length and quantity of co-adsorbed PEG molecules.

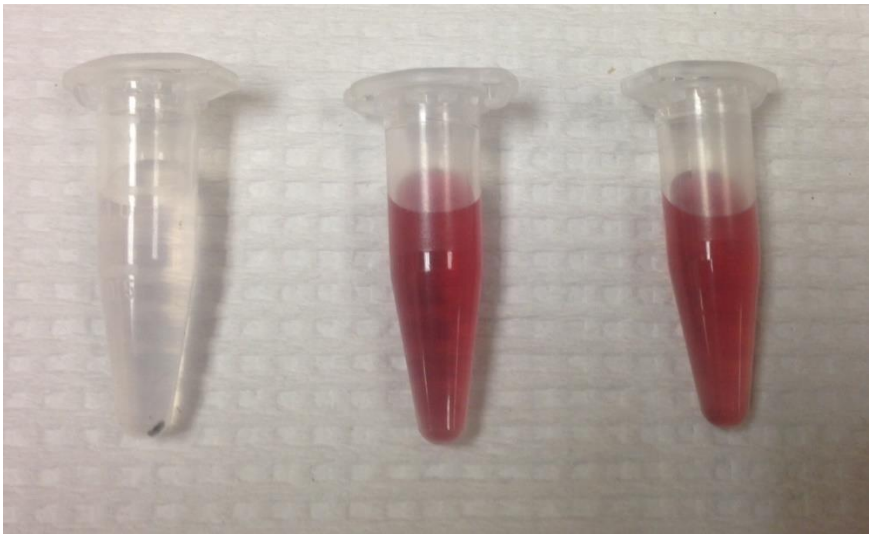

Figure 6.3. 1:1 PEG/PMO SNAs after centrifugation and resuspension in water. PEG molecular weight from left to right: 1000 Da, 3000 Da, 5000 Da

For the 1:1 PEG5K/PMO SNAs employed for biophysical studies, the average loading of PMO oligonucleotides and PEG molecules was determined by co-adsorbing PEG5K-fluorescein and 21-mer morpholino oligonucleotides on 10 nm citrate-capped AuNPs. Three separate batches were prepared by the same protocol and 0.5 mL aliquots of each were subsequently dissolved by sodium cyanide, the gold salts removed by gel filtration, and the relative amounts of each surface ligand determined by UV-Vis spectroscopy. The average loading of PMOs per 10 nm AuNP was

103 ± 7 molecules, whereas the average loading of PEG5K per AuNP was 72 ± 15 molecules, indicating a roughly equal surface absorption ratio.

Kinetics experiments to determine the rate of capture of complementary charged oligonucleotide (15-mer 2´-OMe-RNA) by uncharged PMO SNAs under physiologically relevant conditions were carried out. Briefly, a solution of 100 pM target oligonucleotide (OMe-RNA labeled with Cy5 at the 5´ terminus) was prepared in 1X PBS and allowed to equilibrate to 37° C. The fluorescence intensity of the solution was monitored after an aliquot of 21-mer PEG5K/PMO SNAs was added to the solution, resulting in quenching of the Cy5 fluorescence by the AuNP core as the OMe-RNA molecules hybridized to the particles. The experiment was repeated at varying concentrations of SNAs (from 50 pM to 800 pM) to determine the rate constant k_{on} for the capture process. (Figure 6.4). In all cases, the number of morpholino strands was in excess relative to the concentration of the target OMe-RNA, since each AuNP bears approximately 100 strands of PMO oligonucleotides.

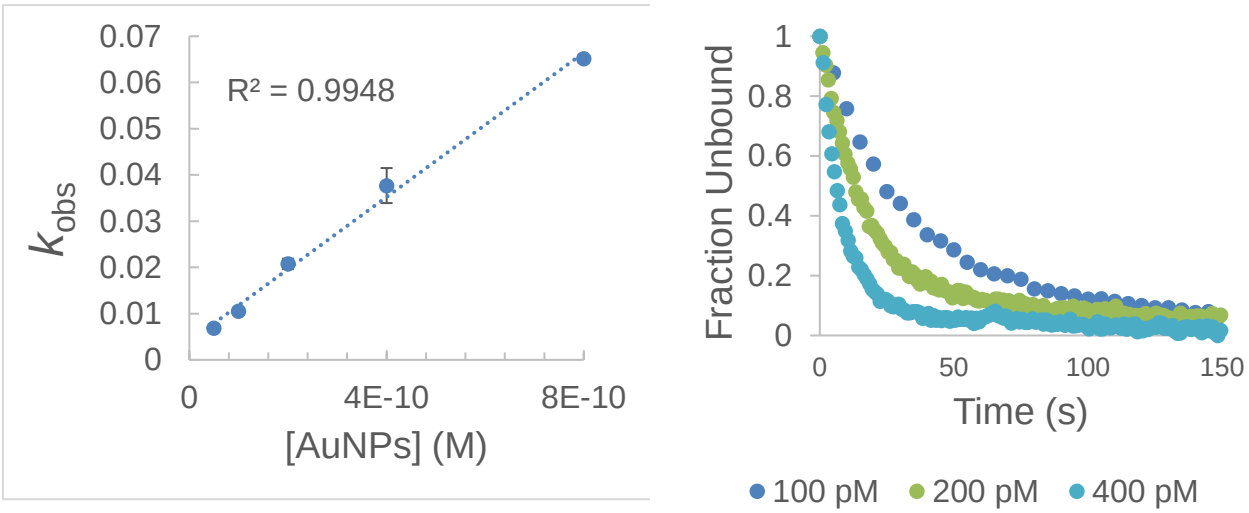

Figure 6.4. Binding kinetics measurements. Left: Dependence of k_{obs} on concentration of SNAs. Slope of line = k_{on}, intercept = k_{off}. Each data point represents the average of three kinetics experiments. Right: Representative binding curves of Cy5-antisense OMe-RNA to PMO SNAs at different SNA concentrations.

We determined that PMO SNA captures the target with a bimolecular rate constant k_{on} of approximately 78,300,000 ± 1,040,000 $M^{-1}s^{-1}$, with a dissociation constant (K_d) of 52.6 ± 5.6 pM, which is many orders of magnitude higher than state-of-the-art *in vivo* click reactions such as the tetrazine-cyclooctene Diels-Alder cycloaddition and potentially one of the most rapid bioorthogonal conjugation methods discovered to date.[301] PMO SNAs also capture target oligonucleotides far more rapidly than DNA SNAs at similar concentrations, on the order of seconds rather than minutes.[254] A DNA SNA loaded with the same oligonucleotide sequence (113 ± 17 DNA/AuNP) captured the complementary OMe-RNA at a rate of 2,250,000 ± 230,000 $M^{-1}s^{-1}$, over 30 times slower under identical conditions (Figure A6.2). The associated K_d for the OMe-RNA hybridized to the DNA SNA was 61.3 ± 2.3 nM.

SNA	K_d	k_{on} (M^{-1} s^{-1})	**Surface Area**	**Oligo density**	**PEG density**
AuNP PMO SNA (10 nm)	**52.6 pM**	78,300,000	1257 nm^2	13.6 pmol/cm^2	9.5 pmol/cm^2
AuNC PMO SNA (2.5 nm)	**1.7 nM**	3,360,000	79 nm^2	46.3 pmol/cm^2	40.0 pmol/cm^2
DNA SNA (10 nm)	**61.3 nM**	2,250,000	1257 nm^2	14.9 pmol/cm^2	-

Table 6.2. Rate constants, dissociation constants, and surface coverage of SNAs discussed in Chapters 5 & 6.

Comparison of the rate constants and association constants for the SNAs discussed in this chapter and the previous chapter reveals that the K_d value for the smaller (<3 nm) PMO-based nanocluster falls in the middle ground between the 10 nm PMO SNA and the 10 nm DNA SNA (Table 6.2). There is less correlation in terms of the bimolecular rate constant k_{on}. Due to the higher radius of curvature of the smaller nanoclusters, their surface coverage of oligonucleotides

is significantly higher than that of the 10 nm particles.[302] Other authors investigating the hybridization kinetics of surface-bound PMOs found that lower surface coverage led to faster hybridization rates, which implies that the steric crowding on the smaller nanoclusters inhibits the capture of incoming antisense strands.[303]

It is worth noting that the calculated rate constant for the 10 nm PMO SNA system approaches the maximum experimentally observed rates associated with diffusion-limited reactions (10^9 M^{-1} s^{-1}) and the capture of oligonucleotides seemingly occurs faster than the rate at which the nanoparticle can diffuse through solution.[304] Pinhiero et. al. describe a similar oligonucleotide capture system with DNA nanoparticles.[305] The authors describe nucleation as "the rate-limiting step of hybridization at low DNA concentrations (nano- to micromolar range), relying on efficient collisions between the interacting strands. The subsequent strand realignment and fully complementary base-pairing are expected to proceed at a much faster rate." In our system, the fluorescence quenching of the reporter dye occurs only after the antisense strand has fully hybridized to the SNA. Consequently, hybridization of the antisense strand to the nanoparticle can be simplified to a bimolecular process with an overall rate constant of k_{on}. A large excess of capture strands on the gold nanoparticles further simplifies the kinetics and allows application of a pseudo-first-order kinetic model. Consistent with pseudo-first-order behavior, the reaction was carried out at several different SNA concentrations with a constant antisense strand concentration. The linear dependence of the rate constant as a function of the SNA concentration confirms that a pseudo-first order kinetic model is valid.

Typical bimolecular rate constants for hybridization of unmodified DNA duplexes are on the order of 10^6 M^{-1} s^{-1}.[306] We observed a similar k_{on} rate for a corresponding DNA SNA. In contrast, the hybridization of neutral oligos such as PNA with complementary DNA have been

shown to be accelerated by as much as 500-fold compared to DNA-DNA duplexes.[307-308] Therefore, our observation that a PMO SNA captures a complementary oligonucleotide with kinetics over 1 order of magnitude higher than a DNA SNA agrees with literature reports of hybridization rates between DNA and neutral oligonucleotides in solution. An additional factor to consider is the polyvalent nature of the PMO SNAs. From the perspective of the incoming antisense oligonucleotide, it encounters an extremely high local concentration of its complementary strand when colliding with a PMO SNA, leading to enhanced kinetics due to the increased likelihood of a successful hybridization event. The same rate enhancement effect is often observed when nanoparticles are functionalized with multiple copies of enzymes, despite the slower diffusion of the NP-enzyme nanoconstruct.[309] Therefore, we believe the dramatic enhancement in kinetics calculated for the PMO SNA target capture are consistent with phenomena already observed by other authors.

Since DNA hybridization typically exhibits anti-Arrhenius behavior resulting in small or negative activation energies,[310-311] we calculated the activation energy of capture of a complementary 2´OMe-RNA strand by a PMO SNA. The bimolecular rate constant for OMe-RNA hybridization was measured at 10°C and the activation energy (E_a) for hybridization was estimated using the Arrhenius equation. We calculated E_a to be roughly 3.7 kcal/mol, which is below the activation energy for the diffusion of liquid water (~4.2 kcal/mol),[312] indicating that the hybridization process on the SNA is indeed diffusion-controlled (See *Chapter 6 Supporting Information*).

Having compared the kinetics of PMO SNA hybridization with complementary oligonucleotides to DNA SNAs, we then examined their hybridization behavior with complementary SNAs. DNA SNAs and PMO SNAs were synthesized bearing 20-mer sequences

with a complementary 15-base-pair overlap. The thermal denaturation behavior of the DNA-DNA SNA pairs and PMO-DNA SNA pairs were compared. Briefly, the SNAs were mixed in the presence of salt (0.5M NaCl) and allowed to aggregate. Then, the mixture was gradually heated and monitored by UV-Vis to determine the melting temperature (T_m) of the nanoparticle aggregates. As a control, DNA and PMO SNAs with identical sequences were also mixed to eliminate the possibility of non-specific aggregation. The resulting thermal denaturation curves demonstrate that the morpholino SNA and DNA SNA pair, compared to DNA-DNA SNA pair, exhibits a dramatically increased melting temperature (>20° C) as well as a sharper melting transition. In contrast, the non-complementary pairs did not interact (Figure 6.5). At the same salt concentration (0.5M NaCl), the single-stranded DNA-DNA and DNA-PMO duplexes exhibited broad melting transitions. Interestingly, the melting temperature of the free DNA-DNA duplex exceeded that of the DNA-PMO duplex at 0.5M NaCl, since the T_m of DNA-PMO duplexes remains constant irrespective of salt concentration, whereas the T_m of DNA-DNA duplexes increases nearly linearly with salt concentration. In comparison, the DNA-DNA duplex had a lower T_m than the DNA-PMO duplex in 1X PBS. (Figure 6.6).[313]

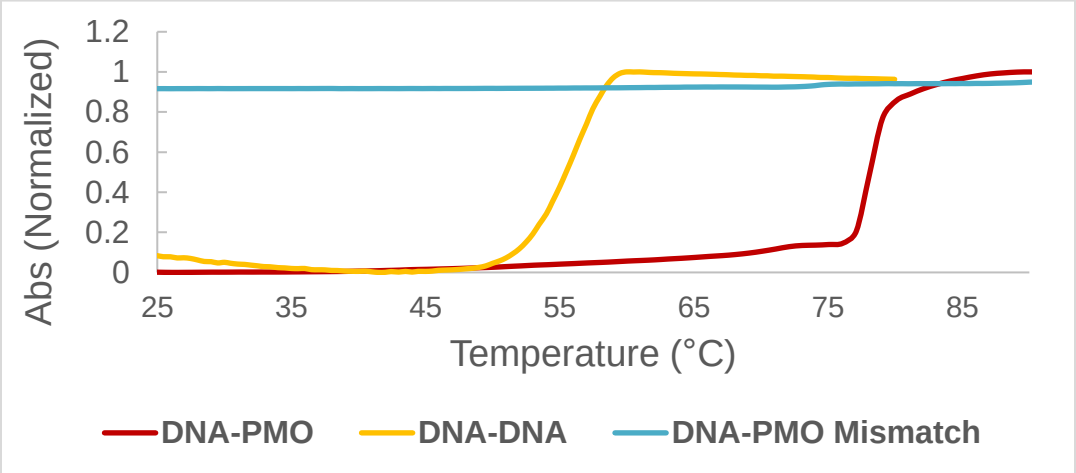

Figure 6.5. Melting behavior of DNA and PMO SNAs bearing complementary or non-complementary sequences.

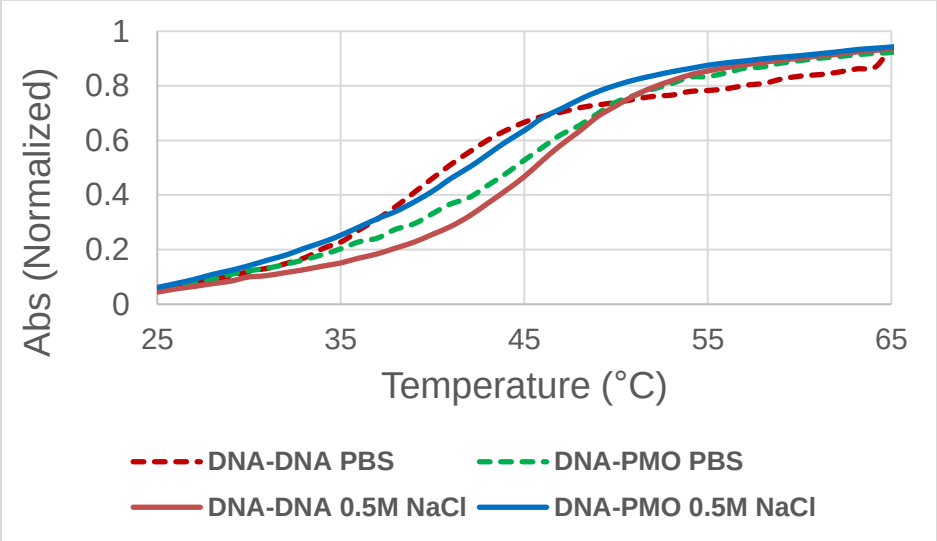

Figure 6.6. Melting behavior of single-stranded DNA-DNA and DNA-PMO pairs at either physiological salt concentration (1X PBS) or elevated salt concentration (0.5M NaCl)

Cellular uptake experiments by flow cytometry and confocal microscopy in ovarian cancer cells (SKOV-3) and human cervix carcinoma (KB) cells demonstrated high uptake of PEG1K/PMO SNAs compared to single-stranded PMOs. The SNAs for cellular uptake were prepared with a 2:1 ratio of PEG1K to PMO oligonucleotides, and consequently their colloidal stability was enhanced. Typically, cationic peptides or polyamines must be appended to morpholinos to aid their passage across the cell membrane. Here, we demonstrate that their dense loading onto a gold nanoparticle is sufficient for transfection to occur. In SKOV-3 cells, uptake of Cy5-labeled PEG/PMO SNAs (2.5 nM) was approximately two orders of magnitude higher than the free Cy5-labeled single-stranded morpholino (250 nM) (Figure 6.7). This same trend is observed when comparing the cellular uptake of single-stranded DNA to DNA-SNAs. Cellular uptake in KB cells was monitored by confocal microscopy at 2 hours and 24 hours, showing low uptake of PMO SNAs at the 2-hour time point but significant punctate perinuclear fluorescence at the 24-hour time point, suggesting their uptake occurs via an endocytotic pathway (Figure 6.8).[314] We hypothesize that the shorter PEG is necessary to expose the nucleobases so that they

can be recognized by cell surface receptor(s), as the outer nucleobase presentation on analogous DNA SNAs has been shown to strongly influence their rate of endocytosis.[71]

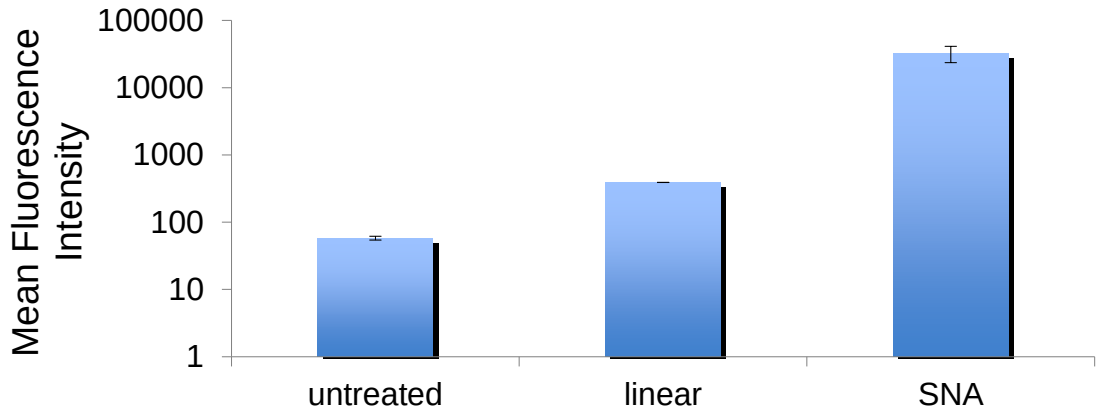

Figure 6.7. Uptake of PMO SNAs in SKOV-3 ovarian cancer cells after 24 h compared to single-stranded PMO oligonucleotides. Note that the y-axis is represented on a logarithmic scale for clarity.

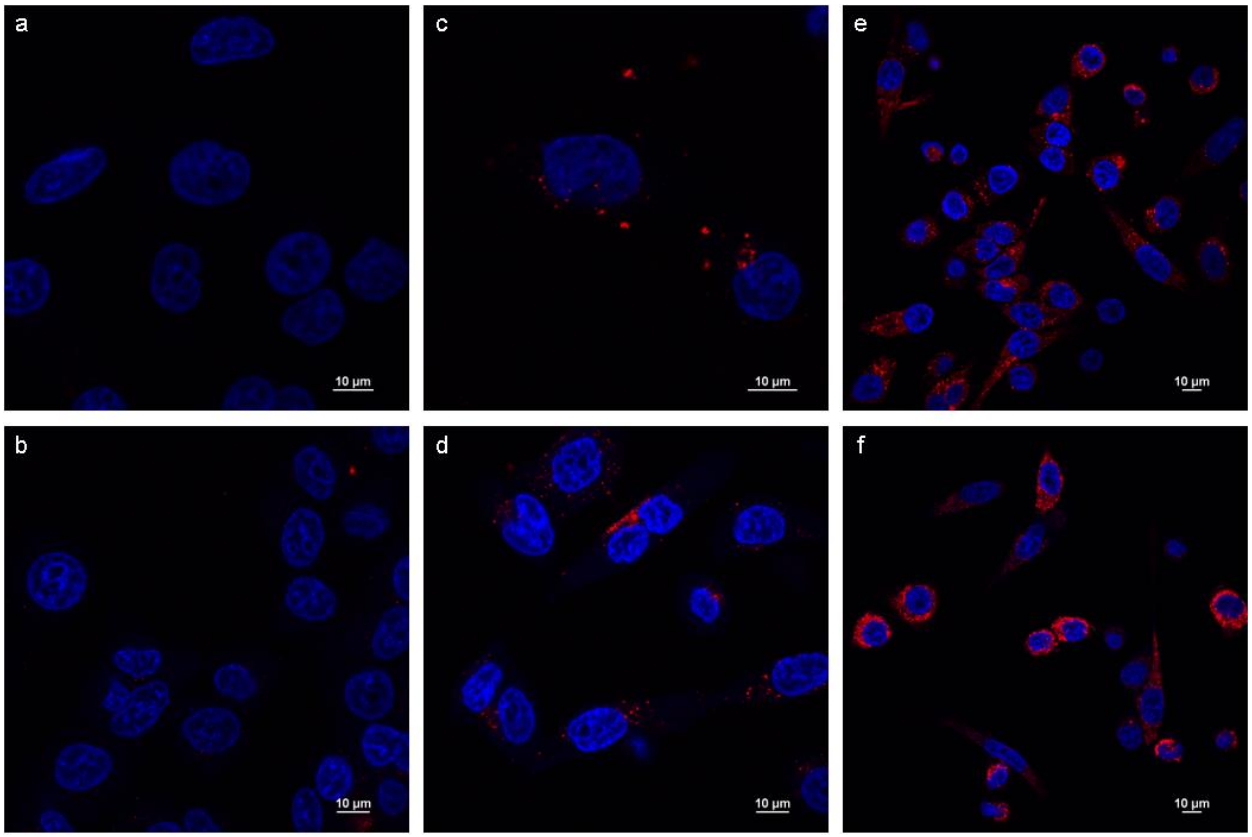

Figure 6.8. Confocal microscope images of cellular uptake in KB cells. Treatments: 250 nM single-stranded Cy5-PMO after a) 2 hours and b) 24 hours, or PMO SNA (2. nM) after c) 2 hours and d) 24 hours, or DNA SNA after e) 2 hours and f) 24 hours. Bright-field images are omitted for clarity.

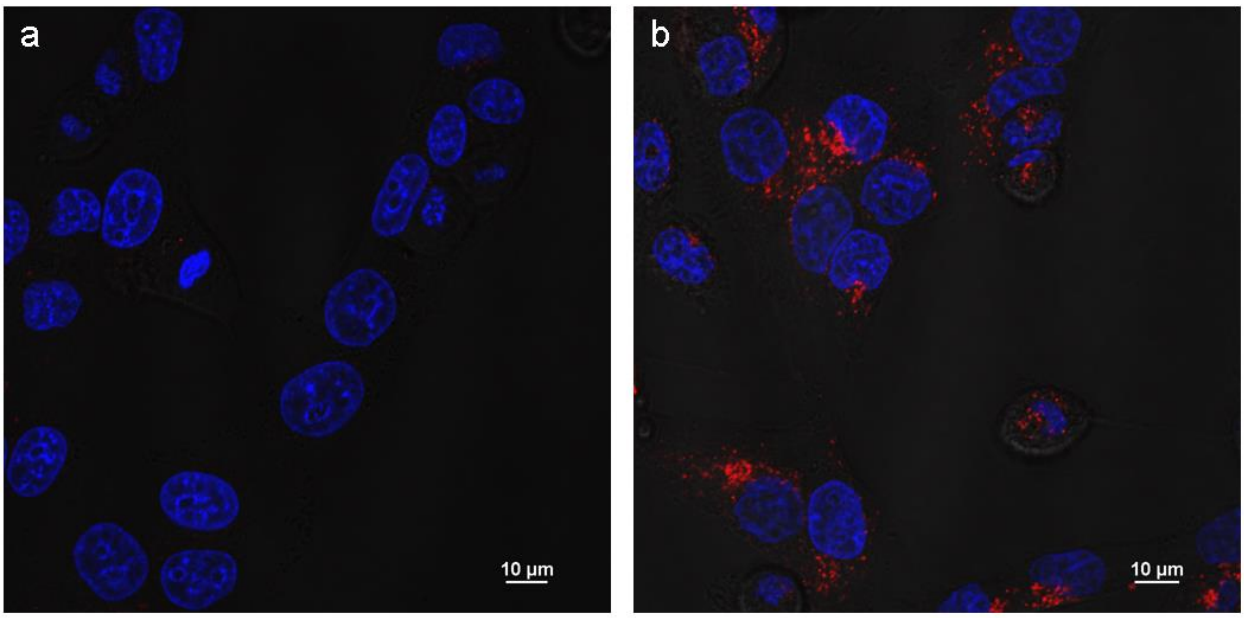

Figure 6.9. Comparison of uptake of PEG5K/PMO and PEG1K/PMO SNAs. a) Uptake in KB cells of PEG5K/PMO SNA after 24 hours. b) Uptake in KB cells of PEG1K/PMO SNA after 24 hours.

Having demonstrated the ability of morpholino-SNAs to enter cells without the need for special transfection agents or chemical modification of the oligonucleotides, we then turned our attention to the ability of the SNA to deliver antisense morpholinos to the cytosol to knock down disease-related mRNA. In contrast to other commonly employed antisense oligonucleotides such as siRNA, which trigger mRNA degradation by RNAse H, morpholino oligonucleotides exert their gene knockdown effect by tightly binding to the target mRNA and physically blocking movement of the ribosome to prevent transcription. For this purpose, we chose two previously-validated morpholino sequences targeting human epithelial growth factor 2 (HER2).[315] HER2 is upregulated in a variety of cancer cell lines and is involved in signal transduction pathways leading to malignant cell growth.[197]

PMO SNAs were synthesized by modifying citrate-capped gold nanoparticles with a 2:1 ratio of 1000 Da PEG-thiol and PMO-OPSS oligonucleotides. Active HER2-targeting SNAs (Target1-SNA, Target2-SNA) along with SNAs bearing an inactive PMO sequence (NonTarget-

SNA) were synthesized and purified (Table 6.1). As a positive control, a validated DNA sequence for antisense HER2 knockdown was also synthesized for delivery with the commercial transfection agent Lipofectamine®. SKOV-3 cells were treated for 24 hours with 2.5 nM of either Target1-SNA, Target2-SNA, or NonTarget-SNA. The cells treated with Lipofectamine and DNA were dosed according to manufacturer instructions (25 nM DNA).

Analysis of HER2 protein expression by Western blot revealed high knockdown efficiency (>50%) for both targeted PMO SNAs (Figure 6.10), with some non-specific knockdown by the non-targeting SNA. However, the positive control failed to produce any knockdown effect. At the time of this writing, studies are currently underway to test other positive controls such as cationic morpholinos or morpholinos co-delivered with Endo-Porter, a novel peptide developed by Gene Tools that facilitates endosomal escape of PMOs and other bioactive macromolecules.

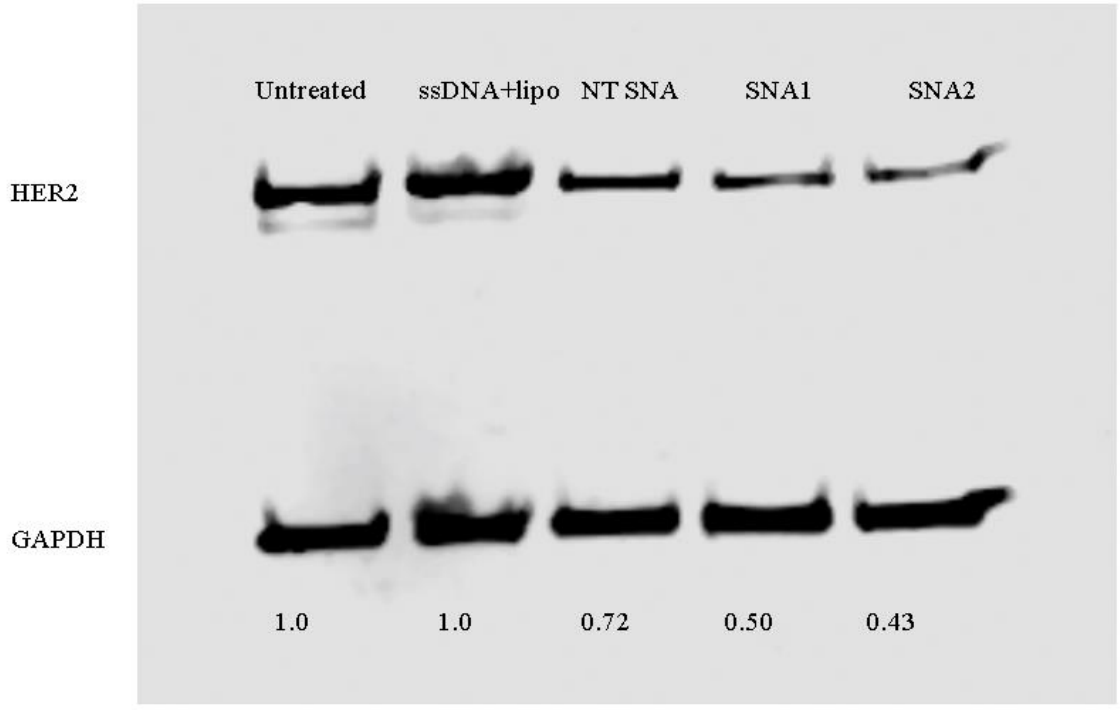

Figure 6.10. Analysis of HER2 expression in SKOV-3 cells by Western Blot. Lighter bands correspond to higher knockdown. Numerical values represent % inhibition of gene expression.

Conclusions. In conclusion, we have described a method for the synthesis of stable phosphorodiamidate morpholino oligonucleotide (PMO)-functionalized gold nanoparticles that exhibit the hallmark properties of spherical nucleic acids traditionally made from charged oligonucleotides (DNA, RNA) as opposed to neutral oligonucleotides. Co-functionalization of the gold surface with PEG enhances the colloidal stability of the nanoparticles and renders them resistant to salt-induced aggregation. Crucially, the PEG does not interfere with the ability of the PMO SNAs to capture target oligonucleotides or hybridize with complementary SNAs. We discovered that the cellular uptake of the PMO SNAs depends on the length of the co-adsorbed PEG, with shorter PEG lengths permitting cellular uptake. The uptake of PMO SNAs was nearly two orders of magnitude higher than their single-stranded PMO counterparts, an effect also observed with DNA SNAs compared to their corresponding linear DNA oligonucleotides. The cellular internalization of PMO SNAs could be visualized by flow cytometry and confocal microscopy in two different mammalian cell lines. Lastly, we examined the ability of the PMO SNAs to engage in gene knockdown without the use of any ancillary transfection agents. Our preliminary data suggests that PMO SNAs, once internalized, can interact with cytosolic mRNA to engage in intracellular gene regulation. Studies are ongoing to validate useful positive controls for quantitative comparison of knockdown efficiency with previously-described antisense therapies, and further improve the knockdown effect with more careful tailoring of the PMO SNA surface composition and the mRNA targeting sequences.

Chapter 7

Conclusions

This dissertation has focused on the development of nucleic acid-based nanoconstructs for cancer therapy and imaging, specifically those fabricated with a dense shell of oligonucleotides arranged around a spherical core (SNAs). The first part of the dissertation (Chapters 2 and 3) emphasizes the use of metal coordination bonds as a chemically orthogonal strategy to assemble oligonucleotides into nanoparticles, and the behavior of coordination polymer-DNA based nanoconstructs in cell culture, specifically their cellular uptake and gene knockdown capability. A metal-ligand pair based on FDA-approved materials was identified comprising Fe^{3+} and 3,4-hydroxypyridinones (3,4-HOPOs) with excellent stability and biocompatibility. Direct crosslinking of DNA strands via Fe^{3+}-mediated assembly afforded nanoparticles and/or metallogels depending on the reaction conditions. The nanoparticles assembled in this fashion did not exhibit spontaneous cellular uptake, demonstrating the importance of controlled oligonucleotide geometric orientation in the nanoparticle fabrication process. However, direct cationic lipid transfection of the particles indicated they were capable of intracellular gene regulation, indicating that the metal-ligand modification of DNA did not affect its binding with mRNA. Thus, a new bioorthogonal assembly strategy for DNA nanomaterials was discovered for further elaboration.

The coordination chemistry developed in Chapter 2 was further adapted to create Fe^{3+} infinite coordination polymer (ICP) nanoparticles which could be subsequently functionalized with oligonucleotides. In Chapter 3, synthesis of colloidal nanoscale ICPs was achieved by

mixing a rigid azide-modified *bis*-hydroxypyridinone ligand with Fe^{3+} under dilute aqueous conditions, leading to the spontaneous formation of "clickable" azide-bearing nanoparticles. The N_3-ICP particles were converted into SNAs in a single step by the addition of NaCl and cyclooctyne-functionalized DNA. The resulting DNA-ICP particles exhibited all the typical properties of conventional AuNP-based SNAs, including cooperative thermal denaturation curves with complementary particles, active cellular uptake, and intracellular gene knockdown. Furthermore, the pH-sensitive nature of the Fe^{3+} coordination bonds employed in the particle core afforded a novel means for biodegradation of the nanoparticles once internalized into cells. In summary, the studies in Chapters 2 and 3 established a new bioorthogonal and biocompatible metal-mediated assembly method for nucleic acids. We also expect this research to lead to development of other therapeutic and diagnostic agents; for example, the Fe^{3+} ICPs described in Chapter 3 could also function as magnetic resonance imaging (MRI) contrast agents.[316] Due to the propensity of the ditopic HOPO ligand to precipitate metal ions out of solution, such molecules may also find applications in heavy metal sequestration and waste remediation.[317-318]

Chapter 4 also explores the fabrication of biocompatible cores for SNAs, this time relying on self-assembly of micelle-type structures to present a dense orientation of oligonucleotides on the particle surface. A rational design approach was also employed in this case, relying on FDA-approved polycaprolactone (PCL) as the core material due to its biocompatibility and pH-dependent hydrolysis in aqueous media. Two separate versions of the micelle SNA were synthesized to study the effect of DNA density on the particle surface: a linear block copolymer of PCL and DNA as well as a brush-type block copolymer comprising PCL bearing multiple DNA strands at the terminus. In agreement with the previous studies, it was found that the DNA-brush block copolymer (DBBC) had enhanced polyvalent behavior compared to the linear DNA

block copolymer (DBC) owing to the higher DNA surface density. Specifically, the T_m of the DBBC SNA with complementary SNAs was enhanced compared to its linear counterpart, as well as the degree of cellular internalization and target mRNA knockdown. The studies in Chapters 3 and 4 add further evidence to the central hypothesis that the properties of SNAs are largely core-independent and instead rely on the spherical orientation of nucleic acids on the surface as well as the density of their packing. Visualization of the cellular uptake of coordination polymer and micelle-cored SNAs by confocal microscopy strongly suggested that they are recognized and endocytosed in the same manner as traditional AuNP SNAs. Although recognition by a receptor other than SR-A cannot be ruled out, the polyvalent nature of the particles and their 3D geometric orientation of DNA is clearly responsible for their cellular uptake.

Chapters 5 and 6 see a return to the use of gold as the core material for SNAs, as the primary interest was in the functionality of their attached oligonucleotides and the need for rapid prototyping and synthesis of modified particles using established gold-thiol chemistry. The work in Chapter 5 was motivated by an idea to develop an *in vivo* pretargeting system for PET imaging based on SNAs, because of their polyvalency and rapid hybridization kinetics. This work led to the serendipitous discovery that replacement of charged nucleic acids (RNA, DNA) on the SNA surface with neutral phosphorodiamidate morpholino oligonucleotides (PMOs) markedly affects their biophysical properties while still retaining the key behaviors normally associated with SNAs such as cooperative hybridization and spontaneous cell entry, as further investigated in Chapter 6. Chapter 5 focuses on the use of ultrasmall (<3 nm) SNA gold nanoclusters (AuNCs) as *in vivo* PET imaging agents via a pre-targeting strategy. Gold was chosen since it can be alloyed with radionuclides for PET imaging and biodistribution studies, as well as the ease of surface functionalization with a variety of commercially available thiolated

ligands. Our initial design of the system relied on tumor-targeted sub-3 nm DNA SNA AuNCs designed to capture and release a radiolabeled oligonucleotide *in vivo*, allowing for sensitive and specific detection of tumor tissue. Specifically, our interest was in targeting the CCR5 receptor which is over-expressed in triple-negative breast cancer. Alloying of the gold core with ^{64}Cu enabled tracking of the biodistribution of the SNAs by PET. Though the DNA AuNC SNAs demonstrated acceptable capture kinetics *in vitro*, their pharmacokinetic behavior was hampered by extremely short blood circulation time and high accumulation in the liver and spleen. Trial-and-error led to the replacement of DNA with PMO oligonucleotides, dramatically enhancing the blood circulation time of the ^{64}CuAuNCs. This discovery alone could have a major impact on the use of SNAs as therapeutic agents, as current human and animal trials rely on charged SNAs of which only a small fraction may end up in the desired organ(s).

With PMO AuNCs in hand, we carried out kinetics experiments to determine the rate of capture of a complementary RNA strand. Under physiological conditions, the bimolecular rate constant for hybridization of the target RNA far exceeded our expectations, outperforming covalent bioorthogonal click reactions employed in other pretargeting systems. We also studied the cellular interactions of PMO AuNCs, specifically to determine whether they would be internalized like their DNA counterparts or remain on the cell surface to facilitate hybridization with a circulating radiotracer. We found that the PMO AuNCs were internalized to a lower degree than DNA AuNCs, and additionally, inclusion of a CCR5-targeting ligand on the particle surface enhanced cell suface association. Our positive *in vitro* data prompted us to examine the pretargeting system *in vivo* with tumor-bearing mice.

We first tested the ability of PMO AuNCs to localize in tumor tissue and capture a complementary radiolabeled RNA strand. Our initial studies focused on optimizing the

pretargeting interval of the nanosystem, also known as the "wait time" between injection of the non-radioactive capture component and the radioactive cargo. In tumor-bearing mice, our results indicated that little ^{64}Cu-RNA accumulated in the tumor tissue four hours after injection of the PMO AuNC, with a significant increase in tumor accumulation observed after a 24 or 48 hour delay. Using this information, we designed a study to determine the specificity of the pretargeting effect by comparing the tumor uptake of a scrambled radiolabeled RNA to a complementary radiolabeled RNA, demonstrating that the complementary sequence exhibits superior tumor accumulation. In addition, we also sought to compare the pretargeting system against a direct-targeted ^{64}CuAuNC SNA, to evaluate whether the pretargeting strategy improves tumor uptake of ^{64}Cu and reduces background in off-target organs relative to delivering the radiotracer directly in nanocluster form. In addition, their targeting efficiency against CCR5-positive tissue must be compared to particles without the CCR5-targeting peptide. This study is currently underway. Future directions for this work include improving the kinetics of hybridization by employing an all-PMO nanosystem (nanocluster, tracer, and competitor) as well as studying PEGylation of the tracer to improve circulation time and subsequent tumor accumulation. The nanosystem is not limited to PET imaging either; the tracer or competitor cargo can also deliver treatment in the form of a cytotoxic drug or a therapeutic radionuclide. Lastly, we expect that the biocompatibility of the pre-targeting nanoclusters can be further enhanced by switching to copper cores, which do not accumulate in the body like gold, yet can still be alloyed with ^{64}Cu for biodistribution and imaging studies.[319]

In Chapter 6, we decided to look more in depth at the chemical and biological properties of PMO-based SNAs using the typical array of experiments used to study SNA behavior. Commercially-available 10 nanometer gold nanoparticles were used as the core material to

generate monodisperse and easy-to-characterize PMO SNAs as a proof of concept, though as discussed in previous chapters, virtually any core material could be utilized for clinical translation of these nanoconstructs. Optimization of synthetic conditions gave colloidally stable PMO SNAs which resisted salt-induced aggregation and exhibited neutral surface charge as evidenced by zeta potential measurements. Loading studies indicated that approximately 100 PMO oligonucleotides could be adsorbed on the surface of a 10 nanometer particle along with PEG to impart colloidal stability. The binding kinetics of the resulting PMO SNAs were studied, demonstrating exceptionally fast bimolecular rate constants for hybridization with complementary oligonucleotides and picomolar binding affinity. The kinetics of the 10 nm PMO SNAs were compared with analogous DNA SNAs as well as the AuNC-based SNAs. Oligonucleotide charge and surface density were found to play a major role in the rate constants for complementary strand capture, in agreement with previously published studies on DNA hybridization kinetics with charged and neutral oligonucleotides both in solution and on surfaces. The PMO SNAs also exhibited cooperative melting behavior and enhanced melting transition temperatures when hybridized with complementary SNAs. These results prompted us to investigate whether PMO SNAs interact with cells in the same way as DNA SNAs.

Optimization of synthetic conditions (namely the molar ratio and length of coadsorbed PEG) afforded PMO SNAs capable of spontaneous cellular entry. By flow cytometry and confocal microscopy, PMO SNAs were found to enter mammalian cells at a greater rate than single-stranded PMOs, in an analogous fashion to DNA SNAs. Compared to DNA SNAs, however, PMO SNAs showed lower cellular uptake. Despite this difference, we decided to test the antisense gene regulation capability of PMO SNAs due to the differing mechanisms of gene knockdown between DNA and PMOs. DNA binding to mRNA triggers degradation of the

mRNA by RNAse-H, preventing ribosomal translation. In contrast, PMO binding to mRNA prevents movement of the ribosome along the mRNA, effectively blocking transcription. Due to the much higher affinity of PMOs for complementary mRNA, we theorized that PMO SNAs could engage in gene regulation despite their modest uptake relative to DNA SNAs. Preliminary results suggest the PMO SNAs are capable of knockdown and further studies are underway to compare against a panel of validated positive controls targeting the same messenger RNA.

Hopefully, this dissertation has conveyed the importance of nucleic acids in nanomedicine, as both chemically programmable structural components and bioactive therapeutic agents. Specifically, the discovery of spherical nucleic acids has advanced the field of biomedicine and enabled new clinically-relevant technologies in gene regulation and biodetection. The work presented herein demonstrates a multi-faceted approach to further increase the clinical viability of SNAs as therapeutic, diagnostic, and bioorthogonal conjugation agents. Detailed studies of SNA core composition as well as oligonucleotide composition have led to a better understanding of the basic chemical properties of SNAs, their cellular interactions, and their *in vivo* pharmacokinetics. Ideally, these advances will have major implications in the treatment and detection of diseases, especially those with poor prognoses, such as cancers of the brain, lung and breast, as well as other afflictions associated with significant mortality such as cardiovascular disease, amyotrophic lateral sclerosis (ALS), and spinal muscular atrophy.

Appendix

Chapter 2 Supporting Information

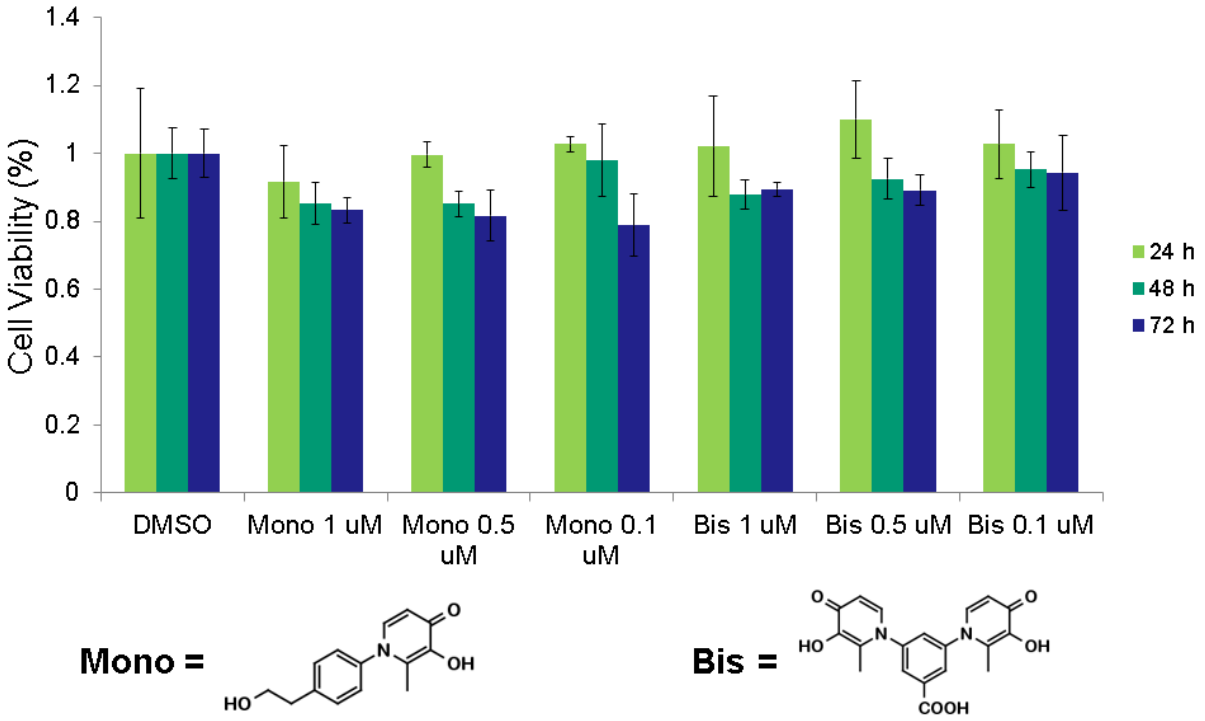

Figure A2.1. MTT toxicity assay of 3,4-HOPO chelating ligands.

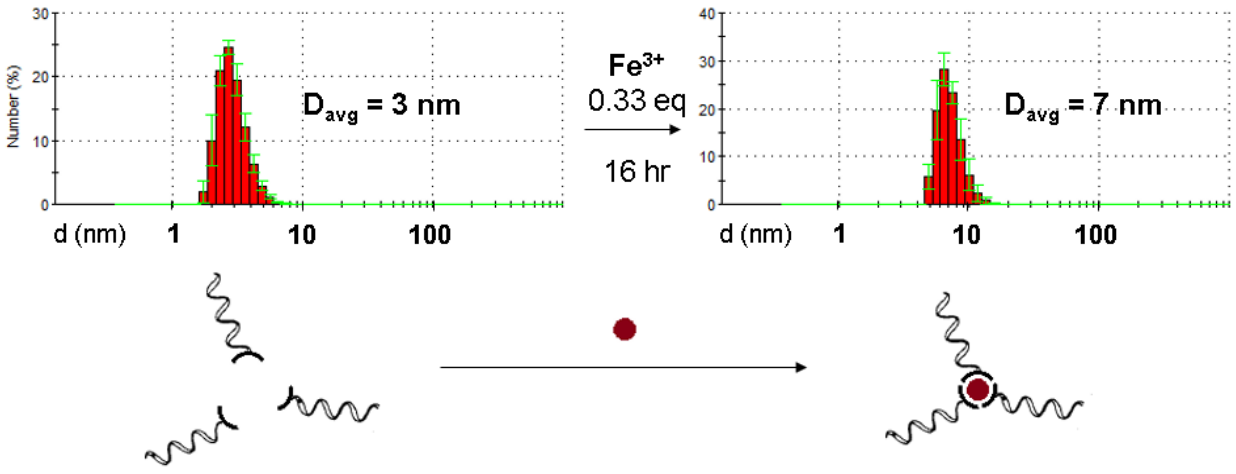

Figure A2.2. Change in hydrodynamic radius upon formation of $Fe(DNA)_3$ complex.

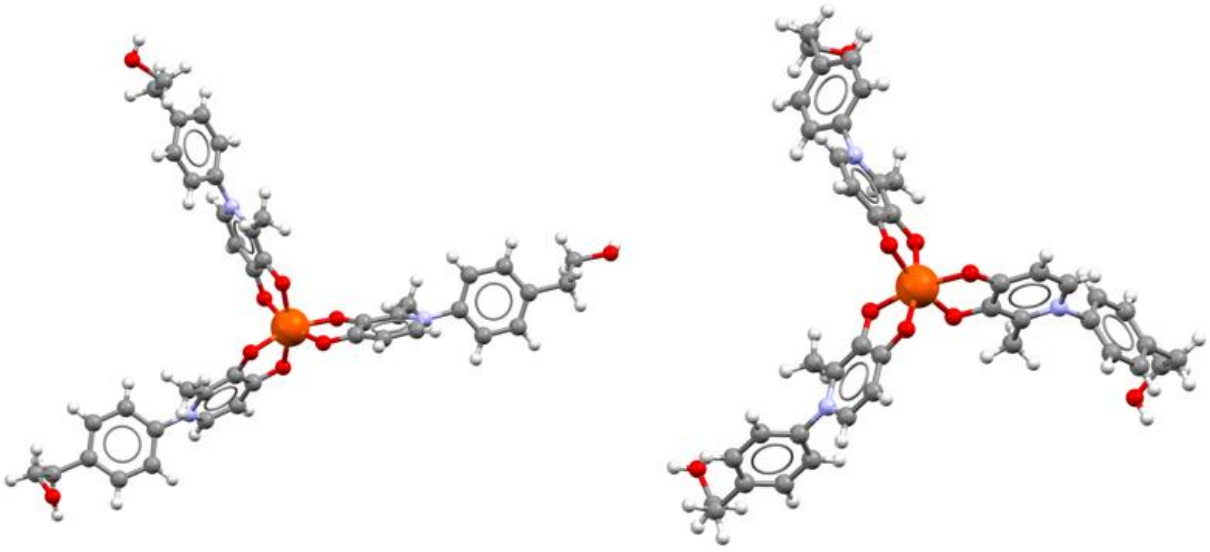

Figure A2.3. Crystal structures of Λ-*mer*-FeL_3 (left) and Δ-*fac*-FeL_3 (right)

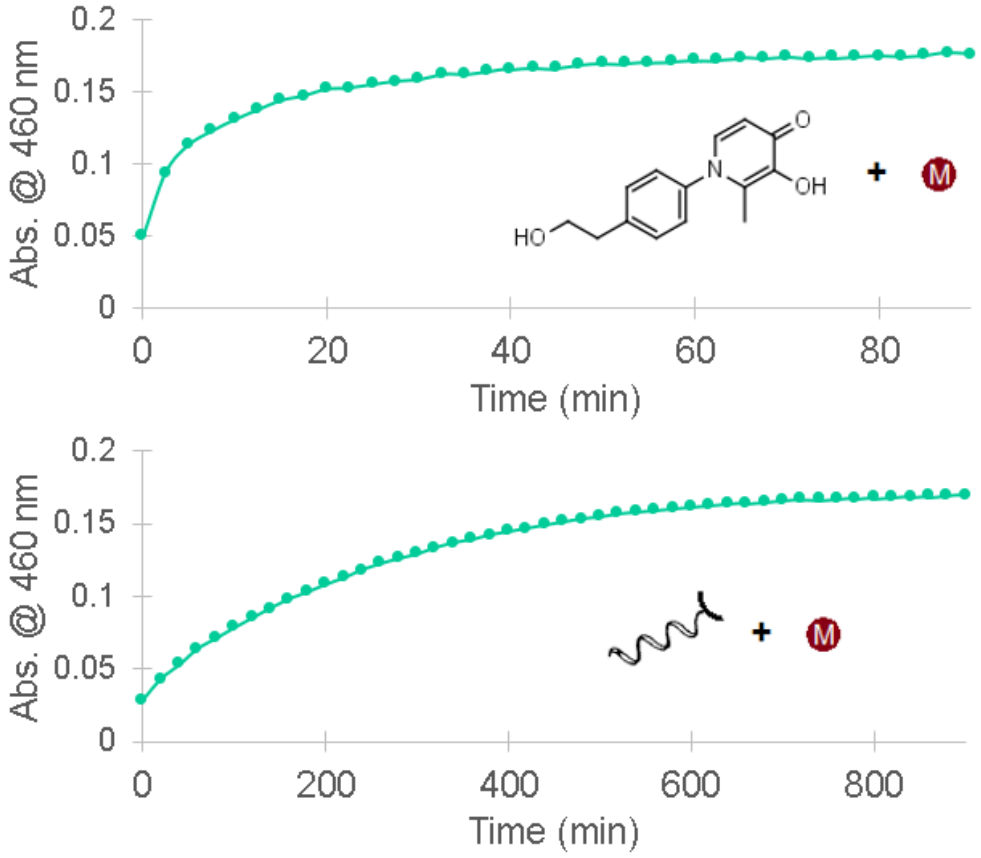

Figure A2.4. Diffusion-limited binding kinetics of free ligand with Fe^{3+} compared to DNA-ligand conjugate. Conditions: 100 µM ligand, 33 µM $Fe(NO_3)_3 \cdot 9H_2O$, 1X PBS, RT

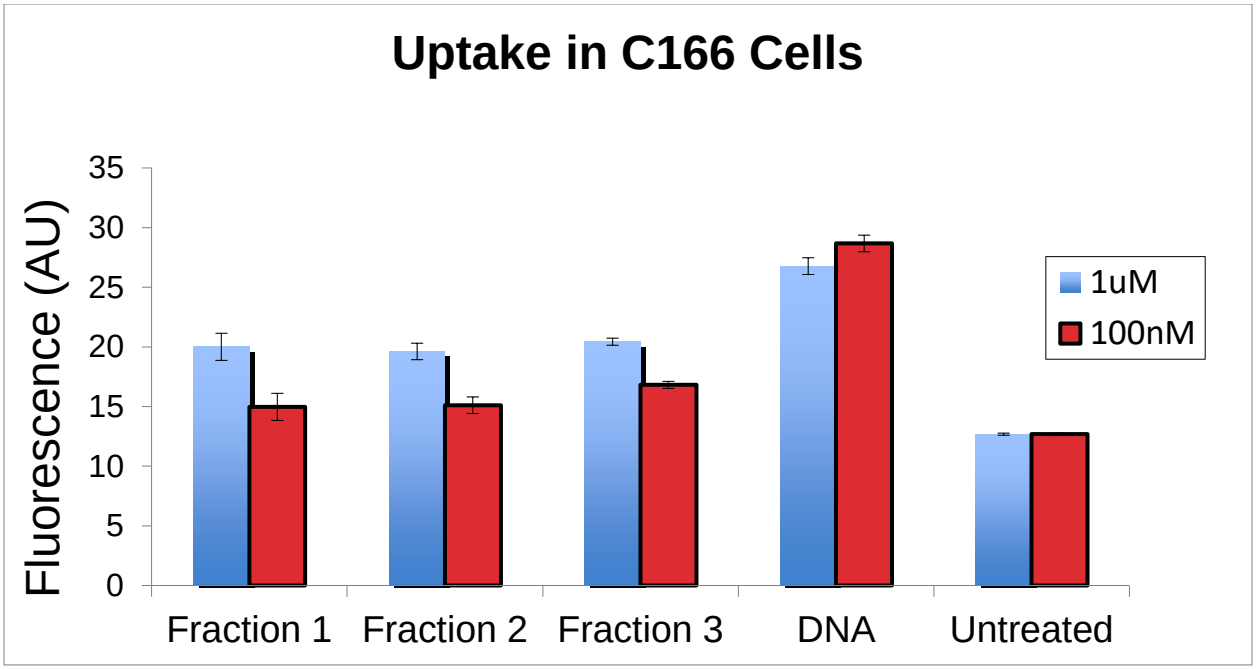

Figure A2.4. Uptake of different fractions of fluorescein labeled DNA-Fe^{3+} nanoparticles in C166 cells compared to the free DNA.

Chapter 3 Supporting Information

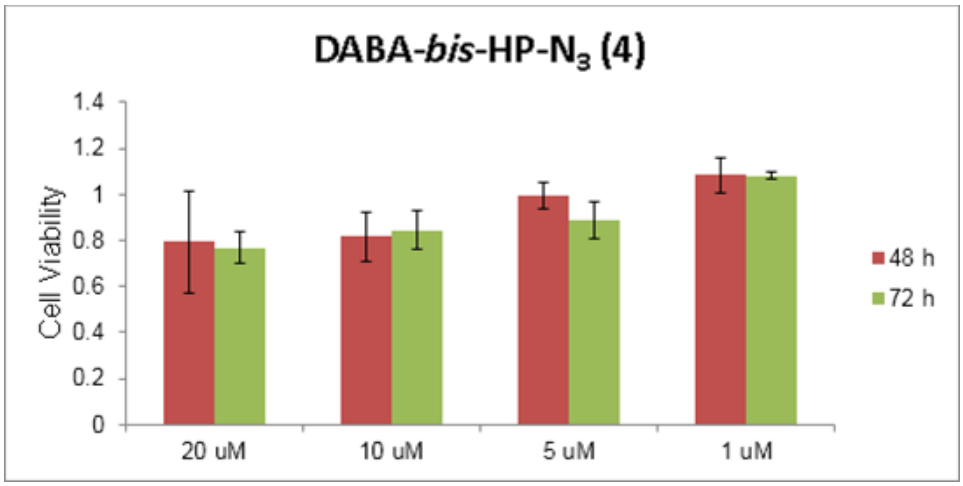

Figure A3.1. MTT toxicity assay of DABA-*bis*-HP-azide ligand.

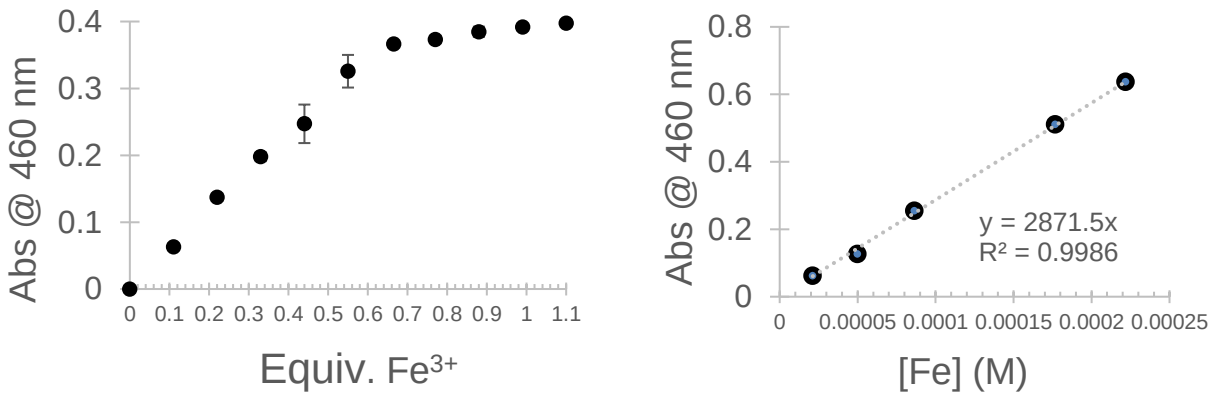

Figure A3.2. Left: titration of ligand **4** with iron(III). Right: determination of ε_{460} of ICP-N_3 particles

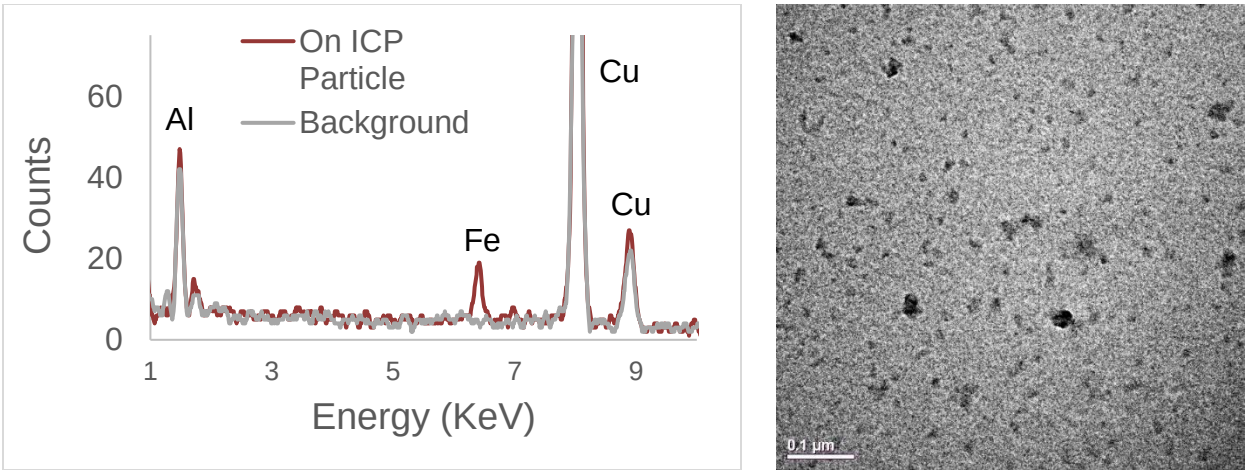

Figure A3.3. Left: EDX spectrum of background (copper TEM grid and aluminum holder) and ICP-N_3 particle. Right: TEM image of the same ICP-N_3 particle sample. Scale bar = 100 nm.

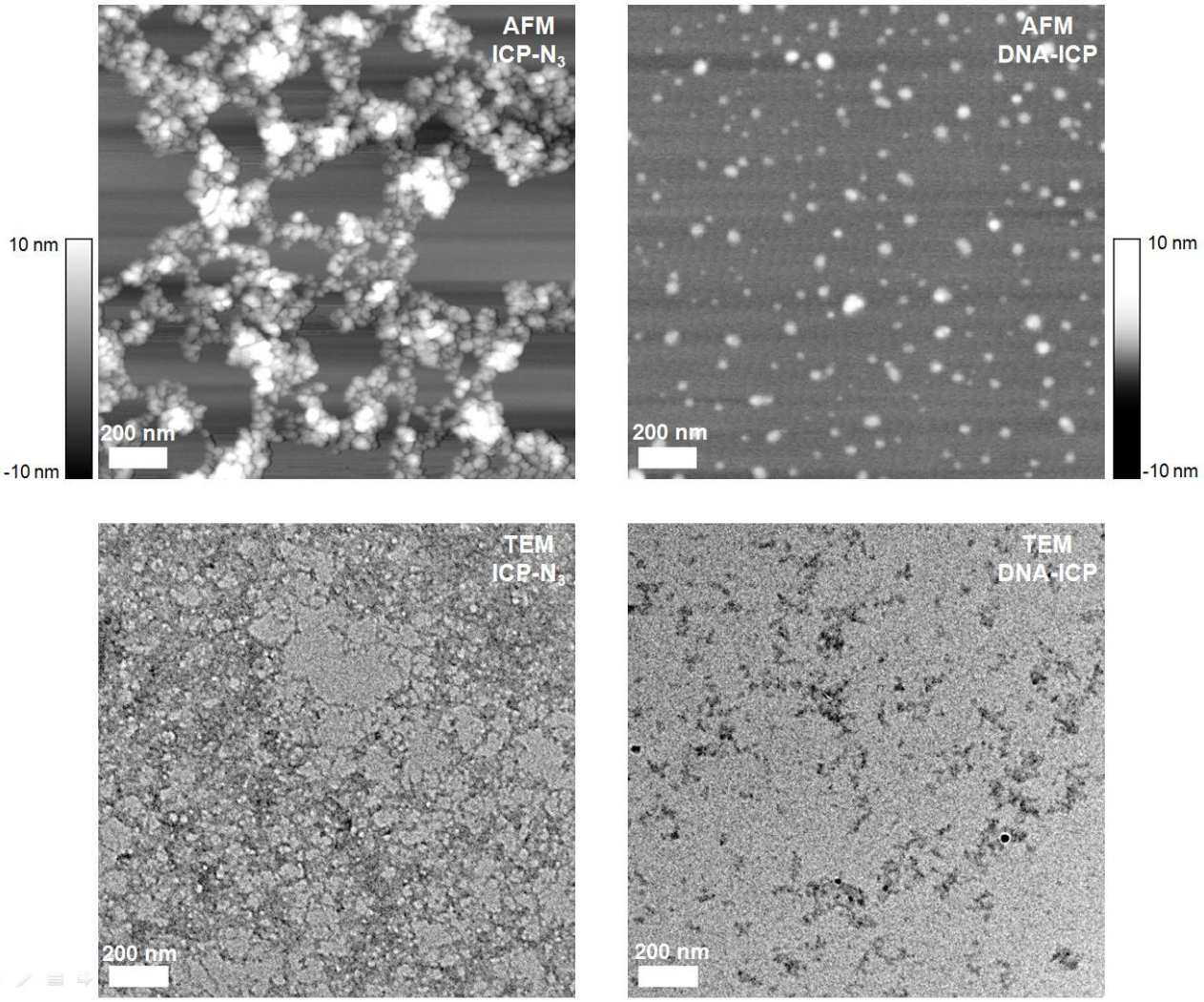

Figure A3.4. AFM and TEM images of ICP particles. Top left: Bare N_3-ICPs. Top right: DNA-ICPs. Bottom left: Bare N_3-ICPs. Bottom right: DNA-ICPs.

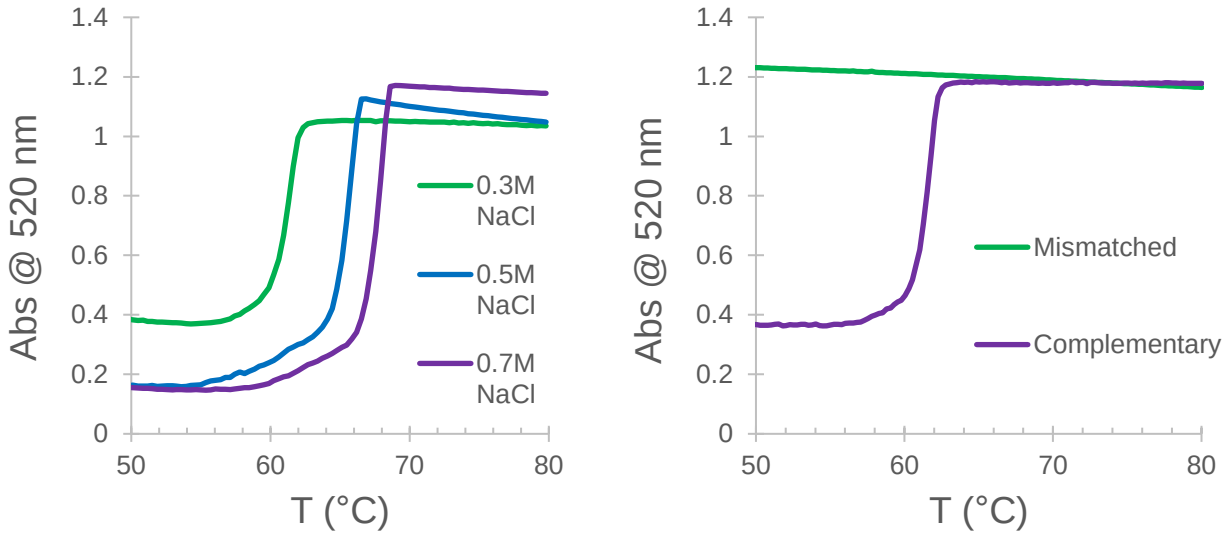

Figure A3.5. Thermal denaturation of complementary (left) and non-complementary (right) ICP/AuNP-DNA conjugates.

ICP Particle Type	ζ_{avg} (mV)	d_H (nm)	%A_{260} DNA
Bare	-18.9	14 ± 2	-
A-ICP	-35.2	31 ± 10	53%
B-ICP	-33.7	32 ± 8	60%
Her2-ICP	-31.1	31 ± 13	61%
NonTarget-ICP	-33.4	31 ± 11	65%
Cy5-ICP	-23.7	n/a*	14%

Table A3.1. Characterization of DNA-ICP conjugates. *DLS was not suitable for analysis of Cy5-containing particles. AFM imaging revealed particles with a similar size distribution. (37 ± 11 nm, NanoScope Analysis software)

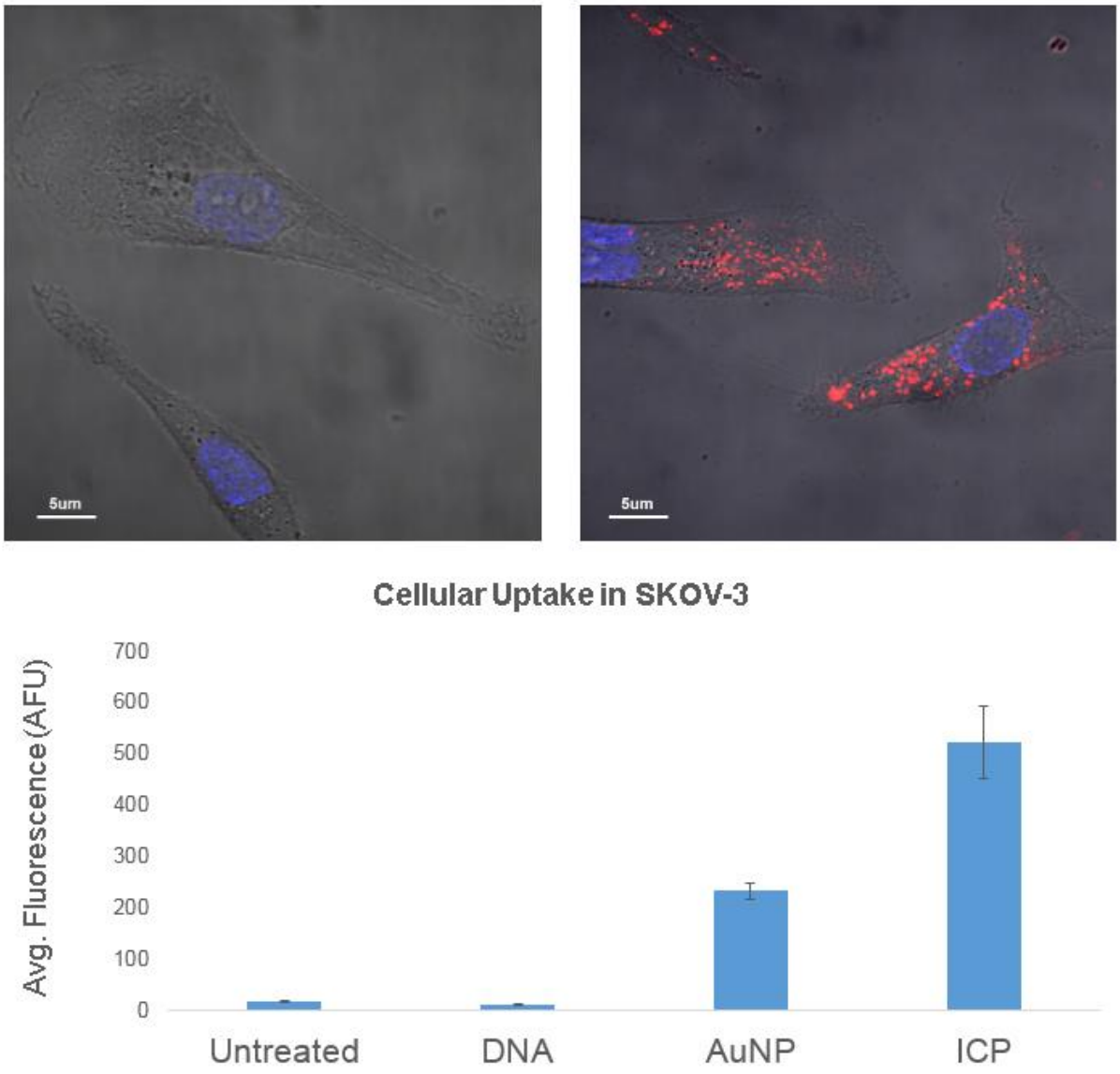

Figure A3.6. Top left: SKOV-3 ovarian cancer cells cells treated with fluorescent ssDNA. Top right: cells treated with DNA-ICPs bearing the same sequence. Bottom: flow cytometry analysis comparing untreated SKOV-3 cells with Cy5-labeled ssDNA, AuNP-SNAs, and DNA-ICPs. All treatments 100 nM total (DNA basis).

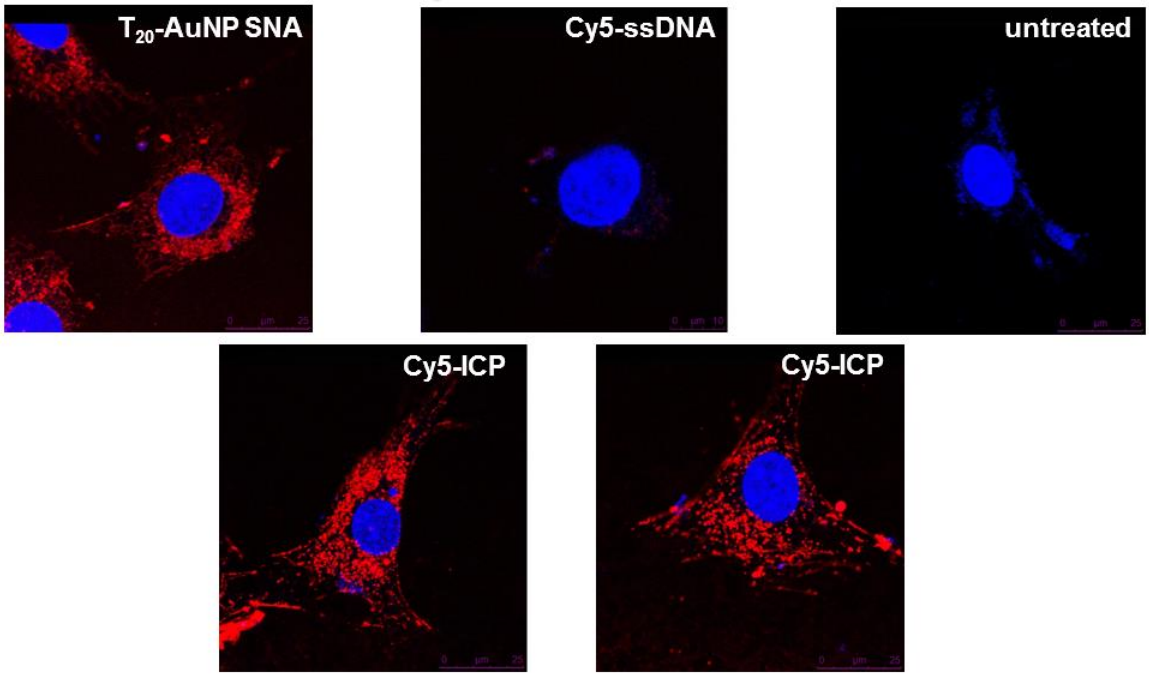

Figure A3.7. Cell uptake (C166 mouse endothelial) of Cy5-labeled AuNP-SNAs (top left) compared to free DNA (top middle), unreated cells (top right), and CCT-Cy5-DNA ICPs (bottom). All treatments 100 nM total (DNA basis).

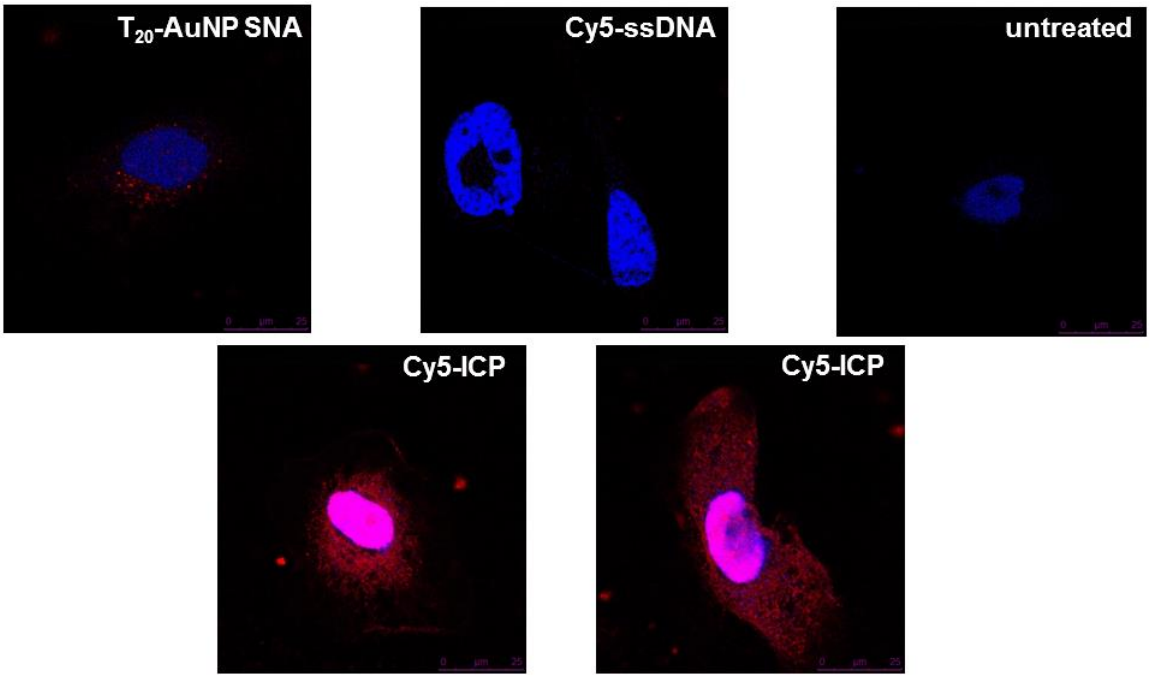

Figure A3.8. Cell uptake (HeLa cells) of Cy5-labeled AuNP-SNAs (top left) compared to free DNA (top middle), unreated cells (top right), and CCT-Cy5-DNA ICPs (bottom). All treatments 100 nM total (DNA basis).

Chapter 4 Supporting Information

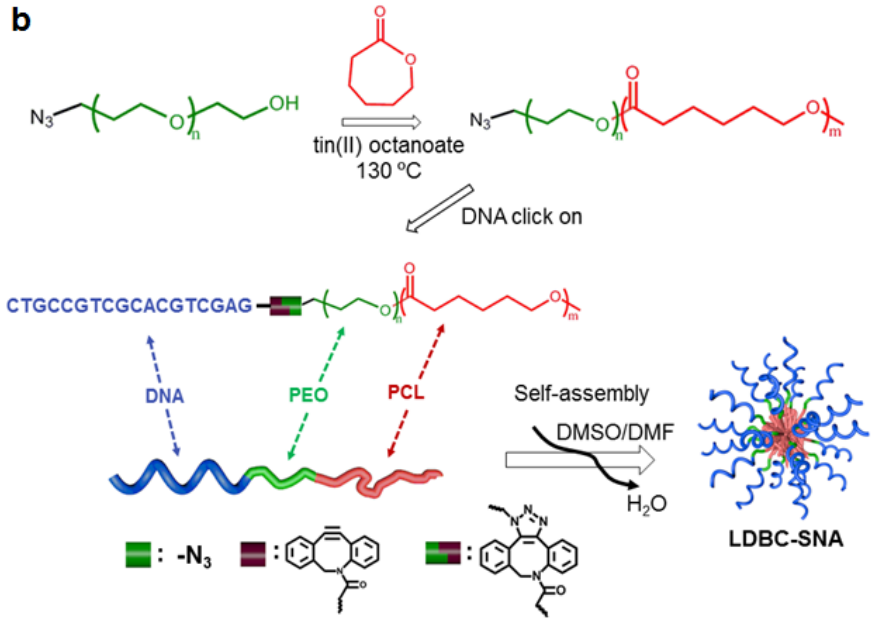

Figure A4.1. Synthetic scheme depicting (a) brush DNA-g-PCL-b-PCL and (b) linear DNA-b-PEO-b-PCL and their self-assembly into micelle-SNAs.

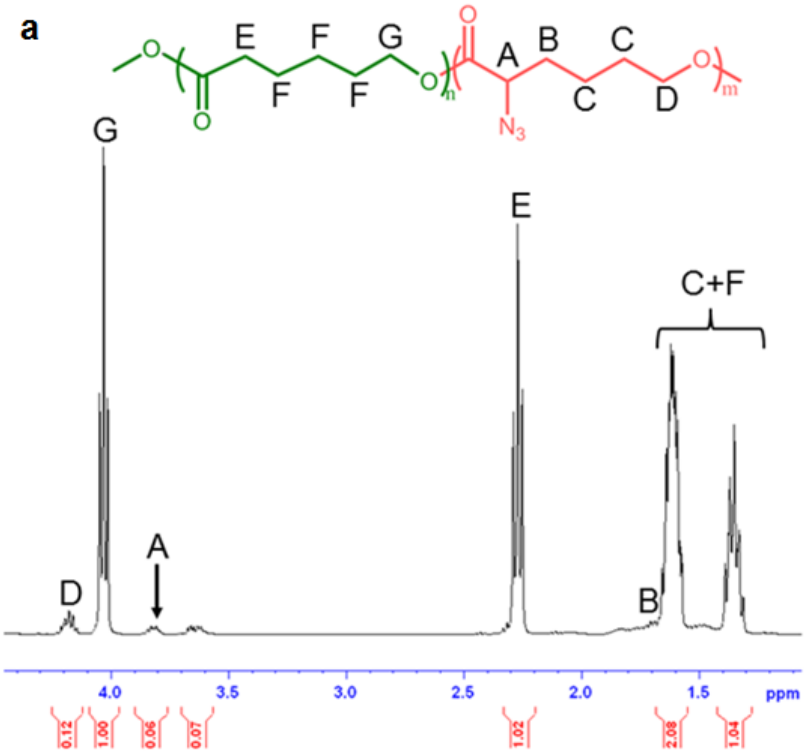

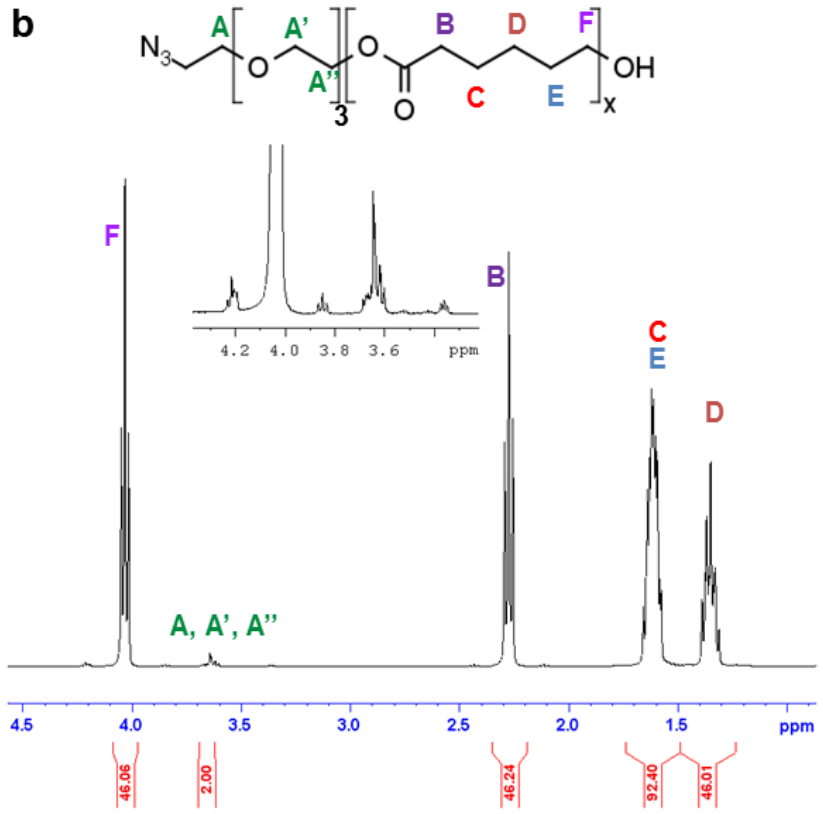

Figure A4.2. The ^{1}H NMR spectra of (a) poly(α-N_3-εCL-b-εCL) and (b) N_3-PEO-b-PCL.

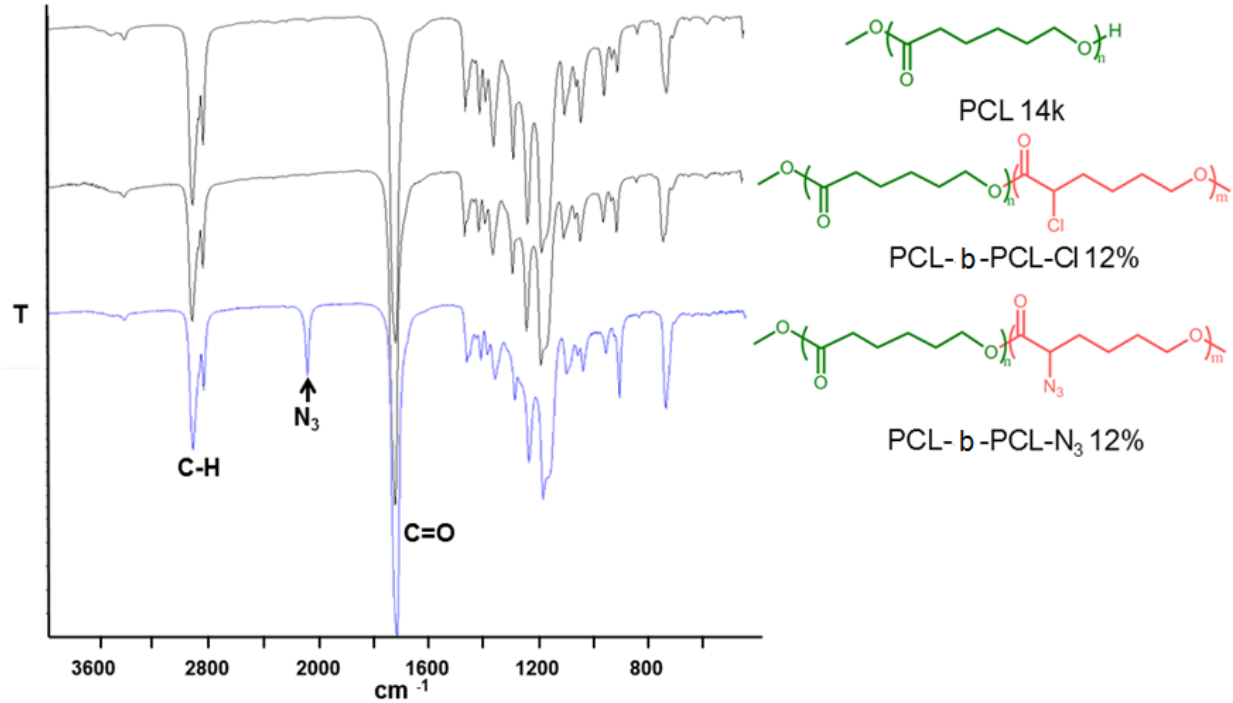

Figure A4.3. FT-IR spectra of as-synthesized azide modified diblock copolymer poly(α-N_3-g-εCL-b-εCL).

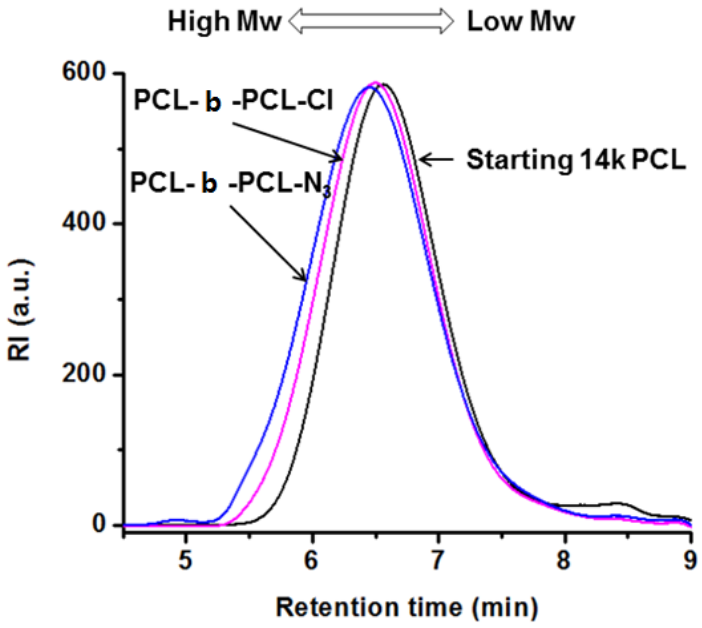

Figure A4.4. GPC analysis of as-synthesized poly(α-N3-εCL-b-εCL) and poly(α-Cl-εCL-b-εCL).

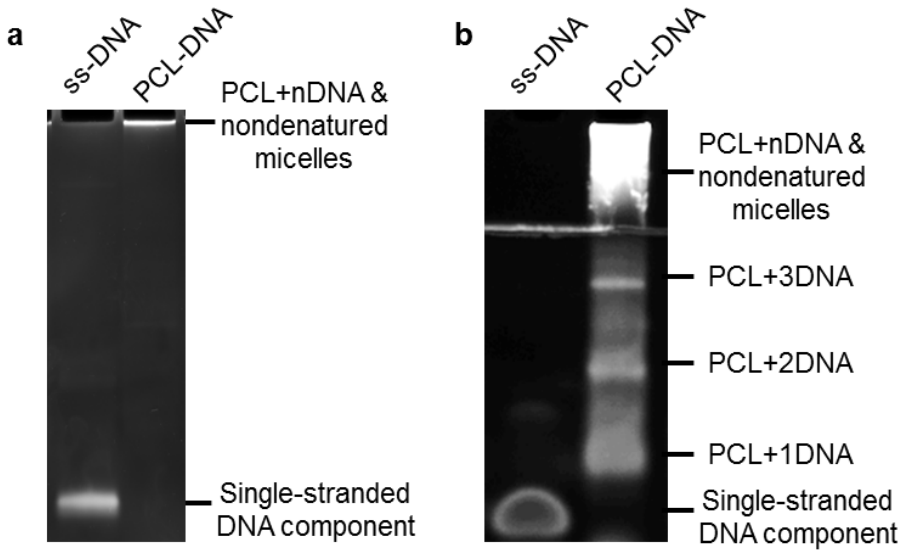

Figure A4.5. Poly acrylamide gel electrophoresis (PAGE) analysis of the DNA-brush block copolymer under denaturing condition (1×TBE buffer with 8 M urea, heated at 95 ºC for 10 min before running the gel). (a) Excess DNA strands were used to conjugate on the poly(α-N3-εCL-b-εCL), the as-synthesized DBBC based micelle-SNAs could not run into the gel, indicating the high stability of the micelle-SNA structure; (b) With lower ratio of DNA/PCL (~ 3) for DNA conjugation, a series of DNA-PCL conjugate strands can be observed on the gel, demonstrating multiple DNA strands can really grafted on a PCL chain. The majority of the DNA-polymer conjugates still remain as micelles which migrate extremely slowly on the gel.

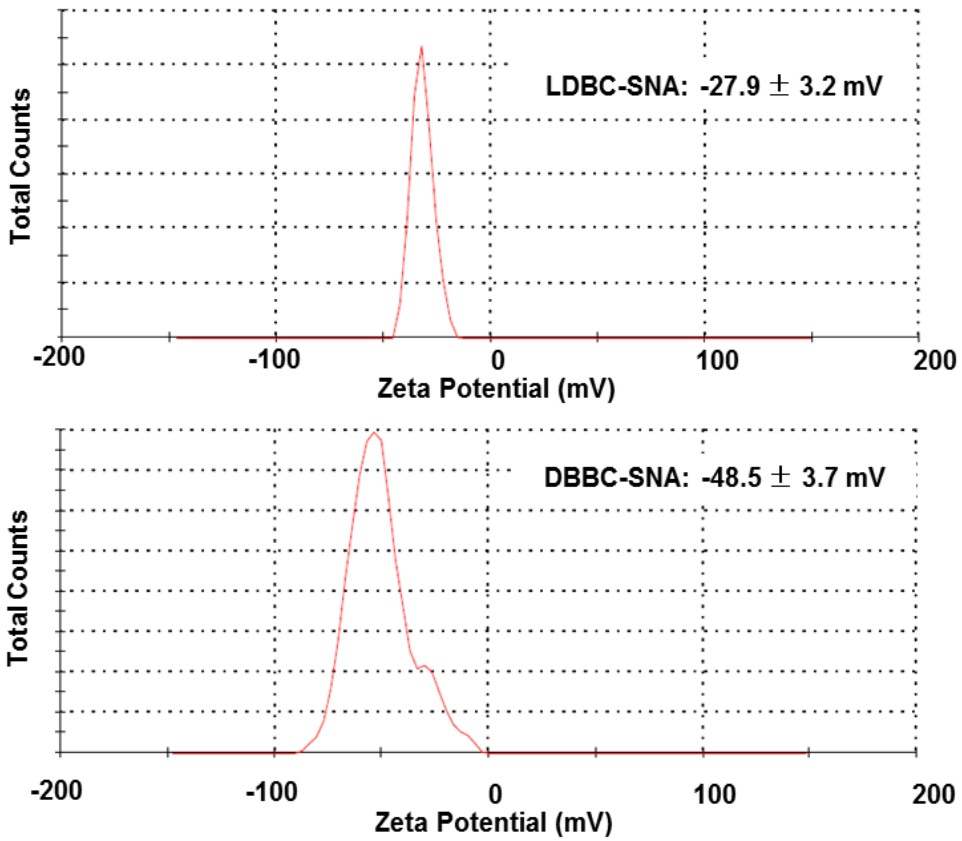

Figure A4.6. Zeta Potential of linear DBC micelle-SNA (upper panel) and DBBC micelle-SNA (lower panel).

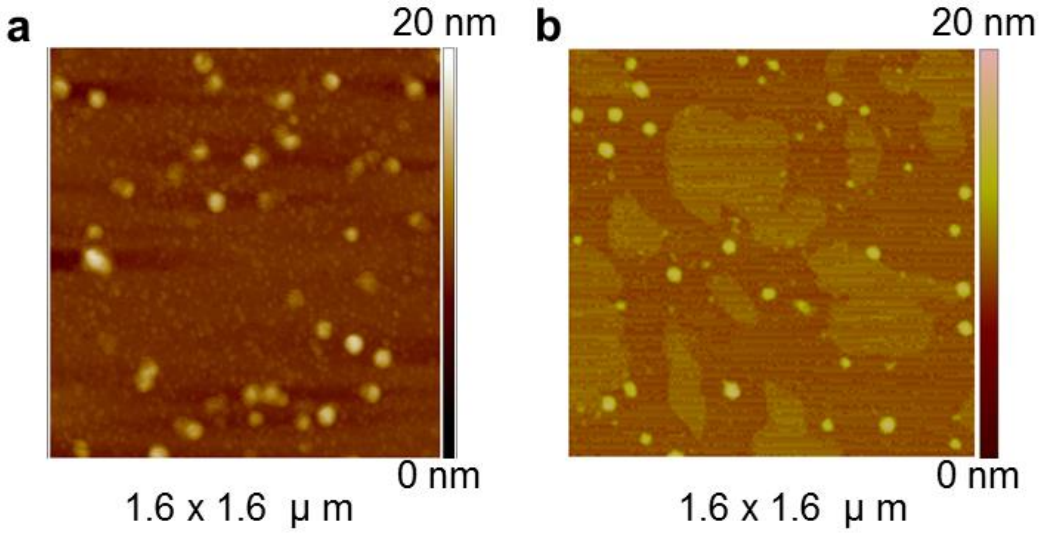

Figure A4.7. AFM images of linear DBC based micelle-SNA and DBBC micelle-SNA samples deposited on mica. (a) AFM image of linear DBC based micelle-SNA samples; (b) AFM image of DBBC micelle-SNA samples.

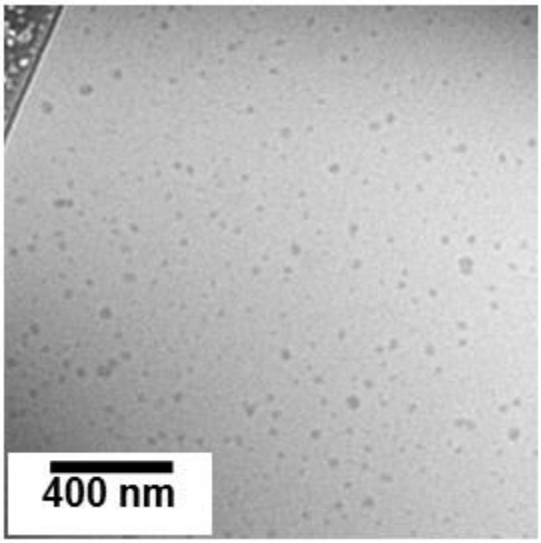

Figure A4.8. Cryo-EM image of linear DBC based micelle-SNA nanoparticles frozen in vitreous ice.

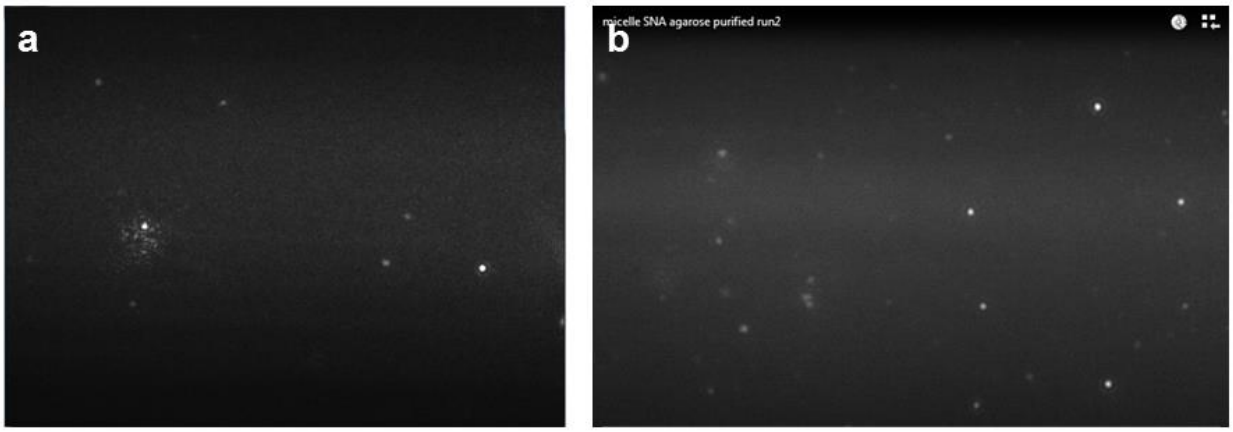

Figure A4.9. Particle concentrations of micelle-SNAs determined by Nanoparticle Tracking Analysis (NTA) using the Nanosight Instrument. (a) Screenshot of scattering pattern for 20 nm AuNP-SNA particles tracked by NTA, the standard sample concentration is 10 nM; (b) Screenshot of scattering pattern for DBBC micelle-SNA nanoparticles tracked by NTA instrument, the total DNA concentration for both linear DBC based micelle-SNA and DBBC micelle-SNA is 20 μM.

Sample	NTA Experiments	NTA Counts (particle/mL)	Average Counts (particle/mL)	Concentration
20 nm AuNP-SNA	1st run	0.64×10^8	0.77×10^8	10 nM
	2nd run	0.85×10^8		
	3rd run	0.82×10^8		
Linear DBC based micelle-SNA w/ total DNA of 20 µM	1st run	8.60×10^8	8.09×10^8	105 nM
	2nd run	8.12×10^8		
	3rd run	7.56×10^8		
DBBC based micelle-SNA w/ total DNA of 20 µM	1st run	5.16×10^8	5.12×10^8	67 nM
	2nd run	5.09×10^8		
	3rd run	5.10×10^8		

Table A4.1. List of nanoparticle concentrations determined by Nanoparticle Tracking Analysis using Nanosight.

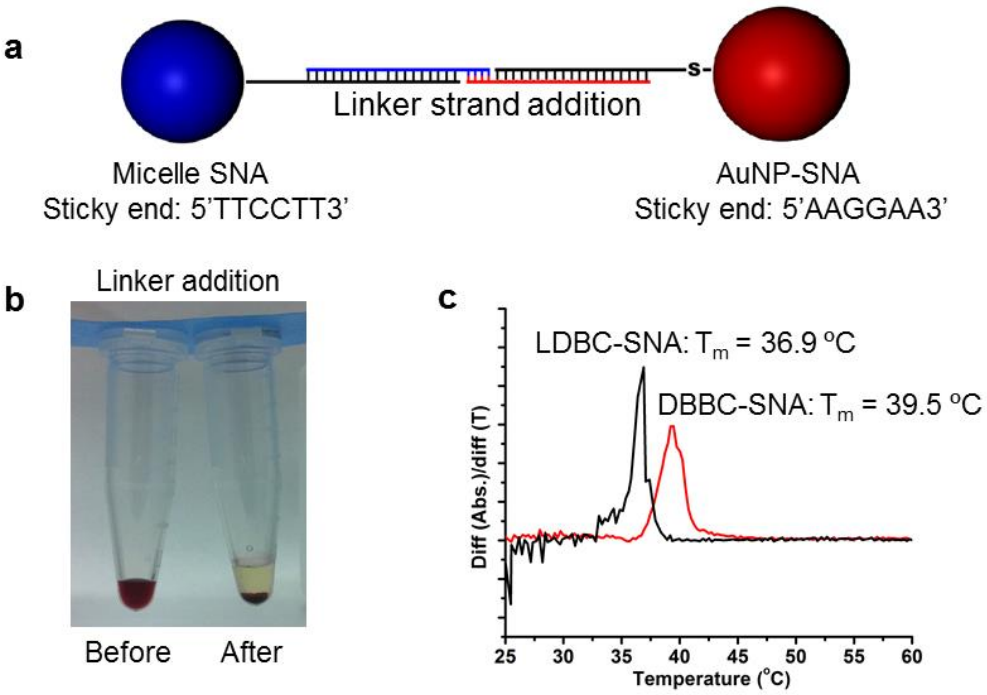

Figure A4.10. Melting transition of binary (2-component) SNA mixture composed of micelle-SNAs and 15 nm AuNP-SNAs. (a) Scheme depicting binary SNA system in which two different types of SNAs can associate together via DNA linker strategy; (b) After addition of the DNA linker, it hybridizes with the complementary strands on either micelle-SNAs or AuNP-SNAs. When the SNAs are mixed, the complementary sticky ends crosslink the particles to form aggregates within minutes; (c) The first derivative of the melting curves reveals the melting temperature for DBBC micelle-SNA /AuNP-SNA and linear DBC based micelle-SNA /AuNP-SNA to be 39.5 °C and 36.9 °C, respectively. Similar to pure AuNP-SNA binary systems, sharp, elevated melting transitions were observed for the aggregates composed of both DBBC micelle-SNA /AuNP-SNA and linear DBC based micelle-SNA /AuNP-SNA.

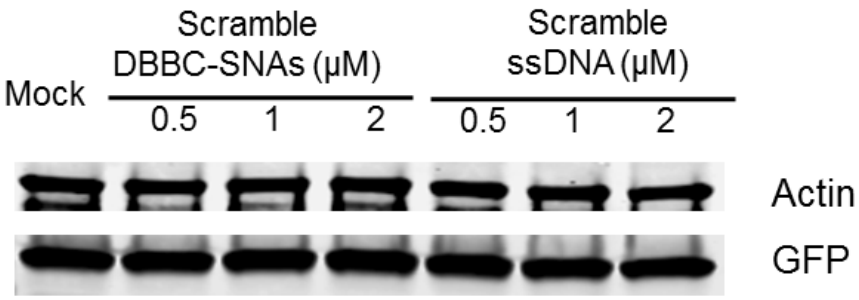

Figure A4.11. Control experiment of gene regulation by DBBC-based micelle-SNAs with scrambled sequence. Western blotting of EGFP expression in C166 cells after treatment with DBBC micelle-SNAs and single-stranded DNA with scrambled sequence. Actin is used as an internal reference. Both DBBC micelle-SNAs and single-stranded scrambled DNA with various total DNA concentrations were incubated with C166 cells overnight. After 72 h, the cells were collected for western blotting. The effect of gene knockdown can be observed with scrabled sequence.

Chapter 5 Supporting Information

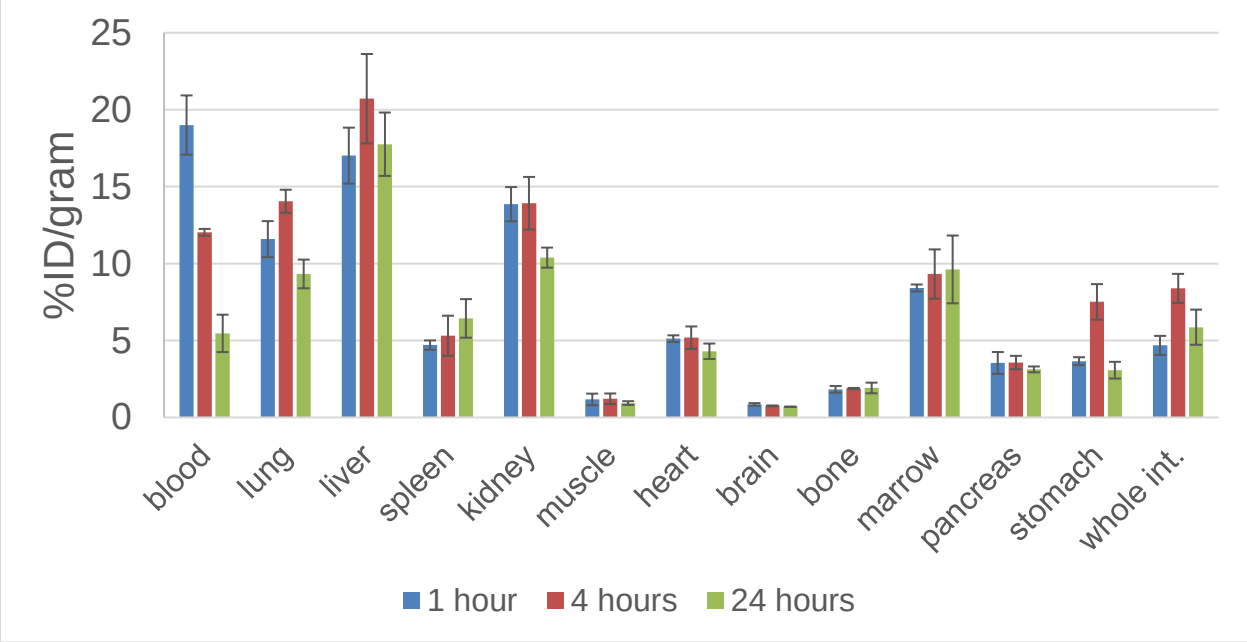

Figure A5.1. Biodistribution of ^{64}Cu-labeled PMO/PEG5K SNA nanoclusters at 1, 4 and 24 hours.

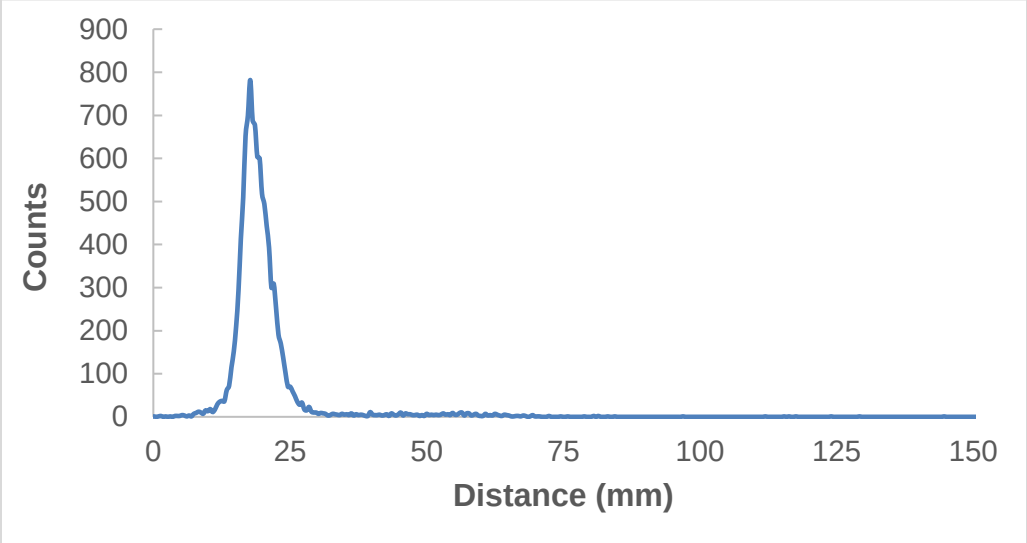

Figure A5.2. Representative radio-iTLC trace of purified ^{64}CuAuNCs.

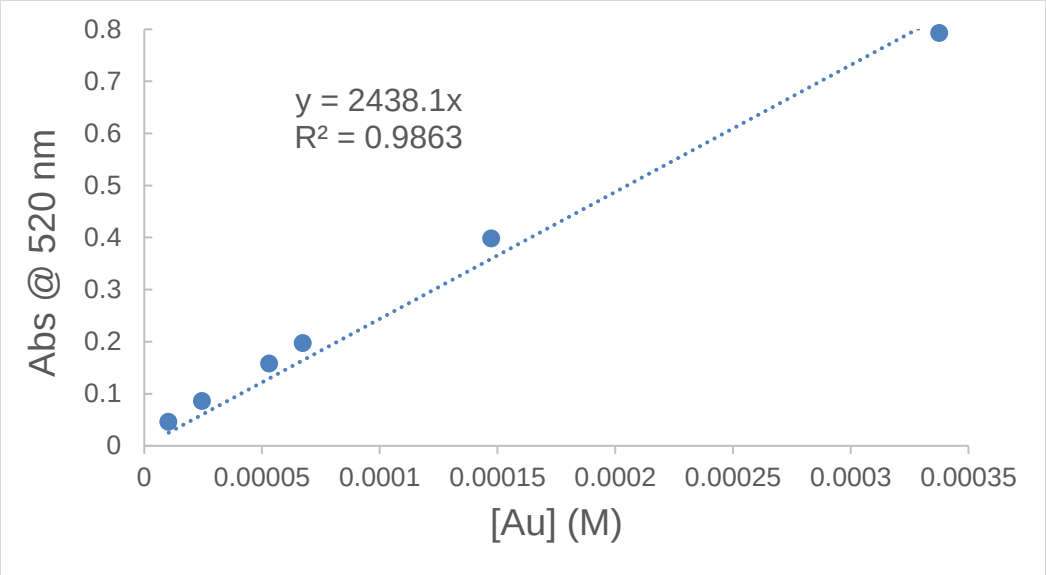

Figure A5.3. Representative calculation of AuNC extinction coefficient ε_{520} by ICP-MS. Slope of linear fit = ε_{520}. For a sample of AuNCs of known core size (TEM average), ε_{520} can be used to calculate [AuNCs].

Chapter 6 Supporting Information

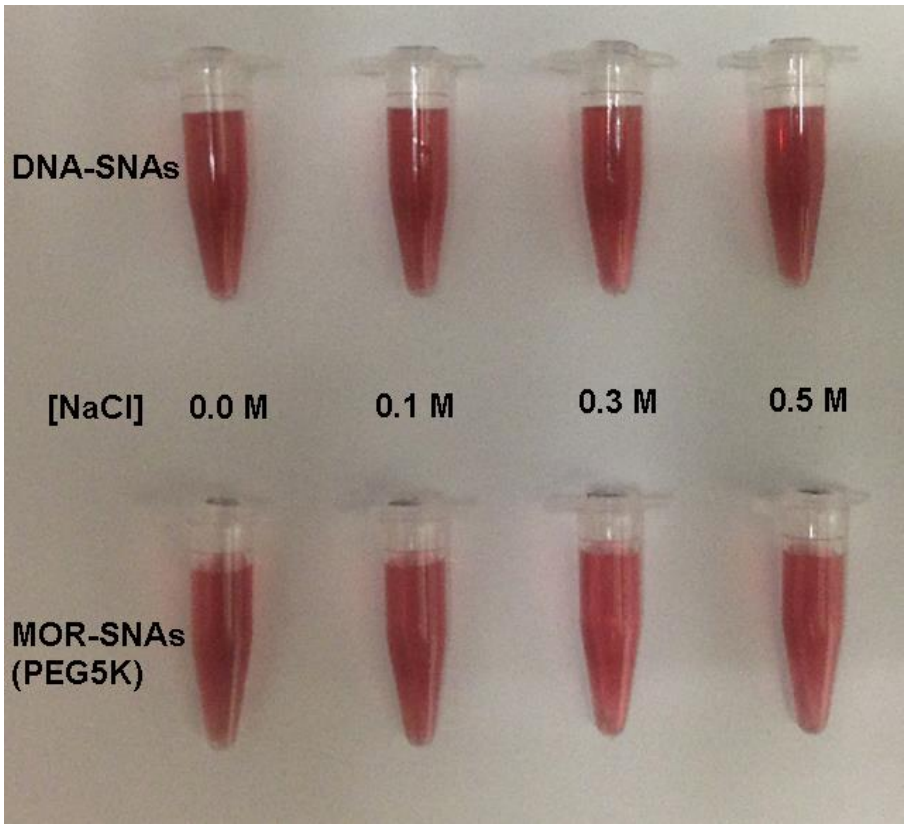

Figure A6.1. Colloidal stability of DNA SNAs and morpholino/PEG5K SNAs bearing the same oligonucleotide sequence at varying salt concentrations (left standing 3 months).

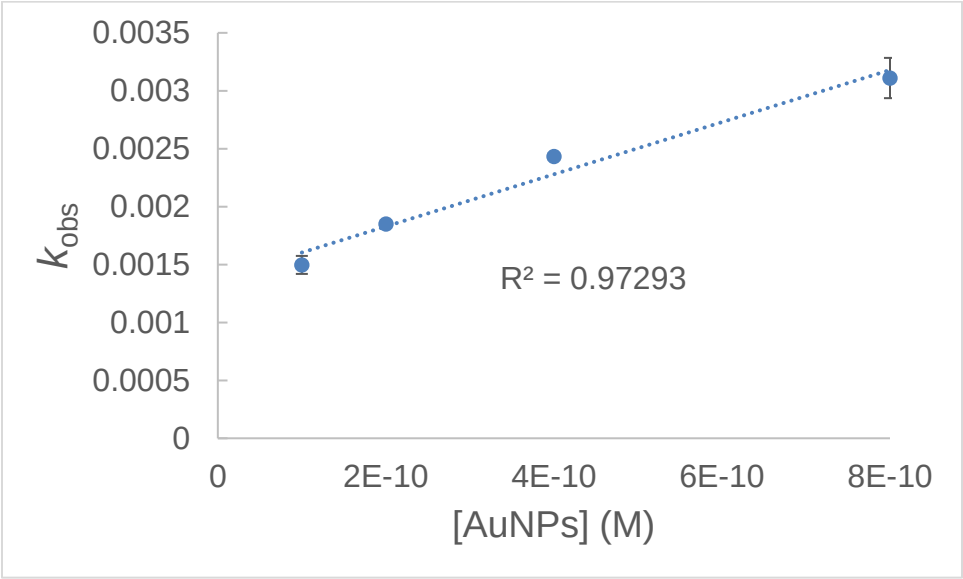

Figure A6.2. Representative linear fit of concentration of DNA SNAs vs. observed rate constant upon hybridization with 100 pM complementary OMe-RNA at 37° C. Each data point represents the mean of 3 experiments.

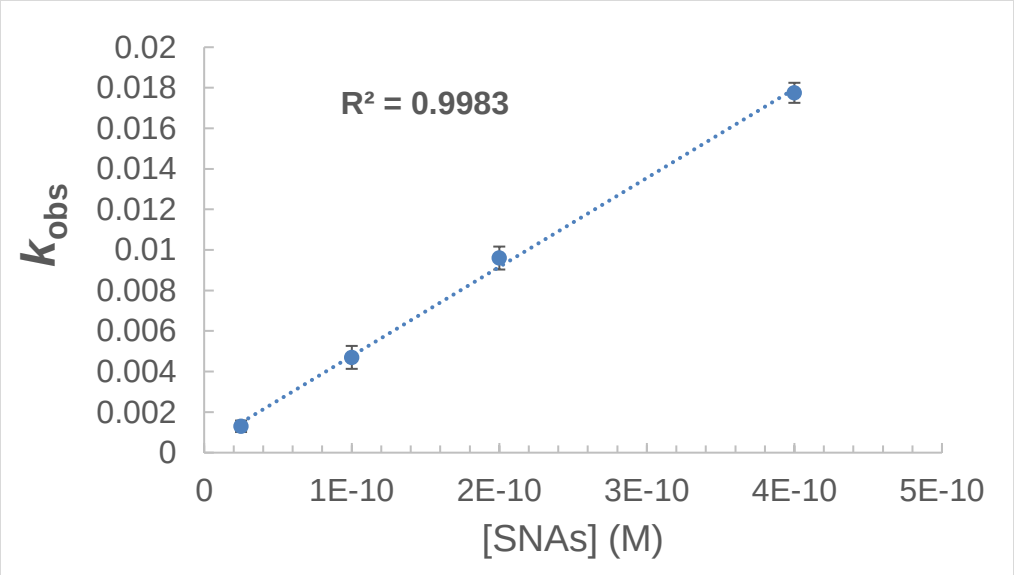

Figure A6.3. Representative linear fit of concentration of PMO SNAs vs. observed rate constant upon hybridization with 100 pM complementary OMe-RNA at 10° C.

T (°C)	k_{on} (M^{-1} s^{-1})	$E_a = \frac{R*T_1*T_2}{(T_1-T_2)} \ln(\frac{k_1}{k_2})$	E_a = 15.6 kJ/mol (3.7 kcal/mol)
10	43,900,000 ± 95,000		
37	78,300,000 ± 1,040,000		

Table A6.1. Estimation of E_a for capture of complementary OMe-RNA by PMO SNAs.

Biblography

1. Lodish, H. F., Structure of Nucleic Acids. In *Molecular cell biology*, Lodish, H. F., Ed. W.H. Freeman and Company: New York, 2004.
2. Giege, R.; Juhling, F.; Putz, J.; Stadler, P.; Sauter, C.; Florentz, C., Structure of transfer RNAs: similarity and variability. *Wiley Interdiscip Rev RNA* **2012,** *3* (1), 37-61.
3. Fedor, M. J.; Williamson, J. R., The catalytic diversity of RNAs. *Nat Rev Mol Cell Biol* **2005,** *6* (5), 399-412.
4. Li, H.; Labean, T. H.; Leong, K. W., Nucleic acid-based nanoengineering: novel structures for biomedical applications. *Interface Focus* **2011,** *1* (5), 702-24.
5. Seeman, N. C., Nanomaterials based on DNA. *Annu Rev Biochem* **2010,** *79*, 65-87.
6. Wang, Z. G.; Ding, B., DNA-based self-assembly for functional nanomaterials. *Adv Mater* **2013,** *25* (28), 3905-14.
7. Wang, H.; Yang, R. H.; Yang, L.; Tan, W. H., Nucleic Acid Conjugated Nanomaterials for Enhanced Molecular Recognition. *Acs Nano* **2009,** *3* (9), 2451-2460.
8. Houlton, A.; Pike, A. R.; Galindo, M. A.; Horrocks, B. R., DNA-based routes to semiconducting nanomaterials. *Chem Commun* **2009,** (14), 1797-1806.
9. Tong, G. J.; Hsiao, S. C.; Carrico, Z. M.; Francis, M. B., Viral Capsid DNA Aptamer Conjugates as Multivalent Cell-Targeting Vehicles. *J Am Chem Soc* **2009,** *131* (31), 11174-11178.
10. Hamedi, M.; Elfwing, A.; Gabrielsson, R.; Inganas, O., Electronic Polymers and DNA Self-Assembled in Nanowire Transistors. *Small* **2013,** *9* (3), 363-368.
11. Kosuri, S.; Church, G. M., Large-scale de novo DNA synthesis: technologies and applications. *Nat Methods* **2014,** *11* (5), 499-507.
12. Caruthers, M. H., The Chemical Synthesis of DNA/RNA: Our Gift to Science. *J Biol Chem* **2013,** *288* (2), 1420-1427.
13. Sacca, B.; Niemeyer, C. M., DNA origami: the art of folding DNA. *Angew Chem Int Ed Engl* **2012,** *51* (1), 58-66.
14. Andersen, E. S.; Dong, M.; Nielsen, M. M.; Jahn, K.; Subramani, R.; Mamdouh, W.; Golas, M. M.; Sander, B.; Stark, H.; Oliveira, C. L.; Pedersen, J. S.; Birkedal, V.; Besenbacher, F.; Gothelf, K. V.; Kjems, J., Self-assembly of a nanoscale DNA box with a controllable lid. *Nature* **2009,** *459* (7243), 73-6.
15. Goodchild, J., Conjugates of Oligonucleotides and Modified Oligonucleotides: A Review of Their Synthesis and Properties. *Bioconjugate Chem* **1990,** *1* (3), 165-187.
16. Aldaye, F. A.; Sleiman, H. F., Sequential self-assembly of a DNA hexagon as a template for the organization of gold nanoparticles. *Angew Chem Int Edit* **2006,** *45* (14), 2204-2209.
17. Liu, H.; Zhu, Z.; Kang, H.; Wu, Y.; Sefan, K.; Tan, W., DNA-based micelles: synthesis, micellar properties and size-dependent cell permeability. *Chemistry* **2010,** *16* (12), 3791-7.
18. Menacher, F.; Stepanenko, V.; Wurthner, F.; Wagenknecht, H. A., Assembly of DNA triangles mediated by perylene bisimide caps. *Chemistry* **2011,** *17* (24), 6683-8.
19. Kuzuya, A.; Ohnishi, T.; Wasano, T.; Nagaoka, S.; Sumaoka, J.; Ihara, T.; Jyo, A.; Komiyama, M., Efficient Guest Inclusion by beta-Cyclodextrin Attached to the Ends of DNA Oligomers upon Hybridization to Various DNA Conjugates. *Bioconjugate Chem* **2009,** *20* (8), 1643-1649.

20. Sargsyan, G.; Balaz, M., Porphyrin-DNA conjugates: porphyrin induced adenine-guanine homoduplex stabilization and interduplex assemblies. *Org Biomol Chem* **2012,** *10* (29), 5533-5540.
21. Yang, X. L.; Meng, X. M.; Li, B.; Chen, Z.; Zhao, D. X.; Tan, X.; Yu, Q., Inhibition of in vitro amplification of targeted DNA fragment and activity of exonuclease I by a fullerene-oligonucleotide conjugate. *Biologicals* **2008,** *36* (4), 223-226.
22. Wang, Y.; Tkachenko, B. A.; Schreiner, P. R.; Marx, A., Diamondoid-modified DNA. *Org Biomol Chem* **2011,** *9* (21), 7482-7490.
23. Malinovskii, V. L.; Wenger, D.; Haner, R., Nucleic acid-guided assembly of aromatic chromophores. *Chem Soc Rev* **2010,** *39* (2), 410-422.
24. Lu, K.; Duan, Q. P.; Ma, L.; Zhao, D. X., Chemical Strategies for the Synthesis of Peptide-Oligonucleotide Conjugates. *Bioconjugate Chem* **2010,** *21* (2), 187-202.
25. Niemeyer, C. M., The developments of semisynthetic DNA-protein conjugates. *Trends Biotechnol* **2002,** *20* (9), 395-401.
26. Lapienc, V.; Kukolka, F.; Kiko, K.; Arndt, A.; Niemeyer, C. M., Conjugation of Fluorescent Proteins with DNA Oligonucleotides. *Bioconjugate Chem* **2010,** *21* (5), 921-927.
27. Kazane, S. A.; Sok, D.; Cho, E. H.; Uson, M. L.; Kuhn, P.; Schultz, P. G.; Smider, V. V., Site-specific DNA-antibody conjugates for specific and sensitive immuno-PCR. *P Natl Acad Sci USA* **2012,** *109* (10), 3731-3736.
28. Bonora, G. M.; Ivanova, E.; Zarytova, V.; Burcovich, B.; Veronese, F. M., Synthesis and characterization of high-molecular mass polyethylene glycol-conjugated oligonucleotides. *Bioconjugate Chem* **1997,** *8* (6), 793-797.
29. Li, Z.; Zhang, Y.; Fullhart, P.; Mirkin, C. A., Reversible and chemically programmable micelle assembly with DNA block-copolymer amphiphiles. *Nano Lett* **2004,** *4* (6), 1055-1058.
30. Gibbs, J. M.; Park, S. J.; Anderson, D. R.; Watson, K. J.; Mirkin, C. A.; Nguyen, S. T., Polymer-DNA hybrids as electrochemical probes for the detection of DNA. *J Am Chem Soc* **2005,** *127* (4), 1170-1178.
31. Averick, S.; Paredes, E.; Li, W. W.; Matyjaszewski, K.; Das, S. R., Direct DNA Conjugation to Star Polymers for Controlled Reversible Assemblies. *Bioconjugate Chem* **2011,** *22* (10), 2030-2037.
32. Carneiro, K. M. M.; Aldaye, F. A.; Sleiman, H. F., Long-Range Assembly of DNA into Nanofibers and Highly Ordered Networks Using a Block Copolymer Approach. *J Am Chem Soc* **2010,** *132* (2), 679-685.
33. Mirkin, C. A.; Letsinger, R. L.; Mucic, R. C.; Storhoff, J. J., A DNA-based method for rationally assembling nanoparticles into macroscopic materials. *Nature* **1996,** *382* (6592), 607-609.
34. Banerjee, A.; Grazon, C.; Nadal, B.; Pons, T.; Krishnan, Y.; Dubertret, B., Fast, Efficient, and Stable Conjugation of Multiple DNA Strands on Colloidal Quantum Dots. *Bioconjugate Chem* **2015,** *26* (8), 1582-1589.
35. Proupin-Perez, M.; Cosstick, R.; Liz-Marzan, L. M.; V, S.-M.; Brust, M., Studies on the attachment of DNA to silica-coated nanoparticles through a Diels-Alder reaction. *Nucleos Nucleot Nucl* **2005,** *24* (5-7), 1075-1079.
36. Thomson, D. A. C.; Tee, E. H. L.; Tran, N. T. D.; Monteiro, M. J.; Cooper, M. A., Oligonucleotide and Polymer Functionalized Nanoparticles for Amplification-Free Detection of DNA. *Biomacromolecules* **2012,** *13* (6), 1981-1989.

37. Chen, C. C.; Lin, Y. P.; Wang, C. W.; Tzeng, H. C.; Wu, C. H.; Chen, Y. C.; Chen, C. P.; Chen, L. C.; Wu, Y. C., DNA-gold nanorod conjugates for remote control of localized gene expression by near infrared irradiation. *J Am Chem Soc* **2006,** *128* (11), 3709-3715.
38. Li, J. X.; Zhu, B. Q.; Zhu, Z.; Zhang, Y. C.; Yao, X. J.; Tu, S.; Liu, R. D.; Jia, S. S.; Yang, C. Y. J., Simple and Rapid Functionalization of Gold Nanorods with Oligonucleotides Using an mPEG-SH/Tween 20-Assisted Approach. *Langmuir* **2015,** *31* (28), 7869-7876.
39. Chou, L. Y. T.; Zagorovsky, K.; Chan, W. C. W., DNA assembly of nanoparticle superstructures for controlled biological delivery and elimination. *Nat Nanotechnol* **2014,** *9* (2), 148-155.
40. Lee, H.; Lytton-Jean, A. K. R.; Chen, Y.; Love, K. T.; Park, A. I.; Karagiannis, E. D.; Sehgal, A.; Querbes, W.; Zurenko, C. S.; Jayaraman, M.; Peng, C. G.; Charisse, K.; Borodovsky, A.; Manoharan, M.; Donahoe, J. S.; Truelove, J.; Nahrendorf, M.; Langer, R.; Anderson, D. G., Molecularly self-assembled nucleic acid nanoparticles for targeted in vivo siRNA delivery. *Nat Nanotechnol* **2012,** *7* (6), 389-393.
41. Macfarlane, R. J.; Lee, B.; Jones, M. R.; Harris, N.; Schatz, G. C.; Mirkin, C. A., Nanoparticle Superlattice Engineering with DNA. *Science* **2011,** *334* (6053), 204-208.
42. He, L. C.; Brasino, M.; Mao, C. C.; Cho, S.; Park, W.; Goodwin, A. P.; Cha, J. N., DNA-Assembled Core-Satellite Upconverting-Metal-Organic Framework Nanoparticle Superstructures for Efficient Photodynamic Therapy. *Small* **2017,** *13* (24).
43. Chou, L. Y. T.; Song, F. Y.; Chan, W. C. W., Engineering the Structure and Properties of DNA-Nanoparticle Superstructures Using Polyvalent Counterions. *J Am Chem Soc* **2016,** *138* (13), 4565-4572.
44. Hellstrom, S. L.; Kim, Y.; Fakonas, J. S.; Senesi, A. J.; Macfarlane, R. J.; Mirkin, C. A.; Atwater, H. A., Epitaxial Growth of DNA-Assembled Nanoparticle Superlattices on Patterned Substrates. *Nano Lett* **2013,** *13* (12), 6084-6090.
45. Gur, F. N.; Schwarz, F. W.; Ye, J. J.; Diez, S.; Schmidt, T. L., Toward Self-Assembled Plasmonic Devices: High-Yield Arrangement of Gold Nanoparticles on DNA Origami Templates. *Acs Nano* **2016,** *10* (5), 5374-5382.
46. Iribarren, A. M.; Sproat, B. S.; Neuner, P.; Sulston, I.; Ryder, U.; Lamond, A. I., 2'-O-Alkyl Oligoribonucleotides as Antisense Probes. *P Natl Acad Sci USA* **1990,** *87* (19), 7747-7751.
47. Deleavey, G. F.; Damha, M. J., Designing Chemically Modified Oligonucleotides for Targeted Gene Silencing. *Chem Biol* **2012,** *19* (8), 937-954.
48. Owczarzy, R.; You, Y.; Groth, C. L.; Tataurov, A. V., Stability and Mismatch Discrimination of Locked Nucleic Acid-DNA Duplexes. *Biochemistry* **2011,** *50* (43), 9352-9367.
49. Chakrabarti, M. C.; Schwarz, F. P., Thermal stability of PNA/DNA and DNA/DNA duplexes by differential scanning calorimetry. *Nucleic Acids Res* **1999,** *27* (24), 4801-4806.
50. Summerton, J.; Weller, D., Morpholino antisense oligomers: Design, preparation, and properties. *Antisense Nucleic A* **1997,** *7* (3), 187-195.
51. Cutler, J. I.; Auyeung, E.; Mirkin, C. A., Spherical Nucleic Acids. *J Am Chem Soc* **2012,** *134* (3), 1376-1391.
52. Qian, E. A.; Wixtrom, A. I.; Axtell, J. C.; Saebi, A.; Jung, D. H.; Rehak, P.; Han, Y. X.; Moully, E. H.; Mosallaei, D.; Chow, S.; Messina, M. S.; Wang, J. Y.; Royappa, A. T.; Rheingold, A. L.; Maynard, H. D.; Kral, P.; Spokoyny, A. M., Atomically precise organomimetic cluster nanomolecules assembled via perfluoroaryl-thiol SNAr chemistry. *Nat Chem* **2017,** *9* (4), 333-340.

53. Hurst, S. J.; Lytton-Jean, A. K. R.; Mirkin, C. A., Maximizing DNA loading on a range of gold nanoparticle sizes. *Anal Chem* **2006,** *78* (24), 8313-8318.
54. Calabrese, C. M.; Merkel, T. J.; Briley, W. E.; Randeria, P. S.; Narayan, S. P.; Rouge, J. L.; Walker, D. A.; Scott, A. W.; Mirkin, C. A., Biocompatible Infinite-Coordination-Polymer Nanoparticle-Nucleic-Acid Conjugates for Antisense Gene Regulation. *Angew Chem Int Edit* **2015,** *54* (2), 476-480.
55. Elghanian, R.; Storhoff, J. J.; Mucic, R. C.; Letsinger, R. L.; Mirkin, C. A., Selective colorimetric detection of polynucleotides based on the distance-dependent optical properties of gold nanoparticles. *Science* **1997,** *277* (5329), 1078-1081.
56. Thaxton, C. S.; Georganopoulou, D. G.; Mirkin, C. A., Gold nanoparticle probes for the detection of nucleic acid targets. *Clin Chim Acta* **2006,** *363* (1-2), 120-126.
57. Nam, J. M.; Thaxton, C. S.; Mirkin, C. A., Nanoparticle-based bio-bar codes for the ultrasensitive detection of proteins. *Science* **2003,** *301* (5641), 1884-1886.
58. Liu, J. W.; Lu, Y., A colorimetric lead biosensor using DNAzyme-directed assembly of gold nanoparticles. *J Am Chem Soc* **2003,** *125* (22), 6642-6643.
59. Lee, J. S.; Han, M. S.; Mirkin, C. A., Colorimetric detection of mercuric ion (Hg2+) in aqueous media using DNA-functionalized gold nanoparticles. *Angew Chem Int Edit* **2007,** *46* (22), 4093-4096.
60. Macfarlane, R. J.; O'Brien, M. N.; Petrosko, S. H.; Mirkin, C. A., Nucleic Acid-Modified Nanostructures as Programmable Atom Equivalents: Forging a New "Table of Elements". *Angew Chem Int Edit* **2013,** *52* (22), 5688-5698.
61. Cheng, W. L.; Campolongo, M. J.; Cha, J. J.; Tan, S. J.; Umbach, C. C.; Muller, D. A.; Luo, D., Free-standing nanoparticle superlattice sheets controlled by DNA. *Nat Mater* **2009,** *8* (6), 519-525.
62. Tian, Y.; Zhang, Y. G.; Wang, T.; Xin, H. L. L.; Li, H. L.; Gang, O., Lattice engineering through nanoparticle-DNA frameworks. *Nat Mater* **2016,** *15* (6), 654-+.
63. Zhang, C.; Macfarlane, R. J.; Young, K. L.; Choi, C. H. J.; Hao, L. L.; Auyeung, E.; Liu, G. L.; Zhou, X. Z.; Mirkin, C. A., A general approach to DNA-programmable atom equivalents. *Nat Mater* **2013,** *12* (8), 741-746.
64. Auyeung, E.; Morris, W.; Mondloch, J. E.; Hupp, J. T.; Farha, O. K.; Mirkin, C. A., Controlling Structure and Porosity in Catalytic Nanoparticle Superlattices with DNA. *J Am Chem Soc* **2015,** *137* (4), 1658-1662.
65. Brodin, J. D.; Auyeung, E.; Mirkin, C. A., DNA-mediated engineering of multicomponent enzyme crystals. *P Natl Acad Sci USA* **2015,** *112* (15), 4564-4569.
66. Felgner, P. L.; Gadek, T. R.; Holm, M.; Roman, R.; Chan, H. W.; Wenz, M.; Northrop, J. P.; Ringold, G. M.; Danielsen, M., Lipofection - a Highly Efficient, Lipid-Mediated DNA-Transfection Procedure. *P Natl Acad Sci USA* **1987,** *84* (21), 7413-7417.
67. Juliano, R. L.; Ming, X.; Nakagawa, O., Cellular Uptake and Intracellular Trafficking of Antisense and siRNA Oligonucleotides. *Bioconjugate Chem* **2012,** *23* (2), 147-157.
68. Rosi, N. L.; Giljohann, D. A.; Thaxton, C. S.; Lytton-Jean, A. K. R.; Han, M. S.; Mirkin, C. A., Oligonucleotide-modified gold nanoparticles for intracellular gene regulation. *Science* **2006,** *312* (5776), 1027-1030.
69. Giljohann, D. A.; Seferos, D. S.; Patel, P. C.; Millstone, J. E.; Rosi, N. L.; Mirkin, C. A., Oligonucleotide loading determines cellular uptake of DNA-modified gold nanoparticles. *Nano Lett* **2007,** *7* (12), 3818-3821.

70. Choi, C. H. J.; Hao, L. L.; Narayan, S. P.; Auyeung, E.; Mirkin, C. A., Mechanism for the endocytosis of spherical nucleic acid nanoparticle conjugates. *P Natl Acad Sci USA* **2013,** *110* (19), 7625-7630.
71. Narayan, S. P.; Choi, C. H. J.; Hao, L. L.; Calabrese, C. M.; Auyeung, E.; Zhang, C.; Goor, O. J. G. M.; Mirkin, C. A., The Sequence-Specific Cellular Uptake of Spherical Nucleic Acid Nanoparticle Conjugates. *Small* **2015,** *11* (33), 4173-4182.
72. Zani, I. A.; Stephen, S. L.; Mughal, N. A.; Russell, D.; Homer-Vanniasinkam, S.; Wheatcroft, S. B.; Ponnambalam, S., Scavenger receptor structure and function in health and disease. *Cells* **2015,** *4* (2), 178-201.
73. Massich, M. D.; Giljohann, D. A.; Schmucker, A. L.; Patel, P. C.; Mirkin, C. A., Cellular Response of Polyvalent Oligonucleotide-Gold Nanoparticle Conjugates. *Acs Nano* **2010,** *4* (10), 5641-5646.
74. Pearson, A. M.; Rich, A.; Krieger, M., Polynucleotide binding to macrophage scavenger receptors depends on the formation of base-quartet-stabilized four-stranded helices. *J Biol Chem* **1993,** *268* (5), 3546-54.
75. Massich, M. D.; Giljohann, D. A.; Seferos, D. S.; Ludlow, L. E.; Horvath, C. M.; Mirkin, C. A., Regulating Immune Response Using Polyvalent Nucleic Acid-Gold Nanoparticle Conjugates. *Mol Pharmaceut* **2009,** *6* (6), 1934-1940.
76. Seferos, D. S.; Prigodich, A. E.; Giljohann, D. A.; Patel, P. C.; Mirkin, C. A., Polyvalent DNA Nanoparticle Conjugates Stabilize Nucleic Acids. *Nano Lett* **2009,** *9* (1), 308-311.
77. Banga, R. J.; Chernyak, N.; Narayan, S. P.; Nguyen, S. T.; Mirkin, C. A., Liposomal Spherical Nucleic Acids. *J Am Chem Soc* **2014,** *136* (28), 9866-9869.
78. Young, K. L.; Scott, A. W.; Hao, L. L.; Mirkin, S. E.; Liu, G. L.; Mirkin, C. A., Hollow Spherical Nucleic Acids for Intracellular Gene Regulation Based upon Biocompatible Silica Shells. *Nano Lett* **2012,** *12* (7), 3867-3871.
79. Jensen, S. A.; Day, E. S.; Ko, C. H.; Hurley, L. A.; Luciano, J. P.; Kouri, F. M.; Merkel, T. J.; Luthi, A. J.; Patel, P. C.; Cutler, J. I.; Daniel, W. L.; Scott, A. W.; Rotz, M. W.; Meade, T. J.; Giljohann, D. A.; Mirkin, C. A.; Stegh, A. H., Spherical Nucleic Acid Nanoparticle Conjugates as an RNAi-Based Therapy for Glioblastoma. *Sci Transl Med* **2013,** *5* (209).
80. Rush, A. M.; Nelles, D. A.; Blum, A. P.; Barnhill, S. A.; Tatro, E. T.; Yeo, G. W.; Gianneschi, N. C., Intracellular mRNA Regulation with Self-Assembled Locked Nucleic Acid Polymer Nanoparticles. *J Am Chem Soc* **2014,** *136* (21), 7615-7618.
81. Rouge, J. L.; Sita, T. L.; Hao, L. L.; Kouri, F. M.; Briley, W. E.; Stegh, A. H.; Mirkin, C. A., Ribozyme-Spherical Nucleic Acids. *J Am Chem Soc* **2015,** *137* (33), 10528-10531.
82. Anstaett, P.; Zheng, Y. H.; Thai, T.; Funston, A. M.; Bach, U.; Gasser, G., Synthesis of Stable Peptide Nucleic Acid-Modified Gold Nanoparticles and their Assembly onto Gold Surfaces. *Angew Chem Int Edit* **2013,** *52* (15), 4217-4220.
83. Radovic-Moreno, A. F.; Chernyak, N.; Mader, C. C.; Nallagatla, S.; Kang, R. S.; Hao, L. L.; Walker, D. A.; Halo, T. L.; Merkel, T. J.; Rische, C. H.; Anantatmula, S.; Burkhart, M.; Mirkin, C. A.; Gryaznov, S. M., Immunomodulatory spherical nucleic acids. *P Natl Acad Sci USA* **2015,** *112* (13), 3892-3897.
84. Halo, T. L.; McMahon, K. M.; Angeloni, N. L.; Xu, Y. L.; Wang, W.; Chinen, A. B.; Malin, D.; Strekalova, E.; Cryns, V. L.; Cheng, C. H.; Mirkin, C. A.; Thaxton, C. S., NanoFlares for the detection, isolation, and culture of live tumor cells from human blood. *P Natl Acad Sci USA* **2014,** *111* (48), 17104-17109.

85. Seferos, D. S.; Giljohann, D. A.; Hill, H. D.; Prigodich, A. E.; Mirkin, C. A., Nano-flares: Probes for transfection and mRNA detection in living cells. *J Am Chem Soc* **2007,** *129* (50), 15477-+.
86. Prigodich, A. E.; Randeria, P. S.; Briley, W. E.; Kim, N. J.; Daniel, W. L.; Giljohann, D. A.; Mirkin, C. A., Multiplexed Nanoflares: mRNA Detection in Live Cells. *Anal Chem* **2012,** *84* (4), 2062-2066.
87. Alkilany, A. M.; Murphy, C. J., Toxicity and cellular uptake of gold nanoparticles: what we have learned so far? *J Nanopart Res* **2010,** *12* (7), 2313-2333.
88. Chinen, A. B.; Guan, C. X. M.; Ko, C. H.; Mirkin, C. A., The Impact of Protein Corona Formation on the Macrophage Cellular Uptake and Biodistribution of Spherical Nucleic Acids. *Small* **2017,** *13* (16).
89. Caruthers, M. H.; Barone, A. D.; Beaucage, S. L.; Dodds, D. R.; Fisher, E. F.; Mcbride, L. J.; Matteucci, M.; Stabinsky, Z.; Tang, J. Y., Chemical Synthesis of Deoxyoligonucleotides by the Phosphoramidite Method. *Method Enzymol* **1987,** *154*, 287-313.
90. Rothemund, P. W. K., Folding DNA to create nanoscale shapes and patterns. *Nature* **2006,** *440* (7082), 297-302.
91. Nangreave, J.; Han, D. R.; Liu, Y.; Yan, H., DNA origami: a history and current perspective. *Curr Opin Chem Biol* **2010,** *14* (5), 608-615.
92. Hong, B. J.; Cho, V. Y.; Bleher, R.; Schatz, G. C.; Nguyen, S. T., Enhancing DNA-Mediated Assemblies of Supramolecular Cage Dimers through Tuning Core Flexibility and DNA Length-A Combined Experimental-Modeling Study. *J Am Chem Soc* **2015,** *137* (41), 13381-13388.
93. Hong, B. J.; Eryazici, I.; Bleher, R.; Thaner, R. V.; Mirkin, C. A.; Nguyen, S. T., Directed Assembly of Nucleic Acid-Based Polymeric Nanoparticles from Molecular Tetravalent Cores. *J Am Chem Soc* **2015,** *137* (25), 8184-8191.
94. Thaner, R. V.; Eryazici, I.; Farha, O. K.; Mirkin, C. A.; Nguyen, S. T., Facile one-step solid-phase synthesis of multitopic organic-DNA hybrids via "click" chemistry. *Chem Sci* **2014,** *5* (3), 1091-1096.
95. Okochi, K. D.; Monfregola, L.; Dickerson, S. M.; McCaffrey, R.; Domaille, D. W.; Yu, C.; Hafenstine, G. R.; Jin, Y.; Cha, J. N.; Kuchta, R. D.; Caruthers, M.; Zhang, W., Synthesis of Small-Molecule/DNA Hybrids through On-Bead Amide-Coupling Approach. *J Org Chem* **2017**.
96. Ensslen, P.; Gartner, S.; Glaser, K.; Colsmann, A.; Wagenknecht, H. A., A DNA-Fullerene Conjugate as a Template for Supramolecular Chromophore Assemblies: Towards DNA-Based Solar Cells. *Angew Chem Int Edit* **2016,** *55* (5), 1904-1908.
97. Mattarella, M.; Berstis, L.; Baldridge, K. K.; Siegel, J. S., Synthesis of Bioconjugated sym-Pentasubstituted Corannulenes: Experimental and Theoretical Investigations of Supramolecular Architectures. *Bioconjugate Chem* **2014,** *25* (1), 115-128.
98. Lee, J. K.; Jung, Y. H.; Tok, J. B. H.; Bao, Z. N., Syntheses of Organic Molecule-DNA Hybrid Structures. *Acs Nano* **2011,** *5* (3), 2067-2074.
99. Vyborna, Y.; Vybornyi, M.; Rudnev, A. V.; Haner, R., DNA-Grafted Supramolecular Polymers: Helical Ribbon Structures Formed by Self-Assembly of Pyrene-DNA Chimeric Oligomers. *Angew Chem Int Edit* **2015,** *54* (27), 7934-7938.
100. Schnitzler, T.; Herrmann, A., DNA Block Copolymers: Functional Materials for Nanoscience and Biomedicine. *Accounts Chem Res* **2012,** *45* (9), 1419-1430.

101. Noro, A.; Nagata, Y.; Tsukamoto, M.; Hayakawa, Y.; Takano, A.; Matsushita, Y., Novel synthesis and characterization of bioconjugate block copolymers having oligonucleotides. *Biomacromolecules* **2005,** *6* (4), 2328-2333.
102. Kamps, A. C.; Cativo, M. H. M.; Chen, X. J.; Park, S. J., Self-Assembly of DNA-Coupled Semiconducting Block Copolymers. *Macromolecules* **2014,** *47* (11), 3720-3726.
103. Ding, K.; Alemdaroglu, F. E.; Borsch, M.; Berger, R.; Herrmann, A., Engineering the structural properties of DNA block copolymer micelles by molecular recognition. *Angew Chem Int Ed Engl* **2007,** *46* (7), 1172-5.
104. Jeong, J. H.; Kim, S. W.; Park, T. G., A new antisense oligonucleotide delivery system based on self-assembled ODN-PEG hybrid conjugate micelles. *J Control Release* **2003,** *93* (2), 183-91.
105. Alemdaroglu, F. E.; Alemdaroglu, N. C.; Langguth, P.; Herrmann, A., Cellular uptake of DNA block copolymer micelles with different shapes. *Macromol Rapid Comm* **2008,** *29* (4), 326-329.
106. Lee, O. S.; Prytkova, T. R.; Schatz, G. C., Using DNA to Link Gold Nanoparticles, Polymers, and Molecules: A Theoretical Perspective. *J Phys Chem Lett* **2010,** *1* (12), 1781-1788.
107. Taton, T. A., Preparation of gold nanoparticle-DNA conjugates. *Curr Protoc Nucleic Acid Chem* **2002,** *Chapter 12*, Unit 12 2.
108. Lalander, C. H.; Zheng, Y.; Dhuey, S.; Cabrini, S.; Bach, U., DNA-Directed Self-Assembly of Gold Nanoparticles onto Nanopatterned Surfaces: Controlled Placement of Individual Nanoparticles into Regular Arrays. *Acs Nano* **2010,** *4* (10), 6153-6161.
109. Park, S. Y.; Lytton-Jean, A. K. R.; Lee, B.; Weigand, S.; Schatz, G. C.; Mirkin, C. A., DNA-programmable nanoparticle crystallization. *Nature* **2008,** *451* (7178), 553-556.
110. Jones, M. R.; Macfarlane, R. J.; Lee, B.; Zhang, J. A.; Young, K. L.; Senesi, A. J.; Mirkin, C. A., DNA-nanoparticle superlattices formed from anisotropic building blocks. *Nat Mater* **2010,** *9* (11), 913-917.
111. McLaughlin, C. K.; Hamblin, G. D.; Aldaye, F. A.; Yang, H.; Sleiman, H. F., A facile, modular and high yield method to assemble three-dimensional DNA structures. *Chem Commun* **2011,** *47* (31), 8925-8927.
112. Jiang, Q.; Song, C.; Nangreave, J.; Liu, X. W.; Lin, L.; Qiu, D. L.; Wang, Z. G.; Zou, G. Z.; Liang, X. J.; Yan, H.; Ding, B. Q., DNA Origami as a Carrier for Circumvention of Drug Resistance. *J Am Chem Soc* **2012,** *134* (32), 13396-13403.
113. Zhang, X. Q.; Xu, X. Y.; Lam, R.; Giljohann, D.; Ho, D.; Mirkin, C. A., Strategy for Increasing Drug Solubility and Efficacy through Covalent Attachment to Polyvalent DNA - Nanoparticle Conjugates. *Acs Nano* **2011,** *5* (9), 6962-6970.
114. Roh, Y. H.; Lee, J. B.; Tan, S. J.; Kim, B.; Park, H.; Rice, E. J.; Luo, D., Photocrosslinked DNA nanospheres for drug delivery. *Macromol Rapid Commun* **2010,** *31* (13), 1207-11.
115. Liu, J.; Ma, X. W.; Lei, C. N.; Xue, X. D.; Wei, T.; Zhao, J.; Li, S. Y.; Liang, X. J., A self-assembled DNA nanostructure for targeted and pH-triggered drug delivery to combat doxorubicin resistance. *J Mater Chem B* **2016,** *4* (22), 3854-3858.
116. Zhang, Q.; Jiang, Q.; Li, N.; Dai, L.; Liu, Q.; Song, L.; Wang, J.; Li, Y.; Tian, J.; Ding, B.; Du, Y., DNA origami as an in vivo drug delivery vehicle for cancer therapy. *Acs Nano* **2014,** *8* (7), 6633-43.
117. Sun, W.; Gu, Z., Engineering DNA scaffolds for delivery of anticancer therapeutics. *Biomater Sci* **2015,** *3* (7), 1018-24.

118. Fakhoury, J. J.; McLaughlin, C. K.; Edwardson, T. W.; Conway, J. W.; Sleiman, H. F., Development and characterization of gene silencing DNA cages. *Biomacromolecules* **2014,** *15* (1), 276-82.
119. Hong, C. A.; Jang, B.; Jeong, E. H.; Jeong, H.; Lee, H., Self-assembled DNA nanostructures prepared by rolling circle amplification for the delivery of siRNA conjugates. *Chem Commun (Camb)* **2014,** *50* (86), 13049-51.
120. Keum, J. W.; Ahn, J. H.; Bermudez, H., Design, assembly, and activity of antisense DNA nanostructures. *Small* **2011,** *7* (24), 3529-35.
121. Scott, A. W.; Garimella, V.; Calabrese, C. M.; Mirkin, C. A., Universal Biotin-PEG-Linked Gold Nanoparticle Probes for the Simultaneous Detection of Nucleic Acids and Proteins. *Bioconjug Chem* **2017,** *28* (1), 203-211.
122. Hu, J.; Wang, L.; Li, F.; Han, Y. L.; Lin, M.; Lu, T. J.; Xu, F., Oligonucleotide-linked gold nanoparticle aggregates for enhanced sensitivity in lateral flow assays. *Lab Chip* **2013,** *13* (22), 4352-7.
123. Xu, F.; Dong, H.; Cao, Y.; Lu, H.; Meng, X.; Dai, W.; Zhang, X.; Al-Ghanim, K. A.; Mahboob, S., Ultrasensitive and Multiple Disease-Related MicroRNA Detection Based on Tetrahedral DNA Nanostructures and Duplex-Specific Nuclease-Assisted Signal Amplification. *ACS Appl Mater Interfaces* **2016,** *8* (49), 33499-33505.
124. Nicodemus, G. D.; Bryant, S. J., Cell encapsulation in biodegradable hydrogels for tissue engineering applications. *Tissue Eng Pt B-Rev* **2008,** *14* (2), 149-165.
125. Lee, S. H.; Lee, C. K.; Shin, S. R.; Kim, S. I.; So, I.; Kim, S. J., The Peculiar Response of DNA Hydrogel Fibers to a Salt and pH Stimulus. *Macromol Rapid Comm* **2009,** *30* (6), 430-434.
126. Um, S. H.; Lee, J. B.; Park, N.; Kwon, S. Y.; Umbach, C. C.; Luo, D., Enzyme-catalysed assembly of DNA hydrogel. *Nat Mater* **2006,** *5* (10), 797-801.
127. Zhang, L.; Lei, J. P.; Liu, L.; Li, C. F.; Ju, H. X., Self-Assembled DNA Hydrogel as Switchable Material for Aptamer-Based Fluorescent Detection of Protein. *Anal Chem* **2013,** *85* (22), 11077-11082.
128. Cheng, E. J.; Xing, Y. Z.; Chen, P.; Yang, Y.; Sun, Y. W.; Zhou, D. J.; Xu, L. J.; Fan, Q. H.; Liu, D. S., A pH-Triggered, Fast-Responding DNA Hydrogel. *Angew Chem Int Edit* **2009,** *48* (41), 7660-7663.
129. Tanaka, K.; Tengeiji, A.; Kato, T.; Toyama, N.; Shiro, M.; Shionoya, M., Efficient incorporation of a copper hydroxypyridone base pair in DNA. *J Am Chem Soc* **2002,** *124* (42), 12494-12498.
130. Tanaka, K.; Tengeiji, A.; Kato, T.; Toyama, N.; Shionoya, M., A discrete self-assembled metal array in artificial DNA. *Science* **2003,** *299* (5610), 1212-1213.
131. Schlegel, M. K.; Zhang, L. L.; Pagano, N.; Meggers, E., Metal-mediated base pairing within the simplified nucleic acid GNA. *Org Biomol Chem* **2009,** *7* (3), 476-482.
132. Takezawa, Y.; Maeda, W.; Tanaka, K.; Shionoya, M., Discrete Self-Assembly of Iron(III) Ions inside Triple-Stranded Artificial DNA. *Angew Chem Int Edit* **2009,** *48* (6), 1081-1084.
133. Duprey, J. L. H. A.; Takezawa, Y.; Shionoya, M., Metal-Locked DNA Three-Way Junction. *Angew Chem Int Edit* **2013,** *52* (4), 1212-1216.
134. Choi, J. S.; Kang, C. W.; Jung, K.; Yang, J. W.; Kim, Y. G.; Han, H. Y., Synthesis of DNA triangles with vertexes of bis(terpyridine)iron(II) complexes. *J Am Chem Soc* **2004,** *126* (28), 8606-8607.

135. Kikuchi, T.; Sato, S.; Fujita, M., Well-Defined DNA Nanoparticles Templated by Self-Assembled M12L24 Molecular Spheres and Binding of Complementary Oligonucleotides. *J Am Chem Soc* **2010,** *132* (45), 15930-15932.
136. Mitra, D.; Di Cesare, N.; Sleiman, H. F., Self-assembly of cyclic metal-DNA nanostructures using ruthenium tris(bipyridine)-branched oligonucleotides. *Angew Chem Int Ed Engl* **2004,** *43* (43), 5804-8.
137. Mitchell, N.; Ebner, A.; Hinterdorfer, P.; Tampe, R.; Howorka, S., Chemical Tags Mediate the Orthogonal Self-Assembly of DNA Duplexes into Supramolecular Structures. *Small* **2010,** *6* (16), 1732-1735.
138. Megger, N.; Welte, L.; Zamora, F.; Muller, J., Metal-mediated aggregation of DNA comprising 2,2 '-bipyridine nucleoside, an asymmetrically substituted chiral bidentate ligand. *Dalton T* **2011,** *40* (8), 1802-1807.
139. Ehrenschwender, T.; Barth, A.; Puchta, H.; Wagenknecht, H. A., Metal-mediated DNA assembly using the ethynyl linked terpyridine ligand. *Org Biomol Chem* **2012,** *10* (1), 46-48.
140. Kalachova, L.; Pohl, R.; Bednarova, L.; Fanfrlik, J.; Hocek, M., Synthesis of nucleosides and dNTPs bearing oligopyridine ligands linked through an octadiyne tether, their incorporation into DNA and complexation with transition metal cations. *Org Biomol Chem* **2013,** *11* (1), 78-89.
141. Dupre, N.; Welte, L.; Gomez-Herrero, J.; Zamora, F.; Muller, J., Bipyridine-modified oligonucleotides: Aggregation in the presence of metal ions. *Inorg Chim Acta* **2009,** *362* (3), 985-992.
142. Burns, J. R.; Zekonyte, J.; Siligardi, G.; Hussain, R.; Stulz, E., Directed Formation of DNA Nanoarrays through Orthogonal Self-Assembly. *Molecules* **2011,** *16* (6), 4912-4922.
143. Stewart, K. M.; McLaughlin, L. W., Design and synthesis of DNA-tethered ruthenium complexes that self-assemble into linear arrays. *Chem Commun* **2003,** (23), 2934-2935.
144. Ghosh, S.; Pignot-Paintrand, I.; Dumy, P.; Defrancq, E., Design and synthesis of novel hybrid metal complex-DNA conjugates: key building blocks for multimetallic linear DNA nanoarrays. *Org Biomol Chem* **2009,** *7* (13), 2729-2737.
145. Stewart, K. M.; Rojo, J.; McLaughlin, L. W., Ru(II) tris(bipyridyl) complexes with six oligonucleotide arms as precursors for the generation of supramolecular assemblies. *Angew Chem Int Edit* **2004,** *43* (43), 5808-5811.
146. Stewart, K. M.; McLaughlin, L. W., Four-arm oligonucleotide Ni(II)-cyclam-centered complexes as precursors for the generation of supramolecular periodic assemblies. *J Am Chem Soc* **2004,** *126* (7), 2050-2057.
147. Yang, H.; Metera, K. L.; Sleiman, H. F., DNA modified with metal complexes: Applications in the construction of higher order metal-DNA nanostructures. *Coordin Chem Rev* **2010,** *254* (19-20), 2403-2415.
148. Ghosh, S.; Defrancq, E., Metal-Complex/DNA Conjugates: A Versatile Building Block for DNA Nanoarrays. *Chem-Eur J* **2010,** *16* (43), 12780-12787.
149. Bandy, T. J.; Brewer, A.; Burns, J. R.; Marth, G.; Nguyen, T.; Stulz, E., DNA as supramolecular scaffold for functional molecules: progress in DNA nanotechnology. *Chem Soc Rev* **2011,** *40* (1), 138-148.
150. McLaughlin, C. K.; Hamblin, G. D.; Sleiman, H. F., Supramolecular DNA assembly. *Chem Soc Rev* **2011,** *40* (12), 5647-5656.
151. Burgess, J.; Rangel, M., Hydroxypyranones, Hydroxypyridinones, and Their Complexes. *Adv Inorg Chem* **2008,** *60*, 167-243.

152. Liu, Z. D.; Hider, R. C., Design of iron chelators with therapeutic application. *Coordin Chem Rev* **2002,** *232* (1-2), 151-171.
153. Menyo, M. S.; Hawker, C. J.; Waite, J. H., Versatile tuning of supramolecular hydrogels through metal complexation of oxidation-resistant catechol-inspired ligands. *Soft Matter* **2013,** *9* (43), 10314-10323.
154. Ciupa, A.; De Bank, P. A.; Caggiano, L., Multicellular aggregation of maltol-modified cells triggered by Fe3+ ions. *Chem Commun* **2013,** *49* (86), 10148-10150.
155. Clarke, E. T.; Martell, A. E., Stabilities of 1,2-Dimethyl-3-Hydroxy-4-Pyridinone Chelates of Divalent and Trivalent Metal-Ions. *Inorg Chim Acta* **1992,** *191* (1), 57-63.
156. Chandele, A.; Prasad, V.; Jagtap, J. C.; Shukla, R.; Shastry, P. R., Upregulation of survivin in G2/M cells and inhibition of caspase 9 activity enhances resistance in staurosporine-induced apoptosis. *Neoplasia* **2004,** *6* (1), 29-40.
157. Holten-Andersen, N.; Harrington, M. J.; Birkedal, H.; Lee, B. P.; Messersmith, P. B.; Lee, K. Y. C.; Waite, J. H., pH-induced metal-ligand cross-links inspired by mussel yield self-healing polymer networks with near-covalent elastic moduli. *P Natl Acad Sci USA* **2011,** *108* (7), 2651-2655.
158. Albanese, A.; Tang, P. S.; Chan, W. C. W., The Effect of Nanoparticle Size, Shape, and Surface Chemistry on Biological Systems. *Annu Rev Biomed Eng* **2012,** *14*, 1-16.
159. Chithrani, B. D.; Ghazani, A. A.; Chan, W. C. W., Determining the size and shape dependence of gold nanoparticle uptake into mammalian cells. *Nano Lett* **2006,** *6* (4), 662-668.
160. Matsuura, K.; Yamashita, T.; Igami, Y.; Kimizuka, N., 'Nucleo-nanocages': designed ternary oligodeoxyribonucleotides spontaneously form nanosized DNA cages. *Chem Commun* **2003,** (3), 376-377.
161. Matsuura, K.; Masumoto, K.; Igami, Y.; Fujioka, T.; Kimizuka, N., In situ observation of spherical DNA assembly in water and the controlled release of bound dyes. *Biomacromolecules* **2007,** *8* (9), 2726-2732.
162. Li, Y. G.; Tseng, Y. D.; Kwon, S. Y.; D'Espaux, L.; Bunch, J. S.; Mceuen, P. L.; Luo, D., Controlled assembly of dendrimer-like DNA. *Nat Mater* **2004,** *3* (1), 38-42.
163. Zimmermann, J.; Cebulla, M. R. J.; Monninghoff, S.; von Kiedrowski, G., Self-assembly of a DNA dodecahedron from 20 trisoligonucleotides with C-3h linkers. *Angew Chem Int Edit* **2008,** *47* (19), 3626-3630.
164. Lee, D. S.; Qian, H.; Tay, C. Y.; Leong, D. T., Cellular processing and destinies of artificial DNA nanostructures. *Chem Soc Rev* **2016,** *45* (15), 4199-4225.
165. Vindigni, G.; Raniolo, S.; Ottaviani, A.; Falconi, M.; Franch, O.; Knudsen, B. R.; Desideri, A.; Biocca, S., Receptor-Mediated Entry of Pristine Octahedral DNA Nanocages in Mammalian Cells. *Acs Nano* **2016,** *10* (6), 5971-5979.
166. Nykypanchuk, D.; Maye, M. M.; van der Lelie, D.; Gang, O., DNA-guided crystallization of colloidal nanoparticles. *Nature* **2008,** *451* (7178), 549-552.
167. Zheng, D.; Seferos, D. S.; Giljohann, D. A.; Patel, P. C.; Mirkin, C. A., Aptamer Nano-flares for Molecular Detection in Living Cells. *Nano Lett* **2009,** *9* (9), 3258-3261.
168. Briley, W. E.; Bondy, M. H.; Randeria, P. S.; Dupper, T. J.; Mirkin, C. A., Quantification and real-time tracking of RNA in live cells using Sticky-flares. *P Natl Acad Sci USA* **2015,** *112* (31), 9591-9595.
169. Giljohann, D. A.; Seferos, D. S.; Prigodich, A. E.; Patel, P. C.; Mirkin, C. A., Gene regulation with polyvalent siRNA-nanoparticle conjugates. *J Am Chem Soc* **2009,** *131* (6), 2072-3.

170. Cutler, J. I.; Zhang, K.; Zheng, D.; Auyeung, E.; Prigodich, A. E.; Mirkin, C. A., Polyvalent nucleic acid nanostructures. *J Am Chem Soc* **2011,** *133* (24), 9254-7.
171. Cutler, J. I.; Zheng, D.; Xu, X. Y.; Giljohann, D. A.; Mirkin, C. A., Polyvalent Oligonucleotide Iron Oxide Nanoparticle "Click" Conjugates. *Nano Lett* **2010,** *10* (4), 1477-1480.
172. Wagner, K.; Kautz, A.; Roder, M.; Schwalbe, M.; Pachmann, K.; Clement, J. H.; Schnabelrauch, M., Synthesis of oligonucleotide-functionalized magnetic nanoparticles and study on their in vitro cell uptake. *Appl Organomet Chem* **2004,** *18* (10), 514-519.
173. Thompson, D. G.; Enright, A.; Faulds, K.; Smith, W. E.; Graham, D., Ultrasensitive DNA detection using oligonucleotide-silver nanoparticle conjugates. *Anal Chem* **2008,** *80* (8), 2805-2810.
174. Dougan, J. A.; Karlsson, C.; Smith, W. E.; Graham, D., Enhanced oligonucleotide-nanoparticle conjugate stability using thioctic acid modified oligonucleotides. *Nucleic Acids Res* **2007,** *35* (11), 3668-3675.
175. Lee, J. S.; Lytton-Jean, A. K. R.; Hurst, S. J.; Mirkin, C. A., Silver nanoparticle-oligonucleotide conjugates based on DNA with triple cyclic disulfide moieties. *Nano Lett* **2007,** *7* (7), 2112-2115.
176. Li, Y. L.; Duan, X.; Jing, L. H.; Yang, C. H.; Qiao, R. R.; Gao, M. Y., Quantum dot-antisense oligonucleotide conjugates for multifunctional gene transfection, mRNA regulation, and tracking of biological processes. *Biomaterials* **2011,** *32* (7), 1923-1931.
177. Sun, D. Z.; Gang, O., DNA-Functionalized Quantum Dots: Fabrication, Structural, and Physicochemical Properties. *Langmuir* **2013,** *29* (23), 7038-7046.
178. Rush, A. M.; Thompson, M. P.; Tatro, E. T.; Gianneschi, N. C., Nuclease-Resistant DNA via High-Density Packing in Polymeric Micellar Nanoparticle Coronas. *Acs Nano* **2013,** *7* (2), 1379-1387.
179. Chien, M. P.; Thompson, M. P.; Gianneschi, N. C., DNA-nanoparticle micelles as supramolecular fluorogenic substrates enabling catalytic signal amplification and detection by DNAzyme probes. *Chem Commun* **2011,** *47* (1), 167-169.
180. Lytton-Jean, A. K. R.; Langer, R.; Anderson, D. G., Five Years of siRNA Delivery: Spotlight on Gold Nanoparticles. *Small* **2011,** *7* (14), 1932-1937.
181. Dhar, S.; Daniel, W. L.; Giljohann, D. A.; Mirkin, C. A.; Lippard, S. J., Polyvalent Oligonucleotide Gold Nanoparticle Conjugates as Delivery Vehicles for Platinum(IV) Warheads (vol 131, pg 14652, 2009). *J Am Chem Soc* **2010,** *132* (48), 17335-17335.
182. Wei, M.; Chen, N.; Li, J.; Yin, M.; Liang, L.; He, Y.; Song, H. Y.; Fan, C. H.; Huang, Q., Polyvalent Immunostimulatory Nanoagents with Self-Assembled CpG Oligonucleotide-Conjugated Gold Nanoparticles. *Angew Chem Int Edit* **2012,** *51* (5), 1202-1206.
183. Patel, P. C.; Giljohann, D. A.; Daniel, W. L.; Zheng, D.; Prigodich, A. E.; Mirkin, C. A., Scavenger Receptors Mediate Cellular Uptake of Polyvalent Oligonucleotide-Functionalized Gold Nanoparticles. *Bioconjugate Chem.* **2010,** *21* (12), 2250-2256.
184. Rambanapasi, C.; Zeevaart, J. R.; Buntting, H.; Bester, C.; Kotze, D.; Hayeshi, R.; Grobler, A., Bioaccumulation and Subchronic Toxicity of 14 nm Gold Nanoparticles in Rats. *Molecules* **2016,** *21* (6).
185. Spokoyny, A. M.; Kim, D.; Sumrein, A.; Mirkin, C. A., Infinite coordination polymer nano- and microparticle structures. *Chem Soc Rev* **2009,** *38* (5), 1218-1227.
186. Lin, W. B.; Rieter, W. J.; Taylor, K. M. L., Modular Synthesis of Functional Nanoscale Coordination Polymers. *Angew Chem Int Edit* **2009,** *48* (4), 650-658.

187. Rieter, W. J.; Pott, K. M.; Taylor, K. M. L.; Lin, W. B., Nanoscale coordination polymers for platinum-based anticancer drug delivery. *J Am Chem Soc* **2008,** *130* (35), 11584-+.
188. Gao, P. F.; Zheng, L. L.; Liang, L. J.; Yang, X. X.; Li, Y. F.; Huang, C. Z., A new type of pH-responsive coordination polymer sphere as a vehicle for targeted anticancer drug delivery and sustained release. *J Mater Chem B* **2013,** *1* (25), 3202-3208.
189. Huxford, R. C.; deKrafft, K. E.; Boyle, W. S.; Liu, D. M.; Lin, W. B., Lipid-coated nanoscale coordination polymers for targeted delivery of antifolates to cancer cells. *Chem Sci* **2012,** *3* (1), 198-204.
190. Nurchi, V. M.; Crisponi, G.; Pivetta, T.; Donatoni, M.; Remelli, M., Potentiometric, spectrophotometric and calorimetric study on iron(III) and copper(II) complexes with 1,2-dimethyl-3-hydroxy-4-pyridinone. *J Inorg Biochem* **2008,** *102* (4), 684-692.
191. Szigethy, G.; Raymond, K. N., Influence of Linker Geometry on Uranyl Complexation by Rigidly Linked Bis(3-hydroxy-N-methyl-pyridin-2-one). *Inorg Chem* **2010,** *49* (14), 6755-6765.
192. Cho, S. H.; Gadzikwa, T.; Afshari, M.; Nguyen, S. T.; Hupp, J. T., [Bis(catechol)salen]Mn-III coordination polymers as support-free heterogeneous asymmetric catalysts for epoxidation. *Eur J Inorg Chem* **2007,** (31), 4863-4867.
193. Caulder, D. L.; Bruckner, C.; Powers, R. E.; Konig, S.; Parac, T. N.; Leary, J. A.; Raymond, K. N., Coordination number incommensurate cluster formation, part 21 - Design, formation and properties of tetrahedral M4L4 and M4L6 supramolecular clusters. *J Am Chem Soc* **2001,** *123* (37), 8923-8938.
194. Scarrow, R. C.; Riley, P. E.; Abudari, K.; White, D. L.; Raymond, K. N., Ferric Ion Sequestering Agents .13. Synthesis, Structures, and Thermodynamics of Complexation of Cobalt(Iii) and Iron(Iii) Tris Complexes of Several Chelating Hydroxypyridinones. *Inorg Chem* **1985,** *24* (6), 954-967.
195. Barrett, D. G.; Fullenkamp, D. E.; He, L. H.; Holten-Andersen, N.; Lee, K. Y. C.; Messersmith, P. B., pH-Based Regulation of Hydrogel Mechanical Properties Through Mussel-Inspired Chemistry and Processing. *Adv Funct Mater* **2013,** *23* (9), 1111-1119.
196. Menyo, M. S.; Hawker, C. J.; Waite, J. H., Rate-Dependent Stiffness and Recovery in Interpenetrating Network Hydrogels through Sacrificial Metal Coordination Bonds. *Acs Macro Lett* **2015,** *4* (11), 1200-1204.
197. Zhang, K.; Hao, L. L.; Hurst, S. J.; Mirkin, C. A., Antibody-Linked Spherical Nucleic Acids for Cellular Targeting. *J Am Chem Soc* **2012,** *134* (40), 16488-16491.
198. Prigodich, A. E.; Seferos, D. S.; Massich, M. D.; Giljohann, D. A.; Lane, B. C.; Mirkin, C. A., Nano-flares for mRNA Regulation and Detection. *Acs Nano* **2009,** *3* (8), 2147-2152.
199. Giljohann, D. A.; Seferos, D. S.; Daniel, W. L.; Massich, M. D.; Patel, P. C.; Mirkin, C. A., Gold Nanoparticles for Biology and Medicine. *Angew Chem Int Edit* **2010,** *49* (19), 3280-3294.
200. Kwak, M.; Herrmann, A., Nucleic Acid/Organic Polymer Hybrid Materials: Synthesis, Superstructures, and Applications. *Angew Chem Int Edit* **2010,** *49* (46), 8574-8587.
201. Kedracki, D.; Safir, I.; Gour, N.; Ngo, K. X.; Vebert-Nardin, C., DNA-Polymer Conjugates: From Synthesis, Through Complex Formation and Self-assembly to Applications. *Adv Polym Sci* **2013,** *253*, 115-149.
202. Alemdaroglu, F. E.; Alemdaroglu, N. C.; Langguth, P.; Herrmann, A., DNA block copolymer micelles - A combinatorial tool for cancer Nanotechnology. *Advanced Materials* **2008,** *20* (5), 899-+.

203. Jeong, J. H.; Park, T. G., Novel polymer-DNA hybrid polymeric micelles composed of hydrophobic poly(D,L-lactic-co-glycolic acid) and hydrophilic oligonucleotides. *Bioconjug Chem* **2001,** *12* (6), 917-23.
204. Yang, C. J.; Pinto, M.; Schanze, K.; Tan, W., Direct synthesis of an oligonucleotide-poly(phenylene ethynylene) conjugate with a precise one-to-one molecular ratio. *Angew Chem Int Ed Engl* **2005,** *44* (17), 2572-6.
205. Peng, L.; Wu, C. S.; You, M. X.; Han, D.; Chen, Y.; Fu, T.; Ye, M.; Tan, W. H., Engineering and applications of DNA-grafted polymer materials. *Chem Sci* **2013,** *4* (5), 1928-1938.
206. Fong, R. B.; Ding, Z. L.; Long, C. J.; Hoffman, A. S.; Stayton, P. S., Thermoprecipitation of streptavidin via oligonucleotide-mediated self-assembly with poly (N-isopropylacrylamide). *Bioconjugate Chem* **1999,** *10* (5), 720-725.
207. Oishi, M.; Nagasaki, Y.; Itaka, K.; Nishiyama, N.; Kataoka, K., Lactosylated poly(ethylene glycol)-siRNA conjugate through acid-labile ss-thiopropionate linkage to construct pH-sensitive polyion complex micelles achieving enhanced gene silencing in hepatoma cells. *J Am Chem Soc* **2005,** *127* (6), 1624-1625.
208. Isoda, K.; Kanayama, N.; Miyamoto, D.; Takarada, T.; Maeda, M., RAFT-generated poly(N-isopropylacrylamide)-DNA block copolymers for temperature-responsive formation of polymer micelles. *React Funct Polym* **2011,** *71* (3), 367-371.
209. Sonavane, G.; Tomoda, K.; Makino, K., Biodistribution of colloidal gold nanoparticles after intravenous administration: Effect of particle size. *Colloid Surface B* **2008,** *66* (2), 274-280.
210. Wu, X. C. A.; Choi, C. H. J.; Zhang, C.; Hao, L. L.; Mirkin, C. A., Intracellular Fate of Spherical Nucleic Acid Nanoparticle Conjugates. *J Am Chem Soc* **2014,** *136* (21), 7726-7733.
211. Lee, S. H.; Mok, H.; Lee, Y.; Park, T. G., Self-assembled siRNA-PLGA conjugate micelles for gene silencing. *J Control Release* **2011,** *152* (1), 152-158.
212. Chien, M. P.; Rush, A. M.; Thompson, M. P.; Gianneschi, N. C., Programmable Shape-Shifting Micelles. *Angew Chem Int Edit* **2010,** *49* (30), 5076-5080.
213. Woodruff, M. A.; Hutmacher, D. W., The return of a forgotten polymer-Polycaprolactone in the 21st century. *Prog Polym Sci* **2010,** *35* (10), 1217-1256.
214. Lenoir, S.; Riva, R.; Lou, X.; Detrembleur, C.; Jerome, R.; Lecomte, P., Ring-opening polymerization of alpha-chloro-is an element of-caprolactone and chemical modification of poly(alpha-chloro-is an element of-caprolactone) by atom transfer radical processes. *Macromolecules* **2004,** *37* (11), 4055-4061.
215. Riva, R.; Schmeits, S.; Jerome, C.; Jerome, R.; Lecomte, P., Combination of ring-opening polymerization and "click chemistry": Toward functionalization and grafting of poly(epsilon-caprolactone). *Macromolecules* **2007,** *40* (4), 796-803.
216. Lin-Vien, D. C., N. B.; Fateley, W. G.; Grasselli, J. G., *Handbook of Infrared and Raman Characteristic Group Frequencies*. Academic Press: London, 1991.
217. Filipe, V.; Hawe, A.; Jiskoot, W., Critical Evaluation of Nanoparticle Tracking Analysis (NTA) by NanoSight for the Measurement of Nanoparticles and Protein Aggregates. *Pharm Res-Dordr* **2010,** *27* (5), 796-810.
218. Domingos, R. F.; Baalousha, M. A.; Ju-Nam, Y.; Reid, M. M.; Tufenkji, N.; Lead, J. R.; Leppard, G. G.; Wilkinson, K. J., Characterizing Manufactured Nanoparticles in the Environment: Multimethod Determination of Particle Sizes. *Environ Sci Technol* **2009,** *43* (19), 7277-7284.

219. Jin, R. C.; Wu, G. S.; Li, Z.; Mirkin, C. A.; Schatz, G. C., What controls the melting properties of DNA-linked gold nanoparticle assemblies? *J Am Chem Soc* **2003,** *125* (6), 1643-1654.
220. Roehm, N. W.; Rodgers, G. H.; Hatfield, S. M.; Glasebrook, A. L., An Improved Colorimetric Assay for Cell-Proliferation and Viability Utilizing the Tetrazolium Salt Xtt. *J Immunol Methods* **1991,** *142* (2), 257-265.
221. Lassalle, V.; Ferreira, M. L., PLA nano- and microparticles for drug delivery: An overview of the methods of preparation. *Macromol Biosci* **2007,** *7* (6), 767-783.
222. Soppimath, K. S.; Aminabhavi, T. M.; Kulkarni, A. R.; Rudzinski, W. E., Biodegradable polymeric nanoparticles as drug delivery devices. *J Control Release* **2001,** *70* (1-2), 1-20.
223. Danhier, F.; Ansorena, E.; Silva, J. M.; Coco, R.; Le Breton, A.; Preat, V., PLGA-based nanoparticles: An overview of biomedical applications. *J Control Release* **2012,** *161* (2), 505-522.
224. Stockmans, G.; Deraedt, K.; Wildiers, H.; Moerman, P.; Paridaens, R., Triple-negative breast cancer. *Curr Opin Oncol* **2008,** *20* (6), 614-620.
225. Specht, J. M.; Mankoff, D. A., Advances in molecular imaging for breast cancer detection and characterization. *Breast Cancer Res* **2012,** *14* (2).
226. Bernardi, R.; Gianni, L., Hallmarks of triple negative breast cancer emerging at last? *Cell Res* **2014,** *24* (8), 904-905.
227. Zhao, Y. F.; Sultan, D.; Detering, L.; Cho, S. H.; Sun, G. R.; Pierce, R.; Wooley, K. L.; Liu, Y. J., Copper-64-Alloyed Gold Nanoparticles for Cancer Imaging: Improved Radiolabel Stability and Diagnostic Accuracy. *Angew Chem Int Edit* **2014,** *53* (1), 156-159.
228. Liu, Y. J.; Welch, M. J., Nanoparticles Labeled with Positron Emitting Nuclides: Advantages, Methods, and Applications. *Bioconjugate Chem* **2012,** *23* (4), 671-682.
229. Gabizon, A.; Bradbury, M.; Prabhakar, U.; Zamboni, W.; Libutti, S.; Grodzinski, P., Cancer nanomedicines: closing the translational gap. *Lancet* **2014,** *384* (9961), 2175-2176.
230. Phillips, E.; Penate-Medina, O.; Zanzonico, P. B.; Carvajal, R. D.; Mohan, P.; Ye, Y. P.; Humm, J.; Gonen, M.; Kalaigian, H.; Schoder, H.; Strauss, H. W.; Larson, S. M.; Wiesner, U.; Bradbury, M. S., Clinical translation of an ultrasmall inorganic optical-PET imaging nanoparticle probe. *Sci Transl Med* **2014,** *6* (260).
231. Benezra, M.; Penate-Medina, O.; Zanzonico, P. B.; Schaer, D.; Ow, H.; Burns, A.; DeStanchina, E.; Longo, V.; Herz, E.; Iyer, S.; Wolchok, J.; Larson, S. M.; Wiesner, U.; Bradbury, M. S., Multimodal silica nanoparticles are effective cancer-targeted probes in a model of human melanoma. *J Clin Invest* **2011,** *121* (7), 2768-2780.
232. Zhao, Y. F.; Sultan, D.; Detering, L.; Luehmann, H.; Liu, Y. J., Facile synthesis, pharmacokinetic and systemic clearance evaluation, and positron emission tomography cancer imaging of Cu-64-Au alloy nanoclusters. *Nanoscale* **2014,** *6* (22), 13501-13509.
233. Winnard, P. T.; Pathak, A. P.; Dhara, S.; Cho, S. Y.; Raman, V.; Pomper, M. G., Molecular imaging of metastatic potential. *J Nucl Med* **2008,** *49*, 96s-112s.
234. Singh, V.; Saunders, C.; Wylie, L.; Bourke, A., New diagnostic techniques for breast cancer detection. *Future Oncol* **2008,** *4* (4), 501-513.
235. Mankoff, D. A.; Link, J. M.; Linden, H. M.; Sundararajan, L.; Krohn, K. A., Tumor receptor imaging. *J Nucl Med* **2008,** *49*, 149s-163s.
236. Weigelt, B.; Peterse, J. L.; van't Veer, L. J., Breast cancer metastasis: Markers and models. *Nat Rev Cancer* **2005,** *5* (8), 591-602.

237. Velasco-Velazquez, M.; Jiao, X. M.; De la Fuente, M.; Pestell, T. G.; Ertel, A.; Lisanti, M. P.; Pestell, R. G., CCR5 Antagonist Blocks Metastasis of Basal Breast Cancer Cells. *Cancer Res* **2012,** *72* (15), 3839-3850.
238. Zhang, Y.; Lv, D. D.; Kim, H. J.; Kurt, R. A.; Bu, W.; Li, Y.; Ma, X. J., A novel role of hematopoietic CCL5 in promoting triple-negative mammary tumor progression by regulating generation of myeloid-derived suppressor cells. *Cell Res* **2013,** *23* (3), 394-408.
239. Lv, D. D.; Zhang, Y.; Kim, H. J.; Zhang, L. X.; Ma, X. J., CCL5 as a potential immunotherapeutic target in triple-negative breast cancer. *Cell Mol Immunol* **2013,** *10* (4), 303-310.
240. Velasco-Velazquez, M.; Pestell, R. G., The CCL5/CCR5 axis promotes metastasis in basal breast cancer. *Oncoimmunology* **2013,** *2* (4).
241. Velasco-Velazquez, M.; Xolalpa, W.; Pestell, R. G., The potential to target CCL5/CCR5 in breast cancer. *Expert Opin Ther Tar* **2014,** *18* (11), 1265-1275.
242. Kuijpers, W. H.; Bos, E. S.; Kaspersen, F. M.; Veeneman, G. H.; van Boeckel, C. A., Specific recognition of antibody-oligonucleotide conjugates by radiolabeled antisense nucleotides: a novel approach for two-step radioimmunotherapy of cancer. *Bioconjug Chem* **1993,** *4* (1), 94-102.
243. Goldenberg, D. M.; Chang, C. H.; Rossi, E. A.; McBride, W. J.; Sharkey, R. M., Pretargeted Molecular Imaging and Radioimmunotherapy. *Theranostics* **2012,** *2* (5), 523-540.
244. Knight, J. C.; Cornelissen, B., Bioorthogonal chemistry: implications for pretargeted nuclear (PET/SPECT) imaging and therapy. *Am J Nucl Med Mol Imaging* **2014,** *4* (2), 96-113.
245. Brudno, Y.; Silva, E. A.; Kearney, C. J.; Lewin, S. A.; Miller, A.; Martinick, K. D.; Aizenberg, M.; Mooney, D. J., Refilling drug delivery depots through the blood. *P Natl Acad Sci USA* **2014,** *111* (35), 12722-12727.
246. Lee, S. B.; Kim, H. L.; Jeong, H. J.; Lim, S. T.; Sohn, M. H.; Kim, D. W., Mesoporous Silica Nanoparticle Pretargeting for PET Imaging Based on a Rapid Bioorthogonal Reaction in a Living Body. *Angew Chem Int Edit* **2013,** *52* (40), 10549-10552.
247. Zeglis, B. M.; Sevak, K. K.; Reiner, T.; Mohindra, P.; Carlin, S. D.; Zanzonico, P.; Weissleder, R.; Lewis, J. S., A Pretargeted PET Imaging Strategy Based on Bioorthogonal Diels-Alder Click Chemistry. *J Nucl Med* **2013,** *54* (8), 1389-1396.
248. Rusckowski, M.; Qu, T.; Chang, F.; Hnatowich, D. J., Pretargeting using peptide nucleic acid. *Cancer* **1997,** *80* (12), 2699-2705.
249. Mallikaratchy, P.; Gardner, J.; Nordstrom, L. U. R.; Veomett, N. J.; McDevitt, M. R.; Heaney, M. L.; Scheinberg, D. A., A Self-Assembling Short Oligonucleotide Duplex Suitable for Pretargeting. *Nucleic Acid Ther* **2013,** *23* (4), 289-299.
250. Liu, G. Z.; Dou, S.; Pretorius, P. H.; Liu, X. R.; Rusckowski, M.; Hnatowich, D. J., Pretargeting CWR22 prostate tumor in mice with MORF-B72.3 antibody and radiolabeled cMORF. *Eur J Nucl Med Mol I* **2008,** *35* (2), 272-280.
251. Schubert, M.; Bergmann, R.; Forster, C.; Sihver, W.; Vonhoff, S.; Klussmann, S.; Bethge, L.; Walther, M.; Schlesinger, J.; Pietzsch, J.; Steinbach, J.; Pietzsch, H. J., Novel Tumor Pretargeting System Based on Complementary (L)-Configured Oligonucleotides. *Bioconjugate Chem* **2017,** *28* (4), 1176-1188.
252. Chen, X.; Dou, S.; Liu, G.; Liu, X.; Wang, Y.; Chen, L.; Rusckowski, M.; Hnatowich, D. J., Synthesis and in vitro characterization of a dendrimer-MORF conjugate for amplification pretargeting. *Bioconjug Chem* **2008,** *19* (8), 1518-25.

253. Lytton-Jean, A. K. R.; Mirkin, C. A., A thermodynamic investigation into the binding properties of DNA functionalized gold nanoparticle probes and molecular fluorophore probes. *J Am Chem Soc* **2005,** *127* (37), 12754-12755.
254. Prigodich, A. E.; Lee, O. S.; Daniel, W. L.; Seferos, D. S.; Schatz, G. C.; Mirkin, C. A., Tailoring DNA Structure To Increase Target Hybridization Kinetics on Surfaces. *J Am Chem Soc* **2010,** *132* (31), 10638-10641.
255. Luehmann, H. P.; Detering, L.; Fors, B. P.; Pressly, E. D.; Woodard, P. K.; Randolph, G. J.; Gropler, R. J.; Hawker, C. J.; Liu, Y. J., PET/CT Imaging of Chemokine Receptors in Inflammatory Atherosclerosis Using Targeted Nanoparticles. *J Nucl Med* **2016,** *57* (7), 1124-1129.
256. Prigodich, A. E.; Lee, O. S.; Daniel, W. L.; Seferos, D. S.; Schatz, G. C.; Mirkin, C. A., Tailoring DNA Structure To Increase Target Hybridization Kinetics on Surfaces (vol 132, 10638, 2010). *J Am Chem Soc* **2010,** *132* (45), 16296-16296.
257. Lesnik, E. A.; Freier, S. M., Relative thermodynamic stability of DNA, RNA, and DNA:RNA hybrid duplexes: relationship with base composition and structure. *Biochemistry* **1995,** *34* (34), 10807-15.
258. Wadas, T. J.; Wong, E. H.; Weisman, G. R.; Anderson, C. J., Coordinating Radiometals of Copper, Gallium, Indium, Yttrium, and Zirconium for PET and SPECT Imaging of Disease. *Chem Rev* **2010,** *110* (5), 2858-2902.
259. Walker, R. C.; Smith, G. T.; Liu, E.; Moore, B.; Clanton, J.; Stabin, M., Measured human dosimetry of 68Ga-DOTATATE. *J Nucl Med* **2013,** *54* (6), 855-60.
260. Lee, J. S.; Seferos, D. S.; Giljohann, D. A.; Mirkin, C. A., Thermodynamically controlled separation of polyvalent 2-nm gold nanoparticle-oligonucleotide conjugates. *J Am Chem Soc* **2008,** *130* (16), 5430-1.
261. Rockey, W. M.; Huang, L.; Kloepping, K. C.; Baumhover, N. J.; Giangrande, P. H.; Schultz, M. K., Synthesis and radiolabeling of chelator-RNA aptamer bioconjugates with copper-64 for targeted molecular imaging. *Bioorgan Med Chem* **2011,** *19* (13), 4080-4090.
262. Viel, T.; Boisgard, R.; Kuhnast, B.; Jego, B.; Siquier-Pernet, K.; Hinnen, F.; Dolle, F.; Tavitian, B., Molecular imaging study on in vivo distribution and pharmacokinetics of modified small interfering RNAs (siRNAs). *Oligonucleotides* **2008,** *18* (3), 201-12.
263. Karver, M. R.; Weissleder, R.; Hilderbrand, S. A., Synthesis and Evaluation of a Series of 1,2,4,5-Tetrazines for Bioorthogonal Conjugation. *Bioconjugate Chem* **2011,** *22* (11), 2263-2270.
264. Rosi, S.; Pert, C. B.; Ruff, M. R.; Mcgann-Gramling, K.; Wenk, G. L., Chemokine receptor 5 antagonist D-Ala-peptide T-amide reduces microglia and astrocyte activation within the hippocampus in a neuroinflammatory rat model of Alzheimer's disease. *Neuroscience* **2005,** *134* (2), 671-676.
265. Kim, Y.; Macfarlane, R. J.; Mirkin, C. A., Dynamically Interchangeable Nanoparticle Superlattices Through the Use of Nucleic Acid-Based Allosteric Effectors. *J Am Chem Soc* **2013,** *135* (28), 10342-10345.
266. Bamaby, S. N.; Ross, M. B.; Thaner, R. V.; Lee, B.; Schatz, G. C.; Mirkin, C. A., Enzymatically Controlled Vacancies in Nanoparticle Crystals. *Nano Lett* **2016,** *16* (8), 5114-5119.
267. Barnaby, S. N.; Thaner, R. V.; Ross, M. B.; Brown, K. A.; Schatz, G. C.; Mirkin, C. A., Modular and Chemically Responsive Oligonucleotide "Bonds" in Nanoparticle Superlattices. *J Am Chem Soc* **2015,** *137* (42), 13566-13571.

268. Alhasan, A. H.; Kim, D. Y.; Daniel, W. L.; Watson, E.; Meeks, J. J.; Thaxton, C. S.; Mirkin, C. A., Scanometric MicroRNA Array Profiling of Prostate Cancer Markers Using Spherical Nucleic Acid-Gold Nanoparticle Conjugates. *Anal Chem* **2012,** *84* (9), 4153-4160.
269. Kim, D.; Daniel, W. L.; Mirkin, C. A., Microarray-Based Multiplexed Scanometric Immunoassay for Protein Cancer Markers Using Gold Nanoparticle Probes. *Anal Chem* **2009,** *81* (21), 9183-9187.
270. Sprangers, A. J.; Hao, L. L.; Banga, R. J.; Mirkin, C. A., Liposomal Spherical Nucleic Acids for Regulating Long Noncoding RNAs in the Nucleus. *Small* **2017,** *13* (10).
271. Wang, Z. L., H.; Zhen, S.; He, N., Preparation of carboxyl group-modified palladium nanoparticles in an aqueous solution and their conjugation with DNA. *Nanoscale* **2012,** *4*, 3536.
272. White, E. E.; Pai, A.; Weng, Y.; Suresh, A. K.; Van Haute, D.; Pailevanian, T.; Alizadeh, D.; Hajimiri, A.; Badie, B.; Berlin, J. M., Functionalized iron oxide nanoparticles for controlling the movement of immune cells. *Nanoscale* **2015,** *7* (17), 7780-9.
273. Paunesku, T.; Rajh, T.; Wiederrecht, G.; Maser, J.; Vogt, S.; Stojicevic, N.; Protic, M.; Lai, B.; Oryhon, J.; Thurnauer, M.; Woloschak, G., Biology of TiO2-oligonucleotide nanocomposites. *Nat Mater* **2003,** *2* (5), 343-6.
274. Paunesku, T.; Vogt, S.; Lai, B.; Maser, J.; Stojicevic, N.; Thurn, K. T.; Osipo, C.; Liu, H.; Legnini, D.; Wang, Z.; Lee, C.; Woloschak, G. E., Intracellular distribution of TiO2-DNA oligonucleotide nanoconjugates directed to nucleolus and mitochondria indicates sequence specificity. *Nano Lett* **2007,** *7* (3), 596-601.
275. Wagner, K. K., A.; Röder, M.; Schwalbe, M.; Pachmann, K.; Clement, J. H.; Schnabelrauch, M., Synthesis of oligonucleotide-functionalized magnetic nanoparticles and study on their *in vitro* cell uptake. *Appl. Organomet. Chem.* **2004,** *18*, 514–519.
276. Chan, D. P. Y.; Deleavey, G. F.; Owen, S. C.; Damha, M. J.; Shoichet, M. S., Click conjugated polymeric immuno-nanoparticles for targeted siRNA and antisense oligonucleotide delivery. *Biomaterials* **2013,** *34* (33), 8408-8415.
277. Lytton-Jean, A. K. R.; Gibbs-Davis, J. M.; Long, H.; Schatz, G. C.; Mirkin, C. A.; Nguyen, S. T., Highly Cooperative Behavior of Peptide Nucleic Acid-Linked DNA-Modified Gold-Nanoparticle and Comb-Polymer Aggregates. *Advanced Materials* **2009,** *21* (6), 706-+.
278. Morris, W.; Briley, W. E.; Auyeung, E.; Cabezas, M. D.; Mirkin, C. A., Nucleic Acid-Metal Organic Framework (MOF) Nanoparticle Conjugates. *J Am Chem Soc* **2014,** *136* (20), 7261-7264.
279. Pokholenko, O. G., A.; Vialet, B.; Bathany, K.; Thiéry, A.; Barthélémy, P., Lipid oligonucleotide conjugates as responsive nanomaterials for drug delivery. *J. Mater. Chem. B* **2013,** *1*, 5329.
280. Mirkin, C. A., The Polyvalent Gold Nanoparticle Conjugate-Materials Synthesis, Biodiagnostics, and Intracellular Gene Regulation. *Mrs Bull* **2010,** *35* (7), 532-539.
281. Banga, R. J.; Krovi, S. A.; Narayan, S. P.; Sprangers, A. J.; Liu, G. L.; Mirkin, C. A.; Nguyen, S. T., Drug-Loaded Polymeric Spherical Nucleic Acids: Enhancing Colloidal Stability and Cellular Uptake of Polymeric Nanoparticles through DNA Surface-Functionalization. *Biomacromolecules* **2017,** *18* (2), 483-489.
282. Wei, M.; Chen, N.; Li, J.; Yin, M.; Liang, L.; He, Y.; Song, H.; Fan, C.; Huang, Q., Polyvalent immunostimulatory nanoagents with self-assembled CpG oligonucleotide-conjugated gold nanoparticles. *Angew Chem Int Ed Engl* **2012,** *51* (5), 1202-6.

283. Choi, C. H. J.; Hao, L.; Narayan, S. P.; Auyeung, E.; Mirkin, C. A., Mechanism for the endocytosis of spherical nucleic acid nanoparticle conjugates. *Proc. Natl. Acad. Sci. U. S. A.* **2013,** *110* (19), 7625-7630.
284. Chinen, A. B.; Guan, C. M.; Mirkin, C. A., Spherical Nucleic Acid Nanoparticle Conjugates Enhance G-Quadruplex Formation and Increase Serum Protein Interactions. *Angew Chem Int Edit* **2015,** *54* (2), 527-531.
285. Barnaby, S. N.; Perelman, G. A.; Kohlstedt, K. L.; Chinen, A. B.; Schatz, G. C.; Mirkin, C. A., Design Considerations for RNA Spherical Nucleic Acids (SNAs). *Bioconjugate Chem* **2016,** *27* (9), 2124-2131.
286. Zheng, D.; Giljohann, D. A.; Chen, D. L.; Massich, M. D.; Wang, X. Q.; Iordanov, H.; Mirkin, C. A.; Paller, A. S., Topical delivery of siRNA-based spherical nucleic acid nanoparticle conjugates for gene regulation. *P Natl Acad Sci USA* **2012,** *109* (30), 11975-11980.
287. Randeria, P. S.; Seeger, M. A.; Wang, X. Q.; Wilson, H.; Shipp, D.; Mirkin, C. A.; Paller, A. S., siRNA-based spherical nucleic acids reverse impaired wound healing in diabetic mice by ganglioside GM3 synthase knockdown. *P Natl Acad Sci USA* **2015,** *112* (18), 5573-5578.
288. Yu, B.; Zhao, X. B.; Lee, L. J.; Lee, R. J., Targeted Delivery Systems for Oligonucleotide Therapeutics. *Aaps J* **2009,** *11* (1), 195-203.
289. Song, L.; Guo, Y.; Roebuck, D.; Chen, C.; Yang, M.; Yang, Z. Q.; Sreedharan, S.; Glover, C.; Thomas, J. A.; Liu, D. S.; Guo, S. R.; Chen, R. J.; Zhout, D. J., Terminal PEGylated DNA-Gold Nanoparticle Conjugates Offering High Resistance to Nuclease Degradation and Efficient Intracellular Delivery of DNA Binding Agents. *Acs Appl Mater Inter* **2015,** *7* (33), 18707-18716.
290. Heasman, J., Morpholino oligos: making sense of antisense? *Dev Biol* **2002,** *243* (2), 209-14.
291. Paul, S.; Caruthers, M. H., Synthesis of Phosphorodiamidate Morpholino Oligonucleotides and Their Chimeras Using Phosphoramidite Chemistry. *J Am Chem Soc* **2016,** *138* (48), 15663-15672.
292. Karkare, S.; Bhatnagar, D., Promising nucleic acid analogs and mimics: characteristic features and applications of PNA, LNA, and morpholino. *Appl Microbiol Biot* **2006,** *71* (5), 575-586.
293. Morcos, P. A., Achieving efficient delivery of morpholino oligos in cultured cells. *Genesis* **2001,** *30* (3), 94-102.
294. Pattanayak, S.; Khatra, H.; Saha, S.; Sinha, S., A cationic morpholino antisense oligomer conjugate: synthesis, cellular uptake and inhibition of Gli1 in the hedgehog signalling pathway. *Rsc Adv* **2014,** *4* (4), 1951-1954.
295. Mellitzer, G.; Hallonet, M.; Chen, L.; Ang, S. L., Spatial and temporal 'knock down' of gene expression by electroporation of double-stranded RNA and morpholinos into early postimplantation mouse embryos. *Mech Develop* **2002,** *118* (1-2), 57-63.
296. Moulton, H. M., In Vivo Delivery of Morpholino Oligos by Cell-Penetrating Peptides. *Curr Pharm Design* **2013,** *19* (16), 2963-2969.
297. Wu, R. P.; Youngblood, D. S.; Hassinger, J. N.; Lovejoy, C. E.; Nelson, M. H.; Iversen, P. L.; Moulton, H. M., Cell-penetrating peptides as transporters for morpholino oligomers: effects of amino acid composition on intracellular delivery and cytotoxicity. *Nucleic Acids Res* **2007,** *35* (15), 5182-5191.

298. Deng, W.; Farnham, M. M. J.; Goldys, E. M.; Mohammed, S.; Pilowsky, P. M., Gene Interference with Morpholinos in a Gold Nanoparticle-Based Delivery Platform in Rat PC12 Cells. *J Biomed Nanotechnol* **2015,** *11* (12), 2111-2123.
299. Zu, Y. B.; Ting, A. L.; Gao, Z. Q., Visualizing Low-Level Point Mutations: Enzyme-like Selectivity Offered by Nanoparticle Probes. *Small* **2011,** *7* (3), 306-310.
300. Zu, Y. B.; Ting, A. L.; Yi, G. S.; Gao, Z. Q., Sequence-Selective Recognition of Nucleic Acids under Extremely Low Salt Conditions Using Nanoparticle Probes. *Anal Chem* **2011,** *83* (11), 4090-4094.
301. McKay, C. S.; Finn, M. G., Click Chemistry in Complex Mixtures: Bioorthogonal Bioconjugation. *Chem Biol* **2014,** *21* (9), 1075-1101.
302. Hill, H. D.; Millstone, J. E.; Banholzer, M. J.; Mirkin, C. A., The Role Radius of Curvature Plays in Thiolated Oligonucleotide Loading on Gold Nanoparticles. *Acs Nano* **2009,** *3* (2), 418-424.
303. Liu, Y. T.; Irving, D.; Qiao, W. Q.; Ge, D. B.; Levicky, R., Kinetic Mechanisms in Morpholino-DNA Surface Hybridization. *J Am Chem Soc* **2011,** *133* (30), 11588-11596.
304. Berg, J. M. T., J. L.; Stryer, L., The Michaelis-Menten Model Accounts for the Kinetic Properties of Many Enzymes. In *Biochemistry, 5th edition*, W H Freeman: New York, 2002.
305. Pinheiro, A. V.; Nangreave, J.; Jiang, S. X.; Yan, H.; Liu, Y., Steric Crowding and the Kinetics of DNA Hybridization within a DNA Nanostructure System. *Acs Nano* **2012,** *6* (6), 5521-5530.
306. Jiang, S. X.; Yan, H.; Liu, Y., Kinetics of DNA Tile Dimerization. *Acs Nano* **2014,** *8* (6), 5826-5832.
307. Kuhn, H.; Demidov, V. V.; Coull, J. M.; Fiandaca, M. J.; Gildea, B. D.; Frank-Kamenetskii, M. D., Hybridization of DNA and PNA molecular beacons to single-stranded and double-stranded DNA targets. *J Am Chem Soc* **2002,** *124* (6), 1097-1103.
308. Iyer, M.; Norton, J. C.; Corey, D. R., Accelerated Hybridization of Oligonucleotides to Duplex DNA. *J Biol Chem* **1995,** *270* (24), 14712-14717.
309. Johnson, B. J.; Algar, W. R.; Malanoski, A. P.; Ancona, M. G.; Medintz, I. L., Understanding enzymatic acceleration at nanoparticle interfaces: Approaches and challenges. *Nano Today* **2014,** *9* (1), 102-131.
310. Sorgenfrei, S.; Chiu, C. Y.; Gonzalez, R. L., Jr.; Yu, Y. J.; Kim, P.; Nuckolls, C.; Shepard, K. L., Label-free single-molecule detection of DNA-hybridization kinetics with a carbon nanotube field-effect transistor. *Nat Nanotechnol* **2011,** *6* (2), 126-32.
311. Markegard, C. B.; Gallivan, C. P.; Cheng, D. D.; Nguyen, H. D., Effects of Concentration and Temperature on DNA Hybridization by Two Closely Related Sequences via Large-Scale Coarse-Grained Simulations. *J Phys Chem B* **2016,** *120* (32), 7795-806.
312. Mills, R., Self-diffusion in normal and heavy water in the range 1-45.deg. *J. Phys. Chem.* **1973,** *77*, 685-688.
313. Summerton, J. E., Morpholinos and PNAs Compared. In *Peptide Nucleic Acids, Morpholinos and Related Antisense Biomolecules*, Janson, C. G. D., M. J., Ed. Klewer Academic / Plenum Publishers: New York, 2006.
314. Ray, M.; Lee, Y. W.; Scaletti, F.; Yu, R. J.; Rotello, V. M., Intracellular delivery of proteins by nanocarriers. *Nanomedicine-Uk* **2017,** *12* (8), 941-952.
315. Inoue, S.; Ding, H.; Portilla-Arias, J.; Hu, J. W.; Konda, B.; Fujita, M.; Espinoza, A.; Riley, S. S. M.; Gates, M.; Patil, R.; Penichet, M. L.; Ljubimov, A. V.; Black, K. L.; Holler, E.; Ljubimova, J. Y., Polymalic Acid-Based Nanobiopolymer Provides Efficient Systemic Breast

Cancer Treatment by Inhibiting both HER2/neu Receptor Synthesis and Activity. *Cancer Res* **2011,** *71* (4), 1454-1464.
316. Kuznik, N.; Wyskocka, M., Iron(III) Contrast Agent Candidates for MRI: a Survey of the Structure-Effect Relationship in the Last 15 Years of Studies. *Eur J Inorg Chem* **2016,** (4), 445-458.
317. Gorden, A. E. V.; Xu, J. D.; Raymond, K. N.; Durbin, P., Rational design of sequestering agents for plutonium and other actinides. *Chem Rev* **2003,** *103* (11), 4207-4282.
318. Lin, Y. H.; Fiskum, S. K.; Yantasee, W.; Wu, H.; Mattigod, S. V.; Vorpagel, E.; Fryxell, G. E.; Raymond, K. N.; Xu, J. D., Incorporation of hydroxypyridinone ligands into self-assembled monolayers on mesoporous supports for selective actinide sequestration. *Environ Sci Technol* **2005,** *39* (5), 1332-1337.
319. Yang, S.; Sun, S.; Zhou, C.; Hao, G.; Liu, J.; Ramezani, S.; Yu, M.; Sun, X.; Zheng, J., Renal clearance and degradation of glutathione-coated copper nanoparticles. *Bioconjug Chem* **2015,** *26* (3), 511-9.